

Hamid Taghavifar  
Aref Mardani

# Off-road Vehicle Dynamics

Analysis, Modelling and Optimization



Springer

# **Studies in Systems, Decision and Control**

Volume 70

## **Series editor**

Janusz Kacprzyk, Polish Academy of Sciences, Warsaw, Poland  
e-mail: kacprzyk@ibspan.waw.pl

### *About this Series*

The series “Studies in Systems, Decision and Control” (SSDC) covers both new developments and advances, as well as the state of the art, in the various areas of broadly perceived systems, decision making and control- quickly, up to date and with a high quality. The intent is to cover the theory, applications, and perspectives on the state of the art and future developments relevant to systems, decision making, control, complex processes and related areas, as embedded in the fields of engineering, computer science, physics, economics, social and life sciences, as well as the paradigms and methodologies behind them. The series contains monographs, textbooks, lecture notes and edited volumes in systems, decision making and control spanning the areas of Cyber-Physical Systems, Autonomous Systems, Sensor Networks, Control Systems, Energy Systems, Automotive Systems, Biological Systems, Vehicular Networking and Connected Vehicles, Aerospace Systems, Automation, Manufacturing, Smart Grids, Nonlinear Systems, Power Systems, Robotics, Social Systems, Economic Systems and other. Of particular value to both the contributors and the readership are the short publication timeframe and the world-wide distribution and exposure which enable both a wide and rapid dissemination of research output.

More information about this series at <http://www.springer.com/series/13304>

Hamid Taghavifar · Aref Mardani

# Off-road Vehicle Dynamics

## Analysis, Modelling and Optimization



Springer

Hamid Taghavifar  
Department of Mechanical Engineering  
in Biosystems  
Urmia University  
Urmia  
Iran

Aref Mardani  
Department of Mechanical Engineering  
in Biosystems  
Urmia University  
Urmia  
Iran

ISSN 2198-4182                   ISSN 2198-4190 (electronic)  
Studies in Systems, Decision and Control  
ISBN 978-3-319-42519-1       ISBN 978-3-319-42520-7 (eBook)  
DOI 10.1007/978-3-319-42520-7

Library of Congress Control Number: 2016945844

© Springer International Publishing Switzerland 2017

This work is subject to copyright. All rights are reserved by the Publisher, whether the whole or part of the material is concerned, specifically the rights of translation, reprinting, reuse of illustrations, recitation, broadcasting, reproduction on microfilms or in any other physical way, and transmission or information storage and retrieval, electronic adaptation, computer software, or by similar or dissimilar methodology now known or hereafter developed.

The use of general descriptive names, registered names, trademarks, service marks, etc. in this publication does not imply, even in the absence of a specific statement, that such names are exempt from the relevant protective laws and regulations and therefore free for general use.

The publisher, the authors and the editors are safe to assume that the advice and information in this book are believed to be true and accurate at the date of publication. Neither the publisher nor the authors or the editors give a warranty, express or implied, with respect to the material contained herein or for any errors or omissions that may have been made.

Printed on acid-free paper

This Springer imprint is published by Springer Nature  
The registered company is Springer International Publishing AG Switzerland

*The first author would like to dedicate  
this book to his family; parents, sister  
and two brothers.*

# Preface

Wheeled off-road vehicles are the vehicles subject to different nonlinear dynamic forces and moments due to nonlinear vehicle dynamics, complex terrain behavior, and irregular traversing surface that the vehicle is engaged with. Off-road vehicles are also considered among the major sources of energy dissipation and pollutant emission owing to their size and rough terrain irregularities they should overcome as well as their operating tasks. The discipline of Terramechanics deals with the development, design, and testing of off-road vehicles and dynamic interaction of the vehicles with their environment in particular tire–ground and wheel–road interactions. As an important subsystem of vehicle, tire has significant effect on the response of driver and road inputs. However, tire performance study is also sophisticated due to tires' composite structure and nonlinear material properties. The role of wheels on vehicle dynamics is considerable given that wheels are the unique elements that connect the vehicle body to the ground and they are subjected to all of the forces and torques applied to the vehicle. The steering, braking, acceleration, traction, handling, and stability are implemented through the wheels. Furthermore, they are a major subsystem of vehicle suspension system. In this manner, those who want to obtain a good understanding of vehicle dynamics have to achieve a good knowledge on wheel dynamics and this requisite is more drastic in the case of off-road vehicles due to the stochastic and nondeterministic wheel–ground interaction condition. Off-road vehicle dynamics is a dynamic system to analyze the traversing behavior of the vehicle over rough irregular terrains. A vehicle is comprised of various components functioning harmoniously and having dynamically interactions. Of these subsystems, propulsion and suspension systems substantially affect the vehicle dynamics. The vehicle performance, handling, and ride comfort are pivotal on aforesaid the important subsystems of the vehicle. However, it is noteworthy that the combination of the components acts as a lumped mass, e.g., in braking process for the reduction of the motion speed.

The classical studies on vehicle dynamics can address those of experimental, analytic, semi-empirical, and numerical approaches. Since the introduction of artificial intelligence, there is an ever-increasing trend toward the application of

different soft computing approaches to be applied in diversity of tasks such as modeling, optimization, and vehicle control strategies. Vehicle dynamics is about the modeling and mathematical description and analysis of vehicle systems based on mechanical concepts and theories. The main goal of this book is to practically overview the dynamics of off-road vehicle systems. The analysis of important mathematical models well agrees with the modeling of vehicle traveling parameters prior to the establishment a first prototype. The tendency to more quick steps toward the development, analysis, and modeling of more efficient vehicles with the optimal performance on rough terrains and the demand of large-sized vehicle designing from the engineers are also the fundamentals of this book that are presented.

This book is intended for students, engineers, and designers who are interested in the scope of off-road vehicle engineering. It provides the essential understanding applied in off-road vehicle dynamics and Terramechanics. This obtained knowledge can potentially serve to develop computer programs for analysis, modeling, and optimization of off-road vehicle dynamics using some state-of-the-art approaches of artificial intelligence. First, the role of Terramechanics and some basic fundamentals and terms are introduced as well as the apparatus for the measuring terrain behavior that is vital for the analysis of any soil-working machinery. Subsequently, tire modeling is presented as a very vital component of vehicle that has a great effect on vehicle dynamics. Different tire parameters are introduced and discussed, and the kinematics and dynamics of wheel are presented at different acceleration and deceleration regimes. While the reader is prepared to the comprehensive models of tire and terrain, the interaction between the wheel and the terrain for the variety of wheel and terrain conditions is covered. The performance of off-road vehicle is then presented through the parameters that influence the performances such as aerodynamic force, rolling resistance, gross traction, and vehicle–obstacle collision. Given this knowledge to the reader, different models of ride comfort from quarter-car, half-car, bicycle-car, and full-car models will be discussed. Stability of motioning and vehicle handling are then covered for different operating conditions. Energetic perspective of off-road vehicle mobility from sources of dissipation to the approaches to harvest/recapture energy from vehicle dynamics is also discussed. Application of different artificial intelligence tools on modeling and optimization is then presented with some case studies and examples with a comparative trend between different approaches and the applicability of such models. Finally, there will be some applied problems in vehicle dynamical systems.

Urmia, Iran  
Spring 2016

Hamid Taghavifar

# Contents

|                      |  |    |
|----------------------|--|----|
| <b>1</b>             | <b>Introduction to Off-road Vehicles . . . . .</b>                         | 1  |
| 1.1                  | Role of Terramechanics . . . . .   | 3  |
| 1.2                  | Basic Concepts in Terramechanics . . . . .                                 | 4  |
| 1.3                  | Characterization of Terrain Behaviour . . . . .                            | 10 |
| 1.3.1                | Elastic Medium. . . . .  | 10 |
| 1.3.2                | Plastic Region. . . . .  | 12 |
| 1.4                  | Identification of Soil Measuring Apparatus . . . . .                       | 13 |
| References . . . . . |  | 15 |
| <b>2</b>             | <b>Wheel and Terrain Interaction . . . . .</b>                             | 17 |
| 2.1                  | Identification of Wheel-Obstacle Collision . . . . .                       | 19 |
| 2.2                  | Tire Modeling . . . . .  | 25 |
| 2.2.1                | Forces and Moments . . . . .   | 29 |
| 2.2.2                | Tire Stiffness . . . . .   | 29 |
| 2.2.3                | Tire Footprint . . . . .   | 34 |
| 2.2.4                | Tire Road Modeling . . . . .   | 39 |
| 2.2.5                | Tire Rolling Resistance . . . . .  | 42 |
| 2.2.6                | Acceleration and Deceleration Characteristics Effects<br>of Tire . . . . . | 45 |
| References . . . . . |  | 51 |
| <b>3</b>             | <b>Performance of Off-road Vehicles . . . . .</b>                          | 53 |
| 3.1                  | Influential Parameters on Off-road Vehicle Performance . . . . .           | 59 |
| 3.1.1                | Aerodynamic Force . . . . .  | 60 |
| 3.1.2                | Rolling Resistance. . . . .  | 62 |
| 3.1.3                | Gross Thrust. . . . .  | 69 |
| 3.1.4                | Dynamic Wheel Loads. . . . .   | 70 |
| 3.2                  | Vehicle Dynamics on Deformable Terrain . . . . .                           | 71 |
| 3.2.1                | Longitudinal Slip and Shear Displacement of Flexible<br>Tire . . . . .     | 80 |
| 3.2.2                | Stresses and Forces of Flexible Tire . . . . .                             | 80 |
| 3.2.3                | Lateral Forces of Flexible Tire . . . . .                                  | 82 |

|          |  |            |
|----------|--|------------|
| 3.3      | Ride Comfort . . . . .   | 83         |
| 3.3.1    | Quarter Car Model . . . . .  | 84         |
| 3.3.2    | Bicycle Car Model . . . . .  | 86         |
| 3.3.3    | Half Car Model . . . . .   | 88         |
| 3.3.4    | Full Car Model . . . . .   | 91         |
| 3.4      | Stability of Motioning/Handling . . . . .  | 94         |
| 3.4.1    | Vehicle Handling Dynamics . . . . .  | 94         |
| 3.4.2    | Off-road Vehicle Stability . . . . .   | 100        |
|          | References . . . . .   | 104        |
| <b>4</b> | <b>Energetic Perspective of Off-road Vehicle Mobility . . . . .</b>  | <b>107</b> |
| 4.1      | Energy and Power Sources for Off-road Vehicle Mobility . . . . .   | 108        |
| 4.2      | Energy Dissipaters of Vehicle Vibrations (Energy Harvesting) . . . . .   | 109        |
| 4.2.1    | Energy Harvesting from Suspension . . . . .  | 109        |
| 4.2.2    | Tire Energy Harvesting . . . . .   | 118        |
| 4.2.3    | Brake Energy Harvesting . . . . .  | 124        |
| 4.3      | Energy Dissipaters Due to Vehicle Dynamics . . . . .   | 125        |
|          | References . . . . .   | 130        |
| <b>5</b> | <b>Application of Artificial Intelligence on Modeling and Optimization . . . . .</b>                                   | <b>133</b> |
| 5.1      | Introduction to Artificial Intelligence Tools . . . . .  | 134        |
| 5.2      | Modeling with Artificial Neural Networks, Support Vector Machines, and Adaptive Neuro-Fuzzy Inference System . . . . . | 136        |
| 5.2.1    | Artificial Neural Networks . . . . .   | 136        |
| 5.2.2    | Adaptive-Neuro Fuzzy Inference System (ANFIS) . . . . .  | 136        |
| 5.2.3    | Support Vector Regression . . . . .  | 140        |
| 5.2.4    | Takagi-Sugeno Type Neuro-Fuzzy Network with Modified Differential Evolution System . . . . .                           | 148        |
| 5.3      | Optimization with Heuristics and Meta-Heuristics . . . . .   | 157        |
| 5.3.1    | Imperialist Competitive Algorithm (ICA) . . . . .  | 157        |
| 5.3.2    | Genetic Algorithm . . . . .  | 163        |
| 5.3.3    | Particle Swarm Optimization . . . . .  | 164        |
| 5.4      | Application of Meta-Heuristics in Suspension Control . . . . .   | 170        |
|          | References . . . . .   | 176        |
| <b>6</b> | <b>Applied Problems . . . . .</b>  | <b>179</b> |

# Chapter 1

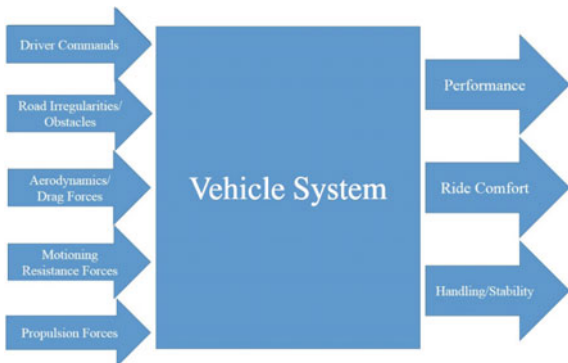
## Introduction to Off-road Vehicles

### Nomenclature

|           |                              |
|-----------|------------------------------|
| A         | Contact area                 |
| $\tau, s$ | Shear stress                 |
| $\sigma$  | Normal stress                |
| c         | Soil cohesion                |
| $\varphi$ | Soil internal friction angle |
| W         | Wheel load, load on a point  |
| $p_0$     | Uniform pressure             |
| z         | Soil sinkage                 |
| v         | Concentration factor         |

Off-road and on-road vehicles are two major subclasses of unguided ground vehicles which can freely traverse over ground usually by a driver if they are not controlled through programming and artificial intelligence. Off-road vehicles versus road vehicles are those which can travel over unpaved surfaces and are intended for extensive operational aims such as mining, civil engineering, transportation, agricultural machinery, military purposes and racing. Off-road vehicles are typically identified through their massive size, tire tread patterns, suspension system and power distribution between wheels. Off-road vehicles are differently treated when compared to road vehicles owing to the irregular surfaces and operational condition of the vehicle. Low ground pressure to avoid sinkage and continuous wheel-surface contact for the provision of uninterrupted traction are of deterministic characterizations of off-road vehicles. Wheeled vehicles approach the aforesaid criteria by having large or dual tires (e.g. for agricultural tractors) and flexible and long suspension as the former satisfies the low ground pressure criterion and the long and flexible suspension to let the wheels freely follow the road irregularities. For the tracked wheels, the adoption of wide and long tracks provide a lower ground pressure and flexible road wheels meet the need for a continuous contact. Each of tracked and wheeled vehicles has the inherent advantages and disadvantages and therefore; the selection of tracked versus wheeled vehicle is pivotal on the objective and suitability. Most off-road vehicles adopt special low gearing system, additional

**Fig. 1.1** Schematic understanding of the vehicle system tradeoff between different input/outputs



gearbox, reduction drive or torque converters to make the most of the engine's available power while traversing over soft deformable terrains. Off-road wheeled vehicles are represented through steerable wheels that are fitted to a rigid body. Many wheeled off-road vehicles have four-wheel drive to keep traction on surfaces which cause greater tire slip. However, the variability from 4WD to 2WD is efficient for travelling over paved roads to achieve lower energy loss and improved mobility. In addition to the complex off-road vehicle performance, the ride comfort, stability, handling and vibration analysis are more or at the very least are equally important for on-road vehicle travelling. The performance is mainly characterized by the acceleration, deceleration, tractive parameters such as drawbar pull, net traction, etc., passing through road irregularities and cleats. Handling and stability are two closely interconnected terms as we expect the vehicle to react promptly and preferably to the operator command while the stability is how the vehicle travels smoothly with the external loads and interruptions are exerted to the system. Ride comfort is concerned with the study of the vehicle response to the vibrations created by road irregularities and obstacles and also the effect of the vibration on the driver and passengers. As previously mentioned, there are three major tasks that the vehicle is expected to provide as affected by different inputs. Figure 1.1 presents a schematic understanding of the vehicle system tradeoff between different input/outputs.

To put in a nutshell, off-road vehicle dynamics is a dynamic system to analyze the traversing behavior of the vehicle over rough irregular terrains. A vehicle is comprised of various components functioning harmoniously and having dynamically interactions. Of these subsystems, propulsion and suspension systems substantially affect the vehicle dynamics. The vehicle performance, handling, and ride comfort are pivotal on aforesaid the important subsystems of the vehicle. However, it is noteworthy that the combination of the components acts as a lumped mass e.g. in braking process for the reduction of the motion speed. Thus, the vehicle can be represented with a lumped mass in the center of mass characterized with inertia of mass. However, for the vibrational analysis of the vehicle, the multibody system is considered while the wheels are represented by separate masses forming unsprung masses.

## 1.1 Role of Terramechanics

A great portion of economical investments and budgeting for developing and developed countries falls within the scope of military, construction, transport and agriculture equipment that justify why one should consider the industry of off-road vehicles. Terramechanics is a technical term that refers to the interaction between the terrain and vehicles but broadly addresses the designing, manufacturing, and development of the soil working machinery (e.g. agricultural machinery) and the response of the vehicle to the terrain characteristics. The concept of Terramechanics was first laid the foundation by Bekker (1956) with the "*Theory of land locomotion*". The terrain-vehicle mechanics as the prime interest for the community both centers on the vehicle response to the terrain inputs as well as terrain reaction to the vehicle feedback. Terramechanics also considers the off-road vehicle multi-body dynamics as affected by ground condition. The scope is dedicated to the designing, and equipment utilization in the field of off-road vehicle and soil working machinery and their subsystems. The basic ideology of Terramechanics is to improve the understanding in terrain-vehicle systems for advancements in engineering practice and innovation, energy conservation, and sustainable development. The problem formulation, setting standards, physical-mechanical synthesis of terrain-vehicle interactions by variety of approaches from experimental to analytic are of significant subject coverage. Terramechanics can serve as a functional catalyst for the designing and optimization of vehicle subsystems and components such as suspension system, steering, power driveline, the size and power of a heavy duty vehicle, and overall performance-ride comfort-stability of the vehicle. It simultaneously considers the terrain properties as a result of the interaction of wheeled or tracked vehicles on various surfaces. The surfaces include snow, soft soil, forestry, wet terrain, etc., and extraterrestrial device traveling atmosphere such as that of Mars rovers.

Terramechanics takes the role as a significant element in the chain of engineer-manufacturer-user chain to increase to usability, optimal design and performance, handling, ride and safety. The latter term, *i.e.* safety, acts as a very crucial criterion to rate any type of run-off-road vehicle owing to a great portion of reported casualties in the scope of vehicles dealing with off-road vehicles. The safety factor is about a reliable designing and performance of vehicle is important to ensure from the overturn avoidances such as pitching, yawing and rolling (Fig. 1.2). As appreciated from Fig. 1.2, in the Cartesian coordinate system, the vehicle motion has six independent degrees of freedom including vertical motion in  $y$  direction, horizontal motion in  $x$  direction, left and right motion in  $z$  direction, rolling motion around  $x$ -axis, pitching motion around  $z$ -axis, and yawing motion around  $y$ -axis.

In general, how to control the vehicle motion in the above mentioned 6 degrees of freedom is a matter of discussion for one major aspect of terramechanics, *i.e.* vehicle reaction to operator-surface inputs. It is noteworthy that the forces and moments oriented in all directions are not those related to the steerability while  $x$ -directional forces correspond to those of acceleration/deceleration, and tractive forces. Vehicle motion in  $y$ -direction is pivotal on the imposed vibrations in

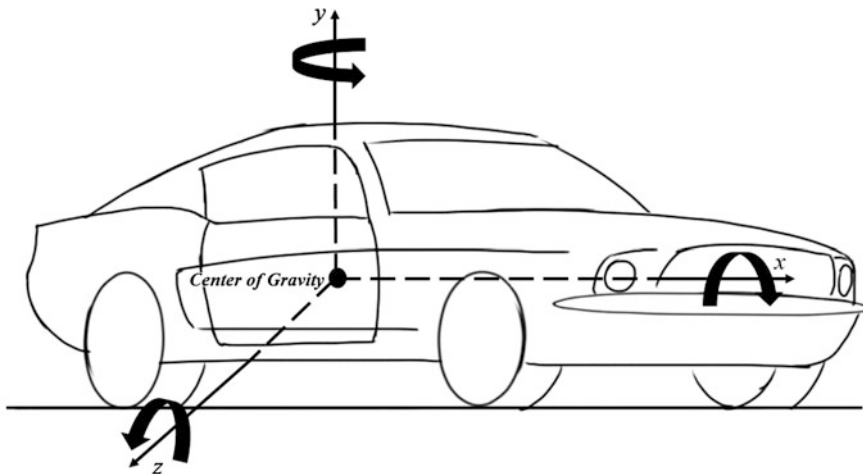


**Fig. 1.2** Vehicle motion six independent degrees of freedom

irregular terrain. The yaw and z-oriented motions, are products of the vehicle steering while this can create the rolling motion; however, this can occur due to road irregularities as well. The lateral forces are also the function of traveling in slope, wind banks, maneuvering/cornering and offset attachment of agricultural implements/tools to the tractors. The running gear plays as the center of attention in Terramechanics from off-road vehicle engineering point of view since it is the only element to make a continuous contact between the vehicle and the terrain. Power distribution and transmission to the driving wheels is of the greatest importance for vehicle performance, kinetics and kinematics simultaneously. On the other side, the steerability and ride comfort, which this book covers mainly, are pivotal on the running gears and therefore, off-road vehicle dynamics is to the greatest extremes depending on vehicle wheels. For typical vehicles, motions are controlled by the driver, while for the run-off-road vehicles, the motion is differently treated by numerous factors. For the on-road vehicles, the lateral, yaw, and roll motions of the vehicle are all generated by the driver's steering based on its dynamic characteristics.

## 1.2 Basic Concepts in Terramechanics

While soil-wheel interaction is of those complex, nonlinear and stochastic phenomena, there are different studies and models to describe the phenomenon in a branch of mechanical engineering discipline, so-called Terramechanics, with the foundation laid on mechanical theories of soil profile such as elasticity and plasticity theories.

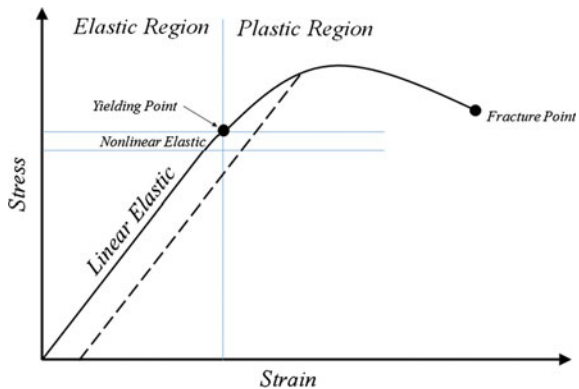
Terramechanics deals with the investigation regarding how the vehicle interacts with the surface it is traveling on, terrain in this case, and the performance of vehicle and its effect on the ground. It includes the fundamental aspects of soil mechanics, vehicle-terrain interaction, performance characteristics of off-road wheeled vehicles, and mechanics of pneumatics tires. In other words, the terminology can be described as the analyses of the dynamic relationship between wheel and the surface beneath (terrain).

The mechanical characteristics of the terrain profile under compression/tension loading that is under the vehicle tires and/or is affected by enables the researchers to estimate the combined vehicle terrain behavior. It is worth to note that soil profile refers to a geometric representation of a terrain surface as an elevation distance curve. There are studies documented in the literature to reveal the complex relationship between the very many characteristics of the terrain and those of the vehicle. The design of the size and shape of tires and tire parameters is very significant while vehicles are required to run over unpaved grounds. This field also attempts to avoid vehicles to experience great sinkage in very soft terrain or snow textures that the bearing capacity for them might be far below than that of the load they are applied. In order to cope with the sinkage difficulty, it is required to gain a comprehensive understanding of the vehicle/ground interaction from dynamics and kinetics perspective as well as the strength of material (for soil medium to provide traction/braking forces, rolling resistance and sinkage phenomenon). On this basis, the identification and comprehensive modeling of the terrain characteristics and the parameters that are closely interacted with vehicle performance are of the basic works in Terramechanics and still of dynamic fields of studying interest. This is a very controversy scope since there should be made a tradeoff between the maximum vehicle performance and minimum detrimental effect on the environment (i.e. ground). A combined quantitative and qualitative analysis is thus needed to first determine the governing condition in terrain profile and how the results could be fed as an input to the vehicle system to optimize the vehicle motion stability and performance.

An important topic is how the terrain reacts to the load applied from the off-road vehicle. Different strategies in past were adopted for terrain modelling such as considering terrain as either of elastic medium or a rigid profile and if the terrain was in irreversible condition, the plastic material theorem was more in use, however, the elasticity theory laid a proper foundation for the development of most of theoretical investigations dealing with dense soil but this had the limitation of not exceeding the soil bearing capacity from which on, the plastic theory could justify the soil rupture (failure) phenomenon that could provide the maximum limit for the traction force for a vehicle. The stress-strain curve in elastic and plastic regions is demonstrated in Fig. 1.3.

Also, critical state soil mechanics being developed based on homogeneous and isotropic assumptions play a substantial role in estimating the maximum force acting on a profile that the terrain can support as well as predicting terrain deformation. A privilege of such a method is that it is valid for an extensive range of

**Fig. 1.3** Typical soil stress-strain curve for elastic and plastic regions



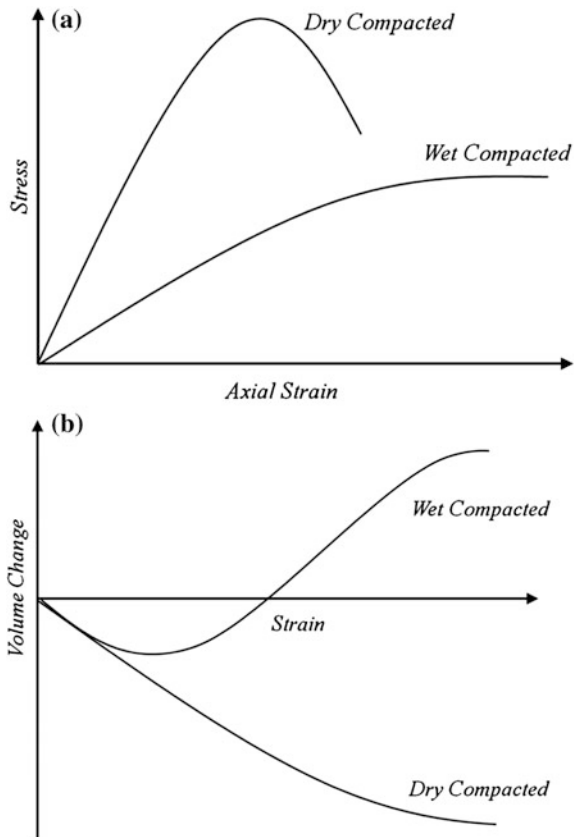
operational modes such as loose to compacted soil but limited to homogeneous and isotropic soil forum.

The attempts so far to adopt numerical based computational methods such as finite element method has failed due to unavailability of some certain deterministic characteristics to be attributed to the finite element parameters and also the non-realistic assumption that soil is always behaving as a continuum medium and thus failing to model discontinued soil deformations. Also for granular particulate soil forum, discrete element method has gained popularity particularly for the studies related to rigid wheel based vehicles such as Mars rovers where the wheels are equipped to grousers. The interaction between the grouser and particles are influential on the overall vehicle performance and stability as well as wheel sinkage in the soil medium. Discrete element method still needs to include the development of a consistent method for determining the quantities of model parameters to realistically represent terrain properties in the field.

Figure 1.4 shows the soil shear stress versus strain in two soil modes of wet compacted and dry compacted. As it can be appreciated from Fig. 1.4, the soil stress curve is dependent on the soil condition and it can provide how it can provide a reliable support for creating traction force. The contracting volume change tends towards a constant value or asymptote is shown in Fig. 1.4. This behavior is common for consolidated clays and loosely accumulated sandy soils. Similarly, the expansive volume change occurs with an expanding phase following an initial decreasing volume change. These hump type behaviors can be usually observed in over-consolidated clays and in compacted sandy soils.

When the vehicle is in one among three possible modes of self-propelling, driving/braking state, or free running, consideration of the vehicle in motion is needed because the running gear (wheel) should satisfactorily yield the shear resistance of the soil which is necessary to provide the necessary thrust or drag. To confirm these products, an appropriate design of the grouser shape of the track and an appropriate selection of pressure distribution as well as the tread pattern and axle load of the tire is needed.

**Fig. 1.4** a shear stress versus strain and b volume change versus strain curves for two soil types



While the net traction force (so-called drawbar pull) is in demand and while the force to override obstacles is needed. This is also valid for the rolling resistance determination that includes the slope resistance, tire deflection and soil deformation processes.

In the concepts of an off-road vehicle it should be distinguished between road and terrain and their outcome on vehicle motion. In the case that the strength and deformation of terrain material can offer the essential flotation and traction to save a vehicle in constant motion and provide the required tractive force, terrain texture characteristics can establish another factor which could limit vehicle velocity, or even create total vehicle control. These factors can be categorized as (a) slope, (b) obstacles, and (c) roughness.

- Slope: In Terramechanics terminology, slope can be the surface up to a vertical wall and side banks while roads do not exceed 18 % [1]. Rolling resistance rises due to the gravitational component of the vehicle along the slope and the torque on the wheels has to be augmented by a great torque of the engine or by the power transmission in the power driveline.

- (b) Obstacles that includes surface features and impediments to vehicles with any kind of natural or manmade road irregularities that bring about a vehicle to move with disturbances and availability of additional traction force to keep up the motion at a constant pace. Also, the shocking forces between the wheel and obstacle can drastically affect the vehicle. Obstacle is also described as definable environmental feature that inhibits the movement of a vehicle while lateral, longitudinal and vertical obstacles are defined as an unsurmountable terrain feature or a combination of such features that forces a vehicle to deviate laterally from a desired path, a surmountable terrain feature that inhibits the movement of a surface vehicle by forcing it to slow down as the feature is negotiated, and a longitudinal obstacle that forces a vehicle to move in the vertical plane while surmounting it, respectively.
- (c) Roughness that is defined as random ground surface irregularities, which are the source of vibrations to the vehicle body through the tire/wheel assembly and at last to the crew. Surface roughness can be described using statistical methods for collecting data of the profile of the ground surface (power spectral density). Terrain data are collected in terms of elevation at regular intervals using land survey or aerial photography techniques and calculated as the root mean square (RMS) of the terrain roughness.

The vehicle physical characteristics of are issues that are essential to define its geometry, size, shape, weight, operational conditions in a variety of environments. The vehicles based on their running gear types are categorized as: Wheeled vehicles, Tracked vehicles and other types such as pneumatic track and walking machines while the terms needed to describe the vehicle and its components have been divided into two major groups: (a) general vehicle terms, and (b) traction and transport element terms. Traction and transport element terms have been subcategorized to deal with the all abovementioned types of vehicles [2].

Vehicle angle of approach in this manner is the maximum angle, equal to or less than  $90^\circ$ , that can be formed by the intersection of the vehicle contact plane and a plane tangent to the forward part of the foremost traction or transport elements and touching the foremost part of the vehicle body while vehicle angle of departure in contradictory is the maximum angle, equal to or less than  $90^\circ$ , that can be formed by the intersection of the vehicle contact plane and a plane tangent to the rearward part of the rearmost traction or transport elements and touching the rearmost part of the vehicle body.

Articulated system is a system in which the steering forces are generated by yaw interaction between two or more units of the vehicle while Skid is a system whereby tracked and wheeled vehicles are steered when the tracks or wheels have no angular freedom in relation to the vehicle hull, steering being effected by changing the relative speeds of the running gear on each side of the vehicle [2].

Internal motion resistance is the resistance to movement of a vehicle provided by the internal friction of its moving parts and the energy losses in the traction elements total motion resistance is the sum of internal and external motion resistance.

The soil physical characteristics can be further described based on ISTVS standards as following [3]:

Adhesion,  $C_a$ , is shearing resistance between soil and another material under zero externally applied pressure.

Angle of internal friction,  $\varphi$  is the angle between the abscissa and the tangent of the curve representing the relationship of shearing resistance to normal stress acting within a soil.

Angle of repose,  $\alpha$ , is the angle between the horizontal and the maximum slope that a soil assumes through natural processes.

Atterberg limits is the moisture content limits used for separating the solid, semisolid, plastic, and semiliquid phases of soil.

Bearing capacity is the average load per unit of area required to produce failure by rupture of a supporting soil mass.

Coefficient of (external) friction,  $\mu$ , is the ratio between the shearing resistance due to friction and the normal stress acting on the contact area between the soil and another material.

Cohesion,  $c$  is the portion of the shear strength of a soil indicated by the term  $c$ , in Coulomb's equation.

Cohesionless soil is a soil that has shearing strength due primarily to internal friction and has negligible cohesion. This soil can be identified as having little or no cohesion when submerged.

Cohesive-frictional soil is a soil that has shearing strength attributable both to cohesion and to internal friction.

Cohesive soil is a soil that has shearing strength due primarily to cohesion and negligible internal friction. This soil can be identified as having significant cohesion when submerged.

Compaction is the densification of soil by means of mechanical manipulation which results in the reduction of air voids in the soil. Cone index, CI. An index of soil strength generally obtained with the WES cone penetrometer.

Coulomb's equation is the relationship between the shearing strength,  $s$ , of soil and the effective stress,  $\sigma$ , on an internal surface. The equation is written  $s = c + \sigma \tan \varphi$  where  $c$  is cohesion and  $\varphi$  is angle of internal friction.

Plasticity is the property of a soil which allows it to be deformed beyond the point of recovery without cracking or appreciable volume change [la]. Plasticity index, PI. The numerical difference between the liquid limit, LL, and the plastic limit, Sinkage, z, is the distance from the lowest point on the track or wheel to the undisturbed soil or snow surface measured normal to the surface.

Soil trafficability is the capacity of soil to withstand the passage of vehicles.

### 1.3 Characterization of Terrain Behaviour

#### 1.3.1 Elastic Medium

As appreciated from Fig. 1.5, for the loads applied to the soil that does not exceed the yielding point, the soil behavior is more likely to be expressed as linear/nonlinear elastic material. Estimation of stress distribution in the soil medium can be justified using the theory of elasticity and the modeled stress distribution in a homogeneous, isotropic semi-infinite elastic medium subject to different forms of loading that can be simplified by a point load can be carried out using the Boussinesq equation that defines the vertical stress and radial stress as following:

If  $r = \sqrt{x^2 + y^2}$  and  $R = \sqrt{z^2 + r^2}$ , then:

$$\sigma_z = \frac{3W}{2\pi \left[ 1 + (r/z)^2 \right]^{5/2} z^2} = \frac{3W}{2\pi R^2} \left( \frac{z}{R} \right)^3 = \frac{3W}{2\pi R^2} \cos^3 \theta \quad (1.1)$$

$$\sigma_r = \frac{3W}{2\pi R^2} \cos \theta \quad (1.2)$$

Based on this model, the amount of stress in a function of distance from the point that the load is applied and the amount of load but soil characteristics and the elastic behavior of the soil are ignored. Another drawback of this model is that it is limited to the distances not in the vicinity of the point that the load is applied because the

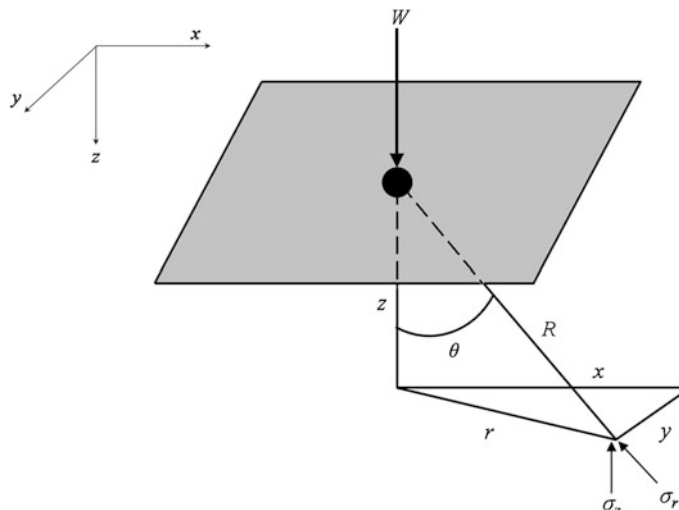


**Fig. 1.5** Stresses in a semi-infinite elastic medium subject to a point load on the surface

material in the vicinity of the point load does not exhibit elastic behavior [4]. The load applied on the contact area can be obtained by accumulation of some discrete point loads using superposition effect as following:

If in the Eq. 1.1,  $dW = p_0 dA$  is replaced, then:

$$d\sigma_z = \frac{3p_0 r dr d\theta}{2\pi \left[1 + (r/z)^2\right]^{5/2} z^2} \quad (1.3)$$

And by a double integration calculation in the polar coordinate [5]

$$\sigma_z = \frac{3p_0}{2\pi} \int_0^{r_0} \int_0^{2\pi} \frac{r dr d\theta}{\left[1 + (r/z)^2\right]^{5/2} z^2} = 3p_0 \int_0^{r_0} \frac{r dr}{\left[1 + (r/z)^2\right]^{5/2} z^2} \quad (1.4)$$

Another important topic of interest is the distribution of stresses in a semi-infinite elastic medium under the action of a strip load on the surface where uniform pressure  $p_0$  over a strip of infinite length and of constant width  $b$  is presented as following [5]:

$$\begin{aligned} \sigma_x &= \frac{p_0}{\pi} (\theta_2 - \theta_1 + \sin \theta_1 \cos \theta_1 - \sin \theta_2 \cos \theta_2) \\ \sigma_z &= \frac{p_0}{\pi} (\theta_2 - \theta_1 - \sin \theta_1 \cos \theta_1 + \sin \theta_2 \cos \theta_2) \\ \tau_{xz} &= \frac{p_0}{\pi} (\sin^2 \theta_2 - \sin^2 \theta_1) \end{aligned} \quad (1.5)$$

The points in the medium that experience the same level of stress may be described in the form of a family of isostress lines (or surfaces), commonly referred to as pressure bulbs (Fig. 1.6).

Observations have revealed that the stress distribution in the soil profile is different from that modeled using the Boussinesq equation, dependent on terrain conditions [6]. There is a tendency for the stress in the terrain to concentrate around the central axis of the loading area and becomes greater as the moisture content of the terrain increases. On this basis, various semi-empirical factors (or parameters) have been introduced to the Boussinesq equation, to account for the behavior of different types of terrain. For instance, Frohlich introduced a concentration factor  $v$  to the Boussinesq equation and introducing the concentration factor  $v$ , the expressions for the vertical and radial stresses in the terrain due to a point load applied on the surface take the following forms [4]:

$$\begin{aligned} \sigma_z &= \frac{vW}{2\pi R^2} (\cos^v \theta) = \frac{vW}{2\pi z^2} (\cos^{v+2} \theta) \\ \sigma_r &= \frac{vW}{2\pi R^2} (\cos^{v-2} \theta) = \frac{vW}{2\pi R^2} (\cos^v \theta) \end{aligned} \quad (1.6)$$

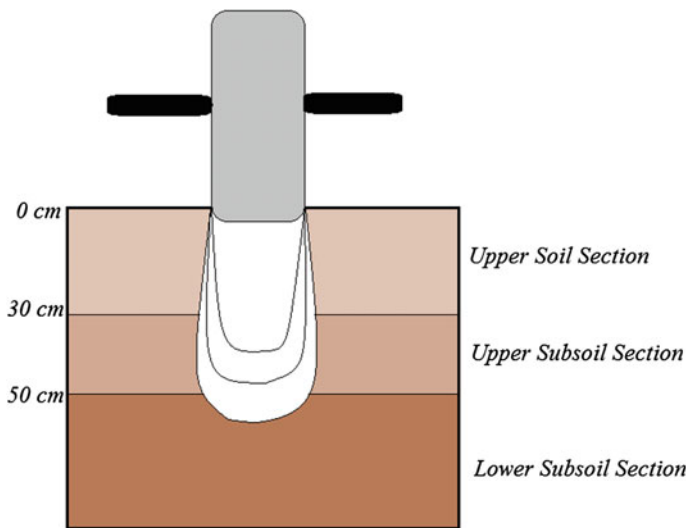


**Fig. 1.6** Distribution of vertical stresses in a semi-infinite elastic medium under a wheeled vehicle

The value of  $v$  depends on the type of terrain and on its moisture content. For instance, for hard, dry soil, the value of  $v$  is 4; for farm soil with normal density and moisture content, the value of  $v$  is 5; and for wet soil, the value of  $v$  may be 6 [6].

### 1.3.2 Plastic Region

In the plasticity region, there are some criteria that have been adopted or developed for defining the failure of terrain, among which, the Mohr-Coulomb failure criterion is one of the most common ones. It assumes that soil will fail at a point in the condition that the shear stress at that point can be in accordance with the following equation:

$$\tau = c + \sigma \tan \phi \quad (1.7)$$

where  $\tau$  is shear stress,  $c$  is the cohesion,  $\sigma$  is the normal stress on the shearing surface, and  $\phi$  is the angle of internal shearing resistance of the material.

The meaning of the Mohr-Coulomb failure criterion may be further illustrated with the aid of the Mohr circle of stress. If specimens of a terrain material are subject to different states of stress, for each mode of failure a Mohr circle can be constructed, as shown in Fig. 1.7:

If a straight line is drawn to envelope the set of Mohr circles so obtained with cohesion of the terrain defined by the intercept of the straight line with the shear stress axis and the angle of internal shearing resistance being represented by the

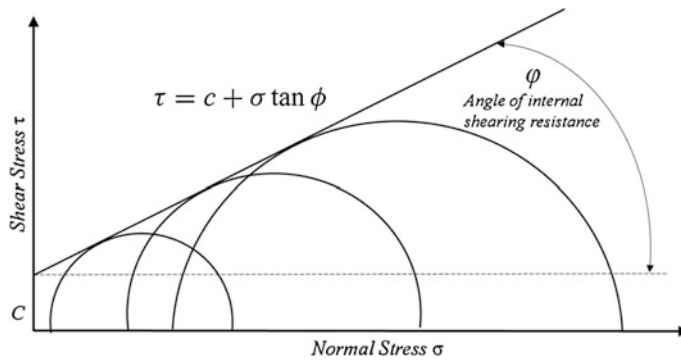


**Fig. 1.7** Mohr-Coulomb failure criterion in plastic region

slope of the straight line. The Mohr-Coulomb failure criterion simply implies that if a Mohr circle representing the state of stress at a point in the terrain touches the enveloping line, failure will take place at that point.

The importance of this test can be appreciated from the fact that the bearing capacity of a terrain as well as the maximum thrust and the maximum drag of a tracked or wheeled vehicle system can be calculated using the cohesion  $c$  and the angle of internal friction  $\phi$ . If the contact area of a tire or a track is available and the pressure on the contact patch is assumed to be uniform, then the maximum traction (thrust) can be estimated by the following equation:

$$F = \tau A = (c + \sigma \tan \phi)A = cA + W \tan \phi \quad (1.8)$$

where  $A$  is the contact area of a tire or a track; the product of contact pressure and contact area is equal to the normal load on the tire or the track  $W$ .

It is noteworthy that for saturated clay, its shear strength is assumed to have the internal friction angle,  $\phi$ , equal to zero and for dry sand, its shear strength is expressed by the terms neglecting the soil cohesion term.

## 1.4 Identification of Soil Measuring Apparatus

Classically, the cone penetrometer technique, the bevameter technique are applied for measuring the mechanical properties of the terrain for the investigations regarding vehicle mobility. The selection of a particular type of technique is a function of the intended purpose of the method of approach. For example, if the method is intended to be used by the off-road vehicle engineer in the development and design of new products, then the technique selected for measuring and characterizing terrain properties would be quite different from that intended to be used by the military personnel for vehicle traffic planning on a go/no go basis. Currently,

there are two major techniques used in measuring and characterizing terrain properties for evaluating off-road vehicle mobility in the field: the cone penetrometer technique and the bevameter technique [4].

Cone penetrometer, developed by Waterways Experimental Station (WES) is an instrument used to obtain an index of in situ shear strength and bearing capacity of soil. It consists of a  $30^\circ$  cone with a  $0.5$  or  $0.2 \text{ in}^2$  ( $3.23$  or  $1.29 \text{ cm}^2$ ) base area mounted on one end of a shaft. The shaft has circumferential bands indicating depths of penetration. At the top of the shaft is mounted a dial indicator within a proving ring which indicates the force applied axially to the penetrometer. The instrument is forced vertically into the soil while records are made of the dial reading for various sinkage depths. The cone penetrometer is associated with the following parameters: Cone Index (CI), Remolding Index (RI), Rating Cone Index (RCI), Vehicle Cone Index (VCI) and Slope Index. An example of Cone Penetrometer is shown in Fig. 1.8.

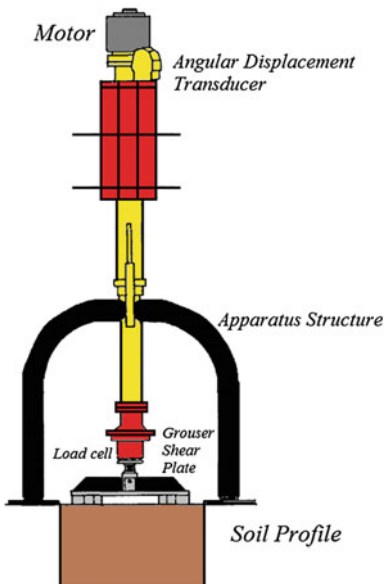
A RIMIK digital penetrometer device (CP20) with tip cone angle of  $30^\circ$ , a standard bar, a load cell and chipset, as shown in Fig. 1.8, that can be utilized to measure cone index. According to ASAE Standards S313.2 the penetration into the soil is performed with  $0.02 \text{ m/s}$  constant velocity.

Bevameter is an instrument used to measure the in situ soil strength. The instrument consists of two separate devices: one to measure the shear strength and another to measure the bearing capacity. The shear device consists of a groused annular ring mounted on the end of a shaft. The shear measurements are made by a number of constant vertical loads to the ring which is then rotated at a constant velocity. Records of the torque and angular displacement are used to calculate shear strength. The bearing capacity device is a plate penetrometer. The bearing capacity measurements are made by forcing different sizes of flat plates into the soil. Records of the penetration force and sinkage are used to calculate bearing capacity. The bevameter is associated with the following parameters: (a) Cohesion ( $C_o$ ) (b) Angle of internal friction (%) (c) Sinkage moduli ( $k, k_c, k_\phi$ ) (d) Sinkage exponent ( $n$ ) [3].

**Fig. 1.8** A typical cone index penetrometer



**Fig. 1.9** Bevameter apparatus with groused shear plate



To conclude, Bevameter technique was developed to measure terrain mechanical properties for the study of vehicle mobility. Bevameter test consists of penetration test to measure normal loads and shear test to determine shear loads exerted by vehicle (Fig. 1.9). Bevameter area size needs to be the size of the wheel or track. DEM analysis can take data from one size and simulate Bevameter performance for a different size.

It should be mentioned that there are also some other applied methods for determination and characterization of soil parameters such as Vane shear test (vane shear test method is the most normal procedure employed for in situ measurement of very soft or weak cohesive terrains) and Triaxial compression test (based on Von-Mises, Tresca and Mohr-Coulomb's failure criteria) that are not commonly used to the theorem of off-road vehicle dynamics as much as CI method and thus are not further extended in this book.

## References

1. Hohl, G. H., & Corrieri, A. (2000). Basic considerations for the concepts of wheeled off-road vehicles. In *Proceedings of FISITA World Automotive Congress, Seoul, Korea*.
2. Janosi, Z., & Green, A. J. (1968). Glossary of terrain-vehicle terms. *Journal of Terramechanics*, 5(2), 53–69.
3. Meyer, M. P., Ehrlich, I. R., Sloss, D., Murphy, N. R., Jr., Wismer, R. D., & Czako, T. (1977). International society for terrain-vehicle systems standards. *Journal of Terramechanics*, 14(3), 153–182.
4. Wong, J. Y. (1989). *Terramechanics and off-road vehicles*. Amsterdam: Elsevier.

5. Bekker, M. G. (1956). *Theory of land locomotion*. Ann Arbor, Michigan: The University of Michigan Press.
6. Sohne, W. (1958). Fundamentals of pressure distribution and soil compaction under tractor tires and 290. *Agricultural Engineering*, 39, 276–281.

# Chapter 2

## Wheel and Terrain Interaction

### Nomenclature

|                       |   |
|-----------------------|---|
| $m$                   | Mass  |
| $v$                   | Velocity  |
| $G$                   | Linear momentum   |
| $F$                   | Force   |
| $M$                   | Moment  |
| $I$                   | Mass inertia of moment  |
| $\alpha$              | Angular acceleration  |
| $N$                   | Reaction force component normal to the contact surface  |
| $N_t$                 | Net traction force  |
| $R_r$                 | Rolling resistance  |
| $l$                   | Length of contact between the tire and surface  |
| $T$                   | Torque applied to the tire  |
| $J_w$                 | The moment of inertia of the wheel  |
| $\omega_w$            | The angular velocity of the wheel, the overdot indicates differentiation with respect to time |
| $R_w$                 | The radius of the wheel   |
| $N_v$                 | Vertical reaction force from the ground   |
| $T_e$                 | The engine torque   |
| $T_b$                 | Brake torque  |
| $F_t$                 | Tractive force  |
| $F_w$                 | Wheel ground friction   |
| $i, \lambda$          | Wheel slip  |
| $\mu(\lambda)$        | Adhesion coefficient  |
| $k_x, k_y,$ and $k_z$ | Tire stiffness in the x, y and z directions   |
| $\Delta z$            | Linear displacement of tire under normal load (vertical tire deformation)                     |
| $\Delta x$            | Longitudinal tire deformation   |
| $\Delta y$            | Lateral tire deformation  |
| $U$                   | Strain energy function  |

|  |  |
|--|--|
| $C_1, C_2$                             | Are temperature-dependent material parameters                        |
| $\lambda_1, \lambda_2$ and $\lambda_3$ | Principal stretch ratios   |
| $I_1, I_2$                             | First and second strain invariants of the Green's deformation tensor |
| $k_r$                                  | Dynamic stiffness of tire  |
| $c$                                    | Damping ratio of the tire  |
| $\omega$                               | Natural frequency  |
| $\sigma_z$                             | z-oriented component of stress                                       |
| $\tau_x$                               | Longitudinal shear stress  |
| $\tau_y$                               | Lateral shear stress   |
| $l_x(y)$                               | Half-length of footprint at $y$ in the $x$ -direction                |
| $W_y(x)$                               | Half width at $x$ in the $y$ -direction                              |
| $V^A$                                  | Constraint of body $A$   |
| $V^B$                                  | Constraint of body $B$   |
| ${}^t x_M^A$                           | Coordinate of the particle $M$ on the surface ${}^t S^A$ of body $A$ |
| ${}^t x^B$                             | Coordinate of any desired particle on surface ${}^t S^B$             |
| $\lambda_N$                            | Normal contact force   |
| $\mu$                                  | Coefficient of friction  |
| $\dot{\gamma}_x$                       | Tangential slip rate in the tire/road contact plane                  |
| $C_{sp}$ and $N_b$                     | Dimensionless road profile constants                                 |
| $S_x(f)$                               | Power spectral density function                                      |
| $\Omega$                               | Spatial frequency  |
| $S_x(\Omega)$                          | Power spectral density function                                      |
| $T$                                    | Period   |
| $u$                                    | Linear velocity of tire  |
| $K_s$                                  | Total longitudinal force per unit longitudinal slip ratio            |
| $K_\beta$                              | Total lateral force per unit side-slip angle                         |
| $V_s$                                  | Slip velocity  |

In wheel-terrain interaction, there are a diversity of influential factors that play a substantial role in the output of the system. Given that the attention of this book is more on the effect of terrain on vehicle performance and mobility index, the effect of environment (terrain) characteristics on wheel should be well covered since the wheels are the unique connections between the ground and the vehicle and nearly all forces and moments applied to the vehicle are transmitted through the wheels. The wheels are also responsible to support the vehicle and perform steering, handling and creating dynamic forces such as traction, braking and also they function as a part of vehicle suspension system. It should also be distinguished between the motion condition on paved road and terrain based off-road that provides different motion condition.

## 2.1 Identification of Wheel-Obstacle Collision

An important topic of specialized interest in wheel kinetics is impact force. The principles of impulse and momentum have an important use in describing the behavior of colliding bodies. Impact refers to the collision between two bodies and is characterized by the generation of relatively large contact forces which act over a very short interval of time. For the linear momentum, we may write the basic equation of motion by:

$$\sum F = m\dot{v} = \frac{d}{dt}(mv) \quad (2.1)$$

where the product of the mass and velocity is defined as the linear momentum  $G = mv$  of the particle. Equation 2.1 can be written in the three scalar components as:

$$\sum F_x = \dot{G}_x \quad \sum F_y = \dot{G}_y \quad \sum F_z = \dot{G}_z \quad (2.2)$$

the effect of the resultant force  $\Sigma F$  on the linear momentum of the over a finite period of time is described as:

$$\int_{t_1}^{t_2} \sum F dt = G_2 - G_1 = \Delta G \quad (2.3)$$

Which can be rewritten as:

$$\begin{aligned} m(v_1)_x + \int_{t_1}^{t_2} \sum F_x dt &= m(v_2)_x \\ m(v_1)_y + \int_{t_1}^{t_2} \sum F_y dt &= m(v_2)_y \end{aligned} \quad (2.4)$$

the third direction is removed since the longitudinal and vertical forces are more significant during wheel traversing on surfaces with no slope that causes no lateral force generation. Different obstacle forms have been presented in Fig. 2.1.

However, velocity should be presented as a vector in both vertical and longitudinal directions:

$$\vec{v} = \dot{x}\hat{i} + \dot{y}\hat{j} \quad (2.5)$$

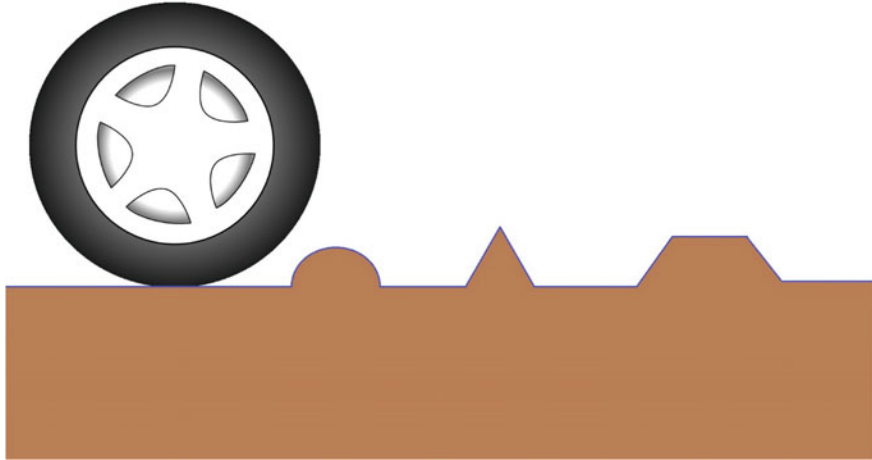


**Fig. 2.1** Schematic representation of the tire traversing over different obstacles

The path of wheel is affected by the obstacle geometry as following:

$$y = \sin \frac{2\pi}{l} x \quad 0 < x < 2\pi \quad (2.6)$$

For the triangular shaped obstacle, the following equation is described:

$$y = \begin{cases} ax & x < \frac{l}{2} \\ -ax & x > \frac{l}{2} \end{cases} \quad (2.7)$$

$l$  in this typical example is the obstacle length and  $a$  is the slope of obstacles at different determine heights, respectively. For a trapezoid type of obstacle Eq. 2.8 can be considered.

$$\text{trapezoid}(x; a, b, c, d) = \begin{cases} 0, & x \leq a \\ \frac{x-a}{b-a}, & a \leq x \leq b \\ 1, & b \leq x \leq c \\ \frac{d-x}{d-c}, & c \leq x \leq d \\ 0, & d \leq x \end{cases} \quad (2.8)$$

The governing equation based on the Newtonian-Eulerian method can be presented for the problem of tire-obstacle collision as following (Fig. 2.2):

$$\begin{aligned} \sum F_x &= m_t a_x \\ \sum F_y &= m_t a_y \\ \sum M &= I\alpha = I\ddot{\theta} \end{aligned} \quad (2.9)$$

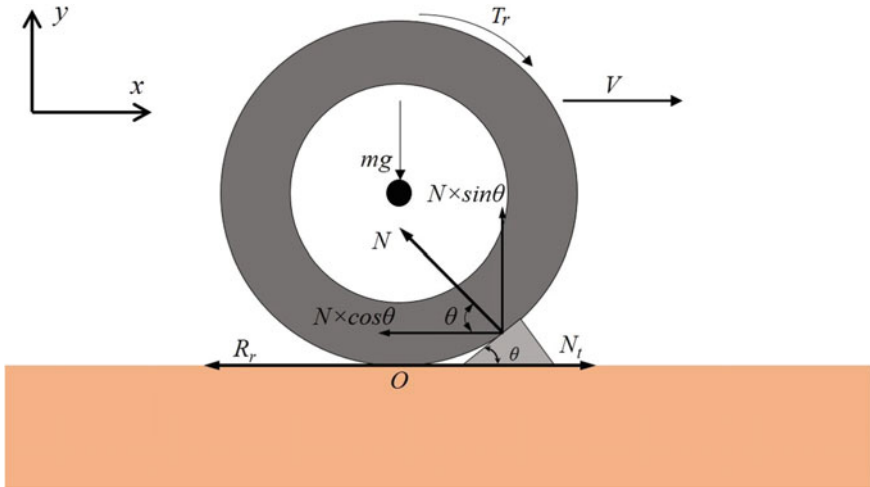


**Fig. 2.2** The free-body diagram of the tire-obstacle impact

where  $m_t$ ,  $M$ ,  $I$  and  $\alpha$  are tire mass, moment, mass inertia of moment and angular acceleration, respectfully. From Eq. 2.9, the following equation can be derived:

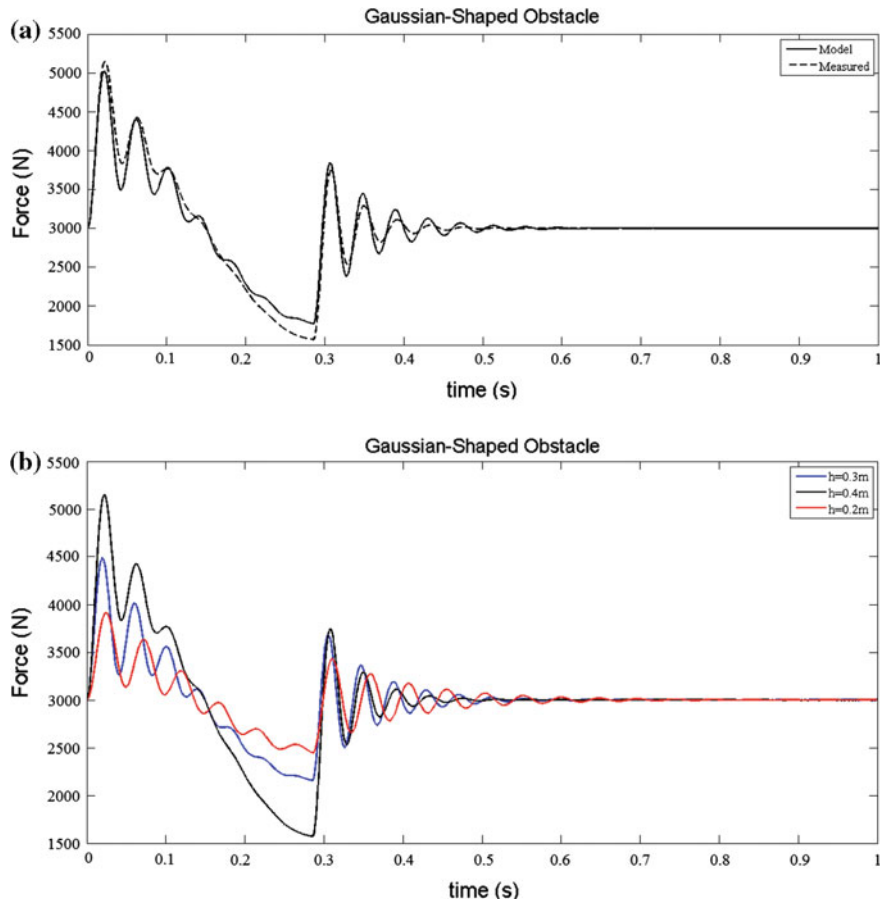
$$\begin{aligned} N_t - N \cos \theta - R_r &= m a_x \\ N \sin \theta - mg &= m a_y \\ N \cos \theta \times l \sin \theta + N \cos \theta \times l \cos \theta - T &= \bar{I} + m_t r^2 \end{aligned} \quad (2.10)$$

where  $N$ ,  $N_t$ ,  $R_r$ ,  $l$  and  $T$  are the reaction force component normal to the contact surface, the net traction force, rolling resistance, length of contact between the tire and surface, and torque applied to the tire, respectively. In this condition, the longitudinal and lateral impact forces for the impact can be rewritten as following:

$$\begin{aligned} F_l &= N \cos \theta = N_t - m a_x - R_r \\ F_v &= N \sin \theta = m(a_y + g) \end{aligned} \quad (2.11)$$

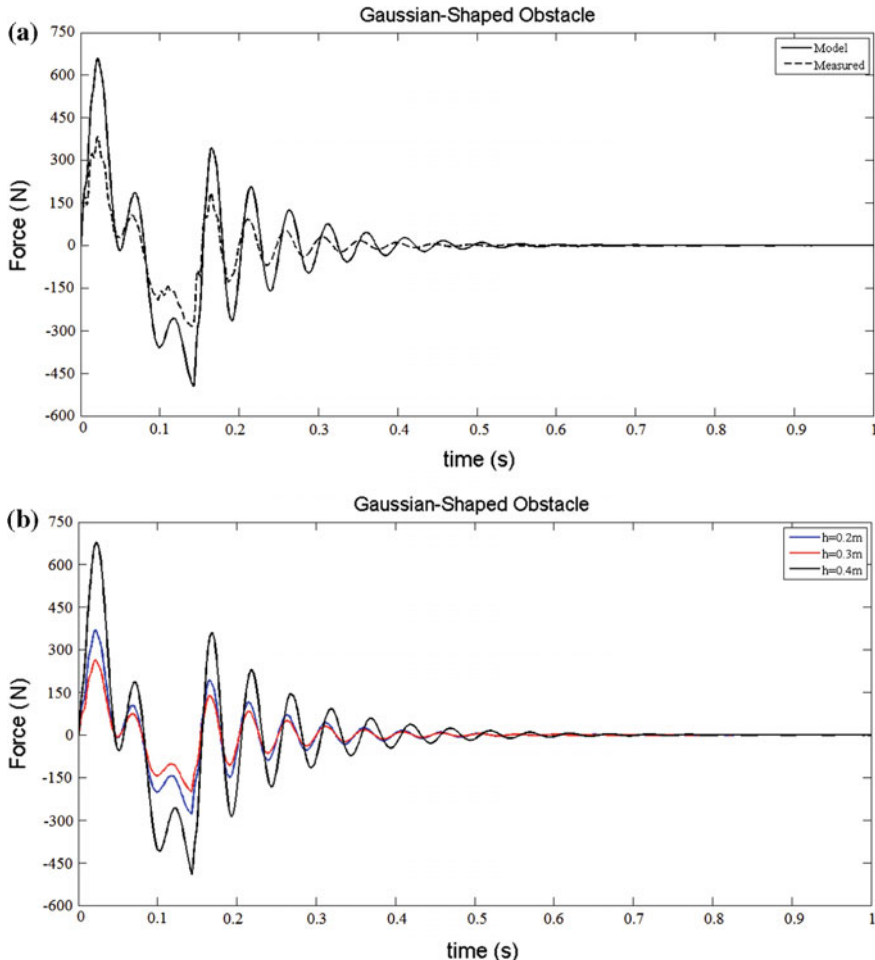
However, it should be also noted that due to the acceleration vector components at x and y directions that should follow the obstacle shapes, the obtained variations of force changes in time domain.

Figure 2.3 shows the force variations in time domain while the tire collides and traverses over the Gaussian shaped obstacle in vertical direction at different obstacle heights. Also, validation process with experimental results can be seen too. As appreciated from Fig. 2.3, after the collision the force disturbance occurs until the shock absorbs and damps after a period of time. The peak values depend on the obstacle height in a manner that increased obstacle height results in the increment of impact force. Furthermore, the vertical force is greatly affected by the impact force



**Fig. 2.3** Force variations in time domain while the tire collides and traverses over the Gaussian shaped obstacle in vertical direction at different obstacle heights; **a** model validation, **b** obtained results at different depths

with greater range of amplitude variation (compressive/extensive loads). In the interest of a balanced vehicle traversing, the accuracy and reliability of the complete vehicle model has to produce rational relation to the performance of the applied tire model. For the effect of obstacle height, it can be pointed out that due to the change of momentum in the vertical direction, a velocity change in the vertical direction of  $y$  (i.e.  $\Delta V_y$ ) is formed which results in the formation of linear impact in the same direction. Hence, an acceleration component at the same vertical direction of  $y$  is created owing to the aforesaid velocity change (i.e.  $\Delta V_y$ ) at the increased obstacle height leading to the increased vertically induced inertia forces. This process well describes the increase of vertical force with respect to the increase of obstacle height. Likewise, the increased obstacle height results in the reduction of the instantaneous velocity of wheel at the horizontal direction which in turn, results in a significant



**Fig. 2.4** Force variations in time domain while the tire collides and traverses over the Gaussian shaped obstacle in longitudinal direction at different obstacle heights; **a** model validation, **b** obtained results at different depths

change of the linear momentum and therefore greater linear impact in the horizontal direction is obtained. Figure 2.4 is dedicated to present the longitudinal force variations in time domain for both model validation and the variations of the force at different obstacle heights versus time. It is expectable, with abovementioned justifications that increased obstacle height results in the increment of impact force.

Figure 2.5 demonstrates the impact force variations in both directions addressing the trapezoidal shaped obstacles at different depths. Owing to the change of momentum in the vertical direction, a velocity change in the vertical direction of y (i.e.  $\Delta V_y$ ) is formed which results in the formation of linear impact in the same direction. Due to the decrease of the instant velocity of wheel at the longitudinal

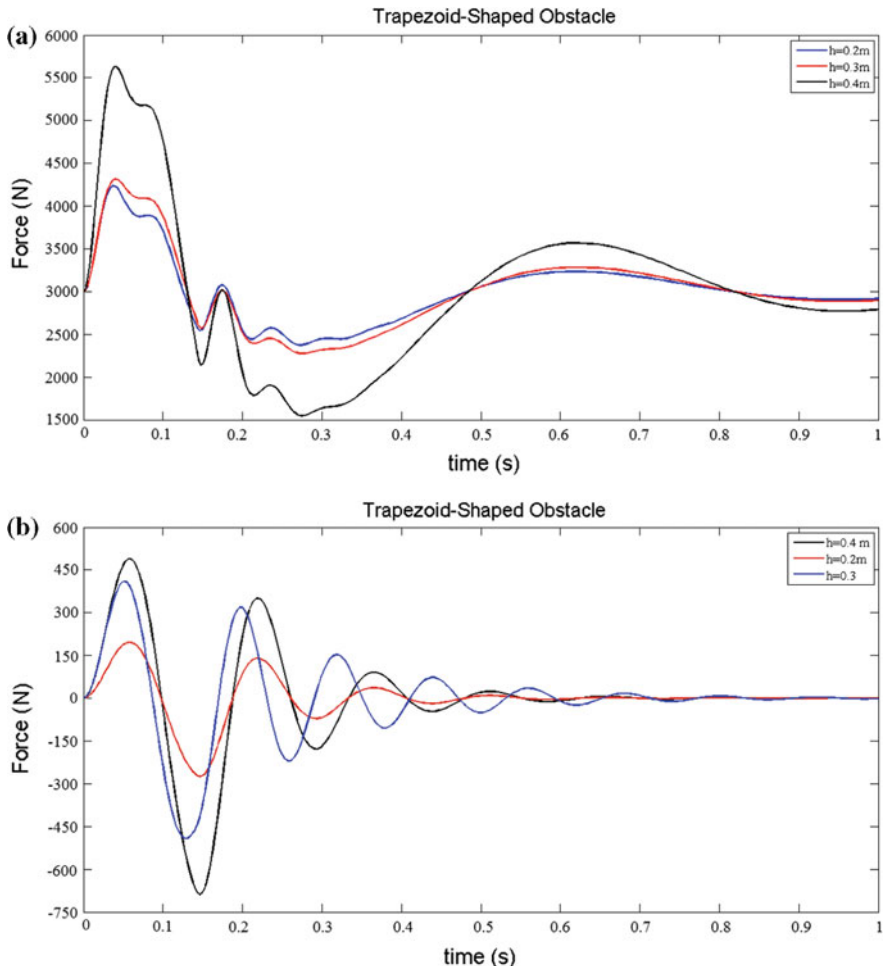


**Fig. 2.5** Force variations in time domain while the tire collides and traverses over the trapezoidal shaped obstacle in **a** vertical and **b** longitudinal directions at different obstacle heights

direction results in variation of the linear momentum and greater longitudinal impact force. Figure 2.6 illustrates the impact force variations in both directions addressing the triangular shaped obstacles at different depths. The variations justifications are previously covered for the other obstacle geometries.

Based on the presented results, it is concluded that the trapezoidal shaped obstacles bring about the lowest values of longitudinally oriented impact force while the greatest values correspond to the triangular obstacles. While the greatest values of impact force in vertical direction correspond to the triangular obstacles, in contradictory to the longitudinal impact force, the lowest force corresponded to the Gaussian shaped obstacles. This can serve as an important step in vehicle suspension design and tire manufacturing industry.

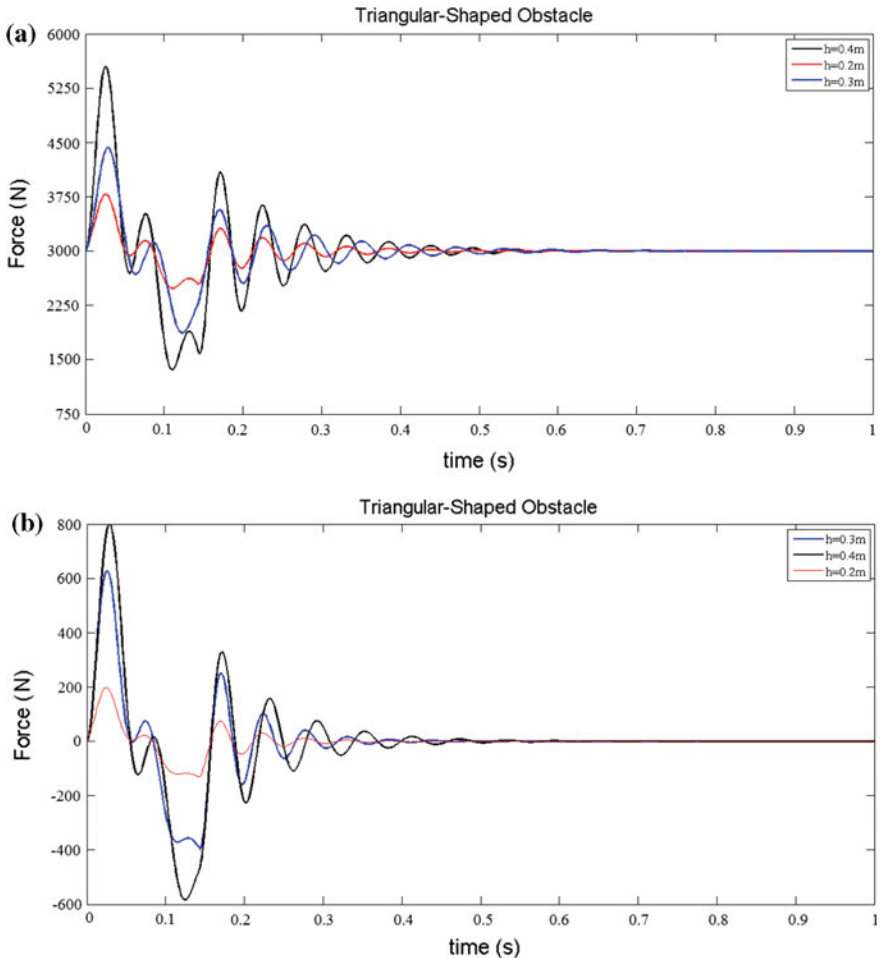


**Fig. 2.6** Force variations in time domain while the tire collides and traverses over the Triangular shaped obstacle in **a** vertical and **b** longitudinal directions at different obstacle heights

## 2.2 Tire Modeling

The angular motion of the wheel can be developed with a dynamic equation of motion:

$$\dot{\omega}_w = \frac{[T_e - T_b - R_w F_t - R_w F_w]}{J_w} \quad (2.12)$$

where  $J_w$  is the moment of inertia of the wheel,  $\omega_w$  is the angular velocity of the wheel, the overdot indicates differentiation with respect to time,  $R_w$  is the radius of

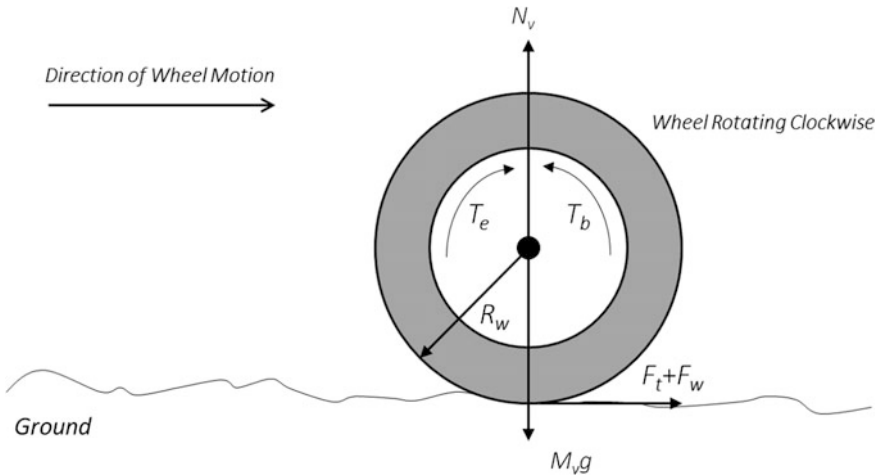


**Fig. 2.7** Schematic description of wheel under the kinetics of motion

the wheel.  $N_v$  is vertical reaction force from the ground,  $T_e$  is the engine torque,  $T_b$  is Brake torque,  $F_t$  Tractive force and  $F_w$  wheel ground friction or so called rolling resistance [1]. The schematic figure of wheel under these kinetics of motion is depicted in Fig. 2.7.

The total torque acting on the wheel divided by the moment of inertia of the wheel equals the wheel angular acceleration (deceleration). The total torque consists of engine torque that acts in opposed direction with that of the brake torque and the torque components owing to the tire tractive force and the wheel ground friction force or rolling resistance force. The tire tractive (braking) force is given by:

$$F_t = \mu(\lambda)N_v \quad (2.13)$$

where the normal tire force (the reaction force from the ground to the tire),  $N_v$ , relies on vehicle parameters such as the mass of the vehicle, position of the vehicle center of gravity, and the steering and suspension dynamics. Applying a driving torque or a braking torque to a pneumatic tire produces tractive (braking) force at the tire-ground contact patch. The driving torque produces compression at the tire tread in front of and within the contact patch. Therefore, the tire travels a shorter distance than it would if it were free rolling. In the same way, when a braking torque is applied, it produces tension at the tire tread within the contact patch and at the front. Because of this tension, the tire travels a larger distance than it would if it were free rolling. This phenomenon is referred as the wheel slip or deformation slip. The adhesion coefficient, which is the ratio between the tractive (braking) force and the normal load, depends on the road-tire conditions and the value of the wheel slip  $\lambda$  while it can be presented as:

$$\lambda = \frac{(\omega_w - \omega_v)}{\omega}, \quad \omega \neq 0 \quad (2.14)$$

where  $\omega_v = \frac{V}{R_w}$  is the vehicle angular velocity of the wheel which is defined as being equal to the linear vehicle velocity, v, divided by the radius of the wheel.

The variable  $\omega$  is defined as:

$$\omega = \max(\omega_w, \omega_v) \quad (2.15)$$

which is the maximum of the vehicle angular velocity and wheel angular velocity. The adhesion coefficient  $\mu(\lambda)$  is a function of wheel slip. For various road conditions  $\mu(\lambda)$  curves have different peak values and slopes. In modeling the following function is used for a nominal

$$\text{curve: } \mu(\lambda) = \frac{2\mu_p \lambda_p \lambda}{\lambda_p^2 + \lambda^2} \quad (2.16)$$

where  $\lambda_p$  and  $\mu_p$  are the peak values. For various road conditions, the curves have different peak values and slopes. The adhesion coefficient slip characteristics are also influenced by operational parameters such as speed and vertical load. The peak value for the adhesion coefficient usually has values between 0.1 (icy road) and 0.9 and for a terrain surface it is about 0.5. A typical adhesion coefficient versus wheel slip is demonstrated in Fig. 2.8.

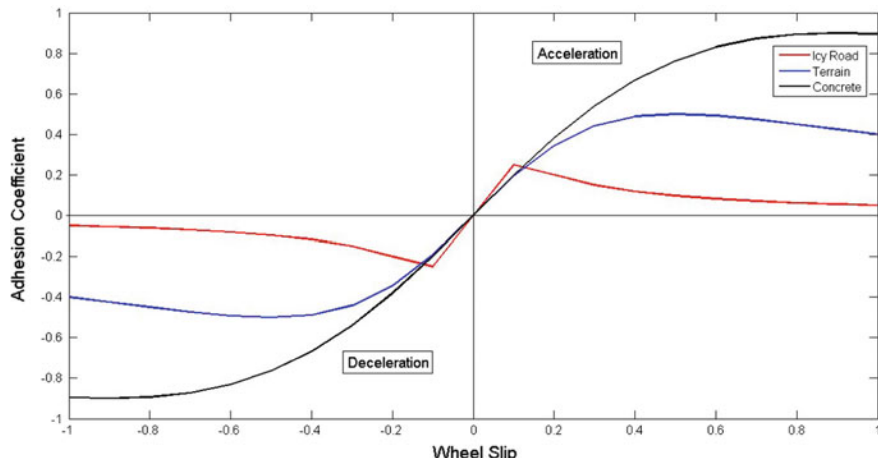


**Fig. 2.8** Adhesion coefficient with respect to wheel slip in acceleration and deceleration regions for three road types

The contact interaction between tire and the road greatly influences the driving performance of vehicles. One dynamic field of study in interest for the engineer is of vehicle dynamics discipline is optimising the tire-road interaction so that the vehicle handles well and operates both safely and comfortably under any circumstance. To assess the effect of tire properties on the dynamic behaviour of vehicles, the researcher needs a precise description of the tire-road contact phenomena.

In order to determine the tire-road interaction and force system, a Cartesian coordinate system can be positioned at the center of the tireprint, as shown in Fig. 2.9. The tire plane and ground when intersects will form a line which can be considered as the x-axis of the coordinate system. In the condition that the tire is very narrow that it is seen as a plane, then the tire plane is formed. The z-axis acts normal to the x-axis in opposite direction to the gravitational acceleration  $\mathbf{g}$ , and the y-axis makes the coordinate system a right-hand triplet [2].

Camber angle  $\gamma$  and sideslip angle  $\alpha$  are used in order to demonstrate the tire orientation. The camber angle is the angle between the tire-plane and the vertical plane measured about the x-axis. The camber angle can be clearly identified in Fig. 2.9. The sideslip angle  $\alpha$  is the angle between the velocity vector  $\mathbf{v}$  and the x-axis measured about the z-axis (Fig. 2.9).

The force system that a tire receives from the ground is assumed to be located at the center of the tireprint and can be decomposed along x, y, and z axes. Therefore, the interaction of a tire with the road generates a 3D force system including three forces and three moments (Fig. 2.9).

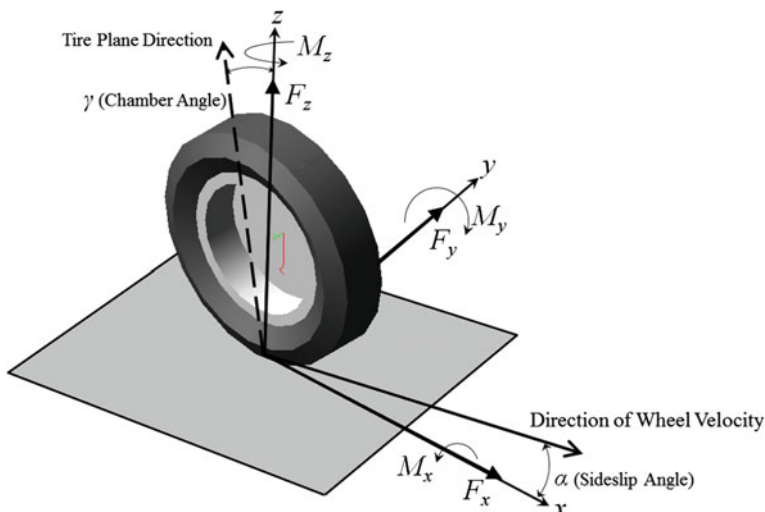


**Fig. 2.9** 3D force system including three forces and three moments

### 2.2.1 Forces and Moments

Longitudinal force  $F_x$  is a force that operates in the direction of the x-axis. In the case that the resultant longitudinal force  $F_x > 0$ , then the vehicle is accelerating, and if  $F_x < 0$  then the vehicle is in deceleration (braking mode). Vertical force  $F_z$  is a vertically oriented force that acts normal to the ground plane. The resultant vertical force  $F_z > 0$  in the case that it is upward and  $F_z < 0$  when it acts downward. Lateral force  $F_y$  is a force that acts tangent to the ground and orthogonal to both  $F_x$  and  $F_z$ . The resultant lateral force  $F_y > 0$  if it is in the y-direction and  $F_y < 0$  when it acts opposite to the y-direction [2].

Roll moment  $M_x$  is a longitudinal moment about the x-axis while the resultant roll moment  $M_x > 0$  when it is more likely to turn the tire about the x-axis. The roll moment is also called the bank moment, tilting torque, or overturning moment. Pitch moment  $M_y$  is a lateral moment about the y-axis while the resultant pitch moment  $M_y > 0$  in the case that it more likely turn the tire about the y-axis and move forward. The pitch moment is also called rolling resistance torque. Yaw moment  $M_z$  is an upward moment about the z-axis. The resultant yaw moment  $M_z > 0$  in the case that it is more likely to turn the tire about the z-axis. The yaw moment is so-called the aligning moment or self-aligning moment [2].

### 2.2.2 Tire Stiffness

It is clear-cut that at a certain value of tire normal deformation if the tire stiffness is available, the amount of applied normal load to the tire is predictable. This is in conformity with the tire elastic behavior, however, the stiffness characteristic determination is a significant step for understanding the tire behavior under different loading conditions. Based on Hooke's law, a principle of physics that states that the force  $F$  needed to extend or compress a spring (or flexible material) by some distance  $X$  is proportional to that distance, it can be approximated that:

$$F_x = k\Delta x \quad (2.17)$$

$$F_y = k\Delta y \quad (2.18)$$

$$F_z = k\Delta z \quad (2.19)$$

The coefficients  $k_x$ ,  $k_y$ , and  $k_z$  represent the tire stiffness in the x, y and z directions, respectively and are also considered as longitudinal, lateral and normal stiffness characteristics.

*Proof*

Let's assume a linear displacement of tire under normal load being  $\Delta z$ , representing  $z_2-z_1$ . Based on Taylor series one can develop the force about the static equilibrium ( $z_0$ ) as following:

$$F_z(z_0 + \Delta z) = F_z(z_0) + \frac{\partial F_z}{\partial z} \Big|_{z=z_0} \Delta z + \frac{1}{2!} \frac{\partial^2 F_z}{\partial z^2} \Big|_{z=z_0} (\Delta z)^2 + \dots \quad (2.20)$$

Then it can be rewritten as:

$$F_z(z_0 + \Delta z) = F_z(z_0) + \Delta F_z \quad (2.21)$$

where  $\Delta F_z$  represents the force variation due to tire deformation.  $\Delta F_z$  can be presented as:

$$\Delta F_z = \frac{\partial F_z}{\partial z} \Big|_{z=z_0} \Delta z + \frac{1}{2} \frac{\partial^2 F_z}{\partial z^2} \Big|_{z=z_0} (\Delta z)^2 + \dots \quad (2.22)$$

If the displacement is negligible, the terms of  $\Delta z$  with higher degree of can be ignored. Therefore, it can be concluded that:

$$\Delta F_z = \frac{\partial F_z}{\partial z} \Big|_{z=z_0} \Delta z \quad (2.23)$$

$$\Delta F_z = k \Delta z \quad (2.24)$$

where  $k$  is a coefficient and is considered as stiffness coefficient as following:

$$k = \frac{\partial F_z}{\partial z} \Big|_{z=z_0} \quad (2.25)$$

It is generally known that the stiffness curve can be influenced by many parameters. The most effective one is the tire inflation pressure. Lateral and longitudinal force/deflection behavior is also determined experimentally by applying a force in the appropriate direction. The lateral and longitudinal forces are limited by the sliding force when the tire is vertically loaded.

It is appreciated from Fig. 2.10 that  $k_x > k_z > k_y$  that the greatest and lowest tire stiffness are in longitudinal and lateral directions, respectively (Fig. 2.10). That is a greater force is needed to make a definite displacement in longitudinal and lateral directions. Vertically, longitudinally, and laterally tire deformations are also presented in Fig. 2.11 based on three forces of normal, longitudinal and lateral.

It is known that tires, being viscoelastic material, have the hysteresis effect that is the loading and unloading stiffness curves are not exactly the same. The area inside the loop in Fig. 2.12. represents the dissipated energy which is in accordance with a part of rolling resistance. Of course for off-road travelling condition, the residual

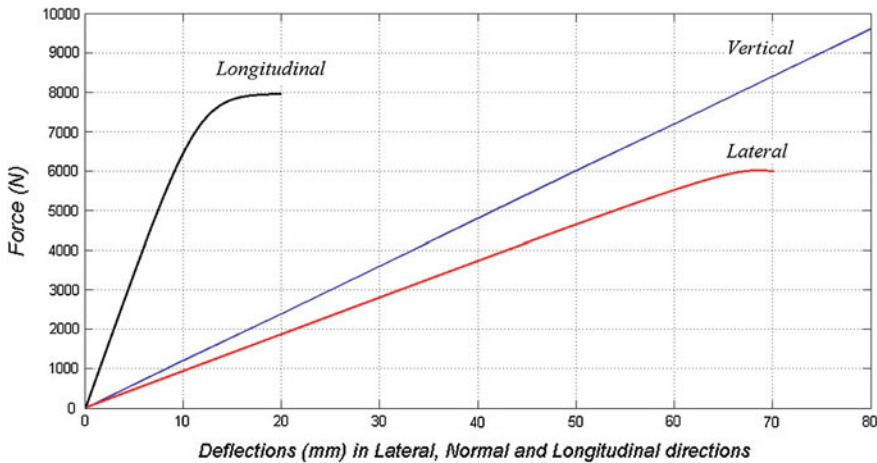


**Fig. 2.10** Vertical, longitudinal, and lateral stiffness curves

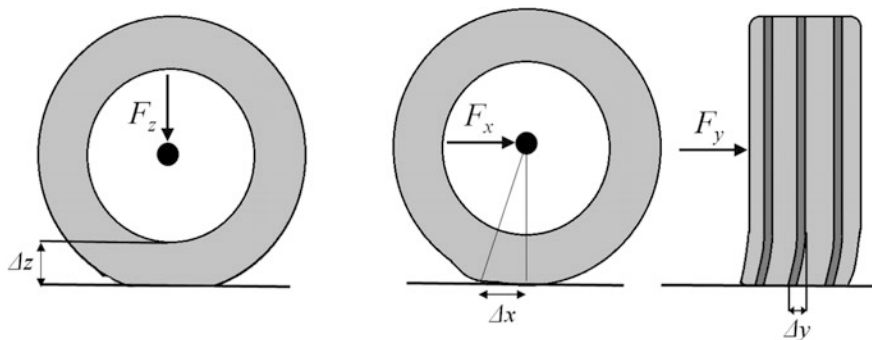
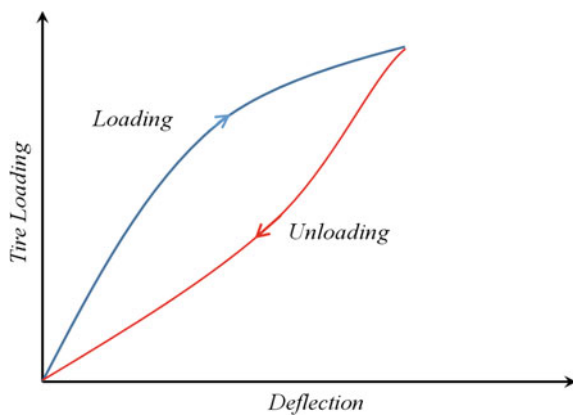


**Fig. 2.11** Vertically, longitudinally, and laterally tire deformations

**Fig. 2.12** Hysteresis loop in a vertically loading and unloading tire



section for rolling resistance is formed by soil sinkage. Tires are subject to cyclic loadings repeated cycles of deformation and recovery that the difference is energy loss released in heat form.

The hysteresis loop increases as a result of hysteresis damping forces that oppose tire deformation. For metallic structures it is clear that hysteresis forces are free from frequency, equal value to a portion of corresponding spring forces shifted in phase by 90°.

It should be pointed out that different experimental approaches have been designed for hyperelastic characterization. Mooney [3] made the first significant effort to establish the mathematical theory of large elastic deformations of rubber materials. The strain energy function was derived by Mooney based on the following:

$$U = C_1(\lambda_1^2 + \lambda_2^2 + \lambda_3^2 - 3) + C_2(\lambda_1^{-2} + \lambda_2^{-2} + \lambda_3^{-2} - 3) \quad (2.26)$$

where  $C_1$  and  $C_2$  are temperature-dependent material parameters, and  $\lambda_1$ ,  $\lambda_2$  and  $\lambda_3$  are the principal stretch ratios. Rivlin [4] considered the rubber material is homogeneous, isotropic and incompressible, and the strain energy function was derived as following:

$$U = \sum_{i+j=1}^{\infty} C_{ij}(I_1 - 3)^i(I_2 - 3)^j \quad (2.27)$$

where  $C_{ij}$  is material parameter,  $I_1$  and  $I_2$  are the first and second strain invariants of the Green's deformation tensor, respectively. If only two terms of the power series are taken, the strain energy function is reduced to

$$U = C_{10}(I_1 - 3) + C_{01}(I_2 - 3) \quad (2.28)$$

which is known as the Mooney-Rivlin equation. Yeoh [5] obtained the Rivlin's strain energy function by removing the dependence on the second invariant as  $I_2$  has lower effect on the variations of strain energy function when compared to the first invariant  $I_1$ . The function can be re-written as following:

$$U = \sum_{i=1}^3 C_{ij}(I_1 - 3)^i \quad (2.29)$$

Ogden developed strain energy model [6], and the strain energy function can be determined as following:

$$U \stackrel{def}{=} \sum_{i=1}^N \frac{2\mu_i}{\alpha_i^2} (\lambda_1^{-\alpha_i} + \lambda_2^{-\alpha_i} + \lambda_3^{-\alpha_i} - 3) \quad (2.30)$$

However, the nonlinear regression method for derivation of the Ogden strain-energy function, which is based on stress-strain data from one mode of deformation tests, is not able to predict behaviour in other deformation modes [7].

It is also important point to determine the dynamic tire characteristics. The dynamic stiffness of tires is one of the important factors influencing vehicle ride. To assess the influence of forward speed and obstacle geometric properties on dynamic stiffness of tires, a derivation method was proposed based on the transient dynamic responses to obtain the dynamic stiffness at resonance [8]. The peak of the mobility function was obtained by quantification of the dynamic stiffness at the natural frequency while the modulus of motion mobility  $\dot{Y}/F$  can be found by the following term.

$$\left| \frac{\dot{Y}}{F} \right| = \frac{\omega}{\sqrt{(k_r - \omega^2 m)^2 + \omega^2 c^2}} \quad (2.31)$$

where  $k_r$  and  $c$  are the dynamic stiffness and damping ratio of the tire respectively,  $\omega$  is natural frequency and  $m$  is the mass of the tire, and the peak of the modulus of motion mobility happens at:

$$\frac{d}{d\omega} \left| \frac{\dot{Y}}{F} \right| = \frac{d}{d\omega} \left( \frac{\omega}{\sqrt{(k_r - \omega^2 m)^2 + \omega^2 c^2}} \right) = 0 \quad (2.32)$$

The following term can be obtained as:

$$\frac{(k_r - \omega^2 m)(k_r + \omega^2 m)}{\sqrt{(k_r - \omega^2 m)^2 + \omega^2 c^2}((k_r - \omega^2 m)^2 + \omega^2 c^2)} = 0 \quad (2.33)$$

Therefore the dynamic stiffness of tire can be obtained as following:

$$k_r = \omega^2 m \quad (2.34)$$

One can conclude that for a tire with a constant mass, the dynamic stiffness is determined by the natural frequency. The natural frequency derived from the vertical spindle responses exhibit little sensitivity to the height of rectangular based obstacles that stands for the vertical dynamic stiffness has a negligible sensitivity to the height of obstacles. Furthermore, the natural frequency of spindle responses in longitudinal direction becomes lower with the increase of height of road obstacle which means that the dynamic stiffness in the longitudinal direction decreases [8].

### 2.2.3 Tire Footprint

The force applied on a tire in a contact patch that can be closely connected with tire stresses can be decomposed into a component vertical to the ground and a tangential component on the ground. It is the portion of a vehicle's tire that is in actual contact with ground and determines the share of the tire's tread that is in contact with the ground. The size and shape of the contact patch, as well as the pressure distribution within the contact patch are significant to the ride comfort, stability and handling parameters of the vehicle in motion.

The vertical stress applied to the tire in contact area is the z-oriented component of stress ( $\sigma_z$ ) while the longitudinal and lateral shear stresses are represented by  $\tau_x$  and  $\tau_y$ . To consider the equilibrium theory in the steady-state loading condition, the following equations should be satisfied:

$$\int_A \tau_x(x, y) dA = 0, \quad \int_A \tau_y(x, y) dA = 0, \quad \int_A \sigma_z(x, y) dA = F_z \quad (2.35)$$

In order to achieve a reliable model of normal stress, it is essential to have a correct estimation of contact patch geometry shape and parameters. On a rigid surface, a better contact patch geometry may be better presented by an elliptic shape (Fig. 2.13):

$$\left(\frac{x}{a}\right)^k + \left(\frac{y}{b}\right)^k = 1, \quad k = 2n, n \in N \quad (2.36)$$

where the number of power for the elliptic shape can be varied based on the tire type between 1 and 3. If the tire is a radial ply tire, and  $n = 3$  is used, the following stress distribution function is used.

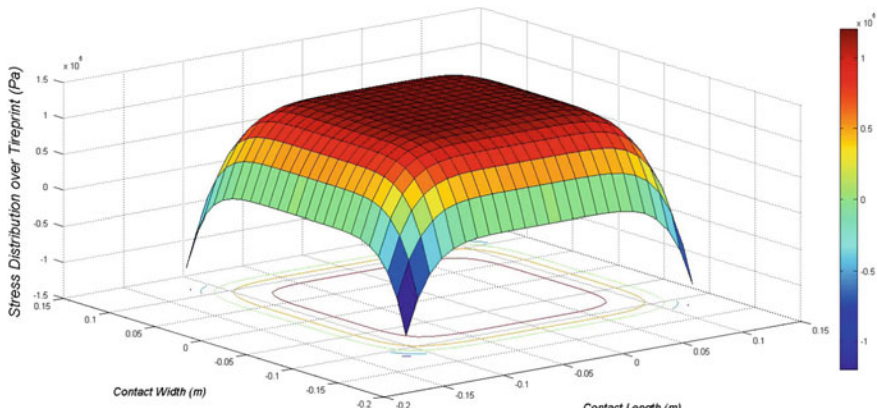


**Fig. 2.13** Normal stress distribution with respect to contact length and contact width

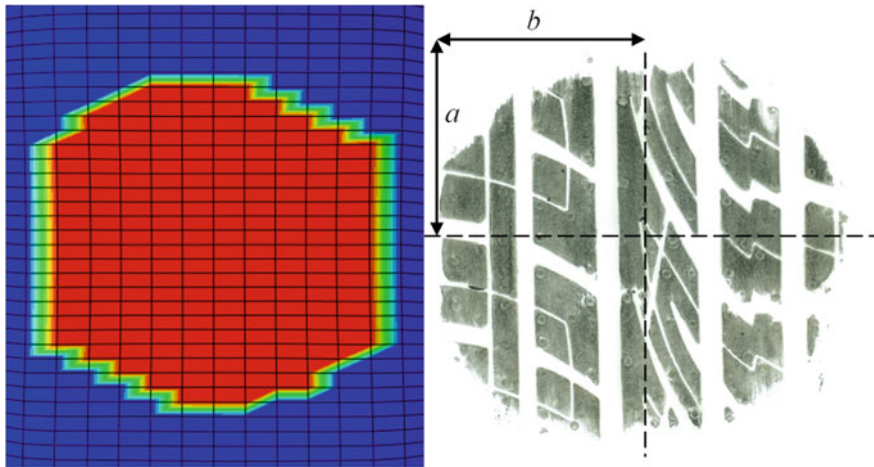


**Fig. 2.14** A typical tire-ground contact area and its tire stress distribution [9]

The normal stress  $\sigma_z(x, y)$  may be approximated by the function [2]:

$$\sigma_z(x, y) = \sigma_{z\max} \left( 1 - \frac{x^6}{a^6} - \frac{y^6}{b^6} \right) \quad (2.37)$$

where  $a$  and  $b$  indicate the dimensions of the tire contact area (Fig. 2.14). In this manner, based on the equilibrium equation, the following function may be used:

$$F_z = \int_A \sigma_z(x, y) dA = \iint_A \sigma_{z\max} \left( 1 - \frac{x^6}{a^6} - \frac{y^6}{b^6} \right) dx dy \quad (2.38)$$

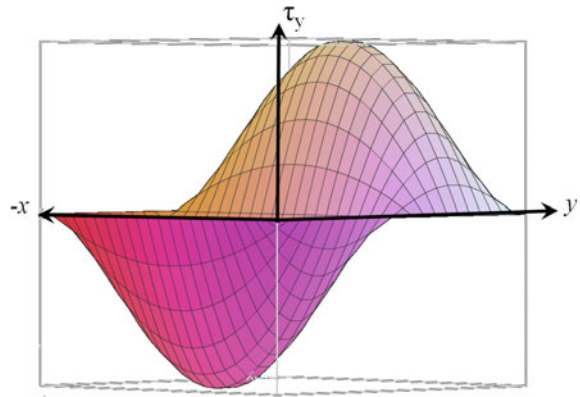
Based on equilibrium theory in the steady-state loading condition, the equations for tangential stresses should also be satisfied. The tangential stress, so-called shear stress,  $\tau$  should be developed based on the contact patch area in both  $x$  and  $y$  directions.

The tangential stress on a tire is inward in  $x$  direction and outward in  $y$  direction. Hence, the tire tries to stretch the ground in the  $x$ -axis and compact the ground on the  $y$ -axis (Fig. 2.15).

It is also well known that the force distribution on the tireprint is not constant and is influenced by tire structure, load, inflation pressure, and environmental conditions. As available in the literature, the tire tangential stresses in  $x$  and  $y$  oriented directions can be presented as:

$$\tau_x(x, y) = -\tau_{x\max} \left( \frac{x^{2n+1}}{a^{2n+1}} \right) \sin^2 \left( \frac{x}{a} \pi \right) \cos \left( \frac{y}{2b} \pi \right) \quad n \in N \quad (2.39)$$

**Fig. 2.15** Tangential tire stress distribution in x-direction and y-direction



$$\tau_y(x, y) = -\tau_{y\max} \left( \frac{x^{2n}}{a^{2n}} - 1 \right) \sin\left(\frac{y}{b}\pi\right) \quad n \in N \quad (2.40)$$

In this manner, the normal stresses for on road and soft soil (terrain) surfaces in the contact patch geometry are presented in Fig. 2.16. The difference between the trends of figures can be attributed to the soil profile sinkage (deformation) when compared with a rigid surface where the stress distribution in the contact area is more homogenous.

For a contact area of soil-tire interface, the periphery of the contact area may be better modeled by a super ellipse which, in an orthogonal coordinate system with center at the origin, is given as following.

$$\left| \frac{x}{a} \right|^n + \left| \frac{y}{b} \right|^n = 1 \quad (2.41)$$

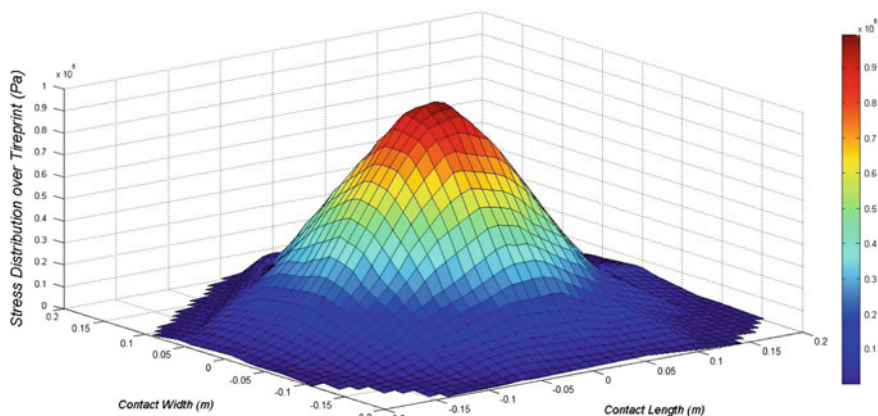
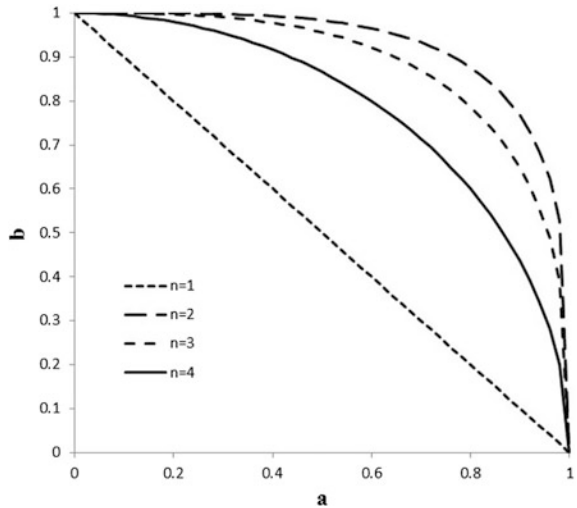


**Fig. 2.16** Normal stresses for on soft soil (terrain)

**Fig. 2.17** The shape of the curve in the first quadrant when  $a = b = 1$  and  $n = 1, 2, 3$  and  $4$  in order from the origin of coordinates



where the exponent  $n$ , is a positive real number that determines the shape, and parameters  $a$  and  $b$  determine the length of half the major axes and thus, the proportions of the surface.

Therefore,  $y$  is yielded as given by:

$$y = b \cdot \left(1 - \frac{x^n}{a^n}\right)^{\frac{1}{n}} \quad (2.42)$$

At a sample  $x$  range of between 0 and 0.6 and  $a = b = 1$ , the output  $y$  is schematically obtained as Fig. 2.17.

The aforementioned description was presented to shed light on some major principles of super ellipse shape and the effect of the exponent  $n$ . The area of one quadrant is given as [10]

$$A = b \int_0^a \left(1 - \frac{x^n}{a^n}\right)^{\frac{1}{n}} dx = kab \quad (2.43)$$

where  $k$  is a constant that is a function of  $n$  which can be found by numerical integration. As proposed by Keller [11], the parameter  $n$  was yielded as following.

$$n = 2.1(a.b)^2 + 2 \quad (2.44)$$

where  $n$  is dimensionless and the width of the tire  $b$ , and length of contact  $a$  are in m. It is noteworthy that for  $n = 2$ , the curve is a pure ellipse whereas it grows towards a rectangle as  $n \rightarrow \infty$ .

Based on Frida Model developed by Per Schjønning et al. [12] the super elliptic assumption is again adopted:

$$\left|\frac{x}{a}\right|^n + \left|\frac{y}{b}\right|^n = 1 \quad (2.45)$$

Based on this model,  $\Omega$  is proposed as following to represent the boundary and interior of the super ellipse.

$$\Omega = \{(x, y) | |x/a|^n + |y/b|^n \leq 1\} \quad (2.46)$$

The distribution of the vertical stress in the contact area may be modelled by the following Eq. 2.47, which is a combination of the equations suggested by Keller [11] except that we have normalised the equation to unit contact area width and to unit stress [12],

$$\begin{aligned} \sigma(x, y) &= F_{\text{wheel}} C(\alpha, \beta, a, b, n) f(x, y) g(x, y) \\ &\text{for } (x, y) \in \Omega \text{ and 0 otherwise,} \end{aligned} \quad (2.47)$$

$$\begin{aligned} f(x, y) &= \left\{ 1 - \left| \frac{x}{l_x(y)} \right|^\alpha \right\} \\ g(x, y) &= \left\{ \left( 1 - \left| \frac{y}{W_y(x)} \right| \right) (1/g_{\max}) \exp \left( -\beta \left( 1 - \left| \frac{y}{W_y(x)} \right| \right) \right) \right\} \end{aligned} \quad (2.48)$$

where  $g_{\max}$  is the maximum value of  $g$  in the range ( $0 < y < W_y(x)$ ) expressed in terms of  $\beta$ :

$$\begin{aligned} \beta \leq 1: g_{\max} &= \exp(-\beta), \\ \beta > 1: g_{\max} &= \exp(-1)/\beta \end{aligned} \quad (2.49)$$

$F_{\text{wheel}}$  is the wheel load in kN,  $C(\alpha, \beta, a, b, n)$  is a function of the parameters an integration constant ensuring that when integrating  $s(x, y)$  over the contact area  $\Omega$  the total load is  $F_{\text{wheel}}$ .

Additionally,  $l_x(y)$  is the half length of footprint at  $y$  in the  $x$ -direction, and  $W_y(x)$  the half width at  $x$  in the  $y$ -direction. The  $f$  function determines the form of stress distribution in the driving direction, that is the relative stress as a function of relative contact area half-length, while the  $g$  function shows the form of stress distribution in the direction vertical to the driving direction (across the wheel). Figure 2.18 represents the  $f$  function and exhibits the stress distribution in the driving direction for some certain amounts of  $\alpha$ . Great values of  $a$  show a satisfactory ability to distribute the stress in the driving direction, while the stress peak in the middle of the contact area (below the axle) gets increasingly steep with decreasing  $\alpha$  [12].

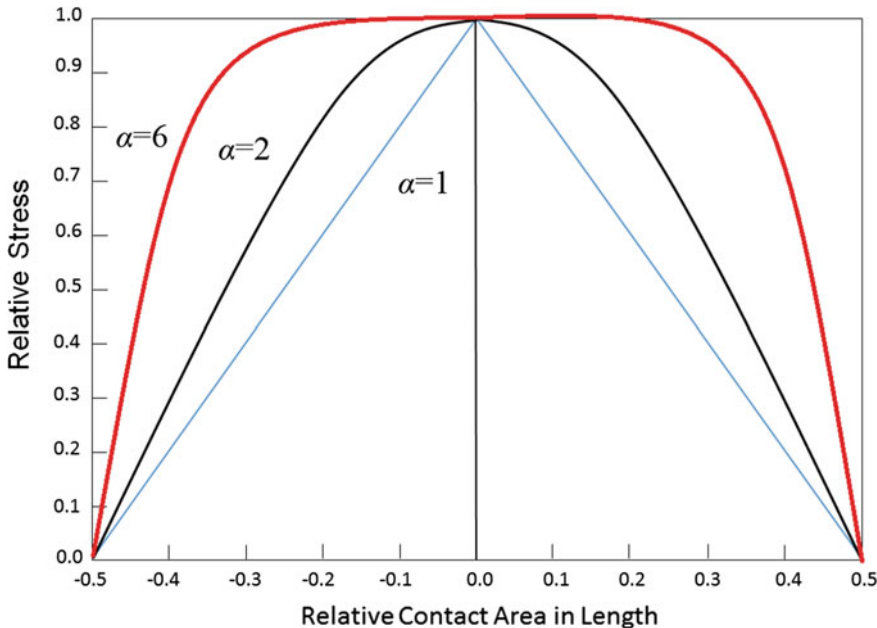


**Fig. 2.18** Relative stress versus relative contact area length

The condition gets more complex for stress distribution across the wheel while the stress will peak in the center of the tire for  $\beta \leq 1$  and the peak will be increased while  $b$  decreases (Fig. 2.19). For  $\beta > 1$  the stress shows two peaks that converge to the edges of tire for increasing levels of  $\beta$ . Consequently, the model is able to describe parabolic-like as well as U-shaped stress distributions which are required to deal with the monitored stresses [12].

#### 2.2.4 Tire Road Modeling

In order to limit the motion of the two bodies that are in contact, a normal contact condition is created (Fig. 2.20). The constraints  $V^A$  of body  $A$  and  $V^B$  of body  $B$  of the system are created so that the bodies in contact cannot penetrate in each other while are in motion [13]. In the tire and ground contact theoretical model,  $C^A$  and  $C^B$  represent the tire and road respectively.

Let's consider that  ${}^t x_M^A$  denotes the coordinate of the particle  $M$  on the surface  ${}^t S^A$  of body  $A$  at time  $t$ , the distance  $l$  between the particle and the nearest particle  $N({}^t x^B)$  on the surface  ${}^t S^B$  Fig. 2.19 can be presented as following:

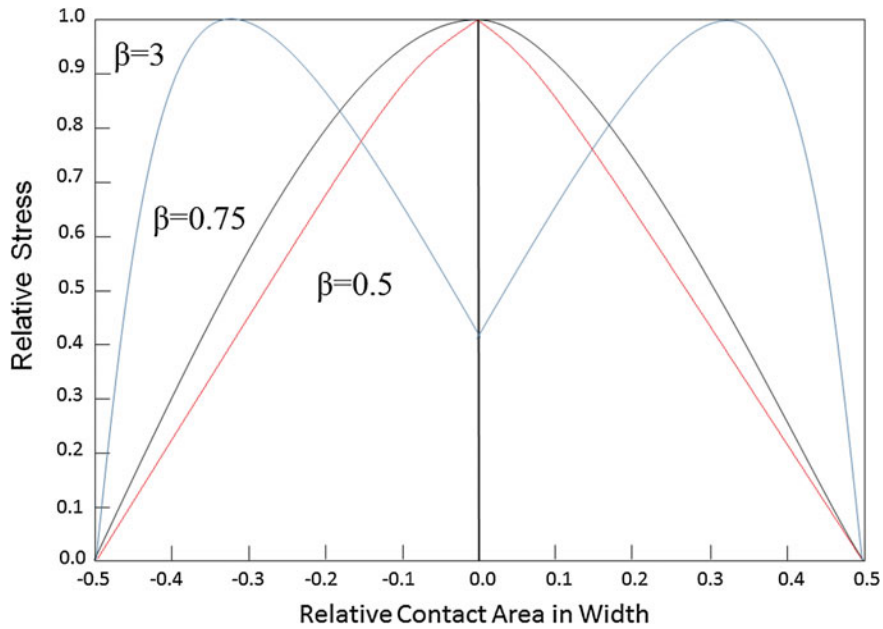


**Fig. 2.19** Relative stress versus relative contact area width

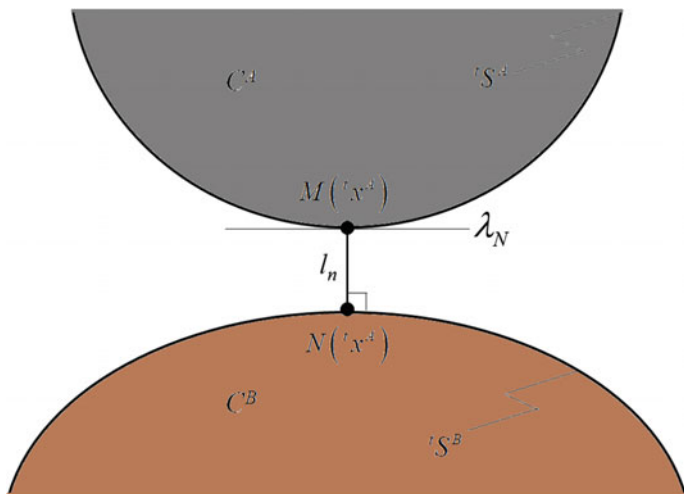


**Fig. 2.20** Schematic representation of two body's contact

$${}^t l = l({}^t x_M^A, t) = \left| {}^t x_M^A - {}^t x_N^B \right| = \min \left| {}^t x_M^A - {}^t x^B \right| \quad (2.50)$$

where  ${}^t x^B$  denotes the coordinate of any desired particle on surface  ${}^t S^B$  and orientation of  $l$  has to be the equal to  ${}^t n^B$  that represents the unit vector normal to the contact plane. Therefore, the vector  ${}^t l$  can be expressed as:

$${}^t l = l({}^t x_M^A, t) = ({}^t x_M^A - {}^t x_N^B) \cdot {}^t n_N^B \quad (2.51)$$

In order to meet the requirement of impenetrability for the two bodies (the tire and the road), we use the following constraint to define any particle  $P$  on the surface  ${}^t S^B$

$${}^t l_n = l({}^t x_M^A, t) = ({}^t x_M^A - {}^t x_N^B) \cdot {}^t n_N^B \geq 0 \quad (2.52)$$

in which  ${}^t l_n > 0$  means a gap exists between the particle  $M$  and the surface  ${}^t S^B$ , while  ${}^t l_n = 0$  means the particle  $M$  has a contact with  ${}^t S^B$ . As the above function is effective for any particle on surface  ${}^t S^A$  and  ${}^t S^B$ , the function can be described by

$${}^t l_n = l({}^t x^A, t) = ({}^t x^A - {}^t x^B) \cdot {}^t n^B \geq 0 \quad (2.53)$$

In addition, since the equivalent normal contact force is provided by the pressure, the condition of normal contact force  $\lambda_N$  (Fig. 2.20) is denoted by:

$$\lambda_N \geq 0 \quad (2.54)$$

In the tangential direction of rolling contact analysis, Coulomb model of friction is adopted to define the tangential contact conditions. In engineering analysis, coulomb model of friction is widely used because of its characteristics of simplicity and applicability [13]. The definition in the Coulomb friction model is that slip occurs when the tangential contact force (frictional resistance)  $\tau_{eq} = \sqrt{\tau_1^2 + \tau_2^2}$  equals to the critical stress  $\tau_{crit} = \mu \lambda_N \geq 0$ , which means that the friction force cannot be allowed to exceed the critical stress, which is

$$\tau_{eq} = \sqrt{\tau_1^2 + \tau_2^2} \leq \mu \lambda_N \quad (2.55)$$

in which  $\mu$  is the coefficient of friction,  $\tau_1$  and  $\tau_2$  are shear stresses in  $t_1$  direction and  $t_2$  direction respectively, and  $\lambda_N$  represents the normal contact force. On the other hand, no relative motion between the tire and the rigid road surface occurs when  $\tau_{eq} < \tau_{crit}$ . The stiff viscous behaviour is adopted to approximately simulate the non-relative-motion condition,

$$\tau_\alpha = \kappa \dot{\gamma}_\alpha \quad (\alpha = 1, 2) \quad (2.56)$$

in which  $\tau_x$  represents the shear stress in the tangential direction,  $\dot{\gamma}_x$  is the tangential slip rate in the tire/road contact plane,  $\kappa = \mu\lambda_N/2\Delta\omega R$  is the stick viscosity,  $\omega$  is the rotation angular velocity and  $R$  is the rolling radius of the tire, and  $\Delta$  is the slip tolerance [7].

### 2.2.5 Tire Rolling Resistance

One of important tire-road force products is the rolling resistance that is basically the parasitic energy dissipated by tire and the main source for loss of energy is the constant deformations of the tire while traversing and the soil beneath wheel. The phenomenon is quite complicated, and almost all operating conditions can influence the final product. In off-road vehicles during wheel motion the tire interacts with soil (depending on contact area) and a phenomenon occur known as rolling resistance wherein mechanical energy is changed to heat which is the consequence of rubber and soil deformation. The converted energy equals with the required energy to deform the rubber (temporary or elastic deformation) or the soil beneath the tire (constant or plastic deformation) in motion. Rolling resistance performs as a resistive force applied to wheel against the direction of traversing. In this manner, the energy loss owing to the irregular road is denoted by the work done by the longitudinal force opposing motion:

$$E_d = \sum |F_x(i)| \cdot U_x(i) \quad (2.57)$$

In the condition that the tire rolls at a constant amount of velocity  $v$  on the uneven road and the tire lose the free rolling condition, the state of leads to a negative longitudinal force, while the state of  $\omega \cdot r > v$  leads to a positive longitudinal force. However, in any form of being negative or positive longitudinal forces, the state of interrupting of tire from free rolling mode occur that are an indication of energy loss in the direction of motion and are considered rolling resistance.

Rolling resistance can be determined as the dissipated energy in unit of traveled distance that can be denoted as following:

$$F_R = D_E/L = D_E / \sum U_x(i) \quad (2.58)$$

where  $F_R$  is rolling resistance force,  $L$  is length of motion, and  $D_E$  is the dissipated energy. As an important factor in vehicle fuel consumption, the rolling resistance has been paid more and more attention by researchers, since the energy dissipation due to tire rolling resistance is a major component of vehicle energy loss. Rolling resistance is the energy that is lost when the tire is rolling and the main reason for loss of energy is the constant deformation of the tire. Rolling resistance is principally created by non-elastic effects; i.e. not all the energy needed for deformation

(or movement) of the wheel is recovered when the pressure is removed. There are two forms of energy loss that are hysteresis losses, and permanent (plastic) deformation of terrain. Another cause of rolling resistance is regarded as the slippage between the wheel and the surface, which dissipates energy. Hence, the condition of road surface and terrain properties plays a significant role in determination of the total rolling resistance force.

In the investigations regarding vehicle ride performance, the road unevenness was considered as sinusoidal harmonic wavy roads, triangular shapes and step functions. However, this easy shape of road profiles may not serve as functional foundation for the investigations about vehicle dynamic performance. To put forward a more realistic type of road profile, a random function may provide a better analysis platform to obtain accurate results about vehicle dynamics products. In the condition that the road profile is identified as a random function, it can be characterized by a power spectral density function while it has been found that the road unevenness related to the power spectral density for the road profiles can be approximated by [14]

$$S_x(\Omega) = C_{sp}\Omega^{-N_b} \quad (2.59)$$

where  $\Omega$  is the spatial frequency,  $S_x(\Omega)$  ( $m^3/cycle$ ) is the power spectral density function of the elevation of the road profile,  $C_{sp}$  and  $N_b$  are dimensionless road profile constants to determine the road unevenness. In order to carry out time domain conversion for road profiles, the power spectral density is expressed in terms of time-frequency, which is given by

$$S_x(f) = C_{sp}v^{N_b-1}f^{-N_b} \quad (2.60)$$

where  $v$  is the travelling velocity of the vehicle,  $f$  is the time frequency, and the unit of the power spectral density function  $S_x(f)$  is  $m^2/Hz$ . Different values of  $N$  and  $C_{sp}$  for different PSD functions for various road surfaces is provided in Table 2.1.

The objective of Discrete Fourier Transform (DFT) is to build the relationship between the time sequence  $x(n)$  and the frequency sequence  $X(k)$  [15], which can be given by

$$\text{DFT } X(k) = DFT[x(n)] = \sum_{n=0}^{N-1} x(n)e^{-j\frac{2\pi}{N}nk} \quad k = 0, 1, 2, \dots, N-1 \quad (2.61)$$

**Table 2.1** Values of  $N$  and  $C_{sp}$  for different PSD functions for various road surfaces [14]

| Road surfaces       | $N_b$ | $C_{sp}$              |
|---------------------|-------|-----------------------|
| Smooth runway       | 3.8   | $4.3 \times 10^{-11}$ |
| Rough runway        | 2.1   | $8.1 \times 10^{-6}$  |
| Smooth highway      | 2.1   | $4.8 \times 10^{-7}$  |
| Highway with gravel | 2.1   | $4.4 \times 10^{-6}$  |

$$\text{IDFT} \quad x(n) = \frac{1}{N} \sum_{k=0}^{N-1} X(k) e^{\frac{j2\pi}{N} nk} \quad k = 0, 1, 2, \dots, N-1 \quad (2.62)$$

in which  $N$  represents the length of the two sequences.

Generally, the definition of power spectral density for road file is limited in  $[0, +\infty)$  in the DFT process, the one-sided PSD  $S_x(f)$  needs to be transformed to the two-sided PSD  $G_x(f)$ . Based on the characteristics of real even function  $G_x(f)$ , the power spectral density, the relationship between  $S_x(f)$  and  $G_x(f)$  can be given by [7]:

$$S_x(f) = \begin{cases} 2G_x(f) & f \geq 0 \\ 0 & f < 0 \end{cases} \quad (2.63)$$

and according to the definition of power spectral density,  $S_x(f)$  can be expressed by

$$S_x(f) = \lim_{T \rightarrow \infty} \frac{2}{T} |X(f)|^2 = \lim_{T \rightarrow \infty} \frac{2}{T} \left| \int_{-\infty}^{+\infty} x(t) e^{-j2\pi ft} dt \right|^2 \quad (2.64)$$

in which  $t$  is the simulation time,  $T$  is the period,  $x(t)$  is the time sequence, and  $X(f)$  is the corresponding sequence in terms of frequency. When  $t > 0$  and the period  $T$  is limited, the Eq. (2.64) can be written as [7]

$$S_x(f) = \frac{2}{T} |X(f)|^2 = \frac{2}{T} \left| \int_0^T x(t) e^{-j2\pi ft} dt \right|^2 \quad (2.65)$$

By applying DFT, the power spectral density can be presented as

$$S_x(f_k) = \frac{2}{N\Delta t} \left| \sum_{n=0}^{N-1} x(n) e^{-j2\pi f_k n \Delta t} \Delta t \right|^2 = \frac{2\Delta t}{N} |X(k)|^2 = \frac{2T}{N^2} |X(k)|^2 = \frac{2}{\Delta f N^2} |X(k)|^2 \quad (2.66)$$

where  $\Delta t$  is the time increment,  $N = T/\Delta t$ ,  $\Delta f = 1/N\Delta t$  and  $f_k = k\Delta f$ . Hence, based on the relationship between power spectral density and the time sequence, the frequency sequence can be achieved as

$$\begin{aligned} |X(k)| &= |DFT[x(n)]| = N \sqrt{S_x(f_k) \Delta f / 2} \\ &= N \sqrt{S_x(f = k\Delta f) \Delta f / 2} \quad (k = 0, 1, \dots, N_r - 1) \end{aligned} \quad (2.67)$$

The time sequence can be obtained by taking the inverse discrete Fourier transform function on the frequency sequence. Based on the above method, the road surface elevations for different kinds of road surfaces are obtained.

As pointed out, the calculation length is used for the derivation of effective rolling resistance. However, the starting point for rolling resistance calculation is the beginning of the uneven road, which consists of the transition length plus the calculation length. As described in Eq. 6.6, for a tire rolling over a distance L of the uneven road, the rolling resistance for this part of the uneven road is calculated in terms of [7]

$$F_R|_{0 \rightarrow L} = \frac{D_E}{L} = \frac{D_E}{\sum U_x(i)} \quad (2.68)$$

in which the  $F_R|_{0 \rightarrow L}$  represents the average rolling resistance for the tire traversing a distance L of the uneven road.

The effective rolling resistance is obtained by extracting the rolling resistance in the distance covered in three revolutions of the tire and calculating the average value of the rolling resistance for this distance, the function of the effective rolling resistance  $F_R|_e$  is defined by [7]

$$F_R|_e = \frac{F_{R1} + F_{R2} + F_{R3}}{3} \quad (2.69)$$

where  $F_{Ri}$ ,  $i = 1, 2, 3$  represent the rolling resistance for revolution 1, revolution 2 and revolution 3, respectively.

### 2.2.6 Acceleration and Deceleration Characteristics Effects of Tire

The longitudinally oriented forces acting on a tire are functional on traction and braking performance and acceleration/deceleration characteristics. The model can be developed to analyze the braking/traction forces if the tire rubber is well fitted with wheel rim. The tread rubber consists of numerous independent springs around the tire circumference which are so-called as the brush model. The tire model provided is adopted from Bernard et al. [16] and Abe studies [17].

During time  $\Delta t$ , the displacement  $x$  is made according to:

$$x = u\Delta t \quad (2.70)$$

Given that the linear velocity of tire equals with the angular velocity multiplied by tire radius ( $u = R_0\omega$ ), the x-coordinate of point  $P'$  from point  $O'$  is (Fig. 2.21):

$$x' = R_0\omega\Delta t \quad (2.71)$$

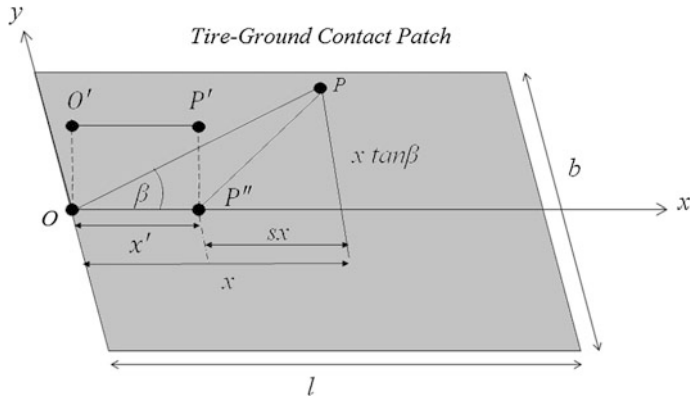


**Fig. 2.21** Tire deformation in contact plane

The difference between the two before terms ( $x$  and  $x'$ ) which represent the tread rubber deformation can be denoted as:

$$\Delta x = x - x' = \frac{u - R_0 \omega}{u} u \Delta t \quad (2.72)$$

If the tire longitudinal slip is considered as:

$$s = \frac{u - R_0 \omega}{u} \quad (2.73)$$

Then

$$\Delta x = xs \quad (2.74)$$

The distance in y-direction from O to P can be found by:

$$y = x \tan \beta = \frac{\tan \beta}{1 - s} x' \quad (2.75)$$

Since there is no displacement of point  $P'$  in the y-direction, the above is the deformation of tread rubber in the y-direction. Therefore, the forces per unit length and width, acting on point P, in the x-direction and y-direction, respectively, are  $\sigma_x$  and  $\sigma_y$

$$\sigma_x = -K_x(x - x') = -K_x \frac{s}{1 - s} x' \quad (2.76)$$

$$\sigma_y = -K_y y = -K_y \frac{\tan \beta}{1 - s} x' \quad (2.77)$$

The sign of these forces is taken as opposite to the axes direction. Moreover, the resultant force magnitude is,

$$\sigma = \left( \sigma_x^2 + \sigma_y^2 \right)^{\frac{1}{2}} = \left( K_x^2 s^2 + K_y^2 \tan^2 \beta \right)^{\frac{1}{2}} \frac{x'}{1-s} \quad (2.78)$$

where  $K_x$  and  $K_y$  are the longitudinal and lateral tread rubber stiffnesses per unit width and unit length. When the tire longitudinal slip ratio and side slip angle are produced, tire deformation occurs. As a result, a distribution of the contact surface force, proportional to  $x'$ , is created at the tire contact surface. Assuming a tire pressure distribution that is the same as in Sect. 2.2.3,

$$p = \frac{6F_z}{bl} \frac{x'}{l} \left( 1 - \frac{x'}{l} \right) \quad (2.79)$$

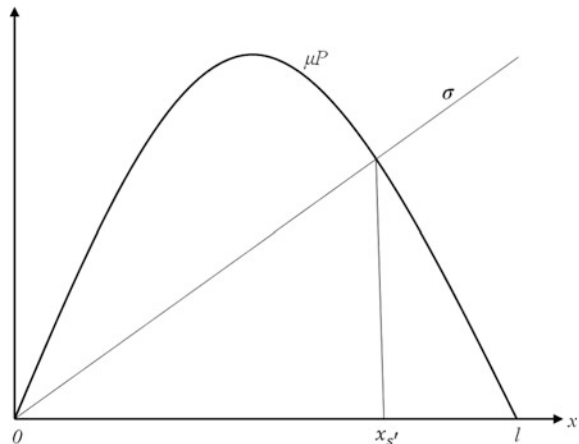
the tire contact surface force, as given by Eq. (2.78), is denoted by  $0 \leq x' \leq x'_s$  in the adhesive region, and  $x' \geq x''_s$  in the slip region where the tire contact surface force is given by  $\mu p$ .

In the adhesive region, the forces acting at the contact surface, in  $x$ - and  $y$ -directions are  $\sigma_x$  and  $\sigma_y$ ; respectively. In the slip region, the forces are  $\mu p \cos \theta$  and  $\mu p \sin \theta$ . Here,  $\theta$  determines the direction of the tire slip. Force distributions in contact plane is provided in Fig. 2.22.

By replacing  $\sigma = \mu p$  to find  $x'_s$  and introducing a dimensionless variable can be provided as:

$$\xi_s = \frac{x'_s}{l} = 1 - \frac{K_s}{3\mu F_z} \frac{\lambda}{1-s} \quad (2.80)$$

**Fig. 2.22** Force distributions in contact plane



where

$$\lambda = \left( s^2 + \left( \frac{K_\beta}{K_s} \right)^2 \tan^2 \beta \right)^{\frac{1}{2}} \quad (2.81)$$

$$K_s = \frac{bl^2}{2} K_x, \quad K_\beta = \frac{bl^2}{2} K_y \quad (2.82)$$

From the above, the overall forces acting on the whole tire contact surface, in x- and y-directions, are expressed as follows.

When  $\xi_s > 0$ , for a contact surface composed of adhesive and slip regions:

$$F_x = b \left( \int_0^{\xi'_s} \sigma_x dx' + \int_{\xi'_s}^l -\mu p \cos \theta dx' \right) \quad (2.83)$$

$$F_y = b \left( \int_0^{\xi'_s} \sigma_y dx' + \int_{\xi'_s}^l -\mu p \sin \theta dx' \right) \quad (2.84)$$

When  $\xi_s > 0$ , for a contact surface composed of slip regions only:

$$F_x = b \int_0^l -\mu p \cos \theta dx' \quad (2.85)$$

$$F_y = b \int_0^l -\mu p \sin \theta dx' \quad (2.86)$$

By replacing Eqs. (2.78)–(2.79) in Eqs. (2.85)–(2.86) denotes  $F_x$ ,  $F_y$  in as following:

If

$$\xi_s = 1 - \frac{K_s}{3\mu F_z} \frac{\lambda}{1-s} > 0 \quad (2.87)$$

Then,

$$F_x = -\frac{K_{ss}}{1-s} \xi_s^2 - 6\mu F_z \cos \theta \left( \frac{1}{6} - \frac{1}{2} \xi_s^2 + \frac{1}{3} \xi_s^3 \right) \quad (2.88)$$

$$F_y = -\frac{K_\beta \tan \beta}{1-s} \xi_s^2 - 6\mu F_z \sin \theta \left( \frac{1}{6} - \frac{1}{2} \xi_s^2 + \frac{1}{3} \xi_s^3 \right) \quad (2.89)$$

If,

$$\xi_s = 1 - \frac{K_s}{3\mu F_z} \frac{\lambda}{1-s} < 0 \quad (2.90)$$

then

$$F_x = -\mu F_z \cos \theta \quad (2.91)$$

$$F_y = -\mu F_z \sin \theta \quad (2.92)$$

The direction of the slip force,  $\theta$ ; is approximated by the slip direction at the slip start point.

$$\tan \theta = \frac{K_y \frac{\tan \beta}{1-s} x'}{K_x \frac{s}{1-s} x'} = \frac{K_\beta \tan \beta}{K_s s} \quad (2.93)$$

Therefore,

$$\cos \theta = \frac{s}{\lambda} \quad (2.94)$$

$$\sin \theta = \frac{K_\beta \tan \beta}{K_s \lambda} \quad (2.95)$$

It can be stated that

$$\begin{cases} K_s = 0 & \text{at } s \rightarrow 0 \\ K_\beta = 0 & \text{at } \beta \rightarrow 0 \end{cases} \quad (2.96)$$

In this condition,  $K_s$  represents the total longitudinal force per unit longitudinal slip ratio and  $K_\beta$  represents the total lateral force per unit side-slip angle.

$F_z$ , slip velocity,  $V_s$ , and friction coefficient  $\mu$  are closely interconnected and  $V_s$  is defined as following [17]:

$$V_s = \left( (u - R_0 \omega)^2 + (\mu^2 \tan^2 \beta) \right)^{\frac{1}{2}} = u(s^2 + \tan^2 \beta)^{\frac{1}{2}} \quad (2.97)$$

It can be thus inferred that the longitudinal slip ratio, slip angle, tire load and tire traveling speed affect tire longitudinal and lateral forces.

In the case of acceleration, the slip ratio is denoted by:

$$s = \frac{u - R_0\omega}{R_0\omega} \quad (2.98)$$

Therefore, the x-oriented and y-oriented stresses can be presented as following:

$$\begin{aligned}\sigma_x &= -K_x s x' \\ \sigma_y &= -K_y (1 + s) \tan \beta x'\end{aligned} \quad (2.99)$$

Since

$$\sigma = \left( \sigma_x^2 + \sigma_y^2 \right)^{\frac{1}{2}} \quad (2.100)$$

Therefore;

$$\sigma = \left( K_x^2 s^2 + K_y^2 (1 + s)^2 \tan^2 \beta x' \right)^{\frac{1}{2}} \quad (2.101)$$

According to the theory for braking condition regarding the point the slip changes from the adhesive region to the slip region, the following can be developed:

$$\xi_s = 1 - \frac{K_s}{3\mu F_z} \lambda \quad (2.102)$$

where

$$\lambda = \left( s^2 + \left( \frac{K_\beta}{K_s} \right)^2 (1 + s^2) \tan^2 \beta \right)^{\frac{1}{2}} \quad (2.103)$$

There are two conditions when  $\xi_s > 0$  and  $\xi_s < 0$ .

If  $\xi_s > 0$ , then:

$$F_x = -K_s s \xi_s^2 + 6\mu F_z \cos \theta \left( \frac{1}{6} - \frac{1}{2} \xi_s^2 + \frac{1}{3} \xi_s^3 \right) \quad (2.104)$$

$$F_y = -K_\beta (1 + s) \tan \beta \xi_s^2 - 6\mu F_z \sin \theta \left( \frac{1}{6} - \frac{1}{2} \xi_s^2 + \frac{1}{3} \xi_s^3 \right) \quad (2.105)$$

If  $\xi_s < 0$ , then:

$$\begin{aligned} F_x &= -\mu F_z \cos \theta \\ F_y &= -\mu F_z \sin \theta \end{aligned} \quad (2.106)$$

where,

$$\tan \theta = \frac{K_y(1+s) \tan \beta x'}{K_x s x'} = \frac{K_\beta \tan \beta(1+s)}{K_s s} \quad (2.107)$$

$$\cos \theta = \frac{s}{\lambda} \quad (2.108)$$

$$\sin \theta = \frac{K_\beta \tan \beta(1+s)}{K_s \lambda} \quad (2.109)$$

and the slip velocity is obtained at:

$$V_s = u \left( \frac{s^2}{(1+s)^2} + \tan^2 \beta \right)^{\frac{1}{2}} \quad (2.110)$$

It is finally concluded that from the theoretical analysis that braking and acceleration affect the tire cornering characteristics.

## References

1. Ming, Q. (1997). *Sliding mode controller design for ABS system*. Master thesis, Poly Technic Institute and State University.
2. Jazar, R. N. (2013). *Vehicle dynamics: Theory and application*. Springer Science & Business Media.
3. Mooney, M. (1940). A theory of large elastic deformation. *Journal of Applied Physics*, 11(9), 582–592.
4. Rivlin, R. S. (1948). Large elastic deformations of isotropic materials. I. Fundamental concepts. *Philosophical Transactions of the Royal Society of London. Series A, Mathematical and Physical Sciences*, 240(822), 459–490.
5. Yeoh, O. H. (1993). Some forms of the strain energy function for rubber. *Rubber Chemistry and Technology*, 66(5), 754–771.
6. Ogden, R. W. (1997). *Non-linear elastic deformations*. Courier Dover Publications.
7. Wei, C. (2015). A finite element based approach to characterising flexible ring tire (FTire) model for extended range of operating conditions (Doctoral dissertation, University of Birmingham).
8. Dunn, J. W., & Olatunbosun, O. A. (1989). Linear and nonlinear modeling of vehicle rolling tyre low-frequency dynamic behavior. *Vehicle System Dynamics*, 18, 179–189.
9. Wei, C., & Yang, X. (2016). Static tire properties analysis and static parameters derivation to characterising tire model using experimental and numerical solutions. *Journal of Advances in Vehicle Engineering*, 2(1).

10. Hallonborg, U. (1996). Super ellipse as tyre-ground contact area. *Journal of Terramechanics*, 33(3), 125–132.
11. Keller, T. (2005). A model for the prediction of the contact area and the distribution of vertical stress below agricultural tyres from readily available tyre parameters. *Biosystems Engineering*, 92(1), 85–96.
12. Schjønning, P., Lamandé, M., Tøgersen, F. A., Arvidsson, J., & Keller, T. (2008). Modelling effects of tyre inflation pressure on the stress distribution near the soil-tyre interface. *Biosystems Engineering*, 99(1), 119–133.
13. Wang, X. (2003). *Finite element method*. Beijing, China: Tsinghua University Press.
14. Wong, J. Y. (2008). *Theory of ground vehicles* (4th ed., vol. xxxi, 560 p). Hoboken, N.J.: Wiley.
15. Pacejka, H. B., & Besselink, I. J. M. (1997). Magic formula tyre model with transient properties. *Vehicle System Dynamics*, 27, 234–249.
16. Bernard J. E., et al. (1977). Tire shear force generation during combined steering and braking maneuvers. SAE Paper 770852.
17. Abe, M. (2015). *Vehicle handling dynamics: Theory and application*. Butterworth-Heinemann.

# Chapter 3

## Performance of Off-road Vehicles

### Nomenclature

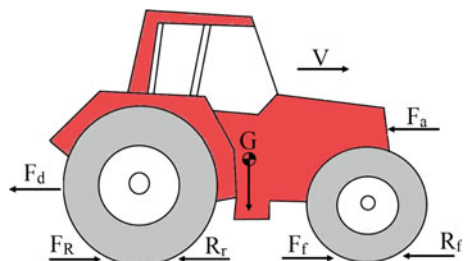
|                       |   |
|-----------------------|---|
| $F_f$                 | Front wheel tractive force  |
| $F_R$                 | Rear wheel tractive force   |
| $R_f$                 | Front wheel rolling resistance  |
| $R_r$                 | Rear wheel rolling resistance   |
| $F_d$                 | Drawbar pull  |
| $F_a$                 | Air resistance force  |
| $m_G$                 | Total vehicle mass at center of gravity                               |
| $a$                   | Vehicle longitudinal acceleration                                     |
| $\theta, \alpha$      | Surface slope   |
| $x_G, y_G, z_G$       | Center of gravity position  |
| $W_f$                 | Wheel load on front wheels  |
| $W_r$                 | Wheel load on rear wheels   |
| $W_{rr}$              | Wheel load on rear right wheel  |
| $W_{rl}$              | Wheel load on rear left wheel   |
| $F_d$                 | Drawbar pull  |
| $y_a$                 | Distance between the tractor rear wheel center and $y_G$              |
| $y$                   | Distance between the tractor rear wheel center and drawbar pull point |
| $c$                   | Soil cohesion   |
| $\varphi$             | Soil internal friction angles   |
| $j$                   | Soil shear modulus  |
| $k$                   | Shear deformation   |
| $\tau$                | Soil shear stress   |
| $p$                   | Pressure  |
| $A$                   | Contact area  |
| $W$                   | Width, wheel load   |
| $\rho$                | Mass density of the air   |
| $C_d$                 | Non-dimensional aerodynamic resistance coefficient                    |
| $A_f$                 | Vehicle front area  |
| $S_w$                 | Wind speed  |
| $K_c$ and $K_\varphi$ | Coefficients from pressure sinkage equation                           |
| $n$                   | Sinkage exponent  |

|                       |   |
|-----------------------|---|
| $b$                   | Smaller dimension of the rectangular contact area |
| $z$                   | The sinkage                                       |
| $p_i$                 | Inflation pressure of tire                        |
| $p_c$                 | Tire stiffness is denoted by                      |
| $d$                   | Wheel diameter                                    |
| $\gamma$              | Bulk density of sand                              |
| $N_q$                 | Terzaghi's bearing capacity solution              |
| $\delta$              | Tire deflection                                   |
| $h$                   | Tire section height                               |
| CI                    | Cone Index  |
| i                     | Wheel slippage                                    |
| $c_n$                 | Wheel numeric                                     |
| CRR                   | Coefficient of rolling resistance                 |
| CMR                   | Coefficient of motion resistance                  |
| $\mu$                 | Thrust coefficient                                |
| $T$                   | Thrust  |
| $T_w$                 | Wheel torque                                      |
| $r$                   | Wheel radius                                      |
| $B_n$                 | Wheel numeric based on Brixius model              |
| $F_z$                 | Dynamic load on the wheel                         |
| $d_z$                 | Vertical displacement of the wheel                |
| $v$                   | Forward speed                                     |
| $k_{1z}$ and $k_{2z}$ | Tire system stiffness                             |
| $c_{1z}$ and $c_{2z}$ | Tire damping parameters                           |
| $V_r$                 | Longitudinal velocity of center of wheel          |
| $\omega$              | Angular velocity of wheel                         |
| $S_l$                 | Longitudinal slip in driven state                 |
| $\alpha$              | Slip angle  |
| $\theta_0$            | Stationary central angle                          |
| $\theta_e$            | Entry angle                                       |
| $\theta_r$            | Exit angle  |
| $\theta$              | Central angle                                     |
| $\theta_N$            | Angle where the radial stress is maximum          |
| R                     | Rigid wheel radius                                |
| $\tau_{max}$          | Limiting shear stress                             |
| $j_x$ and $j_y$       | Shear deformation in x and y directions           |
| $\tau_{ycp}$          | Lateral shear stress across tire width            |
| $\sigma_{nr}(\theta)$ | Tire radial stress                                |
| DB                    | Drawbar pull                                      |
| $\beta$ and $\zeta$   | Dimensionless variables                           |
| $k_i$                 | Spring stiffness                                  |
| $c_i$                 | Damping coefficient                               |
| I                     | Mass moment of inertia                            |
| $v_y$                 | Lateral velocity                                  |

|                       |  |
|-----------------------|--|
| $r$                   | Yaw rate   |
| $M_z$                 | External yaw moment  |
| $\beta_i$             | Individual sideslips   |
| $F_y$                 | Tire lateral force   |
| $C\alpha$             | Tire cornering stiffness   |
| $d\beta$              | Angular displacement of the front axle pivot point relative to the rear axle |
| $b$                   | Wheel width  |
| $\vec{A}$             | Vectors of angular momentum  |
| $\vec{M}$             | Vectors of body external moments   |
| $I_{xx}$ and $I_{yy}$ | Moments of inertia with respect to the x and y                               |
| $I_{xy}$              | Products of inertia  |
| $\omega$              | Rolling angular velocity   |
| $\omega_p$            | Pitching angular velocity  |
| ME                    | Mechanical energy  |
| KE                    | Kinetic energy   |
| PE                    | Potential energy   |
| dr                    | Rolling axis of tractor  |
| dp                    | Pitching axis of tractor   |
| $\gamma$              | Initial angle of side overturn   |
| $\lambda$             | Initial angle of backward overturn   |

Vehicle performance refers to the science of motioning of the vehicle in terms of transient performance (e.g. acceleration, braking, cornering) and those of steady-state performance criteria such as (power driveline losses, gross and net traction, vehicle aerodynamics). However, there are different indices for the assessment of road and off-road vehicles. The very first step is to distinguish between the acting forces on an off-road vehicle. The free body diagram of a vehicle traveling over a soft deformable terrain is presented in Fig. 3.1.

**Fig. 3.1** Free body diagram of a vehicle travelling over a soft deformable terrain



In this case, the dynamic equation of motion along the longitudinal axis  $x$  of motion, can be written as:

$$\sum F_x = m\bar{a} \quad (3.1)$$

Therefore:

$$F_f + F_R - R_r - R_f - F_a - F_d = m_G a \quad (3.2)$$

where  $F_f$ ,  $F_R$ ,  $R_f$ ,  $R_r$ ,  $F_d$  and  $F_a$  are front wheel tractive force, rear wheel tractive force, front wheel rolling resistance, rear wheel rolling resistance, drawbar pull and air resistance force, respectively.  $m_G$  and  $a$  represent the total vehicle mass at center of gravity and vehicle longitudinal acceleration, respectively. It is noteworthy that at travelling over a steeped surface, another term of  $mgsin\theta$  ( $\theta$  represents the surface slope) should be subtracted from the tractive forces. Also, the case of all-wheel-drive or rear-wheel-drive is influential on the production of  $F_r$  or  $F_f$  (Fig. 3.2).

The factors such as rolling resistance, tractive forces, aerodynamic force and drawbar pull have to be meticulously covered to get a better insight into off-road vehicle dynamics.

It is an essential step particularly for agricultural tractors to determine the position of center of gravity in the coordinate system ( $x$ ,  $y$ ,  $z$ ). To this end, there are four steps to be taken as following:

- (I) A weighbridge can be adopted to determine the total weight of the vehicle (Fig. 3.3).
- (II) The weight on front (or rear) wheels has to be determined to find  $x_g$ :

$$\begin{aligned} \sum M_O &= 0; \\ W_f \times C_l &= mg \times x_G; \quad x_G = \frac{W_f}{mg} C_l \end{aligned} \quad (3.3)$$

- (III) In order to determine  $z_G$ , the following process can be adopted (Fig. 3.4).

**Fig. 3.2** Off-road vehicle climbing an inclined surface with slope of  $\theta$

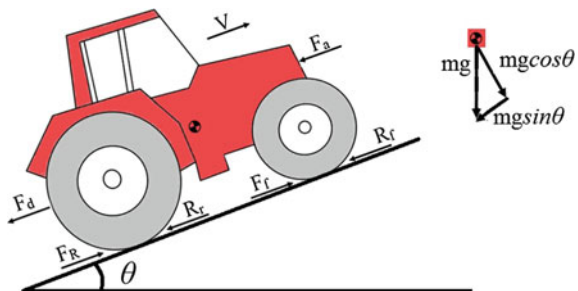


**Fig. 3.3** Determination of vehicle weight on front and rear wheels and  $x_G$

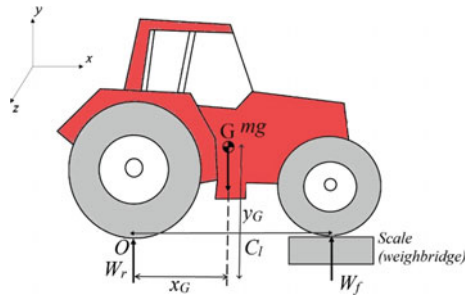


**Fig. 3.4** Determination of lateral position of center of gravity  $z_G$

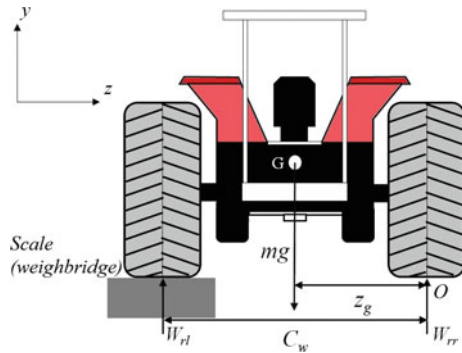
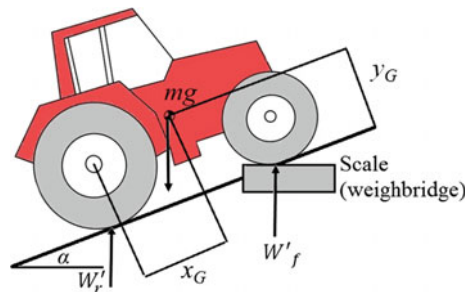


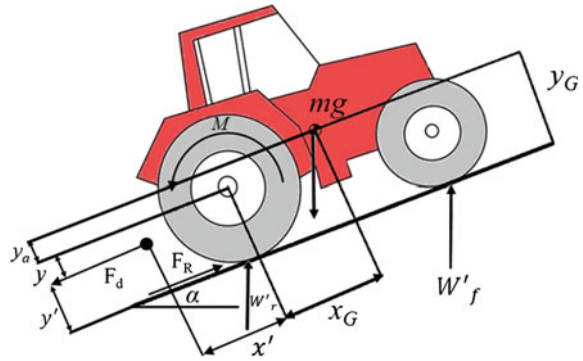
**Fig. 3.5** Determination of vertical position of center of gravity  $y_G$



$$\sum M_O = 0; \\ W_{rr} \times C_w = mg \times z_G; \quad z_G = \frac{W_{rr}}{mg} C_w \quad (3.4)$$

- (IV) If one intends to calculate  $y_G$ , it is typical to measure the weight of front or rear wheels in inclined situation (Fig. 3.5):

**Fig. 3.6** The limiting factors of the objective vehicle performance in the presented instability situation



$$(W'_f \times C_l \times \cos\alpha) + (mg \times \sin\alpha \times y_G) - (mg \times \cos\alpha \times x_G) = 0 \quad (3.5)$$

$$y_G = \frac{mg \times x_G - W'_f \times C_l}{mg} \cot(\alpha) \quad (3.6)$$

The analysis provided in this section demonstrates the limiting factors of the objective vehicle performance in the presented instability situation (Fig. 3.6).

In instability threshold,  $W'_f$  equals zero. Based on the moments applied to the center of rear wheel:

$$M + (mg) \sin \alpha \cdot y_a = (mg) \cos \alpha \cdot x_G + F_d y \quad (3.7)$$

And following terms could also be derived:

$$W'_r = mg \cos \alpha \quad (3.8)$$

$$F_R = mg \sin \alpha + F_d \quad (3.9)$$

$$M = F_R \cdot r \quad (3.10)$$

$$F_R = \psi' W'_r \quad (3.11)$$

Replacing  $M$  and  $F_R$  in Eq. 3.7, one can obtain:

$$\psi(mg) \cos \alpha r = W \cos \alpha x_G + \psi(mg) \cos \alpha y - (mg) \sin \alpha y - (mg) \sin \alpha y_a \quad (3.12)$$

$$\sin \alpha(y + y_a) = \cos \alpha(x_G + \psi(y - r)) \quad (3.13)$$

$$\tan \alpha(y + y_a) = x_G - \psi(y - r) \quad (3.14)$$

$$\tan \alpha(r - y' + y_a) = x_G - \psi(r - y) \quad (3.15)$$

$$\psi' = \frac{x_G - \tan \alpha(r - y' + y_a)}{y'} \quad (3.16)$$

$$\psi' = \tan \alpha + \frac{x_G - \tan \alpha(r + y_a)}{y'} \quad (3.17)$$

$$\psi' = \tan \alpha + \frac{\frac{x_G}{r+y_a} - \tan \alpha}{\frac{y'}{r+y_a}} \quad (3.18)$$

$$\frac{x_G}{r + y_a} = \tan \alpha_s \quad (3.19)$$

where  $\alpha_s$  represents the static condition. In other words, it is the inclination in which the vehicle overturn occurs about the contact point in static condition. In general, it is a limit that without drawbar force ( $F_d$ ),  $\alpha_s$  is equal or more than  $40^\circ$ .

In this manner, it should be noted that:

- (1) In the case that the required  $\psi'$  is lower than the calculated  $\psi'$  obtained from Eq. 3.18, the vehicle will not overturn.
- (2) In the case that the required  $\psi'$  is about the calculated  $\psi'$  obtained from Eq. 3.18, the vehicle will be subject to overturn.
- (3) In the case that the required  $\psi'$  is greater than the calculated  $\psi'$  obtained from Eq. 3.18, the vehicle will overturn.

However, it should be highlighted that the provided definitions may lead to more driving safety, owing to dynamic condition the performance and the developed equations will change such as acceleration for motion in inclined surface can bring about inertia force about the center of gravity and therefore vehicle overturn. A similar condition is also valid for braking condition.

### 3.1 Influential Parameters on Off-road Vehicle Performance

When wheel is in interaction with the soil profile, there are some motion resistive forces such as rolling resistance while there are some motion generator forces that are responsible to provide a robust motion to the vehicle. Driving wheels are usually responsible to provide a traction force that can overcome rolling resistance and provide an appropriate motion to the wheel. In order to run such a tires, it is required to apply a torque to overcome the motion resistive effects. Wheel-soil interaction products are shown in Fig. 3.7.

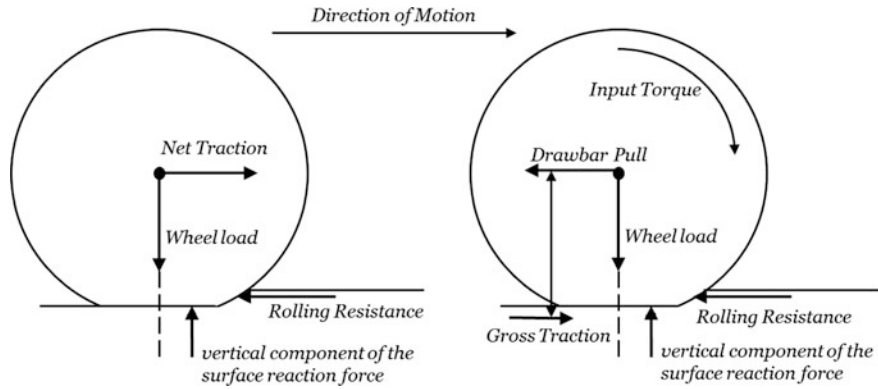


**Fig. 3.7** Wheel-terrain interaction products

Based on Fig. 3.7, the net traction produced by a wheel can be considered as the subtraction of rolling resistance from gross traction. Gross traction is a direct function of shear stress under wheel and is described by Janosi-Hanamoto Equation [1]:

$$\tau = (c + p \tan \varphi) \left( 1 - e^{-\frac{j}{k}} \right) \quad (3.20)$$

where  $c$  and  $\varphi$  are cohesion and internal friction angles, respectively and  $j$  and  $k$  are soil shear modulus and shear deformation, respectively.  $j$  and  $k$  are represented in Fig. 3.8.

If the Janosi-Hanamoto equation is multiplied by contact area, the gross traction can be achieved known as the maximum tractive force:

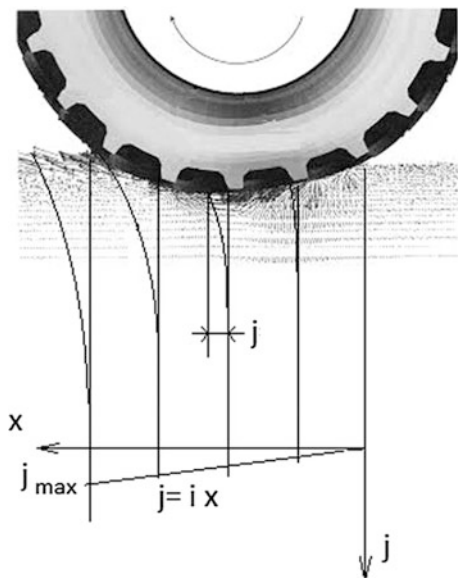
$$H = (Ac + W \cos \theta \tan \varphi) \left( 1 - e^{-\frac{j}{k}} \right) \quad (3.21)$$

It is noteworthy that contact area is of the complex parameters to be determined because of being function of different parameters such as tire geometry and stiffness, tire inflation pressure, wheel load and terrain parameters. In the simplest assumptions, contact area is considered as a rectangular shape while circular, elliptic and super-elliptic based functions may provide more realistic measures.

### 3.1.1 Aerodynamic Force

The main aims of aerodynamic force are to decrease drag and wind noise and avoiding undesired lift forces and other causes of aerodynamic instability at high travelling velocities. For some types of racing vehicles, it may also be important to

**Fig. 3.8** Shear deformation and soil shear modulus



produce downward force to improve traction and thus cornering abilities. Drag coefficient ( $C_d$ ) is a coefficient rating of a vehicle's aerodynamic smoothness, related to the shape of the car. By multiplication of  $C_d$  by the vehicle's frontal area, an index of total drag can be achieved. Also, the optimization of aerodynamic resistance force can result in reduction of fuel consumption, more satisfactory ride comfort and improvement of driving characteristics such as stability, handling, traffic safety, etc.

Aerodynamic resistance is presented as following:

$$F_a = \frac{\rho}{2} C_d A_f S_w^2 \quad (3.22)$$

where  $\rho$  is mass density of the air,  $C_d$  is the non-dimensional aerodynamic resistance coefficient which depends on vehicle shape,  $A_f$  is vehicle front area and  $S_w$  is wind speed or in other term, it is vehicle speed relative to wind speed. Aerodynamic resistance is usually not a significant factor that affects the performance of off-road vehicles operating at speeds lower than 50 m/s. Figure 3.9 shows the aerodynamic resistance with respect to wind speed (or vehicle speed relative to wind speed) for a heavy vehicle with frontal area of  $6.5 \text{ m}^2$  at drag coefficient of 1.17.

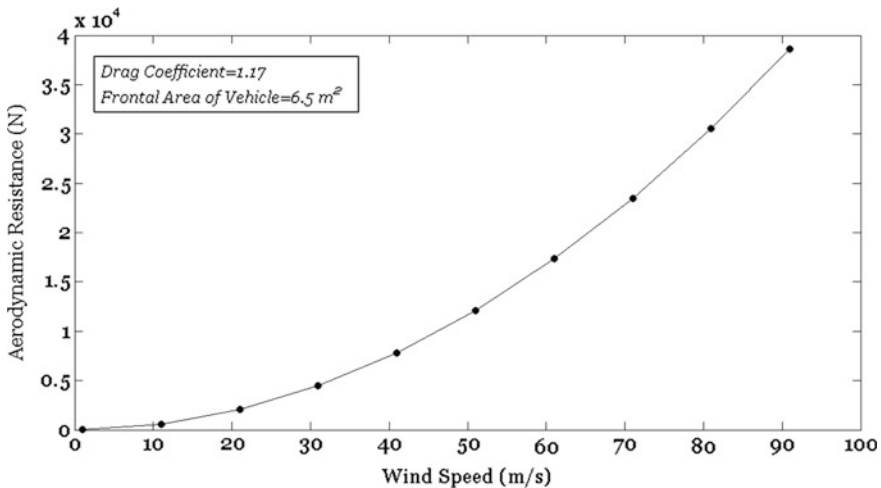


Fig. 3.9 Aerodynamic resistance with respect to wind speed

### 3.1.2 Rolling Resistance

Resistance in the motion status of the vehicle in general term is called as motion resistance. Regarding off-road vehicles, the motion resistance sources from three major factors:

- obstacle resistance (that occurs while the vehicle wheel collides road irregularities such as stumps and rocks while the amount of obstacle resistance relies on the geometry of the obstacle and can be determined theoretically and empirically).
- internal resistance of the wheel system that depends on tire characteristics. If a pneumatic tire is in motion, energy is dissipated mainly through hysteresis of tire material caused by carcass flexing that acts as a resisting force against the rolling direction of the wheel (see Chap. 2).
- resistance that is formed from wheel–terrain interaction such as that created by the sinkage of the wheel in soil profile.

Rolling resistance is a moment applied to wheel against with the direction of motion, while a force is required to move the wheel forward. It is an undesired force applied to wheel while initiating to roll on a surface caused by the energy required for soil or wheel deformation. Therefore, rolling resistance is closely related to soil deformation under the wheels and its quantification without any suitable device and in uncontrolled condition may not lead to the desired output. Furthermore, the assessment of rolling resistance seems to be a difficult task when the wheel rolls since the condition becomes obviously variable during the motion.

Bekkar [2] scientifically studied and established the relations between wheel and soil in 1956. Based on his equation (Eq. 3.23), amount of rolling resistance is influenced by variety of parameters may be expressed by:

$$R = \frac{3W^{\left(\frac{2n+2}{2n+1}\right)}}{(3-n)^{\left(\frac{2n+2}{2n+1}\right)}(n+1)(K_c + bK_\phi)^{\left(\frac{1}{2n+1}\right)}d^{\left(\frac{n+1}{2n+1}\right)}} \quad (3.23)$$

$K_c$  and  $K_\phi$  have been yielded from pressure sinkage equation (Eq. 3.24) as below:

$$P = \left(\frac{K_c}{b} + K_\phi\right)Z^n \quad (3.24)$$

where  $W$  is vehicle weight,  $n$  is sinkage exponent,  $b$  is the smaller dimension of the rectangular contact area,  $Z$  is the sinkage, and  $K_c$  and  $K_\phi$  are the soil condition parameters. The required energy to compact the soil beneath the wheel during movement for a definite distance is equal with a resistive force against movement multiplied by the distance. This resistive force (i.e. rolling resistance) is suggested to be as follows (Eq. 3.25):

$$R = b_w \int_0^{Z_{max}} \left(\frac{K_c}{b} + K_\phi\right) Z^n dZ \quad (3.25)$$

Bekker also proposed a model to predict the motion resistance of pneumatic tire where inflation pressure of tire is presented by  $p_i$  and the tire stiffness is denoted by  $p_c$ .

$$R_c = \frac{[b(p_i + p_c)]^{\frac{n+1}{n}}}{(n+1)(k_c + bk_\phi)^{\frac{1}{n}}} \quad (3.26)$$

Validity of equation above in order to predict rolling resistance based on soil deformation was offered by Wong [3] for wheel diameters more than 50 cm and sinkage levels less than 15 % of wheel diameter.

Later, Hetherington and Littleton [4] suggested a simple approximate equation for calculation of rolling resistance in terms of geometry, load and accepted soil constants as following:

The proposed model describing rolling resistance of wheel over sand is following as:

$$R = \sqrt[3]{\frac{2W^4}{bd^2\gamma N_q}} \quad (3.27)$$

where  $R$  is rolling resistance,  $W$  is vertical load acting on wheel,  $b$  is width of wheel,  $d$  is wheel diameter,  $\gamma$  is bulk density of sand, and  $N_q$  is recognized as Terzaghi's bearing capacity solution.

One important step is classification and determination of rut characteristics and developing equations that explain pressure-sinkage and stress-shear displacement behaviors. On this basis, Rowland [5] proposed an equation for the mean maximum pressure under a pneumatic tire as following:

$$P = \frac{W}{b^{0.85} d^{1.5}} \sqrt{\frac{\delta}{h}} \quad (3.28)$$

where  $W$  is wheel load,  $b$  and  $d$  are tire width and diameter, respectively,  $\delta$  is tire deflection and  $h$  is tire section height.

Rowland also developed a mobility number and coefficient of rolling resistance as following:

$$N_R = \frac{CI \times b^{0.85} \times d^{0.15}}{W} \left( \frac{\delta}{h} \right)^{\frac{1}{2}} \quad (3.29)$$

$$CRR = 3N_R^{-2.7} \quad (3.30)$$

Uffelmann [6] assessed rigid wheels working on shallow soil sinkage and concluded that the pressure under the wheel is  $P = 5.7c$  and sinkage can be presented as following:

$$Z = \frac{W^2}{(5.7c)^2 b^2 d} \quad (3.31)$$

and therefore, rolling resistance can be defined as:

$$\begin{aligned} Rl &= A \int P dz \\ R &= \frac{A}{l} \int_0^z 5.7cdz \rightarrow R = b \left[ \frac{W^2}{(5.7c)^2 b^2 d} \right] (5.7c) = \frac{W^2}{(5.7bcd)} \end{aligned} \quad (3.32)$$

where  $c$  and  $l$  are soil cohesion and contact length respectively.

Gee-Clough [7] developed semi-empirical model for rigid wheels based on the soil radial and tangential stresses with multiplication of Bekker equation by the term  $(i + 1)^{\frac{-n}{2n+1}}$  where  $i$  is the wheel slippage.

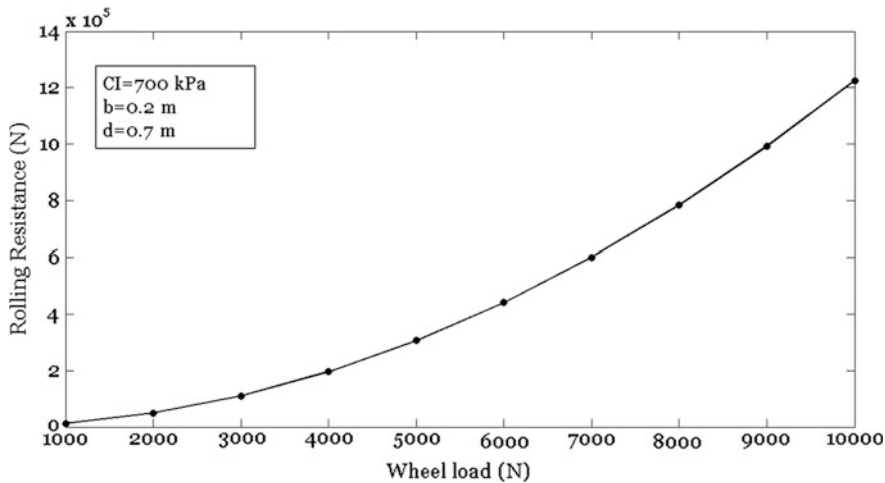


Fig. 3.10 Relation between vertical load and rolling resistance using Wismer-Luth model

Also on the basis of wheel numeric,  $c_n$ , Wismer and Luth [8] developed an equation for the prediction of coefficient of rolling resistance as following:

$$CRR = \left( \frac{1.2}{c_n} \right) + 0.04, \quad c_n = \frac{CI \cdot b \cdot d}{W} \quad (3.33)$$

where CI represents the cone index in kPa.

And therefore, rolling resistance which is the coefficient of rolling resistance multiplied by wheel load can be represented by

$$RR = \frac{1.2 \times W^2}{CI \cdot b \cdot d} + 0.04W \quad (3.34)$$

where  $W$  is vertical load (kN), CI is cone index (kPa),  $b$  is width of tire (m), and  $d$  is wheel diameter (m).

Figure 3.10 demonstrates the relation between vertical load and rolling resistance using Wismer-Luth model where CI is 700 kPa,  $b$  is 0.2 m, and  $d$  is 0.7 m. In this regard, rolling resistance variations with respect to Cone Index and wheel diameter are demonstrated in Fig. 3.11.

Taghavifar and Mardani [9] developed a multiple regression method comprising the tested variables. This equation was evaluated against experimental results obtained indicating relative high correlation and reasonable accurate predicting rolling resistance (RR).

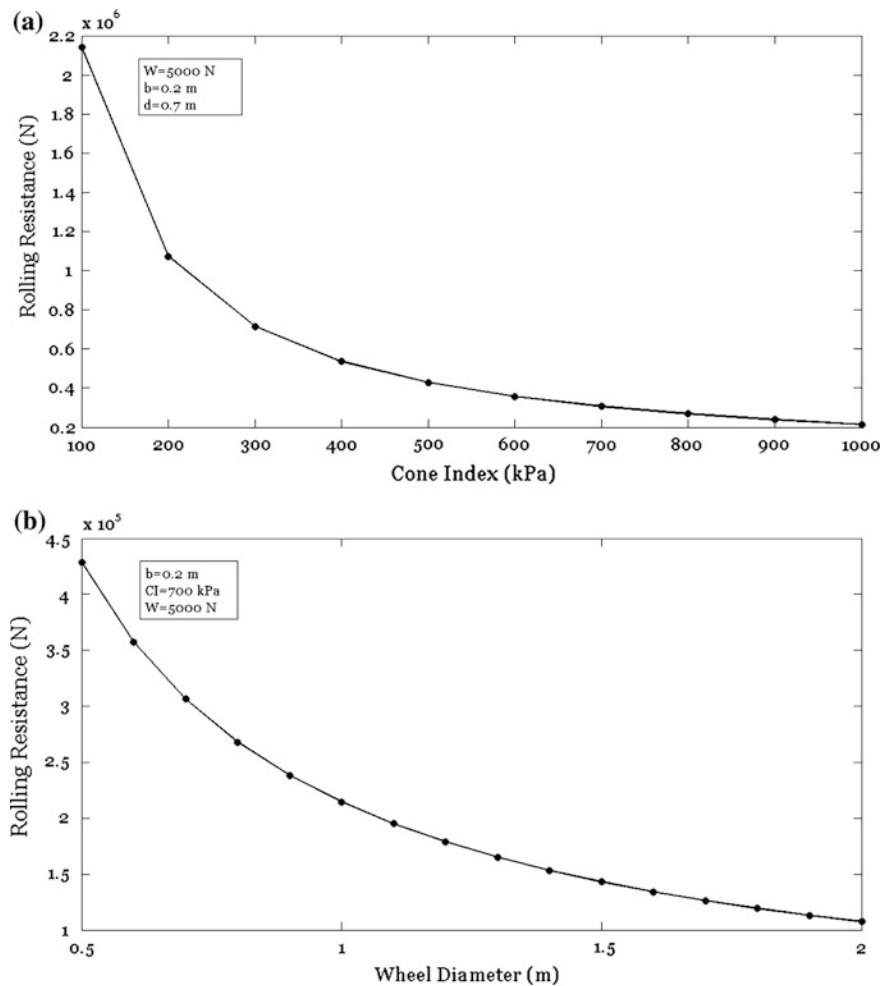


**Fig. 3.11** Rolling resistance variations with respect to **a** Cone Index and **b** wheel diameter

$$RR = 10W^2 + 3.2W - 0.37P - 25V + 103.56 \quad (3.35)$$

where  $W$  is vertical load (kN),  $P$  is inflation pressure (kPa), and  $V$  is velocity (m/s).

Based on the model developed, it was stated that velocity has a negligible effect on rolling resistance in the limited range of velocity while wheel load and tire inflation pressure had the greatest impacts, respectively. Also a relationship was established between rolling resistance and contact area (Fig. 3.12). It is noteworthy that rolling resistance is directly affected by the soil volumetric profile that is deformed under definite load. Hence, the magnitude of contact area affects rolling resistance significantly.

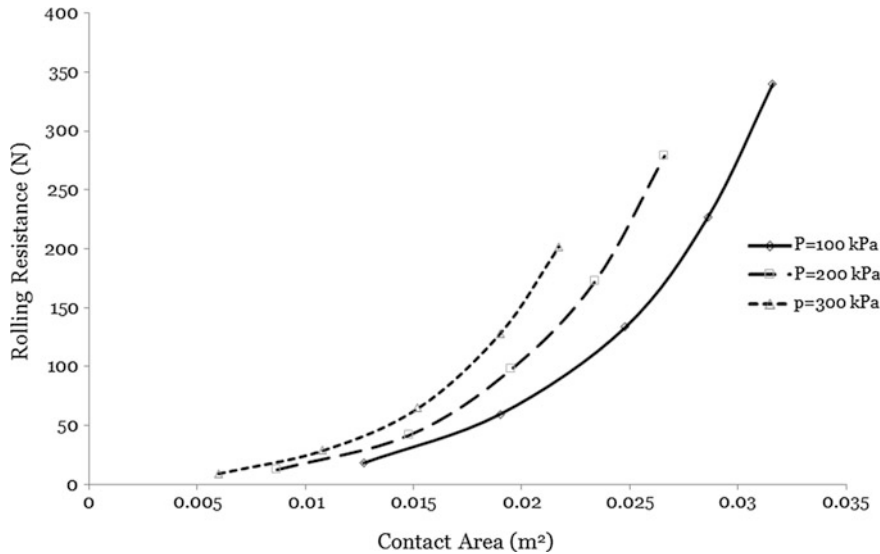


**Fig. 3.12** A relationship was established between rolling resistance and contact area

Freitag [10] developed a model based on dimensional assessment in which, rolling resistance of pneumatic tires were estimated and two dimensionless mobility numbers were reported as following:

$$\begin{aligned} \text{Clay mobility number} &= \frac{CIbd}{W} \left( \frac{\delta}{h} \right)^{\frac{1}{2}} \\ \text{Sand mobility number} &= G(bd)^{\frac{3}{2}} \left( \frac{\delta}{h} \right) \end{aligned} \quad (3.36)$$

In this manner, Freitag applied cone index (CI) and gradient of cone index (G) to identify the soil, and the parameters of wheel load (W), width (b), diameter (d), section height (h) and deflection ( $\delta$ ) to characterize the wheel. Turnage [11] developed the model and improved the models developed by Freitag and included some modifications as following:

$$RR = \frac{CIbd}{W} \left( \frac{\delta}{h} \right)^{\frac{1}{2}} \left( \frac{1}{1 + \frac{b}{2d}} \right) \quad (3.37)$$

Based on Freitag model, it is possible to observe the trend of rolling resistance variation with respect to tire deflection and section height (Fig. 3.13).

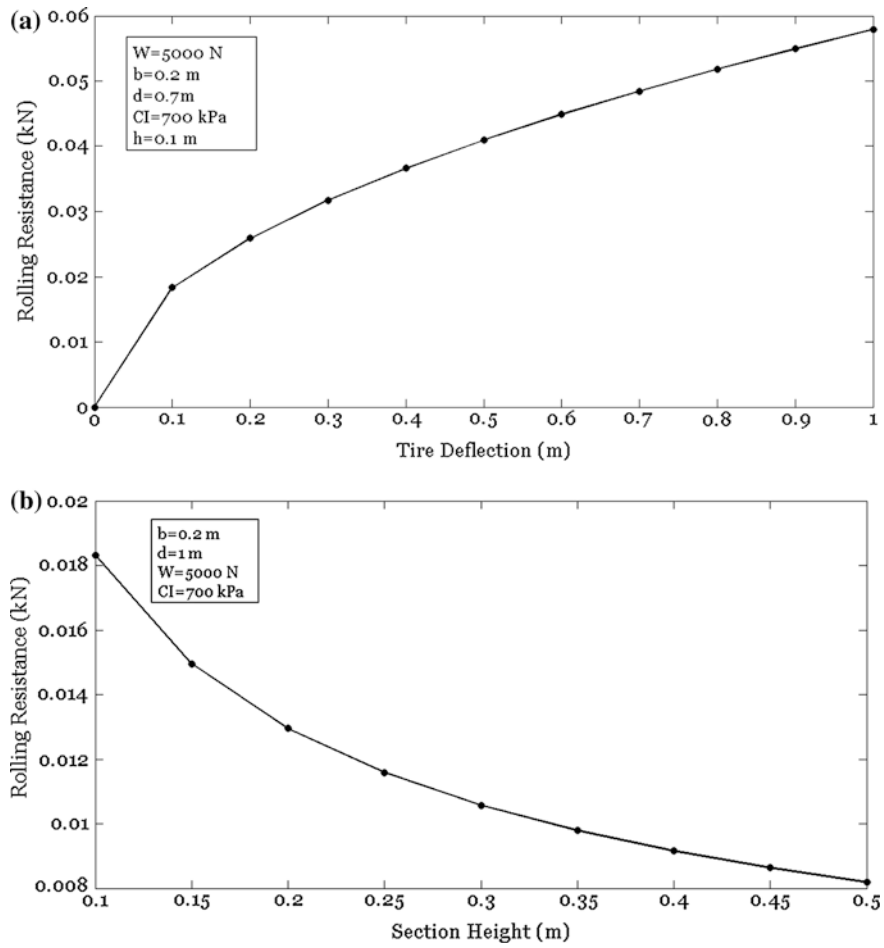


**Fig. 3.13** Rolling resistance variation with respect to **a** tire deflection and **b** tire section height

The validation of the mobility number approach carried out by Dwyer et al. [12] and Gee-Clough et al. [13] resulted in the development of a model for coefficient of rolling resistance based on some experimental works as following:

$$CRR = \frac{0.287}{M} + 0.049 \quad (3.38)$$

where  $M$  represents the mobility number proposed by Turnage [11]. McAllister [14] developed a mobility number based equation for the prediction of coefficient of rolling resistance including the effect of tire structure:

$$\begin{aligned} \text{cross-ply tires: } CRR &= \frac{0.323}{M} + 0.054 \\ \text{radial-ply tires: } CRR &= \frac{0.321}{M} + 0.037 \end{aligned} \quad (3.39)$$

Gee-Clough and Sommer [15] later developed models using four types of mobility number instead of using soil cone index to identify soil mechanical properties. Two forms of mobility numbers are for soil cohesion ( $c$ ) and soil internal friction angle ( $\varphi$ ).

$$\begin{aligned} M_1 &= \frac{cbd}{W} \left( \frac{\delta}{h} \right)^{\frac{1}{2}} \left( \frac{1}{1 + \frac{b}{2d}} \right) \\ M_2 = B_n &= \frac{C Ibd}{W} \left( \frac{\delta}{h} \right)^{\frac{1}{2}} \left( \frac{1 + \frac{5}{h}}{1 + \frac{3b}{d}} \right) \\ M_3 &= \frac{C Ibd}{W} \left( \frac{\delta}{h} \right)^{\frac{1}{2}} \left( \frac{1}{1 + \frac{b}{2d}} \right) \\ M_4 &= \frac{C Ibd}{W} \left( \frac{\delta}{h} \right)^{\frac{1}{2}} \left( \frac{1}{1 + \frac{b}{2d}} \right) \varphi^n \end{aligned} \quad (3.40)$$

### 3.1.3 Gross Thrust

Thrust is a soil-terrain interaction product that can be produced from the soil profile to act against the forces resisting the motion of the vehicle. Thrust is also known as gross traction and can be presented as following:

$$T = \mu W = \mu \frac{T_w}{rW} \quad (3.41)$$

where  $\mu$ ,  $T$ ,  $T_w$ ,  $r$  and  $W$ , are thrust coefficient, thrust (kN), wheel torque (Nm), wheel radius (m), and wheel load (kN), respectively. There are a range of semi-empirical methods to present thrust coefficient models based on the WES-approach which is based on wheel numeric parameter.

There are four common proposed models to semi-empirical determination of the thrust coefficient that were proposed for agricultural tractors on farmlands and for various military vehicle tires on grassland [16].

$$\begin{aligned}
 & \text{Wismer and Luth: } \mu = 0.75(1 - e^{-0.3cn.s}) \\
 & \text{Dwyer: } \mu = \left(0.796 - \frac{0.92}{N_{CI}}\right)(1 - e^{-(4.83 + 0.061N_{CI})s}) \\
 & \text{Brixius: } \mu = 0.88(1 - e^{-0.1B_n})(1 - e^{-7.5s}) + 0.04 \\
 & \text{McLaurin: } \mu = 0.8.17 - \frac{3.2}{N_{CI} + 1.91} + \frac{0.453}{N_{CI}}
 \end{aligned} \tag{3.42}$$

where  $c_n$  is wheel numeric based on Wismer-Luth model ( $c_n = \frac{Cl.b.d}{W}$ ),  $B_n$  is wheel numeric based on Brixius model ( $B_n = \frac{Clbd}{W} \left(\frac{\delta}{h}\right)^{\frac{1}{2}} \left(\frac{1 + \frac{5}{h}}{1 + \frac{3b}{d}}\right)$ ) and  $N_{CI}$  can be described based on McLaurin model as  $\frac{Clbd}{W} \left(\frac{\delta}{h}\right)^{\frac{1}{2}} \left(\frac{1}{1 + \frac{b}{2d}}\right)$ .

### 3.1.4 Dynamic Wheel Loads

Most of the empirical models and semi-empirical models that were early developed were established based on the assumption of static load on wheel while it is obvious that in real applications, tire is subjected to the dynamic loads applied to the wheel while traversing over rough terrain. If the traversing velocity is included in the model, there is a greater level of uncertainty in the dynamics of vehicle motion.

The dynamic load applied to the wheel may source from the normal inertia parameter that is created due to the vertical acceleration of motion. The dynamic load is a function of forward velocity, tire stiffness and contact patch parameters.

$$F_z = k_{1z}d_z^{k_{2z}} + c_{1z} \frac{1}{v^{c_{2z}}} \dot{d}_z \tag{3.43}$$

where  $F_z$  is the dynamic load on the wheel,  $d_z$  is the vertical displacement of the wheel,  $v$  is the forward speed,  $k_{1z}$  and  $k_{2z}$  are the tire system stiffness and  $c_{1z}$  and  $c_{2z}$  are the tire damping parameters. The longitudinally oriented forces can be in a similar dynamic mode and able to be presented as following:

$$F_x = k_{1x}d_x^{k_{2x}} + c_{1x} \frac{1}{v^{c_{2x}}} \dot{d}_x \tag{3.44}$$

where the parameters in this model are the same as the one presented for the dynamic load normal to the wheel but are oriented in longitudinal direction.

## 3.2 Vehicle Dynamics on Deformable Terrain

Vehicle dynamics on deformable terrain is closely related to the quality of soil-wheel interaction. Hence, the wheel-road specifications have to be clearly determined to develop the corresponding models for the performance of vehicle over deformable terrain. The complexity in Terramechanics lies in the surface deformation while for on-road surface, such a complexity is ignored owing to the zero-deformation of the surface.

There are four strategies based on tire-surface interaction:

1. Deformable terrain (soft soil)-flexible tire
2. Hard surface (over-compacted soil)-flexible tire
3. Deformable terrain (soft soil)-rigid wheel (over-inflated tire or metal discs)
4. Hard surface (over-compacted soil)-rigid wheel (over-inflated tire or metal discs)

Any case corresponding the hard surface investigation may be better addressed by vehicle dynamics over on-road surface that are the simple case of deformable terrains where the terrain sinkage is neglected. Hence, this book will more focus on the two strategies of flexible tire and rigid wheel interaction with soft terrain.

The interaction between a rigid wheel and soft soil has been a dynamic field of studying interest [2, 17, 18]. The tire can be sometimes better represented by a rigid wheel owing to their non-deformable structure (e.g. an over-inflated tire) particularly when the tire is travelling over soft terrain leading in a more significant deformation of the terrain compared with the deformation of the tire. Figure 3.14 shows the rigid wheel-deformable soil interaction variables.

$$j_0 = R[(\theta_0 - \theta) - (\sin \theta_0 - \sin \theta)] \quad (3.45)$$

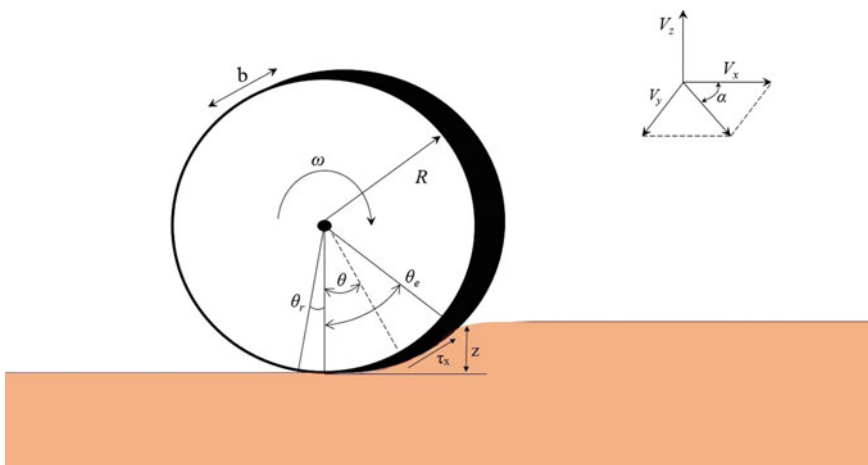


**Fig. 3.14** Rigid wheel-deformable soil interaction variables

The vertical support force acting on the wheel can be calculated from the normal stress as:

$$w_0 = Rb \left( \int_{-\theta_0}^{\theta_0} \sigma_n(\theta) \cos \delta \cos \theta + \tau_{\max}(1 - e^{-j_0/K_x}) \sin \delta \sin \theta d\theta \right) \quad (3.46)$$

where:

$$\delta = \tan^{-1} \left( \frac{\tau_{\max}(1 - e^{-j_0/K_x})}{\sigma_n(\theta)} \right) \quad (3.47)$$

Shear displacement and shear stress versus wheel angle is demonstrated in Fig. 3.15.

It is noteworthy that the shear stress measurements indicate the shear stress undergoes an increases from the starting location of contact between tire edge and terrain up to the point that soil profile shear failure occurs.

$$S_l = \frac{V_t - V_r}{V_t} = \frac{R\omega - V_r}{R\omega} = 1 - \frac{V_r}{R\omega} \quad (3.48)$$

where  $V_r$  is the longitudinal velocity of center of wheel,  $\omega$  is angular velocity of wheel, and  $S_l$  is longitudinal slip in driven state.

From Eq. 3.48, it is deducible that at two conditions, the wheel experiences infinity slip. One is when there is locked wheel at which  $\omega$  is zero. The other case addresses the condition in which  $V_r$  (i.e.  $V_x$ ) is zero that indicates there is no forward motion (i.e. the whole motion is converted to slip) (Fig. 3.16).

As an essential step, the soil profile deformation facilitates the wheel slip that can significantly reduce the vehicle performance. The shear displacement of the profile beneath the wheel is correlated by the shear stress. The relative motion between the wheel and the terrain surface it is traveling on produces the longitudinal slip ratio for a moving wheel that can be determined as:

The lateral slip of a tire is the sideways motion of the wheel which occurs when the sideway forces of a tire are greater than its friction resistance usually in cornering operation. The slip angle can be defined as:

$$\alpha = \arctan \left( \frac{V_y}{|V_x|} \right) \quad (3.49)$$

And thus the lateral slip velocity can be determined by:

$$V_y = V_x \tan(\alpha) \quad (3.50)$$

Wong [19] stated that the soil shear displacement for a wheel can be calculated for any arbitrary angle  $\theta$  on the wheel using the interface velocity of the wheel. One

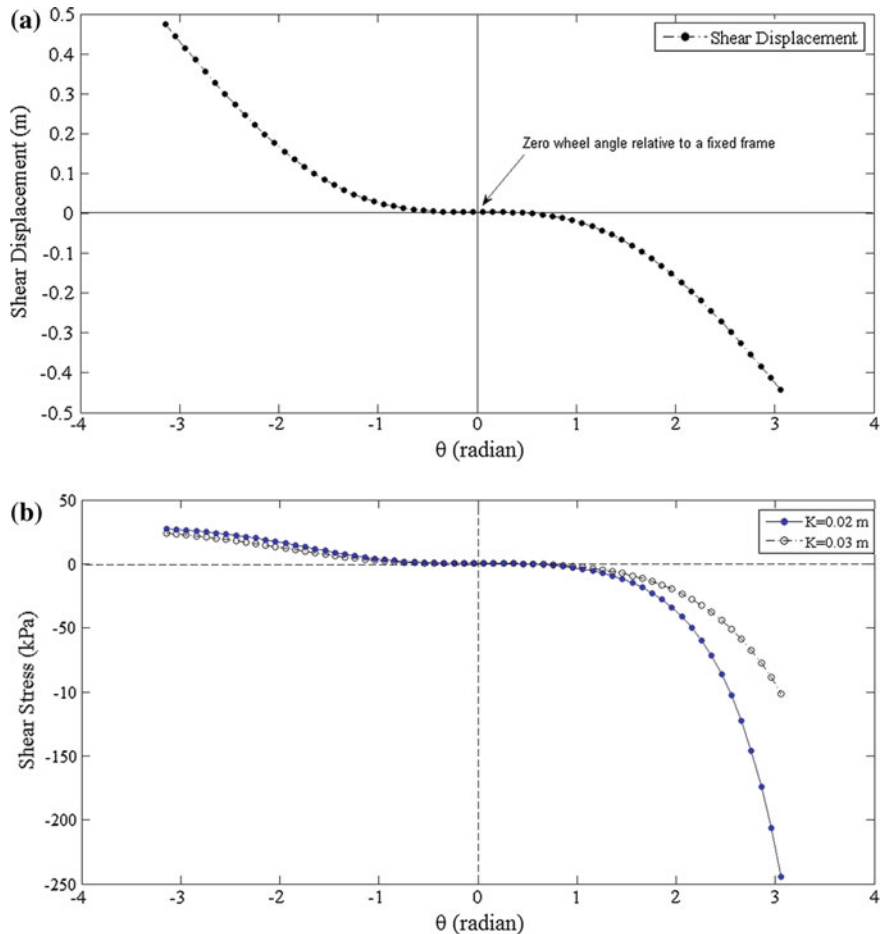


Fig. 3.15 Shear displacement and shear stress versus wheel angle

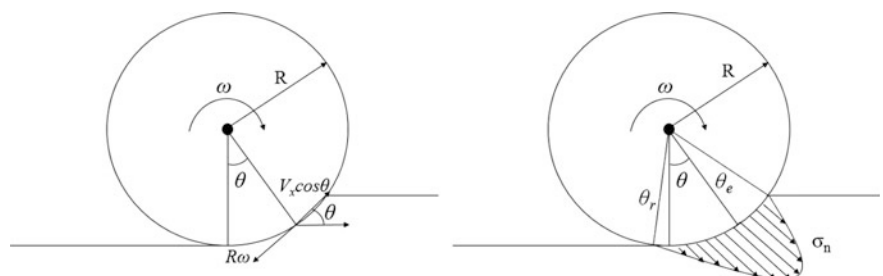


Fig. 3.16 Normal stress distribution from the start to the end of wheel angle

should note that the wheel velocity in the interface direction,  $V_{int}$  differentiates with that of velocity in traveling vector (i.e.  $V_x$ ) as following:

$$V_{int} = R\omega - V_x \cos \theta = R\omega[1 - (1 - s_l) \cos \theta] \quad (3.51)$$

The calculation of the shear stress under the wheel is based on an empirical expression first expressed by Janosi and Hanamoto [1] and widely used:

$$\tau_x(\theta) = \tau_{max} \left(1 - e^{-\frac{j}{k}}\right) \quad (3.52)$$

where  $\tau_{max}$  is the limiting shear stress and can be defined by the normal stress through the Mohr-Coulomb equation:

$$\tau_{max} = c + \sigma_n \tan \varphi \quad (3.53)$$

where  $c$  is soil cohesion and  $\varphi$  is the angle of shear resistance or angle of internal friction.

In this manner, the shear displacement  $j_x$  is calculated integrating the shear velocity of the terrain in contact with the wheel:

$$j_x(\theta) = \int_{\theta}^{\theta_e} R[1 - (1 - s_l) \cos \theta] d\theta = r(\theta_e - \theta - (1 - s_l)(\sin \theta_e - \sin \theta)) \quad (3.54)$$

The amount of soil shear displacement is positive for the contact patch and increases from zero at the entry angle until it reaches a peak value at the rear angle. From Eq. 3.54, it is also appreciated that the soil shear displacement increases with the slip. It should also be mentioned that the slip velocity can be maximum at the angle of entry, with a decrease to a minimum at the bottom center of the wheel and another increase to reach  $\theta_r$ .

If we intend to find the lateral shear displacement, a similar approach to that of lateral soil shear displacement can be adopted. The corresponding soil shear deformation in the lateral direction can be determined by integrating the shear rates using a quasi-static approach:

$$\begin{aligned} j_y &= \int_0^t V_y dt = \int_0^{\theta_e} V_x \tan \alpha dt \\ &= \tan \alpha \int_{\theta}^{\theta_e} \frac{V_x}{\omega} d\theta = R(1 - s_l)(\theta_e - \theta) \tan \alpha \end{aligned} \quad (3.55)$$

Combining the Janosi-Hanamoto equation and Eq. (3.55), we get the expression for the lateral shear stress across the contact patch

$$\tau_{ycp} = (c + \sigma_n \tan \varphi) \left( 1 - e^{-\frac{j_y}{K_y}} \right) \quad (3.56)$$

The forces acting on the wheel from the lateral shear forces at the bottom of the wheel can then be calculated by integrating the shear stresses across the entire contact area, as shown in Eq. (3.56). It is assumed that the width of the contact region remains constant throughout the entire process.

From Eq. 3.56 it can be inferred that the shear stress along the region of contact starts with increases linearly from the entry angle to the rear angle with the longitudinal soil shear displacement. The magnitude of the overall shear deformation is defined as:

$$j = \sqrt{j_x^2 + j_y^2} \quad (3.57)$$

The terrain deformation is based on pressure-sinkage theory that refers to the terrain bearing capacity. The bearing capacity theory adopted from the plasticity theory has laid the foundation for the development of vehicle mobility perspective. Normal load is exerted to the ground through the driving wheel that leads to sinkage. The stresses acting on the soil surface on the wheel in the radial direction are to be computed to find the kinetics and acting forces on the wheel. The first step for a semi-empirical method is to estimate the stress distribution along the contact patch. Normal and shear stresses develop at the interface between a rotating tire and the soil surface. As it is appreciated from Fig. 3.16, the normal stress distribution is zero at the start of the contact region, reaching a maximum somewhere between the entry and the exit angles based on Wong's theory. On this basis, the maximum point for the radial stress distribution under rigid wheels are not located under the wheel center but are more likely to occur to the forward side of the wheel and moves further forward of the wheel with increase in slip. The Bekker method assumes that the wheel is significantly more rigid than the soil such that the wheel does not deform, but rather sinks into the soil. The Bekker method determines the forces acting on the wheel through the integration of the normal and shear stress along the wheel-soil interface. Normal, tangential, and lateral stresses are distributed along the wheel interface. The normal stress can be derived from the pressure-sinkage equation proposed by Bekker [2].

$$p = \left( \frac{k_c}{b} + k_\varphi \right) z^n \quad (3.58)$$

where  $b$  is the smaller dimension of the loading area usually width of contact for rectangular contact area. For small sinkage; however, the length of contact may be assumed in the equation. The deformation parameters of  $k_c$  and  $k_\varphi$  are constant and are usually acquired by sinkage plate tests. It is noteworthy that the pressure-

sinkage parameter test results using rectangular plates of large aspect ratios and those of circular plates having radii equal to the widths of the rectangular plates are almost equal and this is a good reason to adopt circular plates because a lower load level is required to acquire the pressure-sinkage parameters with the same contact pressure.

However, there are two drawbacks to this equation that cannot provide a unified equation that accounts for different plate shapes and also the soil bulk density has not been considered. On this basis, a modified version of the Bekker sinkage-pressure equation, also known as Bekker-Reece equation was proposed:

$$\sigma_n = (ck'_c + b\gamma_s k'_\phi) \left(\frac{z}{b}\right)^n \quad (3.59)$$

The parameters  $k'_c$  and  $k'_\phi$  and exponent  $n$  are obtained through a bevameter or a penetrometer and are important indices for this equation as they are the representative of the relationship's trend. The exponent number typically falls within a range of 0.8–1.2 and close to 1. Soil cohesion value is obtained through uni-axial and tri-axial compression tests [20]. Another privilege of the Bekker-Reece equation is that in contrast to the parameters of Bekker's pressure-sinkage equation, the parameters of the Bekker-Reece equation non-dimensional (because of the  $z/b$  term in the equation) and are independent of the units of the exponent.

$$\sigma_{nf}(\theta) = (ck_1 + \gamma_s bk_2) \left(\frac{R(\cos \theta - \cos \theta_e)}{b}\right)^n \quad (3.60)$$

For the region between the maximum radial stress at  $\theta_N$ , and the rear contact region, the tire radial stress can be stated as:

$$\sigma_{nr}(\theta) = (ck_1 + \gamma_s bk_2) \left(\frac{R}{b}\right)^n \left( \cos \left( \theta_e - \left( \frac{\theta - \theta_r}{\theta_N - \theta_r} \right) (\theta_e - \theta_N) \right) \right)^n \quad (3.61)$$

In Terramechanics' terminology, the drawbar pull, vertical force, and the torque are important terms to be calculated. The radial and tangential stresses can then be integrated across the tire contact patch and be projected along longitudinal and vertical directions to the wheel. In this manner, these soil-wheel interaction products can be presented as following:

$$DP = Rb \left( \int_{-\theta_r}^{\theta_e} \tau_x(\theta) \cos \theta d\theta - \int_{-\theta_r}^{\theta_e} \sigma_n(\theta) \sin \theta d\theta \right) \quad (3.62)$$

In drawbar pull equation, the first term is the shear thrust and the second term addresses the compaction resistance.

$$W = Rb \left( \int_{-\theta_r}^{\theta_e} \sigma_n(\theta) \cos \theta d\theta + \int_{-\theta_r}^{\theta_e} \tau_x(\theta) \sin \theta d\theta \right) \quad (3.63)$$

$$T = R^2 b \int_{-\theta_r}^{\theta_e} \tau_x(\theta) d\theta$$

where  $b$  is the contact width, and  $\tau_x$  and  $\sigma$  are the shear and normal stress components.

These equations are applicable only for rigid wheel since the wheel radius has been kept constant through these equations, however, the stress field has been considered with nonuniform distribution. However, a linear distribution of the shear stress as a function of the normal stress is a common theory. It should also be noted that the integrals in these equations are computed numerically owing to the complexity of estimating the radial and tangential stresses.

The forces and torques exerted on the wheel can be determined by integrating the stress distributions. Assuming a cylindrical surface, the forces and torques can be formulated as:

$$F_x = rb \int_{\theta_r}^{\theta_f} (-\sigma(\theta) \sin \theta + \tau_t(\theta) \cos \theta) d\theta$$

$$F_y = -rb \int_{\theta_r}^{\theta_f} \tau_l(\theta) d\theta$$

$$F_z = rb \int_{\theta_r}^{\theta_f} (\sigma(\theta) \cos \theta + \tau_t(\theta) \sin \theta) d\theta \quad (3.64)$$

$$M_x = -r^2 b \int_{\theta_r}^{\theta_f} \tau_l(\theta) \cos \theta d\theta$$

$$M_y = -r^2 b \int_{\theta_r}^{\theta_f} \tau_t(\theta) d\theta$$

$$M_z = -r^2 b \int_{\theta_r}^{\theta_f} \tau_l(\theta) \sin \theta d\theta$$

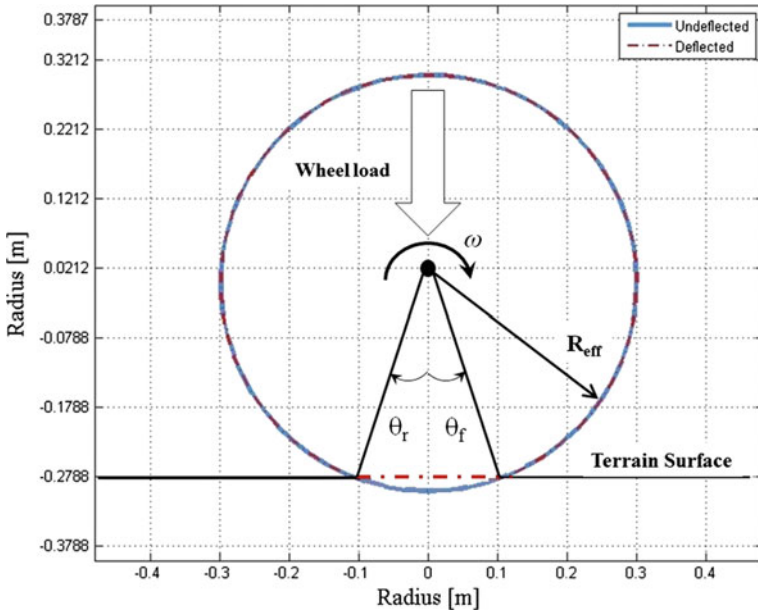


**Fig. 3.17** The radius of deflected and undeflected tire under wheel load given the wheel angles

The lateral forces acting on the wheel in off-road terrain can be decomposed into two sources. The first source of the lateral force is the shear stresses resulting from the average shear force across the contact patch in the lateral direction. The second source is the bulldozing effect acting on the side of the embedded wheel [21].

The flexible tire-terrain interaction may be better described by the tire deflection and soil sinkage approach developed by Chan [21]. The contact patch geometry is an important limiting factor to the tire deflection as affected by a definite level of normal load to the wheel. The radius of deflected and undeflected tire under wheel load given the wheel angles is shown in Fig. 3.17.

It is obvious that the contact patch length and contact width as well as tire deflection are dependent on various tire parameters such as the applied normal load, tire stiffness and tire structure. In this model it is necessary to assume these parameters at a constant level to yield a comprehensive mathematical model for the longitudinal, lateral and normal contact stress. In this case, the relationship between the soil沉降 and the tire deflection as a function of  $\theta$  can be developed for the range of  $\theta$  between the entry and exit angle:

$$z = 1 - \frac{1 - \frac{\delta}{R}}{\cos \theta} \quad (3.65)$$

Hence, we can obtain the derivative of  $z$  in terms of  $\theta$ :

$$\frac{dz}{d\theta} = -\frac{(1 - \frac{\delta}{R}) \sin \theta}{\cos^2 \theta} \quad (3.66)$$

By substituting the entry and front angle in the Eq. 3.66, the Eq. 3.67 can be obtained as following [21]:

$$\begin{aligned} z'(\theta_f) &= -\beta(\sqrt{1 + \varsigma^2} + \zeta)z(\theta_f) \\ \Rightarrow -\frac{\sin \theta(1 - \frac{\delta}{R})}{\cos^2 \theta} + \beta(\sqrt{1 + \varsigma^2} + \zeta)\left(1 - \frac{\delta}{\cos \theta}\right) &= 0 \end{aligned} \quad (3.67)$$

And if the exit angle is substituted, the following equation is obtained:

$$\begin{aligned} z'(\theta_b) &= \beta(\sqrt{1 + \varsigma^2} - \zeta)z(\theta_b) \\ \Rightarrow -\frac{\sin \theta_b(1 - \frac{\delta}{R})}{\cos^2 \theta_b} - \beta(\sqrt{1 + \varsigma^2} - \zeta)\left(1 - \frac{\delta}{\cos \theta_b}\right) &= 0 \end{aligned} \quad (3.68)$$

where,

$$\zeta = \frac{Rc\omega}{2\sqrt{kT}} \quad (3.69)$$

$$\beta = R\sqrt{\frac{k}{T}} \quad (3.70)$$

In the case that the speed is zero, the equations are symmetrically considered and the term  $\varsigma$  is zero. On this basis, the radius of the tire can be expressed as following for different  $\theta$  angle ranges:

$$R_{eff}(\theta) = \begin{cases} \left(\frac{1-\delta}{\cos \theta}\right) & \theta_b < \theta \leq \theta_f \\ \left(\frac{1-\delta}{\cos \theta_f}\right)e^{-\beta(\sqrt{1 + \varsigma^2} + \zeta)(\theta - \theta_f)} & \theta_f < \theta \leq \pi \\ \left(\frac{1-\delta}{\cos(2\pi + \theta_b)}\right)e^{\beta(\sqrt{1 + \varsigma^2} - \zeta)(\theta - (2\pi + \theta_b))} & \pi < \theta \leq 2\pi + \theta_b \end{cases} \quad (3.71)$$

The contact patch length can also be determined according to Eq. 3.72:

$$l_p = (R - \delta) \tan(|\theta_b|) + (R - \delta) \tan(\theta_f) \quad (3.72)$$

It is noteworthy that the proposed contact length equation is a simplified but general one to describe the contact parameters and tire radius-deflection under static loading. However, there may be change based on dynamic loading and rolling or tire in traveling condition that can create a variable radial deflection. It is almost known that the traveling speed, as well as tire slip, affect the contact patch length.

The unloaded soil height,  $u_{ot}$  and the sinkage  $z_{ot}$  for the flexible tire in a similar trend to that of rigid wheel can be developed:

$$\begin{aligned} z_{ot} &= R_{eff}(\theta)(\cos \theta_f - \cos \theta_e) \\ u_{ot} &= R_{eff}(\theta)(\cos \theta_b - \cos \theta_r) \end{aligned} \quad (3.73)$$

The equations developed yet should be included for the longitudinal and lateral forces but a priori is to first determine the static loading to the wheel. Based on the deformed geometry of the flexible tire, the modeling of vertical loading can be proposed as following:

$$w_0 = b \left( \int_{-\theta_0}^{\theta_0} R_{eff}(\theta) \sigma_n(\theta) \cos \delta \cos \theta + R_{eff}(\theta) \tau(\theta) \sin \delta \sin \theta d\theta \right) \quad (3.74)$$

### **3.2.1 Longitudinal Slip and Shear Displacement of Flexible Tire**

In order to characterize the longitudinal forces, the shear displacement and longitudinal slip have to be identified properly. A prerequisite for the progress of model on account of shear deformation is the contact patch shape determination. The shear deformation of soil can be obtained for any angular position  $\theta$  by integrating the shear velocities and for the entire region of the tire that is in contact with the ground, the shear displacement can be calculated by integrating the interface velocity across the entire contact area.

$$j_x(\theta) = \int_{\theta}^{\theta_e} R_{eff}(\theta) [1 - (1 - s_l) \cos \theta] d\theta \quad (3.75)$$

### **3.2.2 Stresses and Forces of Flexible Tire**

Through the hypothesis that the tire width during the sinkage process is kept at a certain level, the tractive parameters such as drawbar pull and also wheel load are possible to be estimated. It is essential to ascertain the location at which the greatest radial force is applied to the tire that can be obtained through the point at which the rear and front slip lines meet. The perquisite in this order is to determine the stresses as proposed by Chan [21].

$$\sigma_n(\theta) = \begin{cases} (ck_1 + \gamma_s b k_2) \left( \frac{R(\theta_e)}{b} \right)^n (\cos \theta - \cos \theta_e)^n & \theta_N \leq \theta \leq \theta_e \\ (ck_1 + \gamma_s b k_2) \left( \frac{R(\theta_e)}{b} \right)^n \left( \cos \left( \theta_e - \left( \frac{\theta - \theta_e}{\theta_N - \theta_e} \right) (\theta_e - \theta_N) \right) - \cos \theta_e \right)^n & -\theta_r \leq \theta \leq \theta_N \end{cases} \quad (3.76)$$

Rigid wheels and flexible tires are liable to have differently distributed radial (normal) stresses along the tire contact patch area. Furthermore, the tire structure and the limitations on the amount of tire deflection can drastically affect the range of normal stress applied to the soil profile from the wheel. A simplified method in order to obtain the amount of the greatest radial stress is to put the objective tire on a rigid surface and quantification of the contact stresses. The contact stress in this manner can be a proper equivalent to the contact pressure. It is noteworthy that the tire carcass stiffness and tire inflation pressure can be influential on the total contact pressure and there is a linear relationship between the contact pressure and tire inflation pressure. The limit pressure has to be equivalent to the stiffness of the deformed section of the tire can be presented as following:

$$q_{\text{limit}} = kb = \frac{b\beta}{2R^2} (\alpha p_i + c) \quad (3.77)$$

where  $c$  is the stiffness of point loading,  $p_i$  is the tire inflation pressure and  $\alpha$  is the rate of change in the stiffness of point loading versus tire inflation pressure.

By the increase of wheel load, tire will undergo an increment in the normal stress and there is a level in which the tread deforms and the normal stress of tire is dependent on yielding the tire stiffness characteristics. The level at which the maximum stress occurs at the tire-ground interface is quantified considering that the maximum deflection always happens at the point of maximum tire normal stress and therefore, the normal (radial) stresses acting on the tire can be presented as following:

$$\sigma_n(\theta) = \min(\sigma_n(\theta), q_{\text{limit}}) \quad (3.78)$$

The longitudinal tire stresses can then be presented by considering the deformed radius of the wheel as following:

$$\tau_x(\theta) = (c + \sigma_n(\theta) \tan \varphi) \left( 1 - e^{-\left( \int_0^{\theta_e} R(\theta) [1 - (1 - s_d) \cos \theta] d\theta \right) / \kappa_x} \right) \quad (3.79)$$

By integrating the stresses across the contact patch through the tire-terrain interface, the vertical wheel load is able to be computed. If the contact width is kept constant between the tire and ground, the vertical wheel load acting on the wheel

from the entry wheel angle to the exit one with an iterative process is possible to be represented as following:

$$W = b \left( \int_{-\theta_r}^{\theta_e} R(\theta) \sigma_n(\theta) \cos \theta d\theta + \int_{-\theta_r}^{\theta_e} R(\theta) \tau_x(\theta) \sin \theta d\theta \right) \quad (3.80)$$

After that the wheel load parameter is successfully determined, it is now possible to achieve longitudinally oriented forces. When the vertical and longitudinal stresses across the contact area are integrated, the longitudinally oriented force is achieved by the quasi-static equilibrium condition. The longitudinally oriented forces achieved by this approach may represent the drawbar pull parameter similar to the rigid wheel based drawbar pull determination.

$$F_x = DP = b \left( \int_{-\theta_r}^{\theta_e} R(\theta) (\tau_x(\theta) \cos \theta - \sigma_n(\theta) \sin \theta) d\theta \right) \quad (3.81)$$

### 3.2.3 Lateral Forces of Flexible Tire

The shear forces obtained at the tire-terrain interaction models depend on the variation in tire stiffness with slip angle while in the on-road traversing mode, the stiffness of the tire was predicted such that it decreases with non-zero slip angle and therefore the effective tire deflection decreases with an increment in slip angle [21].

The lateral shear displacement lays the foundation for the establishment of lateral forces applied to the wheel and can be obtained by integrating the lateral velocity from the wheel angle as following:

$$j_y = \int_0^t V_y dt = \int_{\theta}^{\theta_e} V_x \tan \alpha dt = \tan \alpha \int_{\theta}^{\theta_e} \frac{V_x}{\omega} d\theta = R_{eff}(\theta)(1 - s_l)(\theta_e - \theta) \tan \alpha \quad (3.82)$$

After that the lateral shear displacement is determined, it is possible to define the shear stress applied to the wheel as following:

$$\tau_{ycp} = (c + \sigma_n \tan \varphi) \left( 1 - e^{-\frac{j_y}{K}} \right) \quad (3.83)$$

It is now possible to apply the shear stress being integrated across the contact patch while the contact width is kept constant. It is possible to define the lateral force as following:

$$F_{ycp} = b \int_{-\theta_r}^{\theta_e} R_{eff}(\theta) (c + \sigma_n \tan \varphi) \left( 1 - e^{-\frac{jy}{K}} \right) d\theta \quad (3.84)$$

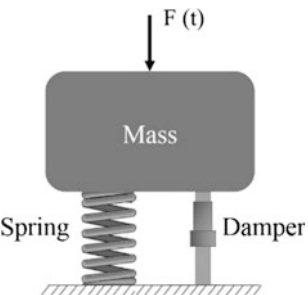
### 3.3 Ride Comfort

The ride comfort addresses the vibrational response of a vehicle to the operational condition and is closely related to different parameters such as the natural frequency of the vehicle system, road profile and system characteristics. A very basic vibration model of a mechanical system can be represented by mass-spring-damper elements (Fig. 3.18) while depending on the problem type, the mass can be subject to force (forced vibration) or not (free vibration).

The strategy to select among the different numbers of DOF relies on the system characteristics and the problem condition. A body in the coordinate frame can be represented by 6 DOF for each of lateral, longitudinal and vertical directions as well as three rotational orientations around the axes (i.e. yaw, pitch and roll). Because of vehicle system constraints, the vibrations in longitudinal, lateral and yaw are ignored. Given that the vehicle chassis is mounted on four wheels, the typical off-road vehicle can be represented by seven DOF system (Fig. 3.19).

One should distinguish among the four potential models of a Quarter Car Model, Half Car Model, Bicycle Car Model and Full Car Model that are typically used to describe the different modes of vibrating. A vehicle with its suspension system is presented in Fig. 3.19.

**Fig. 3.18** A basic vibration model of a mechanical system by mass-spring-damper elements



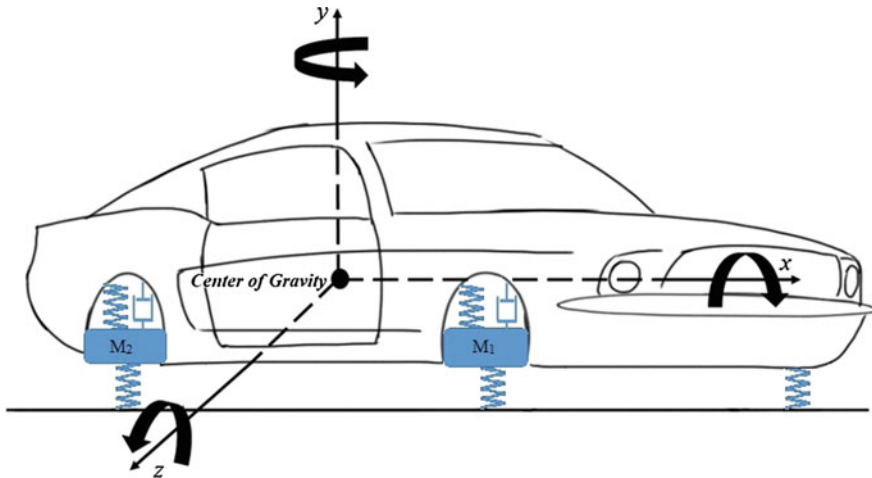


**Fig. 3.19** Vehicle with its suspension system

### 3.3.1 Quarter Car Model

The most typical and functional model to describe the vehicle suspension system is a quarter-car model, shown in Fig. 3.20. A two DOF base excited system free body diagram is plotted based on the assumption that ( $y_2 > y_1$ ). Two-degrees-of-freedom quarter-car (2 DOF Q-Car) models, subjected to road excitation, are extensively adopted in a wide range of automotive industry, being served as a functional catalyst to analyze disciplines including the prediction of dynamic response, identification, optimization and control of ground vehicles. This is attributed to the fact that 2 DOF Q-Car model provides simplicity and correct qualitative and quantitative analysis feasibility of such a model regarding vehicle dynamics, kinematics, ride and handling. Discomfort index in this model is the vertical motion while tire is represented by a stiffness, wheel and connected elements are demonstrated by a mass, and suspension is depicted by a spring and a damper working parallel being in accordance with Kelvin-Voigt model.

In order to derive the equations of motion, the Newton's second of motion gives the following equations for each of the sprung and unsprung masses as following:

$$\begin{aligned} -k_2(y_2 - y_1) - c_2(\dot{y}_2 - \dot{y}_1) &= m_2\ddot{y}_2 \\ -k_1(y_1 - y_b) + k_2(y_2 - y_1) + c_2(\dot{y}_2 - \dot{y}_1) &= m_1\ddot{y}_1 \end{aligned} \quad (3.85)$$

$$\begin{aligned} -\omega_{n_2}^2(y_2 - y_1) - 2\zeta_2\omega_{n_2}(\dot{y}_2 - \dot{y}_1) &= \ddot{y}_2 \\ -\omega_{n_1}^2(y_1 - y_b) + \epsilon\omega_{n_2}^2(y_2 - y_1) - 2\epsilon\zeta_2\omega_{n_2}(\dot{y}_2 - \dot{y}_1) &= \ddot{y}_1 \end{aligned} \quad (3.86)$$

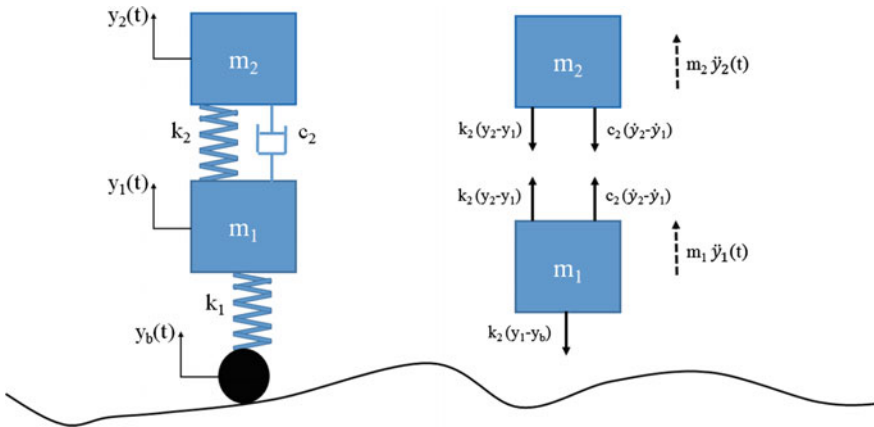


**Fig. 3.20** A quarter-car model with its free body diagram

where the natural frequencies, damping ratio and mass ratio is presented as following:

$$\omega_{n1} = \sqrt{\frac{k_1}{m_1}} \quad \omega_{n2} = \sqrt{\frac{k_2}{m_2}} \quad \zeta_2 = \frac{c_2}{2\sqrt{k_2 m_2}} \quad \varepsilon = \frac{m_2}{m_1} \quad (3.87)$$

Also, the equations of motion can be easily replaced in the classical matrix form:

$$M\underline{\ddot{y}} + C\underline{\dot{y}} + K\underline{y} = \underline{f}(t) \quad (3.88)$$

where  $\underline{y}(t) = (y_1, y_2)$  represents the response vector, and the mass, damping and stiffness matrices are as following:

$$\begin{bmatrix} m_1 & 0 \\ 0 & m_2 \end{bmatrix} \begin{pmatrix} \ddot{y}_1 \\ \ddot{y}_2 \end{pmatrix} + \begin{bmatrix} c_2 & -c_2 \\ -c_2 & -c_2 \end{bmatrix} \begin{pmatrix} \dot{y}_1 \\ \dot{y}_2 \end{pmatrix} + \begin{bmatrix} k_1 + k_2 & -k_2 \\ -k_2 & k_2 \end{bmatrix} \begin{pmatrix} y_1 \\ y_2 \end{pmatrix} = \begin{bmatrix} k_1 \\ 0 \end{bmatrix} y_b \quad (3.89)$$

In this manner, the M, C and K matrices are  $\begin{bmatrix} m_1 & 0 \\ 0 & m_2 \end{bmatrix}$ ,  $\begin{bmatrix} c_2 & -c_2 \\ -c_2 & -c_2 \end{bmatrix}$  and  $\begin{bmatrix} k_1 + k_2 & -k_2 \\ -k_2 & k_2 \end{bmatrix}$ , respectively.

C matrix, serving as the damping values, functions as an important element for attenuation of the disturbances caused when the tire follows a road irregularity, then it also plays a significant role in the dissipation of the kinetic energy caused by mass vertical motion.

The natural frequencies of the system are presented (two natural frequencies based on two degrees of freedom system):

$$\begin{aligned}\omega_1^2 &= \frac{1}{2} \left[ \frac{(k_1 + k_2)m_2 + k_2m_1}{m_2m_1} \right] - \frac{1}{2} \left\{ \left[ \frac{(k_1 + k_2)m_2 + k_2m_1}{m_2m_1} \right]^2 - 4 \left[ \frac{k_1k_2}{m_2m_1} \right] \right\}^{\frac{1}{2}} \\ \omega_2^2 &= \frac{1}{2} \left[ \frac{(k_1 + k_2)m_2 + k_2m_1}{m_2m_1} \right] + \frac{1}{2} \left\{ \left[ \frac{(k_1 + k_2)m_2 + k_2m_1}{m_2m_1} \right]^2 - 4 \left[ \frac{k_1k_2}{m_2m_1} \right] \right\}^{\frac{1}{2}}\end{aligned}\quad (3.90)$$

And the mode shapes of the dual mass based energy regenerative system are:

$$\begin{aligned}u_1 &= \frac{-m_2\omega_1^2 + (k_1 + k_2)}{k_2} = \frac{k_2}{-m_1\omega_1^2 + (k_1 + k_2)} \\ u_2 &= \frac{-m_2\omega_2^2 + (k_1 + k_2)}{k_2} = \frac{k_2}{-m_1\omega_2^2 + (k_1 + k_2)}\end{aligned}\quad (3.91)$$

Mode shape determines the shapes of the system at different natural frequency. This mode shape can be determined by Eigen value of vibration equation like single or two-degree of freedom system. In another term, it is better to say that at a certain frequency known as the natural frequencies of the aforesaid system, the resonance occurs and the mode shapes describe the configurations or the pattern in which a structure will naturally displace when excited at the natural frequency.

From the kinematics of motion, the kinetics such as forces between the sprung and unsprung mass can be achieved. By solving the ordinary differential equations of the motion and providing the road input ( $y_b$ ) as the harmonic road profile, the sprung and unsprung mass displacement and sprung mass acceleration is presented in Fig. 3.21.

### 3.3.2 Bicycle Car Model

Bike model deals with body pitch and bounce degrees of freedom. The front and rear suspension are modeled as spring/damper systems. A more detailed model would include a tire model, and damper nonlinearities such as velocity-dependent damping (with greater damping during rebound than compression). The vehicle body has pitch and bounce degrees of freedom. They are represented in the model by four states: vertical displacement, vertical velocity, pitch angular displacement, and pitch angular velocity. The forces and moments result in body motion according to Newton's Second Law. Figure 3.22 shows the vehicle bicycle model suspension system.

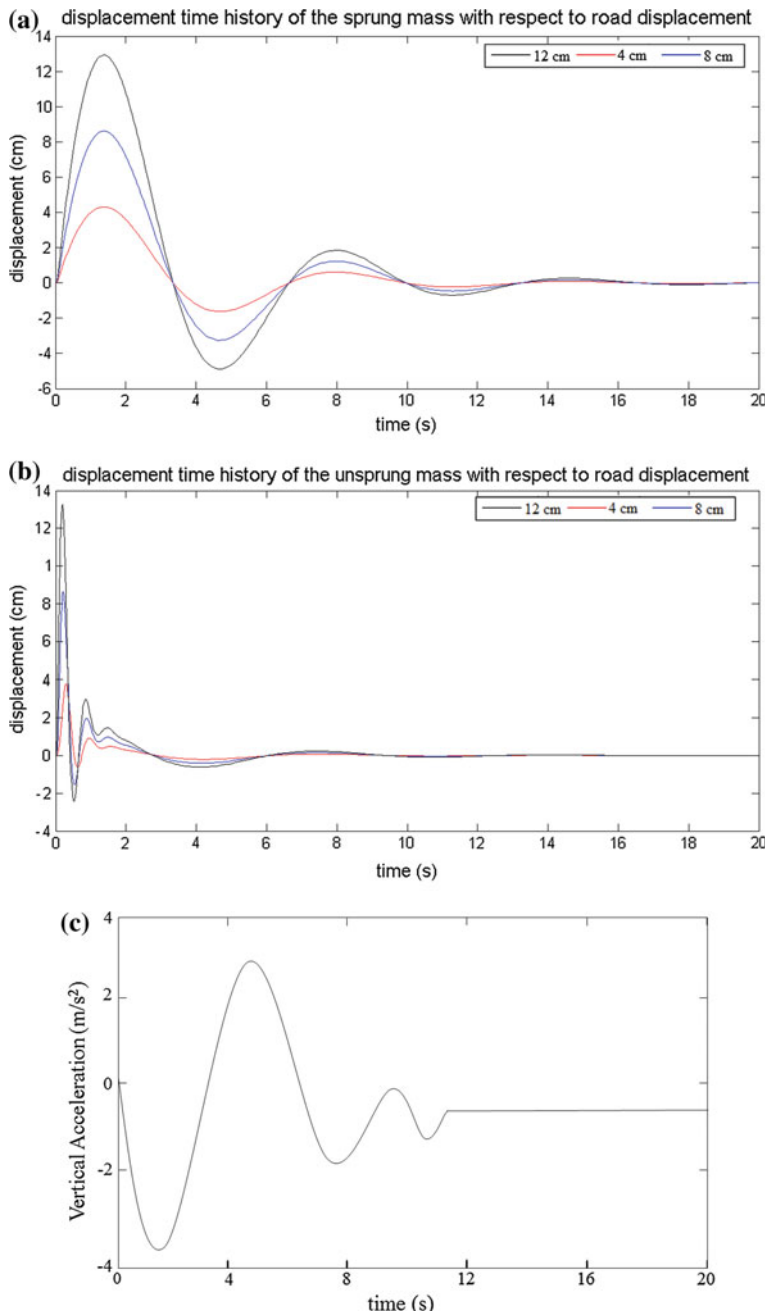


**Fig. 3.21** **a** Sprung mass displacement, **b** unsprung mass displacement and **c** sprung mass acceleration

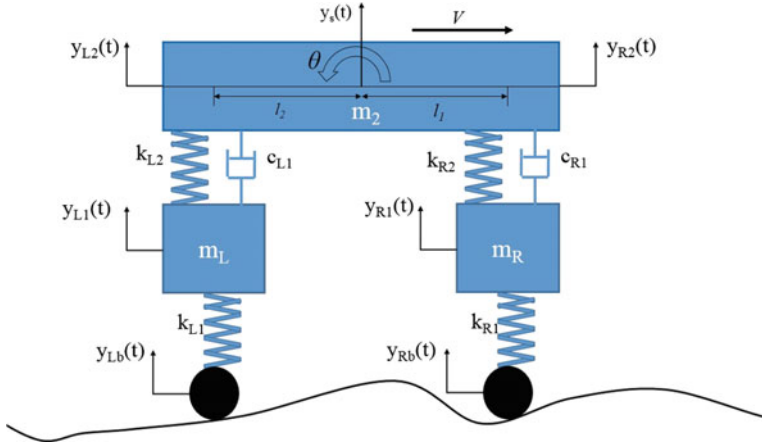


**Fig. 3.22** Vehicle bicycle model suspension system

Based on the Newton's second law of motion, one can develop the governing equations of motion for a system with four degree of freedom. Therefore, there will be four equations in the system as following:

$$m_2 \ddot{y}_s + c_{R1}(\dot{y}_{R2} - \dot{y}_{R1}) + c_{L1}(\dot{y}_{L2} - \dot{y}_{L1}) + k_{R2}(y_{R2} - y_{R1}) + k_{L2}(y_{L2} - y_{L1}) = 0 \quad (3.92)$$

$$I \ddot{\theta} + l_1(c_{R1}(\dot{y}_{R2} - \dot{y}_{R1}) + k_{R2}(y_{R2} - y_{R1})) - l_2(c_{L1}(\dot{y}_{L2} - \dot{y}_{L1}) + k_{L2}(y_{L2} - y_{L1})) = 0 \quad (3.93)$$

$$m_R \ddot{y}_{R1} - c_{R1}(\dot{y}_{R2} - \dot{y}_{R1}) - k_{R2}(y_{R2} - y_{R1}) + k_{R1}(y_{R1} - y_{Rb}) = 0 \quad (3.94)$$

$$m_L \ddot{y}_{L1} - c_{L1}(\dot{y}_{L2} - \dot{y}_{L1}) - k_{L2}(y_{L2} - y_{L1}) + k_{L1}(y_{L1} - y_{Lb}) = 0 \quad (3.95)$$

After solving the equations of motion with a ordinary differential equation solver, and providing an input for the vehicle road profile such as step function (Fig. 3.23), it is possible to observe the trend of pitch differential, the velocity of bounce of sprung mass and the force between the sprung mass and front unsprung mass as well as the momentum due to acceleration or deceleration (Fig. 3.24).

### 3.3.3 Half Car Model

Half car model is similar to the bicycle model of car with the difference that the pitching is not of interest and car roll is important instead. The half car model for suspension system is presented with rolling about y-axis (Fig. 3.25).

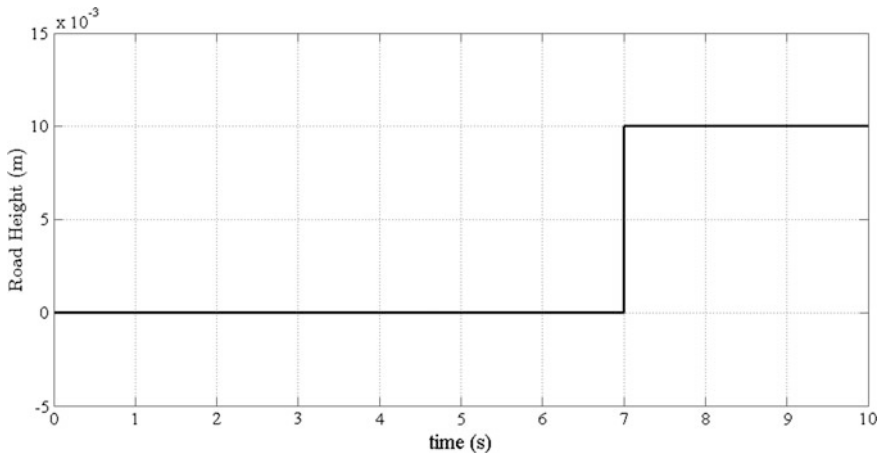


**Fig. 3.23** Road input as a step function

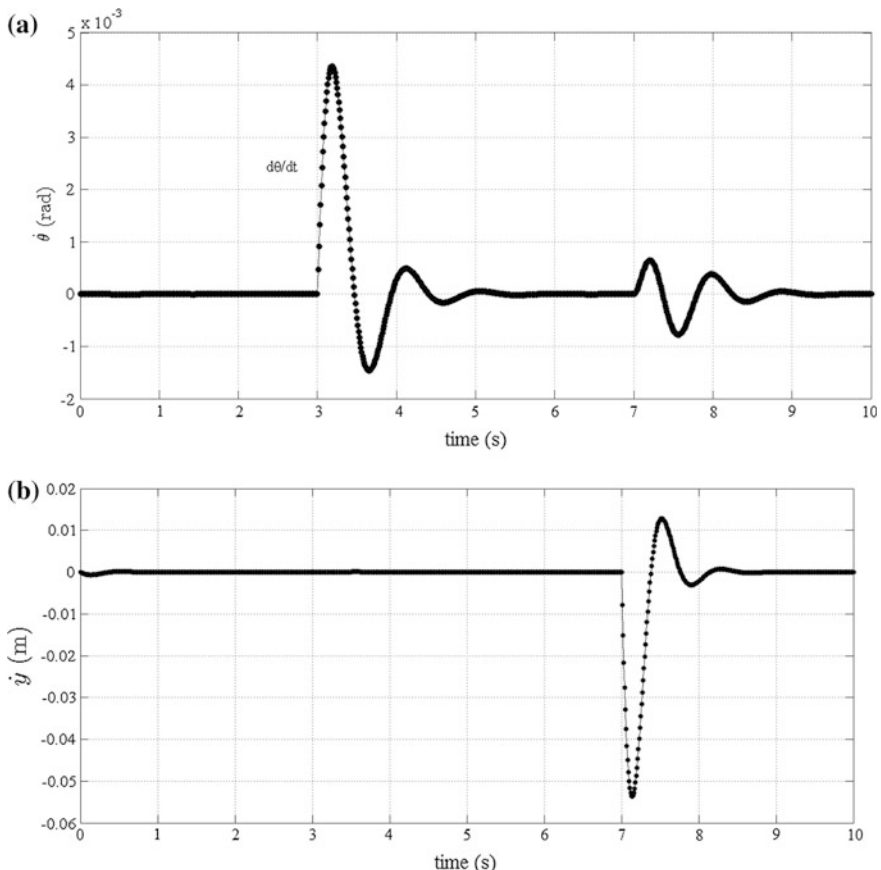


**Fig. 3.24** The half vehicle **a** pitching differential, **b** bounce velocity, **c** force between sprung mass and front unsprung mass and **d** momentum due to acceleration/deceleration

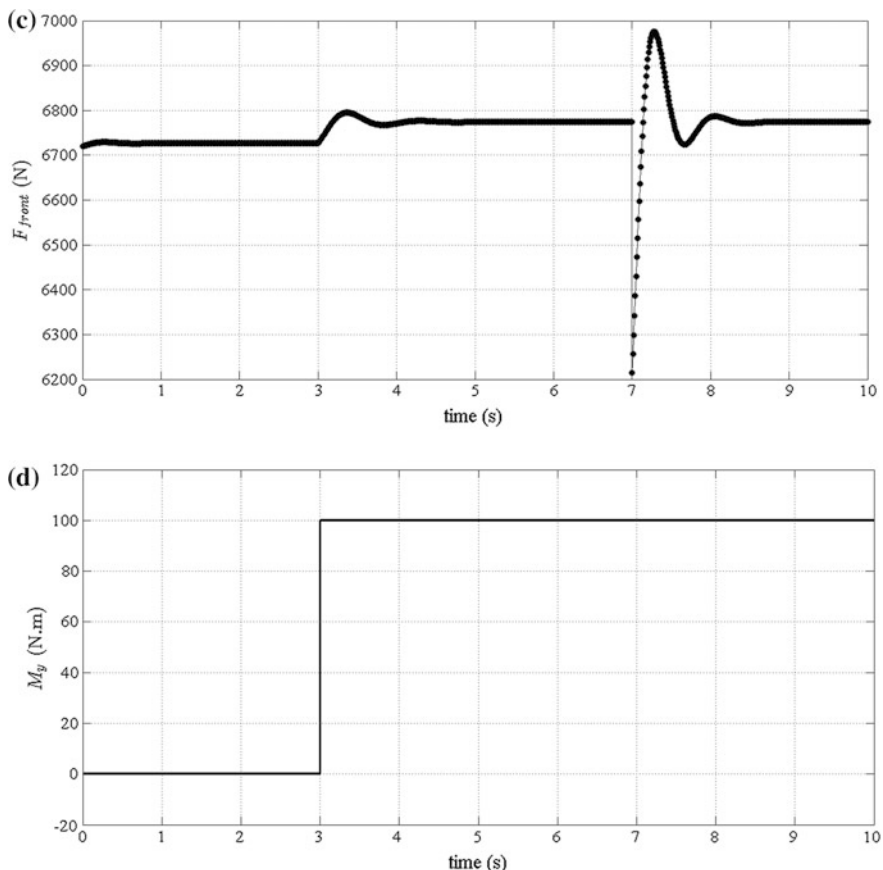


**Fig. 3.24** (continued)

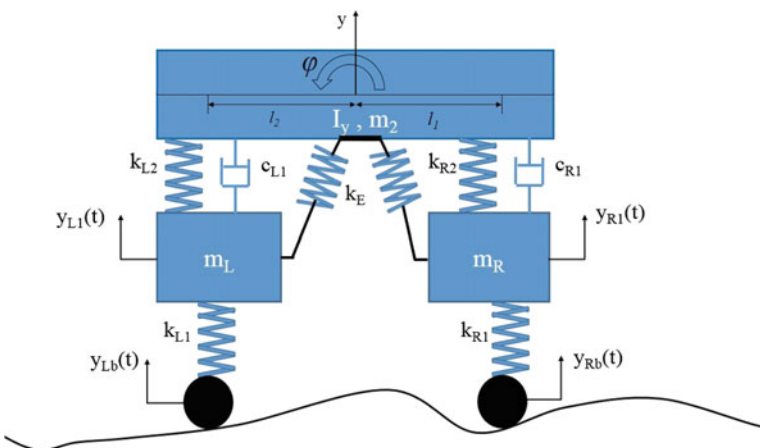


**Fig. 3.25** A half car model for suspension system

Based on the second law of motion, the following equations are developed. There are four equations since the system is a four-degree-of-freedom system three of which are for bounce of the masses and one for the roll of sprung mass.

$$\begin{aligned} m_2\ddot{y} + c_{R1}(\dot{y} - \dot{y}_{R1} + l_1\dot{\phi}) + c_{L1}(\dot{y} - \dot{y}_{L1} - l_2\dot{\phi}) \\ + k_{R2}(y - y_{R1} + l_1\phi) + k_{L2}(y - y_{L1} + l_2\phi) = 0 \end{aligned} \quad (3.96)$$

$$\begin{aligned} I_y\ddot{\phi} + l_1c_{R1}(\dot{y} - \dot{y}_{R1} + l_1\dot{\phi}) - l_2c_{L1}(\dot{y} - \dot{y}_{L1} - l_2\dot{\phi}) \\ + l_1k_{R2}(y - y_{R1} + l_1\phi) - l_2k_{L2}(y - y_{L1} + l_2\phi) + k_E\phi = 0 \end{aligned} \quad (3.97)$$

$$m_R\ddot{y}_{R1} - c_{R1}(\dot{y} - \dot{y}_{R1} + l_1\dot{\phi}) - k_{R2}(y - y_{R1} + l_1\phi) + k_{R1}(y_{R1} - y_{Rb}) = 0 \quad (3.98)$$

$$m_L\ddot{y}_{L1} - c_{L1}(\dot{y} - \dot{y}_{L1} - l_2\dot{\phi}) - k_{L2}(y - y_{L1} - l_2\phi) + k_{L1}(y_{L1} - y_{Lb}) = 0 \quad (3.99)$$

### 3.3.4 Full Car Model

The general vibrating model of a vehicle is called the full car model as shown in Fig. 3.26. The full car model includes the body bounce  $z$ , body roll  $\phi$ , body pitch  $\theta$ , wheels' bounce  $y_1, y_2, y_3$ , and  $y_4$  and independent road excitations  $y_{11}, y_{22}, y_{33}$ , and  $y_{44}$ . In this regard, a full car vibrating model has seven DOF and therefore seven equations of motion.

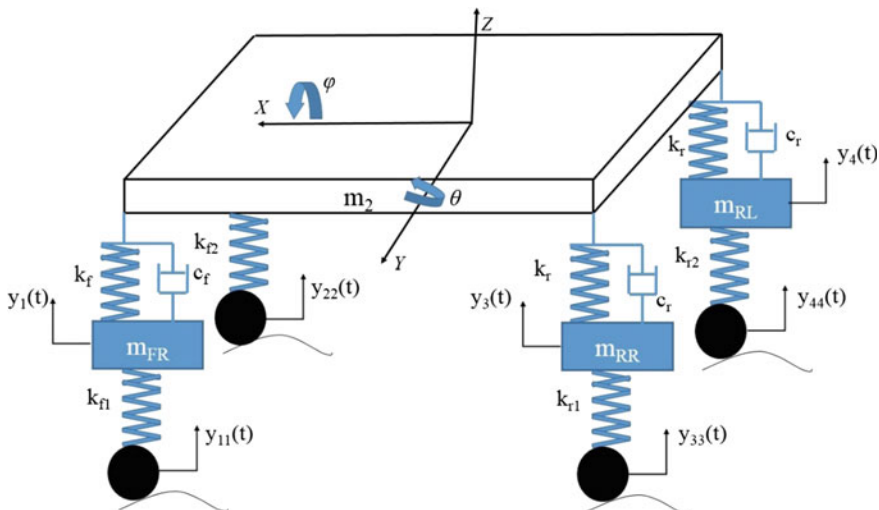


**Fig. 3.26** A full car model with suspension systems

$$\begin{aligned}
& m_2 \ddot{y} + k_f(y - y_1 + l_1 \varphi - s_1 \theta) + k_f(y - y_2 - l_2 \varphi - s_1 \theta) \\
& + k_r(y - y_3 - l_1 \varphi + s_2 \theta) + k_r(y - y_4 + l_2 \varphi + s_2 \theta) \\
& + c_f(\dot{y} - \dot{y}_1 + l_1 \dot{\varphi} - s_1 \dot{\theta}) + c_f(\dot{y} - \dot{y}_2 - l_2 \dot{\varphi} - s_1 \dot{\theta}) \\
& + c_r(\dot{y} - \dot{y}_3 - l_1 \dot{\varphi} + s_2 \dot{\theta}) + c_r(\dot{y} - \dot{y}_4 + l_2 \dot{\varphi} + s_2 \dot{\theta}) = 0
\end{aligned} \tag{3.100}$$

$$\begin{aligned}
& I_x \ddot{\varphi} + k_f l_1(y - y_1 + l_1 \varphi - s_1 \theta) - k_f l_2(y - y_2 - l_2 \varphi - s_1 \theta) \\
& - k_r l_1(y - y_3 - l_1 \varphi + s_2 \theta) + k_r l_2(y - y_4 + l_2 \varphi + s_2 \theta) \\
& + c_f l_1(\dot{y} - \dot{y}_1 + l_1 \dot{\varphi} - s_1 \dot{\theta}) - c_f l_2(\dot{y} - \dot{y}_2 - l_2 \dot{\varphi} - s_1 \dot{\theta}) \\
& - c_r l_1(\dot{y} - \dot{y}_3 - l_1 \dot{\varphi} + s_2 \dot{\theta}) + c_r l_2(\dot{y} - \dot{y}_4 + l_2 \dot{\varphi} + s_2 \dot{\theta}) = 0
\end{aligned} \tag{3.101}$$

$$\begin{aligned}
& I_y \ddot{\theta} - k_f s_1(y - y_1 + l_1 \varphi - s_1 \theta) - k_f s_1(y - y_2 - l_2 \varphi - s_1 \theta) \\
& + k_r s_2(y - y_3 - l_1 \varphi + s_2 \theta) + k_r s_2(y - y_4 + l_2 \varphi + s_2 \theta) \\
& - c_f s_1(\dot{y} - \dot{y}_1 + l_1 \dot{\varphi} - s_1 \dot{\theta}) - c_f s_1(\dot{y} - \dot{y}_2 - l_2 \dot{\varphi} - s_1 \dot{\theta}) \\
& + c_r s_2(\dot{y} - \dot{y}_3 - l_1 \dot{\varphi} + s_2 \dot{\theta}) + c_r s_2(\dot{y} - \dot{y}_4 + l_2 \dot{\varphi} + s_2 \dot{\theta}) = 0
\end{aligned} \tag{3.102}$$

$$m_{FR} \ddot{y}_1 - k_f(y - y_1 + l_1 \varphi - s_1 \theta) - c_f(\dot{y} - \dot{y}_1 + l_1 \dot{\varphi} - s_1 \dot{\theta}) + k_{f1}(y_1 - y_{11}) = 0 \tag{3.103}$$

$$m_{FL} \ddot{y}_2 - k_f(y - y_2 - l_2 \varphi - s_1 \theta) - c_f(\dot{y} - \dot{y}_2 - l_2 \dot{\varphi} - s_1 \dot{\theta}) + k_{f2}(y_2 - y_{22}) = 0 \tag{3.104}$$

$$m_{RR} \ddot{y}_3 - k_r(y - y_3 - l_1 \varphi + s_2 \theta) - c_r(\dot{y} - \dot{y}_3 - l_1 \dot{\varphi} + s_2 \dot{\theta}) + k_{r1}(y_3 - y_{33}) = 0 \tag{3.105}$$

$$m_{RL} \ddot{y}_4 - k_r(y - y_4 + l_2 \varphi + s_2 \theta) - c_r(\dot{y} - \dot{y}_4 + l_2 \dot{\varphi} + s_2 \dot{\theta}) + k_{r2}(y_4 - y_{44}) = 0 \tag{3.106}$$

After solving the equations of motion with an ordinary differential equation solver such as MATLAB, it is possible to observe the trends of tire deformation for the right front wheel, its jounce, damping force and damping factor damping force and damping factor (Fig. 3.27).

It is assumed that the car has independent suspension in front and rear. Therefore, each wheel has only a vertical displacement. In case of a solid axle, the

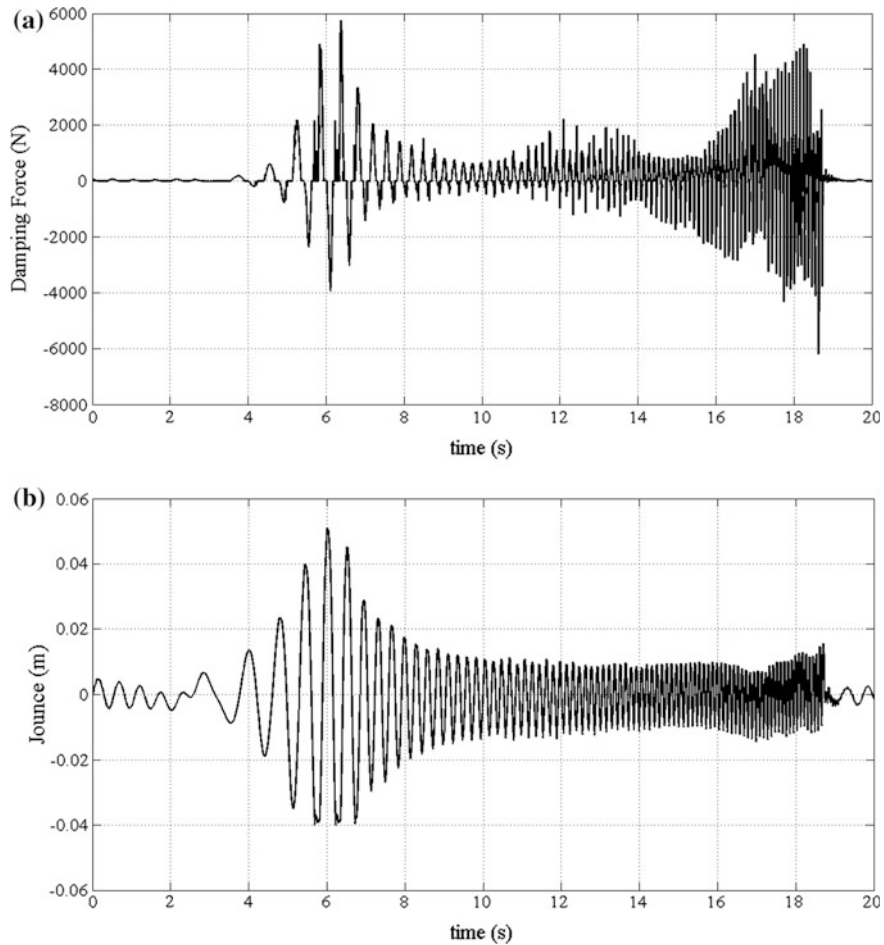


**Fig. 3.27** The full car model results for **a** damping force, **b** jounce, **c** damping factor and **d** tire deformation

left and right wheels make a rigid body with a roll and bounce motion. The energies and, hence, the equations of motion should be revised accordingly to show the bounce and roll of the solid axle.

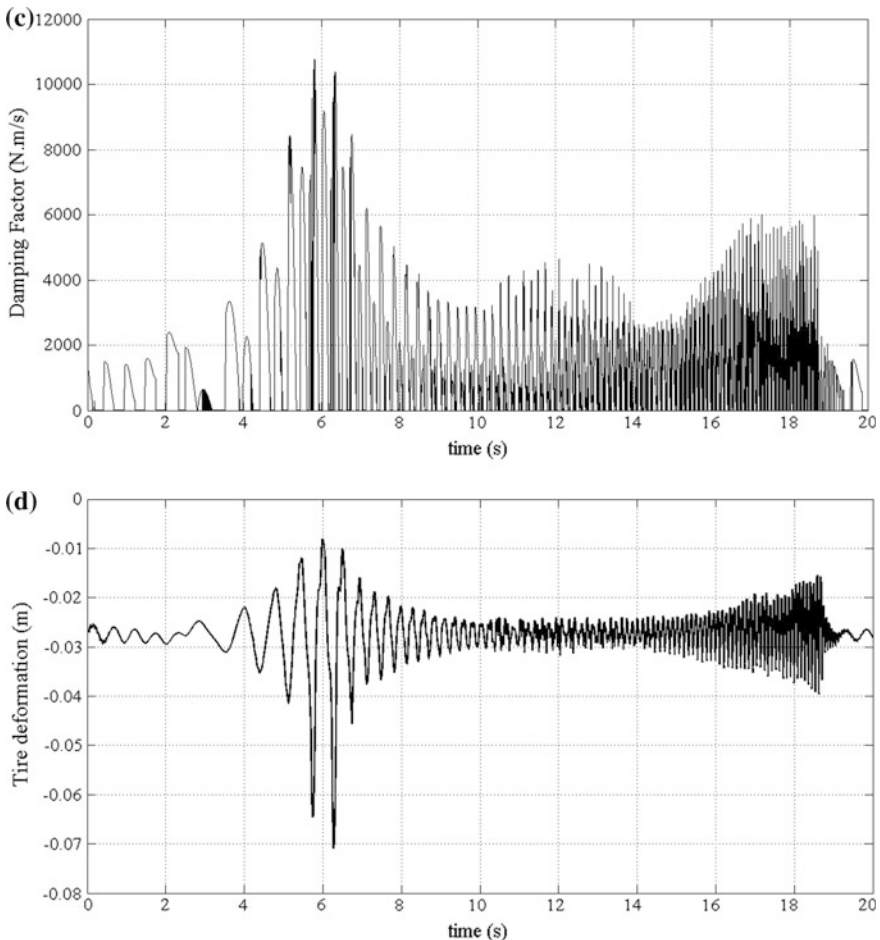
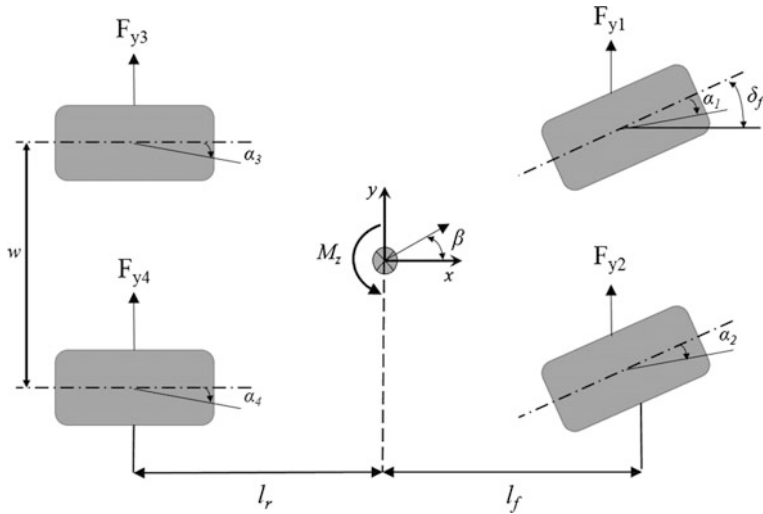


Fig. 3.27 (continued)

### 3.4 Stability of Motioning/Handling

#### 3.4.1 Vehicle Handling Dynamics

In vehicle handling dynamics we are more concerned with the kinetics of the lateral control of motion. Vehicle is the descriptions of the approaches that wheeled vehicles perform transverse to their direction of motion, particularly during cornering, acceleration and braking. It also includes their directional stability when moving in steady state condition. A full vehicle model for the handling is presented in Fig. 3.28.



**Fig. 3.28** A 2-DOF vehicle handling model

By the use of Newton's law of motion and some basic geometric relationships, the longitudinal velocity, the lateral velocity and the yaw rate measured around the Center of Gravity (CoG) of the vehicle can be described by the following differential equations:

$$m(\dot{v}_y + v_x r) - F_{y1} - F_{y2} - F_{y3} - F_{y4} = 0 \quad (3.107)$$

$$I_z \ddot{r} - l_a(F_{y1} + F_{y2}) + l_b(F_{y3} + F_{y4}) - M_z = 0 \quad (3.108)$$

In the above model, the lateral velocity  $v_y$  and the yaw rate  $r$  are the two state variables, while  $M_z$  is the external yaw moment which must be determined by the control law. In this manner, the tire slip angle is another major index for the computation of tire lateral force. The following equations define the slip angles of the front and rear tires:

$$\left. \begin{aligned} \alpha_1 &= \delta_f - \tan^{-1} \left( \frac{v_y + l_f r}{v_x - 0.5 r w} \right) \\ \alpha_2 &= \delta_f - \tan^{-1} \left( \frac{v_y + l_f r}{v_x + 0.5 r w} \right) \\ \alpha_3 &= \tan^{-1} \left( \frac{l_r r - v_y}{v_x - 0.5 r w} \right) \\ \alpha_4 &= \tan^{-1} \left( \frac{l_r r - v_y}{v_x + 0.5 r w} \right) \end{aligned} \right\} \quad (3.109)$$

the responses of linear and vehicle model during a turning maneuver for a typical vehicle is shown in Fig. 3.29. It can be inferred that the nonlinearity of tire force brings about vehicle stable motion through high-g maneuvers. The abundance of

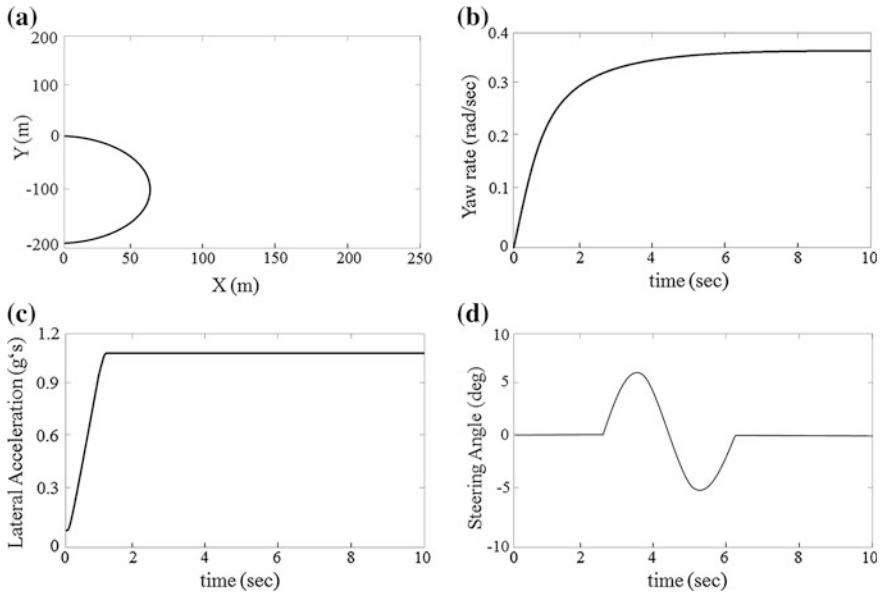


**Fig. 3.29** A two-degree-of-freedom vehicle model during a turning maneuver of **a** motion path, **b** yaw rate, **c** lateral acceleration and **d** steering angle

such a force at high slip angles, lateral load transfer influence, low coefficient of friction and other parameters that influence vehicle stability cannot be estimated when the linear vehicle is adopted.

The adjustment of yaw rate response from second to first order model leads to the increment of the vehicle stability limit and avoids vibration regarding steering input. The formulation of the individual sideslips can be presented as following:

$$\left. \begin{aligned} \beta_1 &= \tan^{-1} \left( \frac{v_y + l_f r}{v_x - 0.5 r w} \right) \\ \beta_2 &= \tan^{-1} \left( \frac{v_y + l_f r}{v_x + 0.5 r w} \right) \\ \beta_3 &= \tan^{-1} \left( \frac{v_y - l_f r}{v_x - 0.5 r w} \right) \\ \beta_4 &= \tan^{-1} \left( \frac{v_y - l_f r}{v_x + 0.5 r w} \right) \end{aligned} \right\} \quad (3.110)$$

In linear tire model the lateral tire force is delivered by the tire cornering stiffness and the tire slip angle as following:

$$F_{yi} = C_\alpha \alpha_i \quad i = 1, 2, 3, 4 \quad (3.111)$$

$$F_y = F_{y1} + F_{y2} + F_{y3} + F_{y4} \quad (3.112)$$

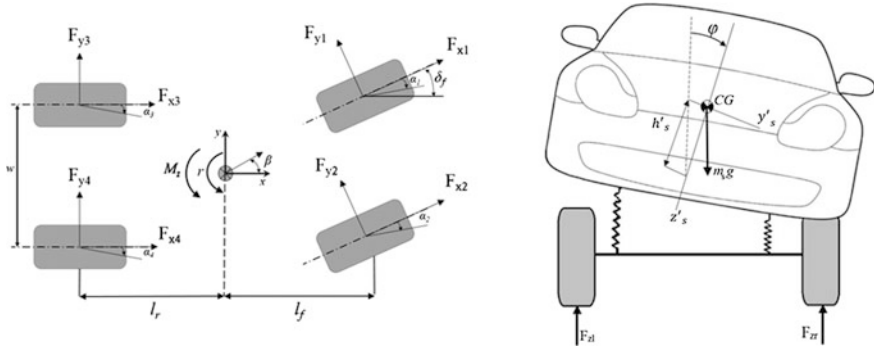


**Fig. 3.30** A full vehicle 9 DOF model for handling

Here we can present the lateral force based on Dugoff's tire model that deals with the friction ellipse idea:

$$F_h = \frac{C_\alpha \tan \alpha}{1 - s} f(h) \quad (3.113)$$

$$\text{where } f(h) = \begin{cases} h(2 - h) & \text{if } h < 1, \\ 1 & \text{if } h > 1, \end{cases} \quad (3.114)$$

and,

$$h = \frac{\gamma F_z (1 - \varepsilon_r x \sqrt{s^2 + \tan^2 \alpha}) (1 - s)}{2 \sqrt{C_s^2 s^2 + C_\alpha^2 \tan^2 \alpha}} \quad (3.115)$$

In addition to yaw, if roll is added into consideration, a 9 DOF model will be presented (Fig. 3.30):

The governing equations for the vehicle based on the Newtonian law of motion can be presented for the longitudinal and lateral forces and yaw momentum and roll degree of freedom as following:

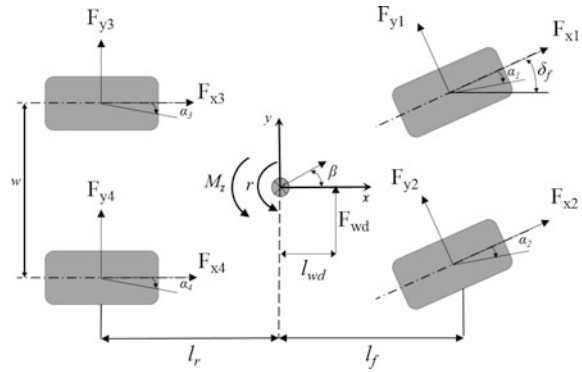
$$m(\dot{v}_x - rv_y) = \sum F_x \quad (3.116)$$

$$m(\dot{v}_y + rv_x) + m_s h'_s \ddot{\phi} = \sum F_y \quad (3.117)$$

$$I_{zz} \dot{r} - I_{xz} \ddot{\phi} = \sum M_z \quad (3.118)$$

$$I_{xx} \ddot{\phi} + m_s h'_s (\dot{v}_y + rv_x) = \sum M_x \quad (3.119)$$

**Fig. 3.31** A full nonlinear handling model



where  $\sum M_x$ ,  $\sum M_z$ ,  $\sum F_x$  and  $\sum F_y$  are described as following:

$$\sum F_x = F_{x1} + F_{x2} + F_{x3} + F_{x4} \quad (3.120)$$

$$\sum F_y = F_{y1} + F_{y2} + F_{y3} + F_{y4} \quad (3.121)$$

$$\sum M_x = (m_s g h'_s - k_\phi) \phi - c_\phi \dot{\phi} \quad (3.122)$$

$$\sum M_z = l_r (F_{y3} + F_{y4}) - l_f (F_{y1} + F_{y2}) + \frac{w}{2} [(F_{x1} + F_{x3}) - (F_{x2} + F_{x4})] - M_z \quad (3.123)$$

If one intends to incorporate the system nonlinearity into the equations along with the effect of wind force blowing to the vehicle body, then the following equations can be extracted (Fig. 3.31):

$$\left\{ \begin{array}{l} m(\dot{v}_x - v_y r) = (f_{x1} + f_{x2}) \cos \delta_f + (f_{x3} + f_{x4}) - (f_{y1} + f_{y2}) \sin \delta_f - a_{dx} v_x |v_x| \\ m(\dot{v}_y + v_x r) = (f_{x1} + f_{x2}) \sin \delta_f + (f_{y3} + f_{y4}) + (f_{y1} + f_{y2}) \sin \delta_f - a_{dy} v_x |v_x| + F_{wd} \\ I\ddot{r} = l_f((f_{x1} + f_{x2}) \cos \delta_f + (f_{x1} + f_{x2}) \sin \delta_f) - l_r(f_{y3} + f_{y4}) + \frac{w}{2} ((-f_{y2} + f_{y1}) \sin \delta_f) + l_{wd} F_{wd} \end{array} \right. \quad (3.124)$$

And the nonlinear formulas of tire slip angles are as following:

$$\left. \begin{array}{l} \alpha_1 = \delta_f - \tan^{-1} \left( \frac{v_y - (n_t \cos \delta_f) \dot{\delta}_f - (n_t \cos \delta_f - l_f) r}{v_x + (n_t \sin \delta_f) \dot{\delta}_f + (n_t \sin \delta_f - \frac{w}{2}) r} \right) \\ \alpha_2 = \delta_f - \tan^{-1} \left( \frac{v_y - (n_t \cos \delta_f) \dot{\delta}_f - (n_t \cos \delta_f - l_f) r}{v_x + (n_t \sin \delta_f) \dot{\delta}_f + (n_t \sin \delta_f + \frac{w}{2}) r} \right) \\ \alpha_3 = -\tan^{-1} \left( \frac{v_y - l_f r}{v_x - \frac{w}{2} r} \right) \\ \alpha_4 = \tan^{-1} \left( \frac{v_y - l_f r}{v_x + \frac{w}{2} r} \right) \end{array} \right\} \quad (3.125)$$

The vehicle longitudinal force, lateral force, roll, and pitch are presented in Fig. 3.32, resulted from the vehicle handling equations of motion.

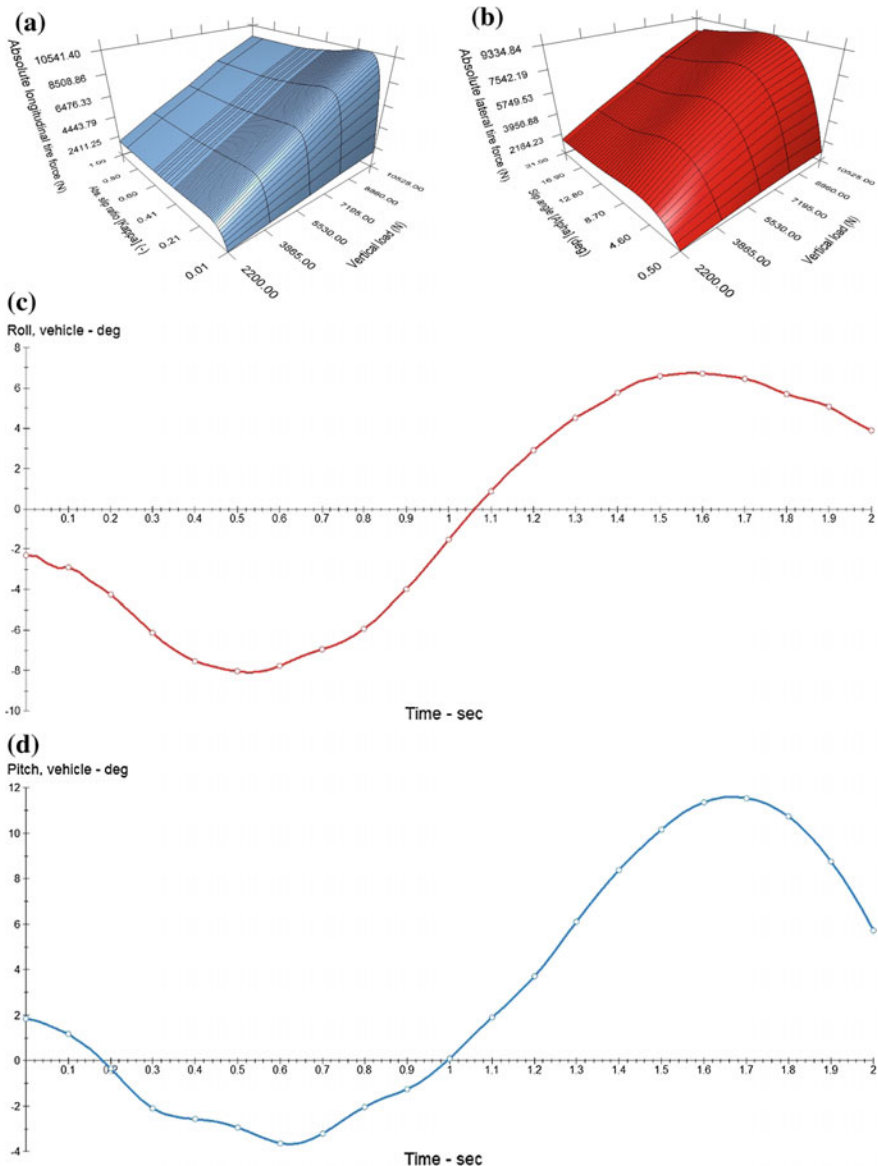


**Fig. 3.32** The vehicle **a** longitudinal force, **b** lateral force, **c** roll, and **d** pitch are presented

### 3.4.2 Off-road Vehicle Stability

The stability and overturn problem herein would be developed and solved for a prototype off-road vehicle such as agricultural tractor that is engaged with operating on steeped slope of mountainous regions and overriding obstacles.

The overturning and instability of off-road vehicles traveling over irregular terrains and steeped slopes have always been a problematic issue for engineers and designers. The rollover situation is closely concerned with the operating condition and a series of vehicle design factors. Amongst the very different types of off-road vehicles, agricultural tractors have been more victim of rollover accidents owing to the inflexible design and inappropriate suspension system. The renewed attention to introduce ROPS (roll-over protective structure) tractors could not prevent such an accidents but only reduced the fatality of those accidents. The tractor safety/stability can be achieved if the tractor kinetics and kinematics are assessed for the objective condition. In this manner, many attempts have been made to develop closed form relationships based on theoretical approaches to achieve a better design of those vehicles that are more liable to the lateral instability. It is noteworthy that the experimental works on overturning and instability are very limited owing to the very risky and perilous outcomes.

The first stage of studying the stability of a road vehicle is the derivation of a reasonable approximation of the equations of motion. The diagram illustrated in Fig. 3.33 a four-wheeled tractor trafficking on sloped surface of  $\theta$ . As aforesaid, the typical tractors are with no suspension system as the one considered herein. Also, let's assume that the tires are overinflated so that they would act similar to rigid wheels while the terrain beneath is not liable to be more deformed compacted soil). These assumptions would provide us with the consideration of the tractor as a conservative system with no loss of energy. Hence, the model could be developed based on the law of conservation of energy since there is no energy dissipater.

Consider that the obstacle is a function  $O = f(x)$  that one can describe the obstacle shape using the given function. The tractor travels with the velocity  $V_v$

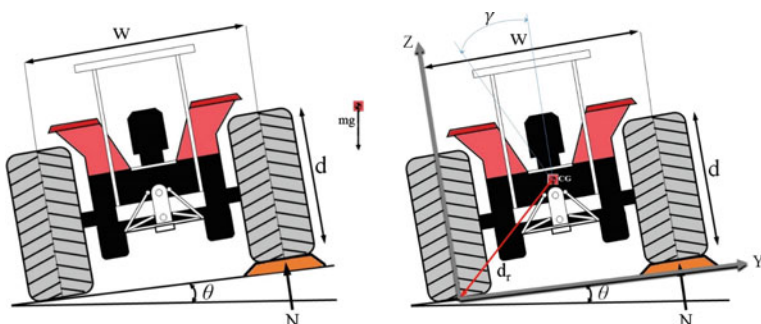


**Fig. 3.33** A four-wheeled tractor trafficking on sloped surface of  $\theta$

over the described obstacle over the sloped surface of  $\theta$ . The velocity and obstacle function could be correlated based on [22] as following:

$$O = f(x) \quad \& \quad V_v = \frac{dx}{dt} \Rightarrow dO/dt = \frac{df(x)}{dx} V_v \quad (3.126)$$

In order to obtain the angular velocity of the wheel, we should couple the Eq. 3.126 above with the following equation.

$$dO = Wd\theta / \cos \theta \xrightarrow{dO/dt = \frac{df(x)}{dx} V_v} d\theta = \frac{\cos \theta \times V_v \times df(x) \times dt}{Wdx} \quad (3.127)$$

This is because the vehicle velocity is different than the linear velocity of the wheel that traverses over the obstacle. We can now obtain the angular velocity and angular acceleration:

$$\omega = \frac{\cos \theta \times V_v \times df(x)}{Wdx} \quad (3.128)$$

$$\alpha = \frac{d\omega}{dt} = \frac{\cos \theta \times V_v \times df(x)}{Wdx} = \left( \frac{d^2f(x)}{dx^2} \times V_v^2 \times \frac{\cos \theta}{W} - \frac{df(x)}{dx} \times \frac{V_v \times \omega \times \sin \theta}{W} \right) \quad (3.129)$$

In addition to the tractor roll, the vehicle is also liable to the pitching because the front axle of the tractor is pivoted to the chassis and the relative movement of the wheels bring about the pitching effect about the rear axle. Hence, the same process adapted to derive the angular velocity and angular acceleration for rolling should also be developed for the tractor pitching.

Similar to Eq. 3.126,

$$dO/dt = \frac{du(x)}{dx} V_v \quad (3.130)$$

The pivot height would be the half of obstacle height and therefore:

$$dO_p = \frac{du(x)}{dx} \times \frac{V_v dt}{2} \quad (3.131)$$

$$b \times d\beta = dO_p \cos \theta \quad (3.132)$$

By combining the above equations, the angular velocity of pitching can be derived:

$$d\beta = \frac{\cos \theta \times V_v \times du(x) \times dt}{2b dx} \rightarrow \frac{d\beta}{dt} \omega_p = \frac{\cos \theta \times V_v \times du(x)}{2b dx} \quad (3.133)$$

where  $d\beta$  is the angular displacement of the front axle pivot point relative to the rear axle and  $b$  is the wheel width. Hence, the angular acceleration of pitching can be calculated by the derivative of angular velocity component.

$$\alpha_p = \frac{d\omega_p}{dt} = \frac{d}{dt} \left( \frac{\cos \theta \times V_v \times du(x)}{2b dx} \right) \quad (3.134)$$

It is also noteworthy that the chain rule in the algebraic calculations to obtain the angular acceleration as following:

$$\begin{aligned} \alpha_p &= \left( \frac{d \frac{du(x)}{dx}}{dx} \times \frac{\cos \theta \times V_v}{2b} \times \frac{dx}{dt} - \frac{du(x)}{dx} \times \frac{V_v \times \sin \theta}{2b} \times \frac{d\theta}{dt} \right) \\ &= \left( \frac{d^2 u(x)}{dx^2} \times \frac{\cos \theta \times V_v^2}{2b} - \frac{du(x)}{dx} \times \frac{V_v \times \sin \theta}{2b} \times \omega \right) \end{aligned} \quad (3.135)$$

If  $\vec{A}$  is considered the vectors of angular momentum in terms of ( $\text{kg m}^2 \text{ s}^{-1}$ ),  $\vec{l}$  is the vectors of linear momentum in terms of ( $\text{kg m}^2 \text{ s}^{-1}$ ),  $\vec{F}$  is the vectors of body external force (N), and  $\vec{M}$  is the vectors of body external moments (N m), then the following dynamic classical equations of force vector and moment vector can be modified:

$$\begin{aligned} \vec{M} &= \frac{d \vec{A}}{dt} \Rightarrow \vec{M} = \frac{d(I \cdot \vec{\omega})}{dt} = I \cdot \frac{d \vec{\omega}}{dt} \\ \vec{F} &= \frac{d \vec{l}}{dt} \Rightarrow \vec{F} = m \cdot \frac{d(\vec{V}_v)}{dt} = m \cdot \vec{g} \end{aligned} \quad (3.136)$$

One can define the kinetic energy of the tractor based on the tractor mass and inertia as well as the variation of the angular and linear velocity of the tractor:

$$KE = \frac{1}{2} (I\omega^2 + mV_v^2) \quad (3.137)$$

In the Eq. 3.137, the term related to the moment has to be more extended for the moments of inertia with respect to the x and y (i.e.  $I_{xx}$  and  $I_{yy}$ ) as well as products of inertia ( $I_{xy}$ ). It is noteworthy that the moment of inertia with respect to z ( $I_{zz}$ ) and its products of inertia ( $I_{xz}$  and  $I_{yz}$ ) are included in the initial model but because tractor

yaw is ignored, the angular velocity about axis z is zero ( $\omega_z = 0$ ) and these terms would be removed later. Thus the kinetic energy can be rewritten as following:

$$KE = \frac{1}{2}mV_v^2 + \frac{1}{2}\left(I_{xx}\omega_x^2 + I_{yy}\omega_y^2 + I_{yy}\omega_z^2\right) - I_{xy}\omega_x\omega_y - I_{xz}\omega_x\omega_z - I_{yz}\omega_y\omega_z \quad (3.138)$$

Equation 3.138 can be written in the short form because ( $\omega_z = 0$ ) as following:

$$KE = \frac{1}{2}mV_v^2 + \frac{1}{2}\left(I_{xx}\omega_x^2 + I_{yy}\omega_y^2\right) - I_{xy}\omega_x\omega_y \quad (3.139)$$

It is clear-cut that the product of inertia ( $I_{xy}$ ) is zero because of the tractor symmetry. Hence, the final form of the kinetic energy could be described as following given that the  $\omega_x$  and  $\omega_y$  represent the  $\omega$  and  $\omega_p$  (rolling angular velocity and pitching angular velocity), respectively.

$$KE = \frac{1}{2}mV_v^2 + \frac{1}{2}\left(I_{xx}\omega^2 + I_{yy}\omega_p^2\right) \quad (3.140)$$

Here, law of conservation of energy can be applied to solve the problem where the work done by external forces known as the mechanical energy which is zero at the time of wheel-ground separation (traversing over obstacle). The elastic energy source of the system would be ignored since tractor functions as no-suspension system and the tires are assumed to act as rigid wheels where the terrain beneath is incompressible. It is concluded that the summation of kinetic energy and potential energy equals zero:

$$ME = KE + PE \xrightarrow{ME=0} KE + PE \quad (3.141)$$

where ME is mechanical energy, KE and PE are kinetic and potential energy, respectively.

In overturn problem, the kinetic energy at two phases is substantial; the first is the start of tractor overturn and the next one is when the tractor's center of gravity (C.G.) is in its maximum position where the velocity of tractor's CG is represented by  $V_c$  [22]. On this basis, the velocity of tractor's C.G. at the initial time of an overturn ( $V_c$ ) can be achieved if the distance between the tractor's C.G. and the rolling axis of tractor ( $d_r$ ) and also the distance between the tractor's C.G. and the pitching axis of tractor ( $d_p$ ) are known and this can be used to establish the changes in kinetic and potential energy and the final height of the tractor's C.G. proposed by Ahmadi [22]:

$$\overrightarrow{V_c} = \overrightarrow{V_f} + \overrightarrow{\omega} \times \overrightarrow{d_r} + \overrightarrow{\omega_p} \times \overrightarrow{d_p} \quad (3.142)$$

where,

$$\begin{aligned}\vec{\omega} \times \vec{d}_r &= d_r \times \omega_r (\cos \gamma \vec{k} - \sin \gamma \vec{j}) \\ \vec{\omega}_p \times \vec{d}_p &= d_p \times \omega_p (\cos \lambda \vec{k} - \sin \lambda \vec{i})\end{aligned}\quad (3.143)$$

Here,  $d_p$  is constant and  $d_r$ ,  $\gamma$  (the initial angle of side overturn) and  $\lambda$  (the initial angle of backward overturn) can be identified as following.

$$\begin{aligned}d_r &= \sqrt{\frac{W^2}{4} + d^2} \\ \lambda &= \operatorname{tg}^{-1} \left( \frac{O}{2b} \right) \\ \gamma &= \operatorname{tg}^{-1} \left( \frac{O}{W} \right) + \operatorname{tg}^{-1} \left( \frac{2d}{W} \right)\end{aligned}\quad (3.144)$$

Now the change in kinetic and potential energy between the two before-said substantial phases (start of overturn and the maximum height of CG) can be determined as following:

$$\Delta KE = KE_v - KE_c = \frac{1}{2}m(V_v^2 - V_c^2) - \frac{1}{2}(I_{xx}\omega^2 + I_{yy}\omega_p^2) \quad (3.145)$$

$$\Delta PE = PE_v - PE_c = mg \left( h - \sqrt{\frac{W^2}{4} + d^2 \sin \left( \theta + \operatorname{arctg} \left( \frac{2d}{W} \right) \right)} \right) \quad (3.146)$$

If  $h$  is lower than  $\sqrt{\frac{W^2}{4} + d^2}$  tractor will be safe but for the height more than it, the tractor will be instable.

## References

1. Janosi, Z., & Hanamoto, B. (1961). Analytical determination of drawbar pull as a function of slip for tracked vehicles in deformable soils. In *Proceedings of the 1st International Conference on Terrain-Vehicle Systems*, Turin, Italy.
2. Bekker, M. G. (1956). *Theory of land locomotion* (520pp). Ann Arbor: University of Michigan Press.
3. Wong, J. Y. (1984). On the study of wheel-soil interaction. *Journal of Terramechanics*, 21(2), 117–131.
4. Hetherington, J. G., & Littleton, I. (1978). The rolling resistance of towed, rigid wheels in sand. *Journal of Terramechanics*, 15(2), 95–105.
5. Rowland, D. (1972). Tracked vehicle ground pressure and its effort on soft ground performance. In *Proceedings of the 4th Internattional ISTVS Conference*, April 24–28, 1972, Stockholm-Koruna, Sweden (pp. 353–384).

6. Uffelmann, F. L. (1961). The performance of rigid wheels on clay soils. In *Proceedings of the First International Conference on the Mechanics of Soil-Vehicle Systems*, Turin (pp. 153–159).
7. Gee-Clough, D. (1980). Selection of tire sizes for agricultural vehicles. *Journal of Agricultural Engineering Research*, 24(3), 261–278.
8. Wismer, R. D., & Luth, H. J. (1973). Off-road traction prediction for wheeled vehicles. *Journal of Terramechanics*, 10(2), 49–61.
9. Taghavifar, H., & Mardani, A. (2013). Investigating the effect of velocity, inflation pressure, and vertical load on rolling resistance of a radial ply tire. *Journal of Terramechanics*, 50(2), 99–106.
10. Freitag, D. R. (1965). *A dimensional analysis of the performance of pneumatic tires on soft soils*. Technical Report 3-688, US Army Corps of Engineers, Waterways Experimental Station, USA.
11. Turnage, G. W. (1972). Tire selection and performance prediction for off-road wheeled-vehicle operations. In *Proceedings of the 4th International Society for Terrain-Vehicle System*, Stockholm, Sweden (pp. 89–98).
12. Dwyer, M. J., Comely, D. R., & Evernden, D. W. (1975). Development of the NIAE handbook of agricultural tire performance. In *Proceedings of the 5th International Society for Terrain-Vehicle Systems*, Detroit, USA, pp. 132–139 (26 pp).
13. Gee-Clough, D., McAllister, M., & Evernden, D. W. (1977). Tractive performance of tractor drive tires, II. A comparison of radial and cross-ply carcass construction. *Journal of Agricultural Engineering Research*, 22(4), 385–395.
14. McAllister, M. D. (1983). Reduction in the rolling resistance of tires for trailed agricultural machinery. *Journal of Agricultural Engineering Research*, 28(127), 137.
15. Gee-Clough, D., & Sommer, M. S. (1981). Steering forces on un-driven angled wheels. *Journal of Terramechanics*, 18(1), 25–49.
16. Saarilahti, M. (2002). Soil interaction model. Development of a protocol for coefficient wood harvesting on sensitive sites (ECOWOOD). *Project Deliverable D*, 2, 2–87.
17. Karafathi, L. L., & Nowatzki, E. A. (1978). *Soil mechanics for off-road vehicle engineering*. Trans Tech Publications.
18. Shibly, H., Iagnemma, K., & Dubowsky, S. (2005). An equivalent soil mechanics formulation for rigid wheels in deformable terrain, with application to planetary exploration rovers. *Journal of Terramechanics*, 42(1), 1–13.
19. Wong, J. Y., & Reece, A. R. (1967). Prediction of rigid wheel performance based on the analysis of soil-wheel stresses—part I. *Journal of Terramechanics*, 4(1), 81–98.
20. Dowling, N. E. (1993). *Mechanical behavior of materials: engineering methods for deformation, fracture, and fatigue*. Upper Saddle River, NJ: Prentice Hall.
21. Chan, B. J. Y. (2008). Development of an off-road capable tire model for vehicle dynamics simulations.
22. Ahmadi, I. (2011). Dynamics of tractor lateral overturn on slopes under the influence of position disturbances (model development). *Journal of Terramechanics*, 48(5), 339–346.

# Chapter 4

## Energetic Perspective of Off-road Vehicle Mobility

### Nomenclature

|           |                             |
|-----------|-----------------------------|
| W         | Work                        |
| P         | Power                       |
| c         | Damping coefficient         |
| k         | Spring stiffness            |
| $\dot{y}$ | Velocity                    |
| $m_s$     | Sprung mass                 |
| $m_u$     | Unsprung mass               |
| $F_a$     | Active force                |
| y         | Displacement                |
| $v_0$     | Reference spatial frequency |
| $S_0$     | Displacement PSD at $v_0$   |
| Gr        | Road-roughness coefficient  |
| $\omega$  | Frequency                   |
| $y_b$     | Tire road input profile     |
| Y         | Harmonic function magnitude |
| $\eta$    | Frequency ratio             |
| $\zeta$   | Damping ratio               |
| F         | Force                       |
| V         | Velocity                    |
| E         | Energy                      |

Energy flow analysis in off-road vehicles is of primary subjects in energetic analysis of off-road vehicles. One should bear in mind that the energy dissipation in off-road vehicles is more significant than on-road vehicles due to the size of these vehicles and difficult operating condition of off-road vehicles. Rolling resistance, suspension system, tires, and brake system are the main sources of energy dissipation in off-road vehicles and steps should be taken to recapture the dissipated energy.

## 4.1 Energy and Power Sources for Off-road Vehicle Mobility

It is well documented in the literature that based on the investigation performed by California Energy Commission (CEC) on light trucks and by applying the low-motion resistance tires, it was concluded that in the case that all light truck tires in California were changed to low-rolling resistance tires, the energy recapturing could be approximately  $1135623.53 \text{ m}^3/\text{y}$  of gasoline [1]. This figure focuses on the result of correct management of optimized rolling resistance on energy recapturing. The motion resistance of a tire during the traversing is quantified on the basis that it is in the subject of hysteresis losses of the rubber in repetitive deformation. In terrain running condition, energy loss is increased due to both hysteresis losses in cyclic deformation of the rubber and also soil deformation under the traversing wheel. Mobility progression and enhanced fuel efficiency of off-road vehicles are contradictory technical problems to be achieved simultaneously, since in order to improve vehicle mobility, it is usually required to have extra fuel available, and the optimization of fuel consumption reduces the vehicle mobility [2]. Motion resistance, soil sinkage and skid are of the most prominent factors for the determination of the performance characteristics of a towed wheel, amongst which, motion resistance is the most fundamental performance parameter of the towed pneumatic wheel [3]. It is, however, well documented in literature that motion resistance is commonly influenced by tire parameters and system parameters, including traditional design parameters of the tire such as diameter, section width, section height, inflation pressure and load deflection relationship. It is believed that these parameters have varying degree of influence on tire soil interaction [4]. To study the interaction between wheel and soil, the related tire parameters of wheel are the basic inputs and must, therefore, be quantitatively and qualitatively defined.

As mentioned earlier in Chap. 3, rolling resistance is the parasitic energy dissipated by the continuous deformation of travelling tire along with the soil profile sinkage under wheel load [5]. The phenomenon is quite complicated due to the elasto-plastic semi-infinite characteristic of soil medium interacted by stochastic wheel dynamics wherein mechanical energy is changed to heat [6]. The converted energy is the summation of the required energy to deform the rubber (elastic deformation) and/or the soil beneath the tire (plastic deformation) in motion added with friction in the bearings of wheel [7]. Rolling resistance performs as a resistive force applied to the wheel against the direction of traversing. Due to sinkage, wheels operating on soft soils must handle much superior resistance leading to greater waste of power. In another term, tire rolling resistance is expressed as the amount of energy required to keep tires rolling at a steady pace, and has a momentous impact on vehicle fuel efficiency.

Energy efficiency of vehicles has been a momentous subject owing to the termination of crude oil resources in addition to the geopolitical turmoil of oil providers in the contemporary age. The traction performance of a wheeled tractor, as an important index of energy efficiency, is the result of stress-strain interaction

between the tractor wheel and the topsoil [8]. The soil-tire interface is responsible for approximately 20–55 % of the losses of tractor power and hence, drastically affects the amount of fuel used in drawbar—implement applications [9]. Therefore, a detailed analysis is essential to reduce the tractive power loss to gain the optimal energy efficiency in terrain-vehicle context because of the considerable size of the off-road vehicles that demand greater power supply. Consequently, off-road vehicles are accountable for more serious energy loss drawback and this highlights the requirement for studies that are dedicated to the energy flow of these vehicles.

## 4.2 Energy Dissipaters of Vehicle Vibrations (Energy Harvesting)

### 4.2.1 *Energy Harvesting from Suspension*

Vehicle kinetic energy (vibrations) are attractive source of energy recapturing for running some of the electric based vehicle systems/subsystems. A very small portion of the energy obtained from fuel combustion inside the engine is transferred to the wheel because of energy dissipation inside the engine as heat, energy loss in power transmission system and engine vibration. To make it worse, a very small amount of the delivered power to the wheels is used to drive the vehicle and most of the energy dissipating during vibrations and motions. The case of energy harvesting/recapturing from vehicle suspension system is for sure more vital for the off-road vehicles since they are more liable to be vibrated through the random excitations of the road irregularities. The primary step is to capture the vibration motion of the suspension system and then utilize it as effectively as possible for active suspension control and also as energy regenerating devices. A great amount of energy dissipated in undesirable vertical motions induced by road irregularities is done through the conventional shock absorbers as they dampen the vertical motions and thus the kinetic energy. In most shock absorbers, the energy is dissipated into heat via viscous fluid and dry friction. The regenerative suspension can be categorized into two types: mechanical and electromagnetic regenerative suspension. The mechanical regenerative suspension absorbs the kinetic energy of suspension and converts into potential hydraulic/pneumatic energy to be stored in accumulator. Hydraulic passive dampers are conventionally utilized in vehicle suspension systems that are cheap and simple. However, these hydraulic/pneumatic systems characterize some disadvantages. One, the complex pipeline system has considerable weight and need more installation room. Two, hose leaks and ruptures may disable the whole system. Three, the responding bandwidth of hydraulic/pneumatic systems is narrow, which confines the suspension performance. Four, the reuse of the regenerated hydraulic/pneumatic energy are limited, especially when the automotive industry is toward commercializing hybrid electric vehicles and fully electric vehicles. Recently a significant advancement in the domain of mechatronics

and sensors have led to the adoption of semi-active and active suspension systems. In hydraulic cylinders, the hydraulic fluid is heated up and consequently, the hot air is transferred into the ambient medium.

Off-road vehicles are subject to a variety of road unevenness and random road profiles that may cause the vehicle to experience a greater portion of energy loss in addition to the typical rolling resistance. The energy loss due to vibration which is more pronounced in off-road vehicles can be harvested/recaptured for the vehicle suspension system. In following, the analysis of energy harvesting from off-road vehicle suspension under random road excitation with power spectral density (PSD) road profile. The potential of energy harvesting from harmonic road profile is also covered. It will be shown that the energy recapturing is closely related to the system frequency, mode shapes, and the relative velocity between the sprung and unsprung masses as well as road surface shape.

While active suspensions are characterized by outstanding performance, they are energy-consumer and are bulky and costly when compared to other technologies such as electromagnetic-valve and Magneto-Rheological (MR) fluid dampers and mechanical regenerative dampers. The benefit of mechanical regenerative suspension is that the accumulator can be added to the current hydraulic or pneumatic suspension and decrease the energy demand on actively controlling vibration. Nevertheless, the low frequency and slow response are the principal shortcomings.

The maximum energy that is available for harvesting is the amount that is dissipated by the viscous damping  $c_2$ . The instant damping force is proportional to the suspension velocity, and the instant power is the force times the suspension velocity. Therefore, the instant power dissipation is

$$P = c_1(\dot{y}_2 - \dot{y}_1)^2 \quad (4.1)$$

In this manner, if one intends to yield the harvestable energy, the following eq. should be considered:

$$W = \int P dt = \int c(\dot{y}_1 - \dot{y}_2)^2 dt \quad (4.2)$$

In a unit time, the work per sec in J is closely correlated with that of the power presented in abovementioned form. Thus, the harvested energy can be calculated through the power harvesting index.

The average power in the shock absorber is hence proportional to the mean square (not RMS) of the suspension velocity. Power harvesting over this among will yield a suspension with a damping coefficient more than the desired value.

Energy savings by using optimized regenerative magnetic shock absorber in vehicles is a useful solution as by the use of the mentioned shock absorbers it is applicable to enhance the energy efficiency in electrical vehicles through the conversion of mechanical power losses into electrical energy and store it for a longer period of running for the batteries.

The sprung and unsprung masses as well as the passive damping coefficient ( $c_1$ ) are presented in Fig. 4.1.  $F_a$  is the actuator active force in case of the active suspension system, and is set by the control strategy. For a single DOF system, the general equation has been discussed in the ride comfort section. The governing equation for a 2DOF suspension system with an active force can be considered as following:

$$\begin{aligned} m_s \ddot{y}_2 &= -k_2(y_2 - y_1) - c_1(\dot{y}_2 - \dot{y}_1) - F_a, \\ m_u \ddot{y}_1 &= k_2(y_2 - y_1) - k_1(y_1 - y_b) + c_1(\dot{y}_2 - \dot{y}_1) + F_a, \end{aligned} \quad (4.3)$$

The road irregularities can be considered as any basic harmonic form such as sinusoidal (i.e.  $y_b = Y \sin \omega t$ ) or any random and varying functions such as displacement power spectral density (PSD) in  $\text{m}^3/\text{cycle}$  [10].

$$PSD(v) = S_0 v^\beta / v_0^\beta = G_r v^\beta, \quad (4.4)$$

where  $v$  is the spatial frequency in cycle/m,  $v_0$  is the reference spatial frequency equal with  $v_0 = 1/2\pi$ ,  $S_0$  is the displacement PSD at  $v_0$ ,  $G_r$  is the road-roughness coefficient, and the exponent  $\beta$  is commonly approximated as—2.

Based on the system being adopted such as piezoelectric or electromagnetic, etc., the relative velocity between the sprung and unsprung mass can create a potential power ( $P = c_1(\dot{y}_2 - \dot{y}_1)^2$ ) wherein this is greatly affected by the spring force of  $k_1(y_1 - y_b)$ . Therefore, it can be stated that the mean power in the suspension due to road roughness is proportional to the roughness coefficient  $G_r$ , the vehicle travel speed  $V$ , and the tire stiffness  $k_1$ .

Let's assume that a single degree of freedom quarter car model is considered (Fig. 4.2). Also the vehicle-harmonic road traversing mode is demonstrated in Fig. 4.3.

For the mass-spring-damper system presented, the dynamic response of the system is investigated to determine the magnitude of the potential energy to be harvested through the vehicle suspension system due to the road irregularities and the vibrations from vehicle suspension. It is though a common process to replace regenerative shock absorbers, which convert the vehicle vibration in the suspension system to the electric energy source for the system, instead of the classical hydraulic based dampers. It is also known that the aforementioned electric energy can be fed to the hybrid or electric vehicles. We can develop the equation of motion for this system as following:

$$m \ddot{y}_1 + c(\dot{y}_1 - \dot{y}_b) + k(y_1 - y_b) = 0 \quad (4.5)$$

Now let's assume that  $y_1 - y_b = u$  and rewrite the equation:

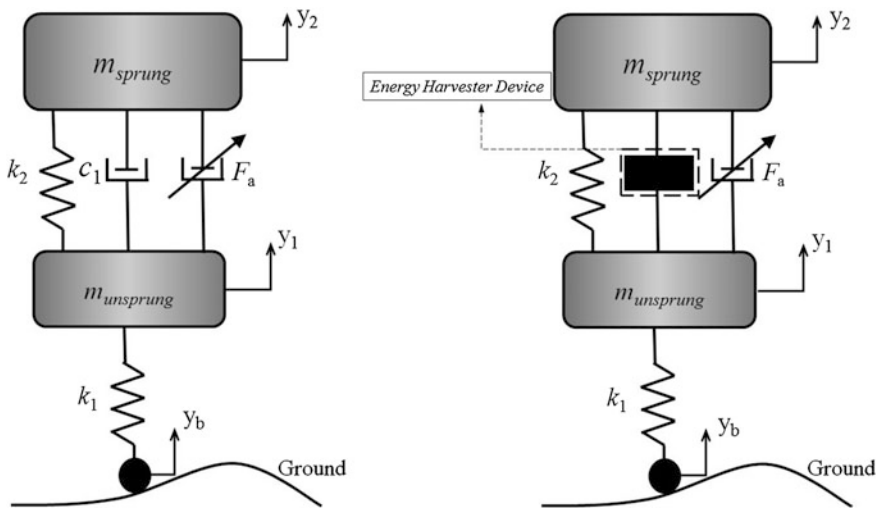


**Fig. 4.1** Sprung and unsprung masses as well as the passive damping coefficient ( $c_1$ )

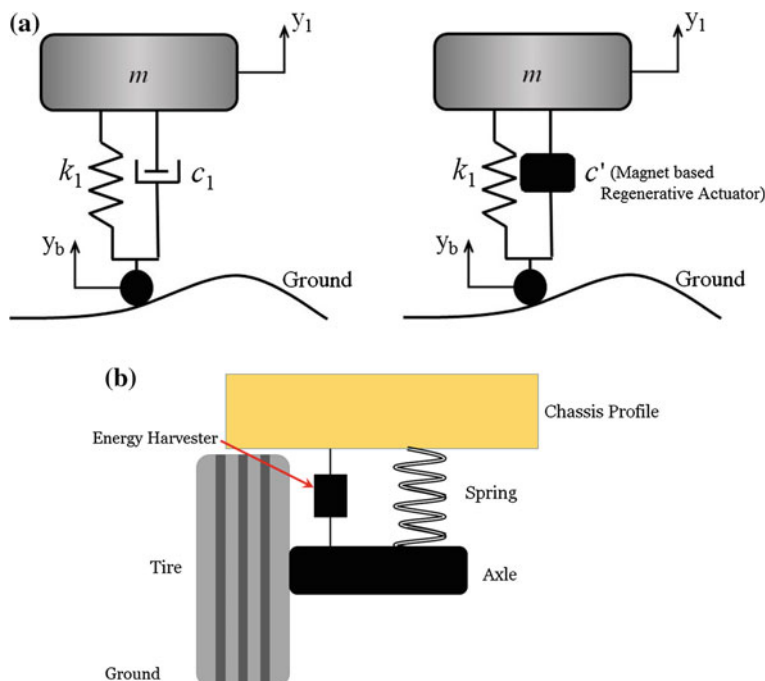


**Fig. 4.2** **a** Single degree of freedom model for vehicle suspension energy harvesting and **b** the dual-mass piezoelectric energy harvester

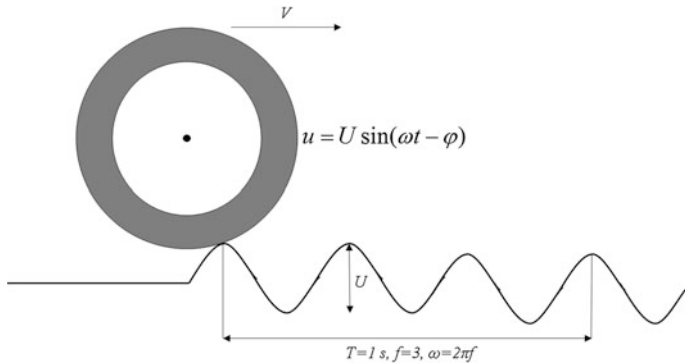


**Fig. 4.3** A typical harmonic based road profile with the harmonic road equation

$$m\ddot{u} + c\dot{u} + ku = m\ddot{y}_b \quad (4.6)$$

If the road irregularities is considered as any basic harmonic form such as sinusoidal (i.e.  $y_b = Y \sin \omega t$ ). Then the  $\ddot{y}$  product equals with  $-\omega^2 Y \sin \omega t$ :

$$m\ddot{u} + c\dot{u} + ku = m\omega^2 Y \sin \omega t \quad (4.7)$$

If it is considered that  $u = U \sin(\omega t - \varphi)$  :

$$U = \frac{m\omega^2 Y}{\sqrt{(k - m\omega^2)^2 + c^2\omega^2}} \quad (4.8)$$

One can obtain the harvested power as following:

$$P = c_1 \dot{u}^2 \quad (4.9)$$

By substituting  $\dot{u} = \omega U \cos(\omega t - \varphi)$  in Eq. 4.9, the dissipated energy can be obtained in a cycle as:

$$E = c\omega^2 U^2 \int_0^{\frac{2\pi}{\omega}} \cos^2(\omega t - \varphi) dt = \pi c\omega U^2 \quad (4.10)$$

And the power per cycle can be derived as:

$$P = \frac{E}{\frac{2\pi}{\omega}} \quad (4.11)$$

From Eqs. 4.10 and 4.11, the power can be presented as:

$$P = \frac{cm^2\omega^6Y^2}{2((k - m\omega^2)^2 + c^2\omega^2)} \quad (4.12)$$

If the maximum road profile magnitude is presented by  $Y_{\max}$ , it can be obtained as:

$$Y_{\max} = \frac{\sqrt{(k - m\omega^2)^2 + c^2\omega^2} \times U_{\max}}{m\omega^2} \quad (4.13)$$

As a result, the power can be re-written as:

$$P = \frac{cm\omega^4 Y U_{\max}}{2\sqrt{(k - m\omega^2)^2 + c^2\omega^2}} \quad (4.14)$$

And the dimensionless power [11] can be considered as:

$$P_d = \frac{P}{m\omega^3 Y U_{\max}} = \frac{\zeta \times \eta}{\sqrt{(1 - \eta^2)^2 + (2\zeta\eta)^2}} \quad (4.15)$$

The dimensionless power  $P_d$  variations with respect to damping ratio  $\zeta$  and frequency ratio  $\eta$  can be illustrated in Fig. 4.4. It is clear that by an increment in damping ration the dissipated power (harvested power) increases. There is an inconsistency for the frequency ratio of 1 at which the resonance occurs.

Since the dimensionless power does not demonstrate the effect of vehicle velocity on power magnitudes. Hence, the actual power can be determined as following:

$$P = \frac{m\omega^3 Y U_{\max} \zeta \eta}{\sqrt{(1 - \eta^2)^2 + (2\eta\zeta)^2}} \quad (4.16)$$

The power  $P$  with respect to the damping ratio and the frequency is demonstrated in Fig. 4.5. It can be inferred that higher power is harvested for larger values of frequency, where the power is proportional to the frequency in the power of 3. It can be concluded that the exciting frequency equal to its natural frequency provides greater power values and the power is proportional to the frequency in the power of 3.

The studies regarding regenerative vibration absorbers of vehicles so far have been centered on development of systems to generate electric energy from vibrations of vehicles by electromagnetic materials while the shock absorbers were situated parallel with suspension spring which indispensably dissipates a part of

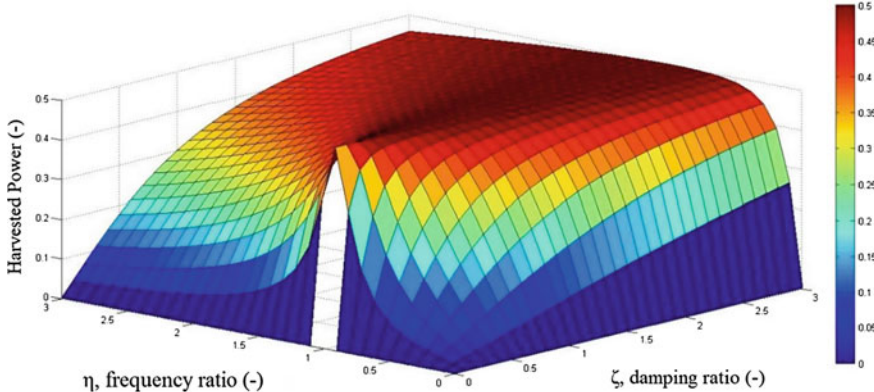


**Fig. 4.4** The dimensionless power  $P_d$  variations with respect to damping ratio  $\zeta$  and frequency ratio  $\eta$

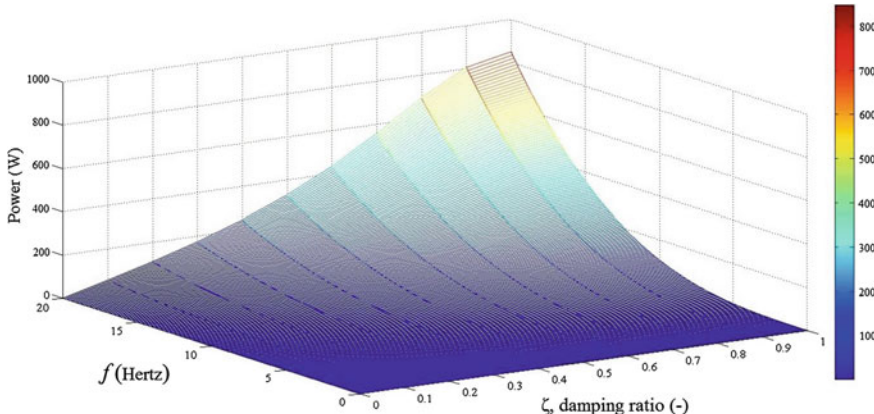


**Fig. 4.5** Harvested power versus frequency and damping ratio

vehicle vibration energy, and hence cannot fully absorb and transfer the kinetic energy from the suspension system (Fig. 4.5). In addition, the conversion efficiency of electromagnetic materials is not very high. Currently, the mostly available vibration-to-electric conversion mechanisms are electromagnetic, electrostatic, and piezoelectric transductions while among the three types of energy transductions, the efficiency of piezoelectric transductions is preferred and much higher than the other two mentioned ones [12]. The kinetic energy versus time and in frequency domain are presented in Fig. 4.6.

Figures 4.7 and 4.8 show the relative acceleration between the unsprung mass and road surface and the tire displacement in vertical direction subject to the described PSD based road. Figure 4.9 shows a typical displacement profile for the

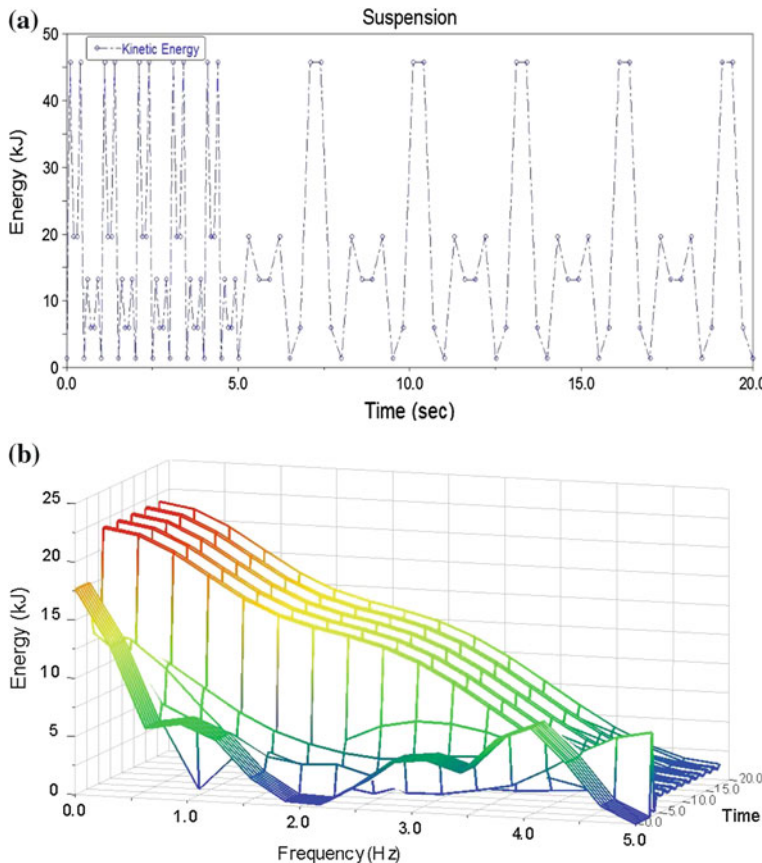


**Fig. 4.6** The kinetic energy versus time and in frequency domain

vehicle at the speed of 40 m/s and relative peak to peak shock displacement with the maximum amplitude of 0.13 m for the sprung mass and unsprung mass excited by the random road transversal was observed. The relative displacement between the masses is also important on the ride comfort of the vehicle and is shown how the displacement between the masses would change during the 30 s of motion on the described irregular road with random excitation.

Figure 4.10 shows the RMS of harvested power based on the data presented from Figs. 4.7, 4.8 and 4.9 and the relative velocity between the sprung and unsprung masses within a range of velocity between 5 and 60 m/s. It was resulted that a maximum magnitude of 67.5 W power is harvestable at the speed of 60 m/s. It can be also appreciated that at a range of 5–40 m/s the energy harvesting trend seems to be linear while a curve-shaped behavior can be seen after this range with far decreased slope of line.

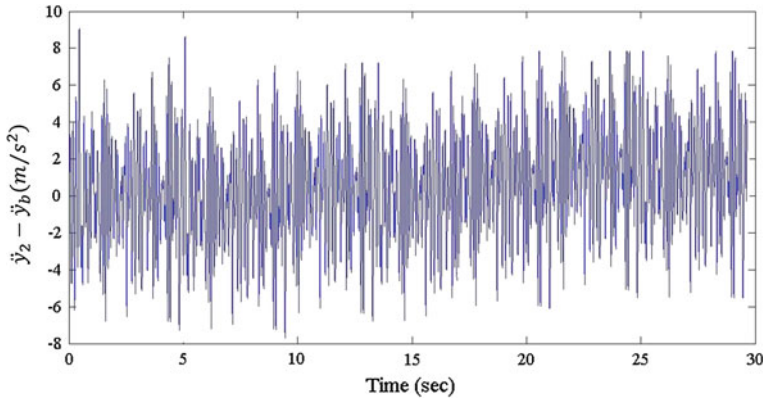


**Fig. 4.7** Relative acceleration of the unsprung mass and road surface

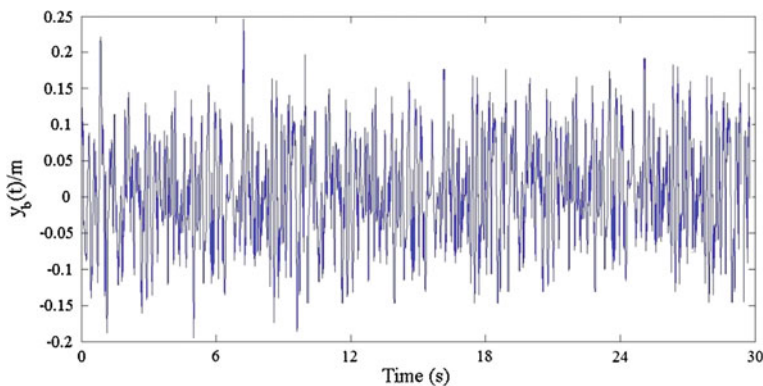


**Fig. 4.8** Transverse displacement of road profile

Frequency response from road irregularities for the suspension deflection, tire deformation and body acceleration for the perturbed vehicle system is presented in Fig. 4.11. For a lower range of frequency 0–10 rad/s which is more important for the real-world applications, there is a decreased value for the first peak when the active suspension system that uses the energy harvesting device is applied. This decreases the tire deformation (as an important index of energy dissipation due to rolling resistance) and also the body acceleration that is closely connected with the ride comfort index.

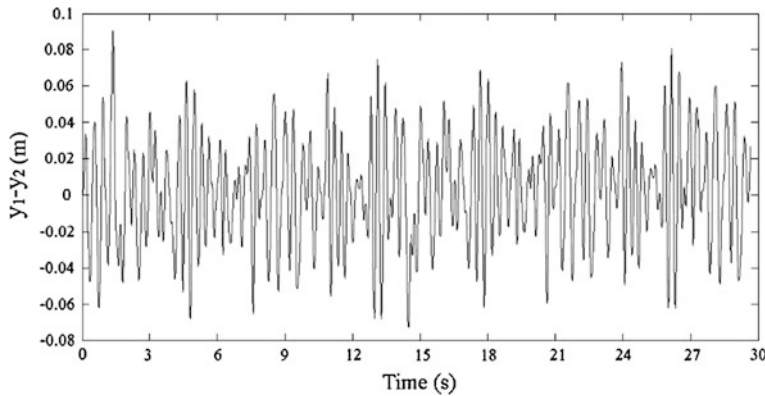


**Fig. 4.9** Relative displacement of sprung mass and unsprung mass

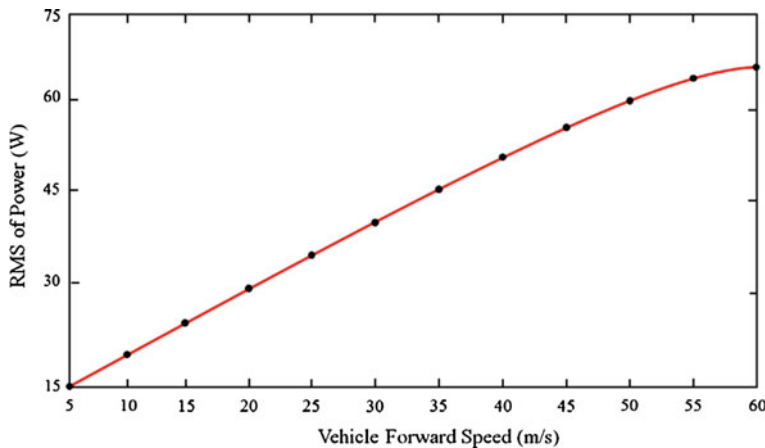


**Fig. 4.10** RMS of harvestable energy (electromagnetic based electric power) versus speed of vehicle

#### 4.2.2 Tire Energy Harvesting

Energy harvesting to provide power for TPMS (Tire Pressure Monitoring System) has been a dynamic field of studying interest to reduce the maintenance and running costs of the system. More, if such a systems are pivotal on batteries as energy source, then there might be some environmental problems owing to the release of battery toxics to the environment. There are some new emerging trends in technologies that adopt functional systems to energy harvesting while the core fundamental principle is laid on the use of mechanical vibrations as energy source. It is noteworthy that the energy harvesting in its essence is associated with the

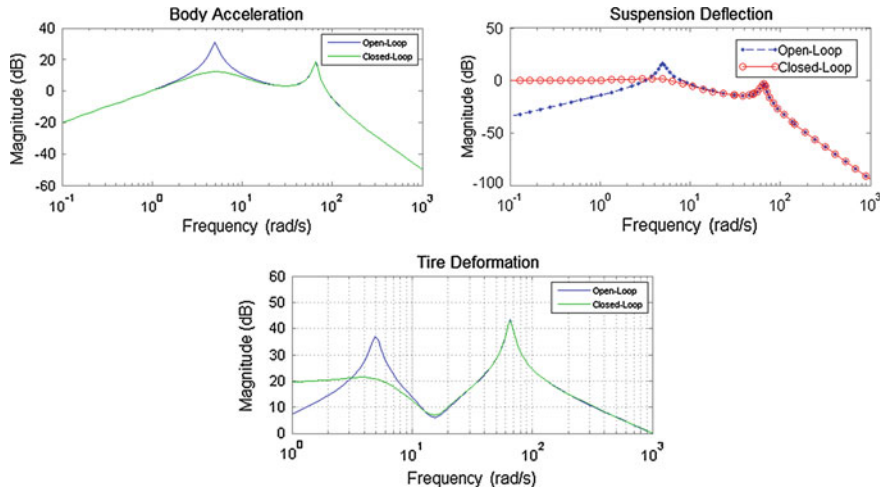


**Fig. 4.11** Frequency response from road irregularities for the suspension deflection, tire deformation and body acceleration for the perturbed vehicle system

conversion of ambient energy (usually mechanical) into electric energy to run small instruments (e.g. TPMS). This process is usually carried out through one or hybridization of two systems. The most commonly used kinetic energy generator systems include electromagnetic energy harvesting, electrostatic energy harvesting, piezoelectric energy harvesting, and thermal energy harvesting although some classifications, magnetostrictive, triboelectric and electroactive polymers are also included [13]. Each of the systems inherits their advantages and disadvantages while there are numerous studies documented in the literature with the comparative trend among the aforementioned systems to determine the most optimal system for tire energy harvesting. However, the final goal of each system is to develop a competitive battery-free tire TPMS and to test its feasibility in the laboratory and on the road. The source to provide energy can be found in the continuous deformation of pneumatic tire that can be divided into two forms of tire deflection at the contact patch and vibration of tire. The tire deflection relies on different parameters such as tire materials, exerted load to the wheel, tire inflation pressure and tire-ground interface condition.

#### 4.2.2.1 Electromagnetic Energy Harvesting

The theory behind the electromagnetic method is laid foundation based on the relative linear movement of an electrical coil attached to a mass with respect to a stable magnet (Fig. 4.12). The source to the linear relative movement of the coil-mass component with respect to the magnet is provided by the tire cyclic deformation and the vibration to generate electric current in the coil based on the

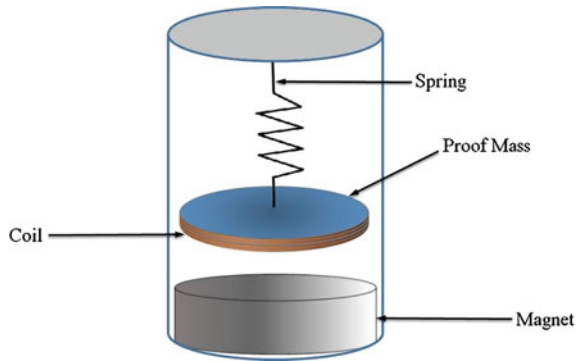
Faraday's law of electromagnetic induction. Although linear vibration is probably the most typical configuration of electromagnetic energy harvesters, a significant share of the harvesters documented in the literature address the cantilever beam system with a seismic mass attached to the free end of the beam that can both accommodate each of the coil or the magnet so that the electric current is generated [14–17]. It has been reported that electromagnetic energy systems provide power levels ranging from 0.3 to 800  $\mu\text{W}$  from vibration frequencies of several hundred hertz [18]. In this regard, Glynne-Jones et al. [19] demonstrated an electromagnetic generator able to provide 157  $\mu\text{W}$ . However, Roundy et al. have estimated the practical maximum energy density of an electromagnetic converter to be approx. 4  $\text{mJ}/\text{cm}^3$  assuming a magnetic field of 0.1 T and a magnetic permeability of free space [20]. Overall, it is clear-cut that energy density is pivotal on the magnetic field strength. Since the capability of electromagnetic approach is closely dependent on the vibrational performance of the system, one can design the spring of the spring-mass system in which the resonance frequency of the system is excitation frequency for which the harvester is intended to run; however, this means that this approach is restricted to drive in a limited bound of frequency [21]. The most important advantage of these systems is the simplicity in design and operational condition owing to the contactless condition that increases the accuracy and depreciation of its components. However, the main disadvantages are the size of the system to be embedded in tire [22] and also low output voltage and low power density [21, 23, 24].

#### 4.2.2.2 Electrostatic Energy Harvesting

The core ideology behind this approach is the voltage induction to a dielectric capacitor sandwiched between two plates with movement with respect to each other. The voltage across the capacitor is dependent on stored charge, electrode separation, electrode area and the permittivity of the dielectric. This type of harvesting is based on the variation capacitance of vibration-dependent capacitors that source from the vibration of the tire. The vibrations isolate the plates of a charged variable capacitor and therefore, the mechanical energy is converted into electrical energy while a polarization source is needed to run.

The voltage obtained in the capacitor relies on stored charge, the capacitor material, distance between the plates, electrode displacement and area. To this end, there are two practical approaches. In the case that the electric potential is stable, there is an increment in charge with decreasing electrode distance during mechanical vibration. The change in the electric potential ( $V$ ) across the capacitor ( $Q = CV$ ), where  $Q$  is electric charge and  $C$  is the variable capacitor. In the next approach, the voltage increases with decreasing the capacitor when the charge is constant. In both cases the energy stored on the capacitor increases and can be extracted to power a device [13]. Since the ambient vibrations are generally low in amplitude, the use of a mass-spring system generates a phenomenon of resonance, amplifying the relative movement amplitude of the mobile mass compared to the

**Fig. 4.12** A typical electromagnetic based energy harvester



vibrations amplitude, increasing the harvested power [25]. The most optimal energy power possible to be harvested by an electrostatic converter is about  $4 \text{ mJ/cm}^3$  while an electric field of  $30 \text{ V}/\mu\text{m}$  and a dielectric constant of free space are provided [20]. In general, electrostatic devices are more appropriate for small scale energy harvesters while electromagnetic converters are better for larger devices. However, unlike electromagnetic energy harvesting systems, the electrostatic systems are compatible to be micromachined and can be functionally integrated with the MEMS systems [21]. The considerable portion of output voltages, size reduction, simplicity and convenient in costs are of the advantages of this system. No direct mechanical to electrical energy for electret-free converters and the need for continuous pre-charging are of major drawbacks [26]. Furthermore, there is a risk of contact between the electrodes of the capacitor [27].

#### 4.2.2.3 Piezoelectric Energy Harvesting

For this purpose, the piezoelectric materials that are capable of generating charges while being imposed to stress/strain processes are used (Fig. 4.13). The electric charge is induced in definite type of materials when subjected to mechanical stress/strain. The piezoelectric effect is understood as the linear electromechanical interaction between the mechanical and the electrical state in crystalline materials with no inversion symmetry [28]. The piezoelectric based devices have found popularity in quantification of the processes in which pressure, acceleration, temperature, strain, or force are engaged. In this manner, the polarization effect which is the intrinsic feature of the materials, electrical energy is generated in response to the material to the mechanical energy. The generated electricity is by the inverse piezoelectric effect so that converting mechanical vibrations into deformation of the piezoelectric will generate an alternating electrical current [13]. This approach inherits the advantage of being micromachined and being integrated by micro devices. Although there are different types of applying the system, the most common type is probably a cantilever-based resonant structure so that the

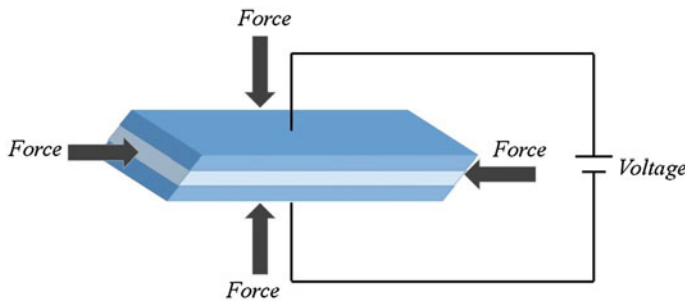
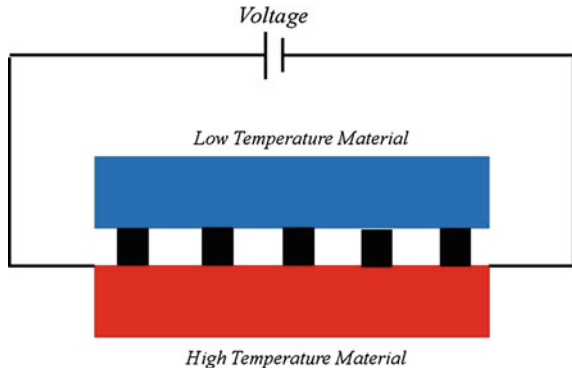


**Fig. 4.13** Piezoelectric energy harvester system

mechanical vibration energy is converted to electric charge [13]. In this condition, there is a cantilever beam housing a piezoelectric material while an inertia mass is inserted at the end of the beam. There are a charging circuit and a storage buffer in the piezoelectric element. Hence, the piezoelectric vibrational energy harvesters are functioning based on inertia mass, where a cantilever with a piezoelectric layer is subjected into resonance by a vibration source at the end of the cantilever while the vibration source emanates from the rolling tire. There are studies documented in the literature which has applied the cantilever based tip mass piezoelectric energy harvesting [29–32]. This approach has the ability of being adopted for a greater range of resonance frequency domain particularly when compared to the electromagnetic energy harvesters. Moreover, there is a close relationship between the vibration based mechanical deformation and the electricity generation in which as there is an increment in the electricity charge by the increase of the applied frequency. The amount of electric charge is dependent on the piezoelectric material as well as the amount of mechanical deformation applied to the material. Based on the investigation documented in the literature, the greatest amount of piezoelectric energy to be harvested is to be  $17.5 \text{ mJ/cm}^3$  based on a Lead zirconate titanate material with safety factor of equal to 2 [20]. This device is robust, and reliable with no need to control while considerable output voltage can be obtained. For the inclusion of such a system in the tire, the inner wall of the tire can be served as a functional housing for the system while the deformation of the tire at while traversing brings about accelerations which are aggravated particularly while traveling over irregular terrain. In the case that the amount of acceleration is more than expected, there is the risk of mechanical damage to the system [13]. Although of its privileges, they are not economically convenient added with the drawback of coupling coefficient linked to material properties. More, there is also a difficulty of system size when compared to the electrostatic energy harvesting system.

**Fig. 4.14** A thermal energy harvester system



#### 4.2.2.4 Thermal Energy Harvesting

Based on the Seebeck effect that is a physical process, the temperature gradient between two different semiconductors generates a voltage leading to the electric potential. This is also called as the thermoelectric effect which is the direct conversion of temperature gradient to electric voltage. This can be represented by:

$$V_g = \alpha_{a,b} \Delta T \quad (4.17)$$

where  $V_g$  is the voltage,  $\Delta T$  is the difference in temperature and  $\alpha_{a,b}$  is the Seebeck coefficient.

The thermal energy harvesters, so-called thermoelectric energy harvesting system, includes thermoelectric generator, the heat sink, voltage regulator, and energy storage device while there is a need for heat source to produce the heat gradient (Fig. 4.14).

This approach has gained popularity and interest due to the abundance of heat as an essential by-product in several locations in the vehicle, including engine compartment, exhaust system and brakes [13], however, tire can be a target destination for the insertion of this device since the heat in tire as a bi-product of tire rolling over terrain in the form of rolling resistance is a very famous energy dissipater source. The price and a need for a constant provision of the temperature gradient are the major drawbacks of this system.

The aim in micromachining is the adoption of thermal gradient in the MEMS due to heat flow in elements with different thermal resistances, however, this can be difficult to keep thermal gradients.

#### 4.2.2.5 Magnetostrictive, Electroactive Polymers, and Triboelectric Materials

Although the main types of tire energy harvesting system are electrostatic, electromagnetic and piezoelectric, however, there are magnetostrictive, triboelectric and

electroactive polymers are also included [13]. A magnetostrictive material is included of ferromagnetism parts that change in size and geometry as affected by the external magnetic field. As a result of the rotation of magnetic fields, the randomly located magnets are realigned. These supplies are able to generate electric energy from tire mechanical vibrations by generating an electric current in a coil [33]. At the exertion of a mechanical force to the material, the inverse magnetostrictive effect is formed in which the material generates a magnetic field that can be applied to produce an electric current particularly in the coil and therefore the electric energy is obtained. Triboelectric charging is a kind of contact electric current harvesting that some definite materials are charged as a result of a friction typed contact between two surfaces while a space is sandwiched in between. The output electrification is dependent on the duration of contact as well as the type of material and its characteristics, contact area and cyclic contact. There are studies in which the detailed information are provided with the advancements in the domain of Triboelectric charging [34, 35].

Electroactive polymers are more in use in the industry of sensors, transducers and actuators while the main characteristics of these materials are that they are deformed considerably in response to applying an external load. There are two main types of electroactive polymers being dielectric and Ionic. While electroactive polymers have remarkably shown energy densities approximated at 550 mJ/g, they have been based on films with widths of some micrometers and therefore, a generator covering a large area would be required to provide useful power [36]. Some advances in this approach have been documented in the literature for different applications with the aim of energy harvesting [37, 38]. The large strain capability has been reported as an advantage of this approach while the need to external voltage is of drawbacks [22].

#### 4.2.3 *Brake Energy Harvesting*

An important source for energy harvesting can be the vehicle parts such as suspension system, tires, braking system, engine vibrations, etc., the objective use of which can be to power the microelectronic devices, sensors, actuators, wireless systems and also optimization of fuel consumption. Braking energy harvesting in this regard can be mentioned as a source in braking pad contact and contactless ways. Han et al. [39] presented an approach for energy harvesting from a rotating disc structure during both braking and non-braking processes with application to vehicles and trains by the hybridized use of triboelectrication and electrostatic-induction. Waste heat recovery in brake pad using a Thermoelectric generator was experimentally covered since as documented in the literature, a heavy vehicle wastes from 400 to 3000 [kW] mostly converted into heat during breaking [40]. One of the challenging issues in this regard is however, to find an optimal sized system to be aligned with the braking system. Thermoelectric generator (TEG) has been a good choice of solution to the problem while Triboelectric

Nanogenerator (TENG) has shown good applicability for harvesting energy [41, 42]. It is clear-cut that a major portion of energy is wasted during the braking process through heat while the amount of the energy dissipated is pivotal on the forward velocity and the vehicle mass. There are some different types of energy harvesting/recovery systems from the braking process such as the regenerative braking system commonly being adopted by hybrid cars. A regenerative brake is a type of energy harvesting that slows down a vehicle and converts the kinetic energy to the electric energy utilizing an electric motor and in some vehicles the energy is stored in chemical form in the battery. Another recognized approach is also flywheel part in which the flywheel energy storage runs by accelerating a rotor to a very high speed and maintaining the energy as rotational energy while a large maximum output power can be obtained in this approach [40]. The greatest problem of these systems is their bulky size and weight. Thermoelectric generators, so called, Seebeck generators that convert the temperature gradient to electrical energy is the most commonly approach to use the wasted heat in the breaking pad to the electric energy.

A TEG is formed up from semiconductor materials that create thermocouples which are electrically connected. The thermocouples are in the middle of two ceramic material surfaces. When a temperature gradient is applied, the device then generates electricity [43]. There are the drawbacks of high output resistance and adverse thermal characteristics because thermal conductivity is needed for a reliable thermoelectric generator, however, this can drastically reduce the heat loss of the device. Instead, thermoelectric generator is cheap, small, and reliable, with no moving parts or fluid and no add extra weight [44].

Magneto-rheological based brake-by-wire system with self-energizing and braking energy harvesting was also assessed in a research work given that the brake-by-wire system is a compact and efficient brake system using electromechanical actuators instead of conventional hydraulic actuators [45]. This system is a regenerative brake based approach in which a typical single-disk-type MR brake with a wedge mechanism for self-energizing purpose, and a generator is employed to conduct regenerative braking and harvest brake energy.

To conclude, based on heat behavior and the energy recovery in different brake pads the application of TEG to recover the dissipated heat energy is the most commonly used brake energy harvesting system although it is not flexible to light vehicles, however, some modifications can make them applicable to be used in heavy and midsized vehicles. The improved version of this system by adoption of nanoparticles can be the Triboelectric Nanogenerator (TENG) which has demonstrated a promising usage for brake system energy harvesting.

### 4.3 Energy Dissipaters Due to Vehicle Dynamics

Vehicle energy dissipaters due to vehicle dynamics can be divided into different categories such as the kinetics of motion such as rolling resistance which was discussed in details in Chap. 3. However, there could be some other sources such as

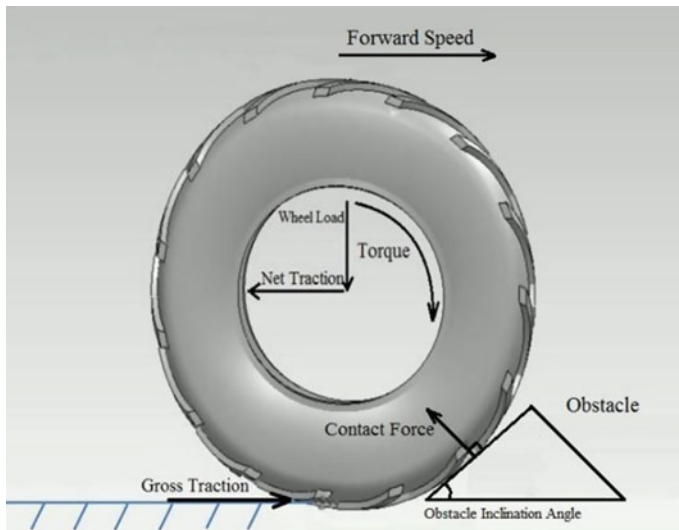


**Fig. 4.15** Free body diagram of wheel-obstacle collision for determination of wheel-obstacle collision based dissipated energy

tractor drawbar pull force in the case of off-road vehicles. Drawbar pull is a function of forward speed, and generally there is a decrement in drawbar pull when the speed of the vehicle increases (owing to both increment of resistance and decrement of power driveline gear ratios). Drawbar pull is the difference between tractive effort available and tractive effort required to overcome resistance at a specified speed while the resistance could source from road irregularities, obstacles and motion on slopes. In another term, drawbar pull is the value of horizontal force available to a vehicle at the drawbar for accelerating or trailing a vehicle.

Drawbar pull data for a vehicle is usually determined by measuring the amount of available tractive force using a dynamometer, and then combining that data with coast down data to obtain the available drawbar pull force at each speed. Probably the most common example of drawbar pull is displayed on rails wherein a locomotive pulling a long train of freight cars is demonstrating drawbar pull.

To find the drawbar pull of a vehicle, it is required to multiply the torque of the vehicle's motor by the gear reduction (including the axle and transmission). The resulted value should be divide by the radius of the drive tire. In other words, it's the gross pulling force the vehicle is capable of. To determine the actual (or net) drawbar pull, it is required to distinguish the rolling resistance of the vehicle. Drawbar pull is the tractive effort minus the rolling resistance. In this manner, drawbar pull discussed in Chap. 3 is another main source of energy dissipation due to vehicle dynamics. Another form of energy dissipation is when a wheeled vehicle collides an obstacle.



**Fig. 4.16** **a** General description of the obstacles used, **b** wheel tester traversing over differently shaped obstacles

In the case that the vertical and longitudinal induced forces at wheel-obstacle collision are measured (Fig. 4.15), the wasted power can be calculated as following:

$$PO = \frac{F \times dx}{dt} = F \times V \quad (4.18)$$

where PO is power (W), F is force (N) with vertical and longitudinal components, and V is forward speed (m/s). Hence, the dissipated energy is computed:

$$E = \int P dt \quad (4.19)$$

By substituting Eqs. 4.18 and 4.19;

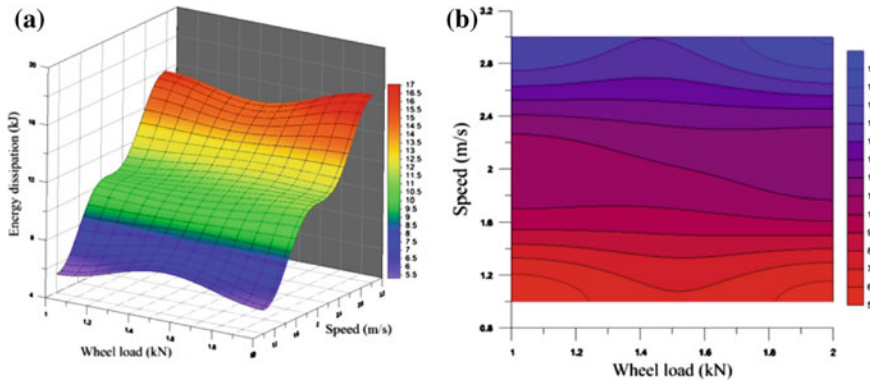


**Fig. 4.17** **a** Three dimensional demonstration of energy dissipation with respect to speed and wheel load and **b** the contour plot of energy dissipation with respect to speed and wheel load

$$E = \int FVdt \quad (4.20)$$

However, velocity should be presented as a vector in both vertical and longitudinal directions:

$$\vec{V} = \dot{x}i + \dot{y}j \quad (4.21)$$

The path of wheel is affected by the obstacle geometry as following:

$$y = \sin \frac{2\pi}{l} x \quad 0 < x < 2\pi \quad (4.22)$$

For the triangular shaped obstacle, the following equation is described:

$$y = \begin{cases} ax & x < \frac{l}{2} \\ -ax & x > \frac{l}{2} \end{cases} \quad (4.23)$$

where  $l$  is the obstacle length and  $a$  is the slope of the obstacles with the desired heights. In addition to the shape of the obstacles and geometries (Fig. 4.16), energy dissipation due to vehicle-obstacle contact can depend on many factors such as the speed at which the vehicle and the wheels collide, tire slippage, wheel load, tire inflation pressure, etc.

Taghavifar et al. [46] developed a multiple regressed technique to be applicably used for prediction of energy loss as a function of input variables as following.

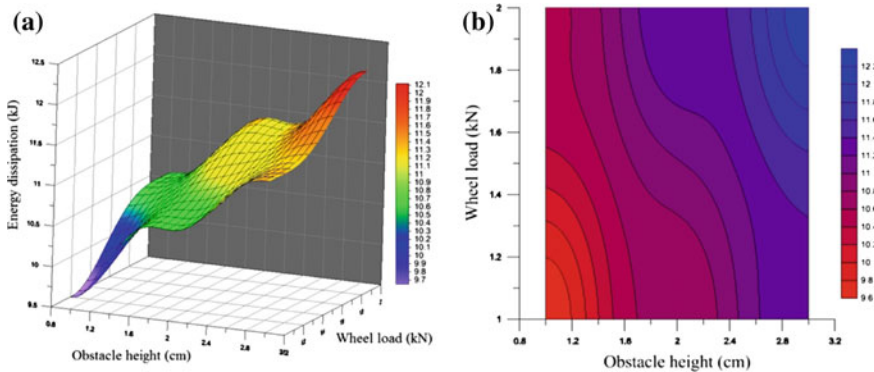


**Fig. 4.18** **a** Three dimensional demonstration of energy dissipation with respect to obstacle height and wheel load and **b** the contour plot of energy dissipation with respect to obstacle height and wheel load

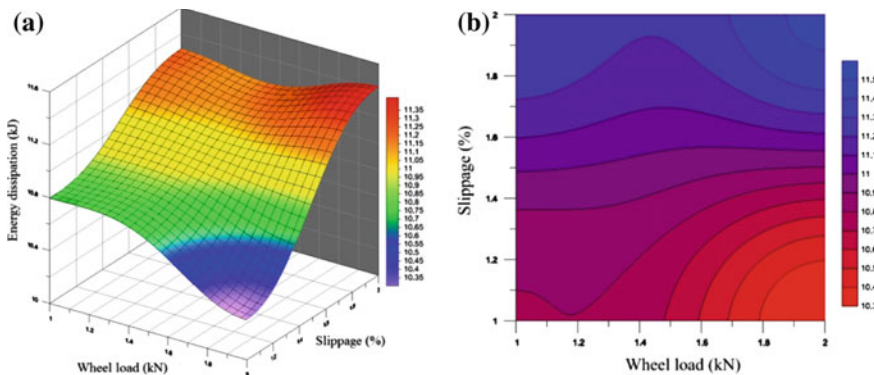


**Fig. 4.19** **a** Three dimensional demonstration of energy dissipation with respect to slippage and wheel load and **b** the contour plot of energy dissipation with respect to slippage and wheel load

$$E = -0.23943 + (4.80147 \times V) + (0.02701 \times HW) + (0.09068 \times H^2V) \\ + (0.12042 \times VHSW)$$

where E is energy dissipation (kJ), W is wheel load (kN), S is tire slippage (%), V is speed (m/s), and H is obstacle height (cm).

In this regard, the results and variations of energy dissipation due to wheel-obstacle collision as a function of wheel load, slippage, forward speed and obstacle height are presented through Figs. 4.17, 4.18 and 4.19.

It can be seen that the energy dissipation increases by the increment of wheel load, forward speed, slippage and obstacle height since there is a need for the

vehicle to keep up its constant motion on ground and to overcome any interruption such as increased obstacle height, there is a need for the vehicle to acquire greater energy. This implies that due to the introduced parameters, there is a greater portion of energy loss.

## References

1. Taghavifar, H., & Mardani, A. (2014). Analyses of energy dissipation of run-off-road wheeled vehicles utilizing controlled soil bin facility environment. *Energy*, 66, 973–980.
2. Tiwari, G. S., & Pandey, K. P. (2008). Performance prediction of animal drawn vehicle tyres in sand. *Journal of Terramechanics*, 45(6), 193–200.
3. Pandey, K. P., & Tiwari, G. (2006). Rolling resistance of automobile discarded tyres for use in camel carts in sand. In *ASABE Annual International Meeting*. St. Joseph-Mich: ASABE. ASABE Paper No. 061097.
4. Wong, J. Y. (1984). On the study of wheel-soil interaction. *Journal of Terramechanics*, 21(2), 117–131.
5. Kurjenluoma, J., Alakukku, L., & Ahokas, J. (2007). Rolling resistance and rut formation by implement tyres on tilled clay soil. *Journal of Terramechanics*, 46(6), 267–275.
6. Taghavifar, H., Mardani, A., & Taghavifar, L. (2013). A hybridized artificial neural network and imperialist competitive algorithm optimization approach for prediction of soil compaction in soil bin facility. *Measurement*, 46(8), 2288–2299.
7. Shmulevich, I., & Osetinsky, A. (2003). Traction performance of a pushed/pulled drive wheel. *Journal of Terramechanics*, 40, 33–50.
8. Battiatto, A., & Diserens, E. (2013). Influence of tyre inflation pressure and wheel load on the traction performance of a 65 kW MFWD tractor on a cohesive soil. *Journal of Agricultural Science*, 5(8), 197–215.
9. Elwaleed, A. K., Yahya, A., Zohadie, M., Ahmad, D., & Kheiralla, A. F. (2006). Net traction ratio prediction for high-lug agricultural tyre. *Journal of Terramechanics*, 43, 119–139.
10. Zuo, L., & Zhang, P. S. (2013). Energy harvesting, ride comfort, and road handling of regenerative vehicle suspensions. *Journal of Vibration and Acoustics*, 135(1), 011002.
11. Khoshnoud, F., Sundar, D. B., Badi, M. N. M., Chen, Y. K., Calay, R. K., & De Silva, C. W. (2013). Energy harvesting from suspension systems using regenerative force actuators. *International Journal of Vehicle Noise and Vibration*, 9(3–4), 294–311.
12. Xie, X. D., & Wang, Q. (2015). Energy harvesting from a vehicle suspension system. *Energy*, 86, 385–392.
13. Bowen, C. R., & Arafa, M. H. (2015). Energy harvesting technologies for tire pressure monitoring systems. *Advanced Energy Materials*, 5(7).
14. Worthington, E. (2010). Piezoelectric energy harvesting: Enhancing power output by device optimisation and circuit techniques.
15. Bouendeu, E., Greiner, A., Smith, P. J., & Korvink, J. G. (2011). A low-cost electromagnetic generator for vibration energy harvesting. *IEEE Sensors Journal*, 11, 107–113.
16. Shen, D., Park, J. H., Ajitsaria, J., Choe, S. Y., Wikle, H. C., I. I. I., & Kim, D. J. (2008). The design, fabrication and evaluation of a MEMS PZT cantilever with an integrated Si proof mass for vibration energy harvesting. *Journal of Micromechanics and Microengineering*, 18(5), 055017.
17. Erturk, A., & Inman, D. J. (2009). An experimentally validated bimorph cantilever model for piezoelectric energy harvesting from base excitations. *Smart Materials and Structures*, 18(2), 025009.
18. Saha, C. R., O'Donnell, T., Loder, H., Beeby, S., & Tudor, J. (2006). Optimization of an electromagnetic energy harvesting device. *IEEE Transactions on Magnetics*, 42, 3509.

19. Glynne-Jones, P., Tudor, M. J., Beeby, S. P., & White, N. M. (2003). An electro-magnetic, vibration-powered generator for intelligent sensor systems. *Sensors and Actuators*, 1–3, 344–349.
20. Roundy, S., Wright, P. K., & Rabaey, J. M. (2004). *Energy scavenging for wireless sensor networks*. New York: Kluwer Academic Press.
21. Kubba, A. E., & Jiang, K. (2014). A comprehensive study on technologies of tyre monitoring systems and possible energy solutions. *Sensors*, 14(6), 10306–10345.
22. Wang, L., & Yuan, F. (2008). Vibration energy harvesting by magnetostrictive material. *Smart Materials and Structures*, 17, 045009.
23. Worthington, E. L. (2010). *Piezoelectric energy harvesting: Enhancing power output by device optimisation and circuit techniques, in school of applied sciences microsystems and nanotechnology centre*. Ph. D. thesis, Cranfield University: Cranfield, UK, 30 August 2010.
24. Stephen, B., & White, N. (2010). Chapter 4 kinetic energy harvesting. In *Energy harvesting for autonomous systems* (pp. 90–131). Norwood, MA, USA: Artech House.
25. Boisseau, S., Despesse, G., & Seddik, B. A. (2012). *Electrostatic conversion for vibration energy harvesting*. arXiv preprint [arXiv:1210.5191](https://arxiv.org/abs/1210.5191).
26. Kroener, M. (2012). Energy harvesting technologies: Energy sources, generators and management for wireless autonomous applications. In *9th International Multi-Conference on Systems, Signals and Devices, Chemnitz, Germany*, 20–23 March 2012.
27. Manoli, Y. (2010). Energy harvesting—from devices to systems. In *Proceedings of the ESSCIRC, Seville, Spain*, 14–16 September 2010.
28. Gautschi, G. (2002). *Piezoelectric sensorics: Force, strain, pressure, acceleration and acoustic emission sensors, materials and amplifiers*. Berlin: Springer.
29. Wu, L., Wang, Y., Jia, C., & Zhang, C. (2009). Battery-less piezoceramics mode energy harvesting for automobile TPMS. In *ASICON '09, Changsha*.
30. Chen, Y., & Pan, H. (2011). A piezoelectric vibration energy harvester for tire pressure monitoring systems. In *Proceedings of Symposium on Ultrasonic Electronics*.
31. Mak, K. H., McWilliam, S., & Popov, A. A. (2013). Piezoelectric energy harvesting for tyre pressure measurement applications. *Proceedings of the Institution of Mechanical Engineers, Part D*, 227, 842–852.
32. Gao, Z., Sham, M., & Chung, C. H. (2011). *Piezoelectric module for energy harvesting, such as in tire pressure monitoring system*. Patent US8011237B2.
33. Zhang, H. (2011). Power generation transducer from magnetostrictive materials. *Applied Physics Letters*, 98, 232505.
34. Dhakar, L., Liu, H., Tay, F. H., & Lee, C. (2013). A wideband triboelectric energy harvester. *Journal of Physics: Conference Series*, 476, 012128.
35. Guo, X., & Helseth, L. E. (2015). Optical and wetting properties of nanostructured fluorinated ethylene propylene changed by mechanical deformation and its application in triboelectric nanogenerators. *Materials Research Express*, 2(1), 015302.
36. McKay, T. G., Rosset, S., Anderson, I. A., & Shea, H. (2013). An electroactive polymer energy harvester for wireless sensor networks. In *Journal of Physics: Conference Series* (Vol. 476, No. 1, p. 012117). IOP Publishing.
37. Tiwari, R., Kim, K. J., & Kim, S. M. (2008). Ionic polymer-metal composite as energy harvesters. *Smart Structures and Systems*, 4(5), 549–563.
38. Chiba, S., Waki, M., Kornbluh, R., & Peltre, R. (2008). Innovative power generators for energy harvesting using electroactive polymer artificial muscles. In *The 15th International Symposium on: Smart Structures and Materials & Nondestructive Evaluation and Health Monitoring* (pp. 692715–692715). International Society for Optics and Photonics.
39. Han, C. B., Du, W., Zhang, C., Tang, W., Zhang, L., & Wang, Z. L. (2014). Harvesting energy from automobile brake in contact and non-contact mode by conjunction of triboelectrification and electrostatic-induction processes. *Nano Energy*, 6, 59–65.
40. Pedersen, T. H., Schultz, R. H., & Bertelsen, T. B. *Waste Heat Recovery in Brake Pad using a Thermoelectric Generator*.

41. Zhang, X.-S., Han, M.-D., Wang, R.-X., Zhu, F.-Y., Li, Z.-H., Wang, W., & Zhang, H.-X. (2013). *Nano Letters*, 13, 1168–1172.
42. Lin, L., Wang, S., Xie, Y., Jing, Q., Niu, S., Hu, Y., & Wang, Z. L. (2013). *Nano Letters*, 13, 2916–2923.
43. <http://www.tegpower.com/>
44. Rosendahl, L. A., Mortensen, P. V., & Enkeshafi, A. A. (2011). Hybrid solid oxide fuel cell and thermoelectric generator for maximum power output in micro-CHP systems. *Journal of Electronic Materials*, 40(5), 1111–1114.
45. Yu, L., Liu, X., Ma, L., Zuo, L., & Song, J. (2014). MR based brake-by-wire system with self-energizing and brake energy harvesting capability. In *ASME 2014 International Design Engineering Technical Conferences and Computers and Information in Engineering Conference* (pp. V008T11A099–V008T11A099). American Society of Mechanical Engineers.
46. Taghavifar, H., Mardani, A., & Hosseinloo, A. H. (2015). Experimental analysis of the dissipated energy through tire-obstacle collision dynamics. *Energy*, 91, 573–578.

# **Chapter 5**

## **Application of Artificial Intelligence on Modeling and Optimization**

Modeling and optimization are two dynamic fields of studying interest for engineers and researchers in a variety of disciplines from science to engineering. Modeling is a process in which a process or phenomenon is predicted with adoption of the trend or a code of response from the system that is under investigation. When data on the problem are available, it is possible to extract a model (mathematical, statistical, numerical, etc.) based on which the prediction in a similar condition or a defined situation is predictable. In order to model a system, it is necessary to first distinguish the system parameters and system boundaries and then set a relationship between the parameters as the input of the system and the parameter(s) that perform as the output of the system. A model may help to explain a system and to study the effects of different components, and to make predictions about behaviour. For an instance, a mathematical model is a description of a system using mathematical concepts and theories. Mathematical models different forms such as, but not limited to dynamical systems, statistical models, differential equations, and geometric models which may have significant overlapping between the methodologies and approaches however all of which may have the logical approach in common. In some conditions, the quality of a scientific domain relies on the appropriateness of the mathematical models developed on the theoretical side are in accordance with the results of empirically obtained data if repeated. In the case that the agreement between mathematical models and experimental quantifications are not satisfied, it may lay the foundation for development of some other approaches such as artificial intelligence.

On the other side, optimization is adoption of a best element or solution to the problem (based on some predefined criteria) from the total of possible solution. Optimization has great application in mathematics, computer-based solutions and artificial intelligence domains.

Optimization problems usually include maximizing or minimizing a defined function by adoption of inputs in a pre-defined constraint that is valid for the

function. Mathematics is a great applied domain for the generalization of optimization concepts and techniques. As aforesaid, optimization includes finding best available values of some objective functions by introducing some definite constraints.

Artificial intelligence (AI) is the intelligence provided by computers and human-developed software to computational techniques and is related to the science of generation of intelligent systems and techniques that are capable of monitoring a system, controlling, classifying or modeling it. The major aim of artificial intelligence is reasoning, knowledging, learning and perception and system processing as well as enabling a system with the capacity to be self-controlled.

Very close in implication to AI, computational intelligence deals with the capacity of the system to learn a specific pattern from data or experimental observation and extend it for a later application such as modeling and optimization. Computational intelligence is an arrangement of ways and techniques that are inspired by nature to overcome some complex and nonlinear real-world problems in which classical and mathematical, numerical and statistical approaches may fail to be successfully applied mainly due to the complexity of the system for the mathematical approach to do reasoning, there might be some uncertainties and that the system might be of highly stochastic and nonlinear to be modeled.

## 5.1 Introduction to Artificial Intelligence Tools

A novel application of artificial intelligence in Terramechanics is adoption of image processing technique for the estimation of tire-ground contact area. Computer based systems include a digital camera to capture the image of the object and specific developed software to analyze the images. This phase of experiment consisted of a digital camera (Panasonic LUMIX DMC-TZ25), a glass plane to place the camera on it, and MATLAB software for image analysis. The images should be taken from constant distance on a glass plane attached to the carriage while traversing. Taken images can be imported to “Adobe Photoshop CS4” software (Adobe System Inc.) and should be converted to background colors. In order to perform image processing, an algorithm should be written with MATLAB software.

In this example, the taken images were taken at RGB space. Utilizing s component in HSV space as well as b in Lab space, an excellent separation of tire track and the image background was obtained. Pixel intensities of both components were normalized at the range of 0–1. The components were then added and the result was again normalized at the same range.

$$X_1 = (s + b) \quad (5.1)$$

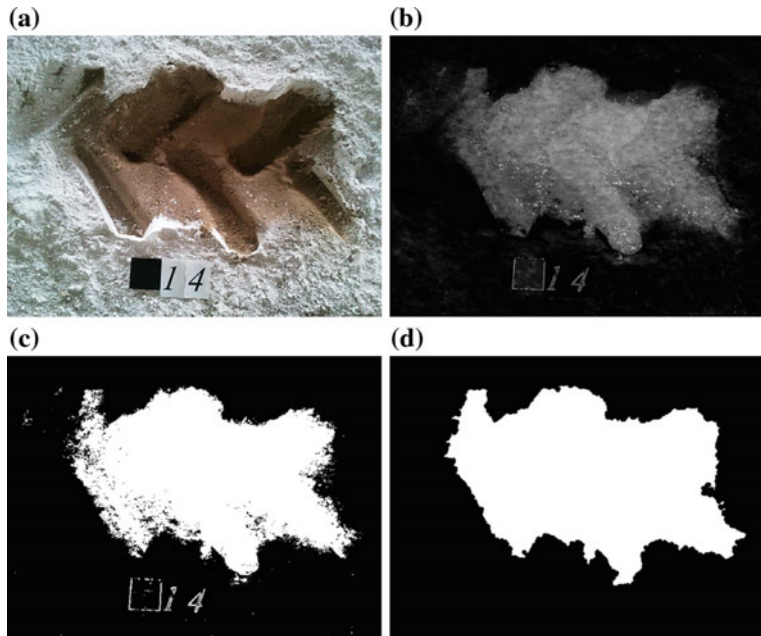


**Fig. 5.1** A sample of contact area image (a), converted image to gray scale image (b), (c) enhancing the separation of image background and tire track (d) and thresholding process to obtain the final analyzed image

To achieve more enhanced separation of image background and tire track, Gamma Transform was used as follows:

$$X_2 = (X_1)^{\alpha} \quad (5.2)$$

where the optimal value of  $\alpha$  was obtained to be 2. To separate tire track and background, a threshold level was required which Otsu method was utilized to gain optimum level. Binary image was obtained using the resulted image of dilation and thresholding processes. Figure 5.1 demonstrates a sample of contact area image and its processed images. Objects were extracted from binary images and their qualifications such as pixel area (number of pixels in the object region) and calibrated area (number of pixels in the object region  $\times$  ratio of actual to predicted values) were measured in  $\text{cm}^2$ . An index with predefined dimensions was used in each image to calibrate the determinations.

## 5.2 Modeling with Artificial Neural Networks, Support Vector Machines, and Adaptive Neuro-Fuzzy Inference System

### 5.2.1 Artificial Neural Networks

Artificial neural networks (ANN) are extensively in use to tackle solving complicated problems in variety of science and engineering fields mainly wherever conventional and mathematical models fail to accomplish. They can learn examples from incomplete data, dealing with non-linear problems, and once trained can carry out predictions and generalizations with high performances. ANNs are suitable tools for fitting a function, data clustering and distinguishing the model samples. As well, they have been used in diverse applications in control, robotics, pattern recognition, forecasting, medicine, power systems, manufacturing, optimization, signal processing. ANNs have successfully been applied in the fields of pattern, recognition, modeling, and control [1]. ANN models and their estimating ability are relying on training experimental data followed by validating and testing the model by independent data. Holding multiple input variables, while it has the ability to improve its performance with new series of data, multiple output variables can be efficiently predicted and modeled. Conventional models, as well as mathematical ones, are usually incapable of predicting complex nonlinear phenomena with no simplifying the models by neglecting interactions between parameters that bring about rising inaccuracy. Appropriate ANN topology is significant to attain simple models with lower mean squared error (MSE), root mean squared error (RMSE) scattering around the line (1:1), high coefficient of determination ( $R^2$ ), and reliable performance during training, validation and test partitions. Each input to the artificial neural network is multiplied by the synaptic weight, added together and dealt with an activation function while ANNs are trained by frequently exploring the best relationship between the input and output values creating a model after a sufficient number of learning repetitions, or training known as epochs [2]. It is known that, the computational models using ANN of the type Multilayers Perceptron (MLP) are dependent on the network structure (topology, connections, neurons number) and their operational parameters (learning rate, momentum, etc.). The form in which the network architecture is defined affects significantly its performance that can be classified in learning speed, generalization capacity, fault tolerance and accuracy in the learning.

### 5.2.2 Adaptive-Neuro Fuzzy Inference System (ANFIS)

Soft computing based approaches serve as inexact solutions to computationally hard tasks with great applicability in the science and engineering domains. Adaptive neuro-fuzzy inference system (ANFIS) is a neural network based fuzzy

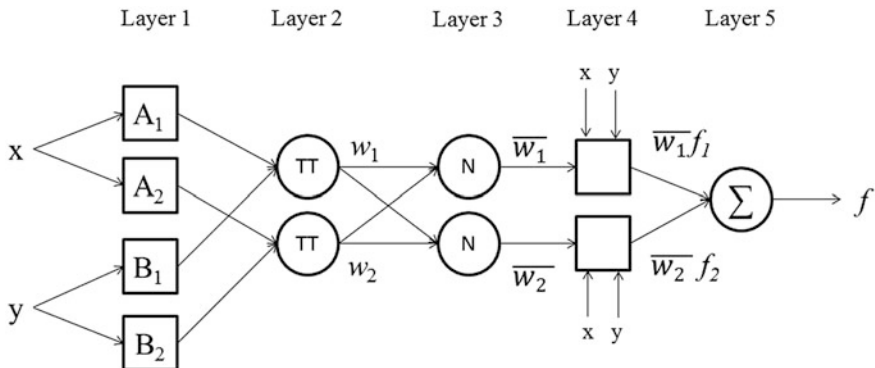


**Fig. 5.2** A schematic Takagi-Sugeno fuzzy system architecture

logic system as a global approximator that takes the advantages of the both modeling approaches. Artificial neural network is used to determine the fuzzy inference system parameters. ANFIS being first introduced by Jang et al. [3, 4] constructs a set of fuzzy IF-THEN rules with adoption of appropriate membership functions of fuzzy set system to provide input-output mapping. One of the typical fuzzy inference system types is Sugeno [5] that was adopted in the present work to synthesize the amount of dissipated energy by the vehicles trafficking over rough and irregular terrains. The basic structure of FIS consists of three conceptual components; (i) the first one is a rule base, which contains a selection of fuzzy rules, (ii) a database, which defines the membership functions used in the fuzzy rules, and (iii) is a reasoning mechanism, which performs the inference procedure upon the rules and the given facts to derive a reasonable output or conclusion [6].

With the capability to combine the numeric power of a neural system with the verbal power of a fuzzy system, ANFIS has been found to be promising in modeling problems. The model works on a set of linguistic rules developed using expert knowledge. The fuzzy rule base of the ANFIS model is set up by combining all categories of variables. A typical ANFIS structure, which can be seen in Fig. 5.2, includes 6 layers. The first layer contains membership functions (MFs). The most common MF involves triangular and bell-shaped functions.

A typical rule set with two fuzzy IF-THEN rules for the first-order Sugeno fuzzy model is the following:

- Rule 1: IF  $x = A_1$  and  $y = B_1$  THEN  $f = p_1 x + q_1 y + r_1$
- Rule 2: IF  $x = A_2$  and  $y = B_2$  THEN  $f = p_2 x + q_2 y + r_2$ .

Including input layer into considerations, ANFIS structure includes six layers. The authors, to avoid paper overextension, describe the procedure briefly.

- First layer is the input layer which has  $n$  nodes where  $n$  is the representative of the system inputs number.

- Second layer is the fuzzification in which each node represents a membership function. The node function of a node  $i$  can be expressed by:

$$\begin{aligned} O_i^1 &= \mu_{A_i}(x), \quad i = 1, 2 \\ O_i^1 &= \mu_{B_{i=2}}(y), \quad i = 3, 4 \end{aligned} \quad (5.3)$$

- Third layer provides the strength of the rule by means of multiplication operator in each node.

$$O_i^2 = \mu_{A_i}(x)\mu_{B_i}(y), \quad i = 1, 2 \quad (5.4)$$

- Fourth layer is the normalization layer which normalizes the firing strength of the rules according to the following equation:

$$\bar{z}_i = \frac{z_i}{z_1 + z_2}, \quad i = 1, 2 \quad (5.5)$$

- Fifth layer consists adaptive nodes each of which computes a linear function whose coefficients referred to as consequent parameters are adapted by using the error function of the feed-forward neural network [7].

$$\bar{z}_i f_i = \bar{z}_i(p_i x + q_i y + r_i) \quad (5.6)$$

- Sixth layer has a single node which is fixed the summation of the inputs of the nodes in fifth layer. The output  $f$  is computed as follows:

$$f = \bar{z}_1 f_1 + \bar{z}_2 f_2 = \frac{\bar{z}_1 f_1 + \bar{z}_2 f_2}{\bar{z}_1 + \bar{z}_2} \quad (5.7)$$

ANFIS relates the gradient descent methodology to describe the optimal conditions for tuning the membership functions to map input variables to output variables. The main ideology of ANFIS is based on the back-propagation gradient descent methodology that quantifies error signals repetitively from the output layer backward to the input nodes. However, we used a hybrid method of the gradient descent and the least-squares method to find optimal learning parameters.

Data can be split and shuffled with different configurations for 50 training and testing process to avoid the over-fitting drawback. Various membership functions of 1: Built-in membership function composed of difference between two sigmoidal membership functions (dsigmf), 2: Generalized bell-shaped built-in membership function (gbellmf), 3:  $\Pi$ -shaped built-in membership function (pimf), 4: triangular-shaped built-in membership function (trimf), 5: Trapezoidal-shaped built-in membership function (tramf), 6: Gaussian curve built-in membership function (gaussmf), and 7: Sigmoidally shaped built-in membership function (sigmf) can be adopted in the modeling implementations (Fig. 5.3).

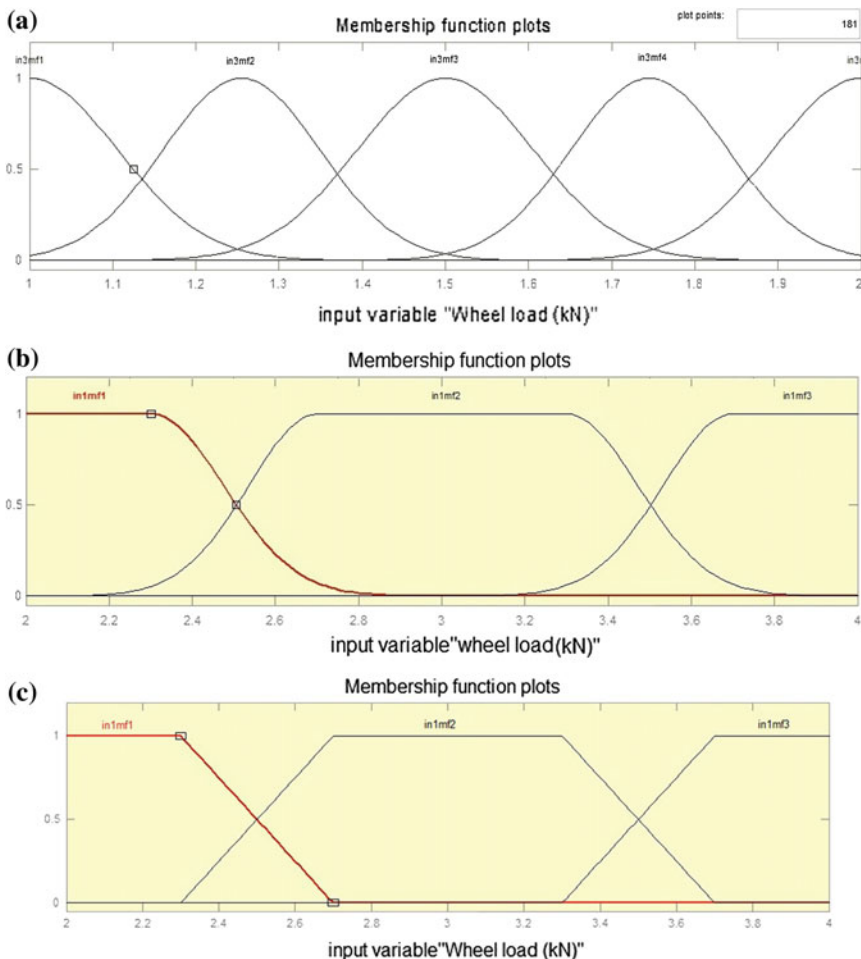


**Fig. 5.3** Different shapes of wheel load in fuzzy theory from **a** Gaussian curve built-in membership function, **b** Generalized bell-shaped built-in membership function and **c** Trapezoidal-shaped built-in membership function

In modeling disciplines, it is absolutely essential to assess the performance of developed models by various statistical criterions. The root mean square error ( $RMSE$ ) and the coefficient of determination ( $R^2$ ) are introduced for analysis of model quality as described below, respectively.

$$RMSE = \sqrt{\frac{1}{n} \sum_{i=1}^n (Y_{predicted} - Y_{actual})^2} \quad (5.8)$$

$$R^2 = \frac{\sum_{i=1}^n (Y_{predicted} - Y_{mean})^2}{\sum_{i=1}^n (Y_{actual} - Y_{mean})^2} \quad (5.9)$$

where  $Y_{actual}$  and  $Y_{predicted}$  are measured and predicted values of the developed models, respectively.

### 5.2.3 Support Vector Regression

A support vector machine (SVM) is a classifier first presented by Vapnik [8] based on statistical learning theory. The SVMs can be adopted both for classification and regression problems. Support vector regression (SVR) is used to define regression with SVMs in the literature. In the case of regression, it is aimed at building a hyper-plane that lies “close” to as many of the data points as possible. Therefore, the objective is to pick a hyper-plane with small norm while concurrently decreasing the sum of the distances from the data points to the hyper-plane. As illustrated in Fig. 5.4, the  $\epsilon$ -insensitive loss function can be pictured as a tube equal to the approximation accuracy that surrounds the training data [9]. The regression estimation with SVR is to estimate a function according to a data set  $\{(x_i, y_i)\}_n$  wherein  $x_i$ ,  $y_i$  and  $n$  are input, output and number of data points, respectively. The regression functions are divided into linear and nonlinear functions.

#### 3.1. Linear

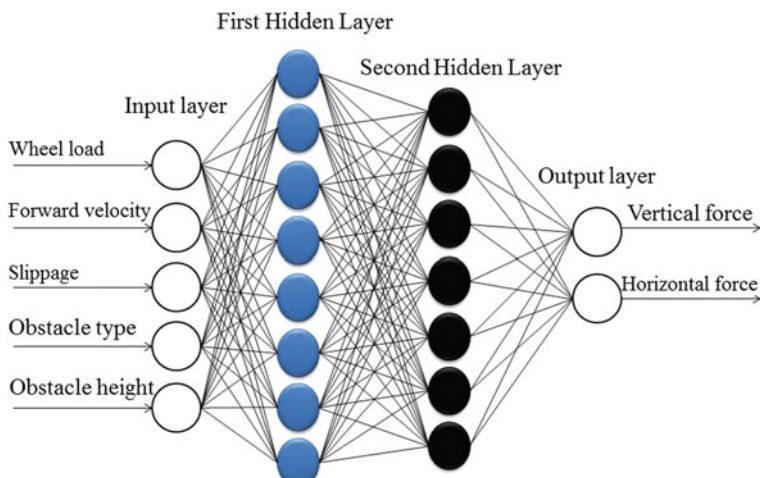


**Fig. 5.4** The schematic configuration of the developed ANN with two hidden layers

In this case the regression model can be expressed by Vapnik [10]:

$$f(x) = \langle w, x \rangle + b \quad (5.10)$$

where  $f(x)$  is an unknown target function,  $\langle \cdot, \cdot \rangle$  denotes the dot product in  $X$  and  $w$  is the weight vector. The most common loss function is the  $\varepsilon$ -insensitive loss function proposed by Vapnik (2000) [10] and is defined by the following function:

$$L_\varepsilon(y) = \begin{cases} 0, & \text{for } |f(x) - y| \leq \varepsilon \\ |f(x) - y| - \varepsilon, & \text{otherwise} \end{cases} \quad (5.11)$$

As a convex optimization problem, it can be written as:

$$\underset{w}{\text{minimize}} \frac{1}{2} \|w\|^2 + C \sum_{i=1}^l (\xi_i + \xi_i^*) \quad (5.12)$$

$$\text{Subject to} \begin{cases} y_i - \langle w, x_i \rangle - b \leq \varepsilon + \xi_i \\ \langle w, x_i \rangle + b - y_i \leq \varepsilon + \xi_i^* \\ \xi_i, \xi_i^* \geq 0 \end{cases} \quad (5.13)$$

where  $\xi_i$  and  $\xi_i^*$  variables are to satisfy the function constraints. The corresponding dual optimization problem is defined as [11]:

$$\underset{\alpha, \alpha^*}{\max} -\frac{1}{2} \sum_{i=1}^l \sum_{j=1}^l (\alpha_i^* - \alpha_i)(\alpha_j^* - \alpha_j) \langle x_i, x_j \rangle - \sum_{i=1}^l y_i(\alpha_i^* - \alpha_i) - \varepsilon \sum_{i=1}^l (\alpha_i^* + \alpha_i) \quad (5.14)$$

With constraints:

$$\begin{aligned} 0 \leq a_i, a_i^* \leq C, \quad i = 1, \dots, l \\ \sum_{i=1}^l (\alpha_i - \alpha_i^*) = 0 \end{aligned} \quad (5.15)$$

where  $\alpha$  and  $\alpha^*$  are Lagrange variables while  $w$  and  $b$  are denoted by the following equation and  $x_r$  and  $x_s$  are support vectors [10].

$$\begin{aligned} w &= \sum_{i=1}^l (\alpha_i^* - \alpha_i)x_i \\ b &= -\frac{1}{2} \langle w, (x_r + x_s) \rangle \end{aligned} \quad (5.16)$$

### 3.2. Nonlinear SVR

For nonlinear regression problems, a nonlinear mapping  $\phi$  of the input space onto a higher dimension feature space can be used, and then linear regression can be performed in this space [12]. The nonlinear model is written as

$$f(x) = \langle w, \phi(x) \rangle + b \quad (5.17)$$

where

$$w = \sum_{i=1}^l (\alpha_i - \alpha_i^*) \phi(x_i) \quad (5.18)$$

$$\langle w, \phi(x) \rangle = \sum_{i=1}^l (\alpha_i - \alpha_i^*) \langle \phi(x_i), \phi(x) \rangle = \sum_{i=1}^l (\alpha_i - \alpha_i^*) K(x_i, x) \quad (5.19)$$

$$b = -\frac{1}{2} \sum_{i=1}^l (\alpha_i - \alpha_i^*) (K(x_i, x_r) + K(x_i, x_s)) \quad (5.20)$$

where  $x_r$  and  $x_s$  are support vectors.

As an example to assess the applicability of support vector regression and artificial neural network to obtain the effect of different operational condition on longitudinal and horizontal force, the following comparative descriptions in a case study is presented. One ANN structure as shown in Fig. 5.4 is developed with a single hidden layer while a soft margin loss setting for a linear support vector regression is developed (Fig. 5.5).

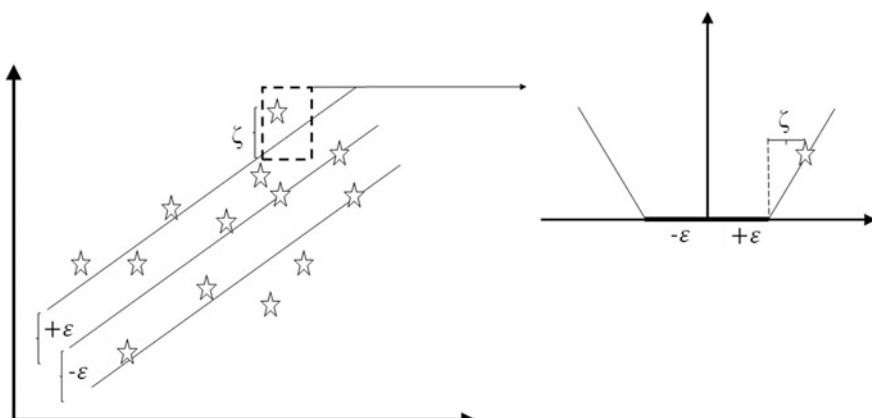


**Fig. 5.5** Soft margin loss setting for a linear SVR

The provision of controlled testing environment is crucially significant for the reliability of the results and the outcomes of the study. Hence, an SWT inside a soil bin facility manufactured in the Department of Mechanical Engineering of Biosystems of Urmia University, Iran, was used to conduct the required experiments. The soil bin channel with the 24 m length, 2 m width and 1 m depth was filled with the soil texture of test region. The holistic system is consisted of soil bin channel, SWT and the carriage. The SWT was connected to the carriage to be enabled to traverse during the soil bin. The carriage was powered with a 22 kW electromotor which was in turn, connected to the inverter to manage the start/stop and velocity control procedures. The power transmission was carried out through the electromotor to the chain system that was linked to the carriage. The carriage was traversing in the channel by means of four ball bearings positioned on the sidewalls of the soil bin. The SWT was connected to the carriage through an L-shaped part and also four horizontal arms each accommodating S-shaped Bongshin load cell with 500 kg capacity. It is worth to note that the horizontal load cells were used to measure the horizontal forces applied to the wheel. A U-shaped frame was used as housing to the tire and a three-phase electromotor of 5 kW to power the driving wheel. An appropriate inverter was also used to control the rotational velocity delivered to the wheel shaft and therefore; the linear velocity was adjustable. It is worth mentioning that the linear speed difference between the carriage and the SWT yielded different levels of adjustable slippage. Furthermore, the SWT was connected to the L-shaped frame by a power bolt rod (to adjust the applied wheel load) which was connected to a vertically situated S-shaped load cell which was responsible to measure the load variations while traversing over the obstacle and irregularities. The load cells were connected to Bongshin digital indicators which were in turn in connection with a data logger with RS232 output signals. The data were subsequently sent to the laptop computer to be stored and processed with the frequency of 30 Hz. The general soil bin facility along with the single-wheel tester is shown in Fig. 5.6.

For all the experiments the tire inflation pressure was maintained at 131 kPa. Two shapes of triangular and Gaussian obstacles were used in the study each at three heights of 2, 3 and 4 cm while two wheel loads of 3 and 4 kN were considered. Three forward velocities for the carriage were planned at three levels of 1.08, 1.8 and 2.52 km/h. In order to remove the soil effect on the experiment outputs due to the soil nonhomogeneous properties, a wooden board with 2 m width and 3 m length was used to mount the obstacles on.

Wheel dynamics is influenced by numerous factors regarding the tire parameters, road irregularities, asymmetric mass rotation, tire mechanical properties (stiffness, elasticity), etc. Although a body of work has already been performed to assess the effect of some aforementioned parameters, there is still a need to undertake drastic investigations to clarify the influence of some important factors such as obstacle geometry, slippage and wheel load on horizontal and vertical forces induced while traversing over obstacles. As appreciated from Fig. 5.7, the effects of wheel load, slippage, obstacle height and forward velocity on the vertical force induced while traversing over the obstacles are observed. The results indicated that the increment

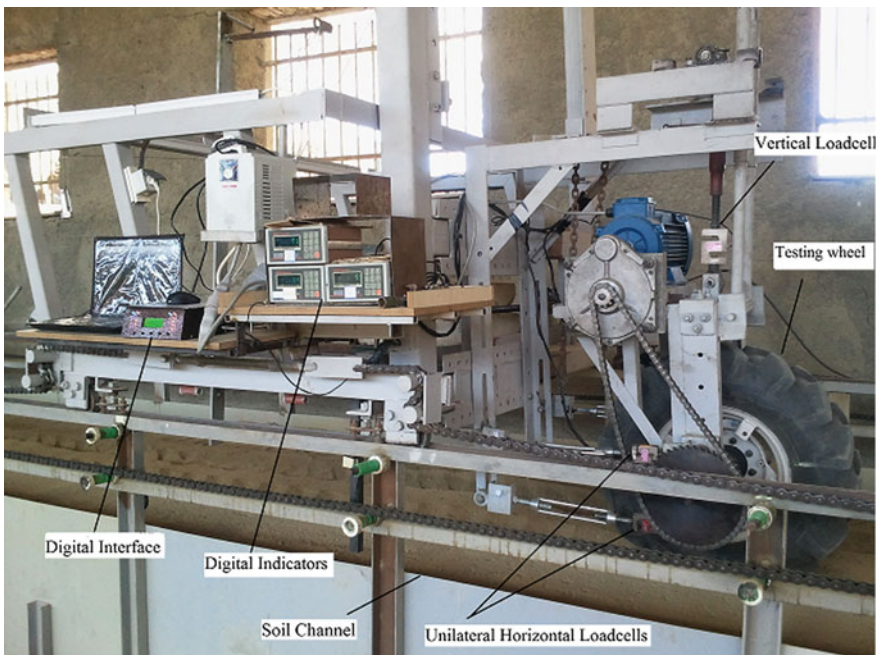


**Fig. 5.6** Soil bin testing facility and the components

of obstacle height and increase of wheel load led to the increase of the vertical force, however; a contradictory trend was observed regarding the increase of slippage. The increased slippage of the wheel resulted in 5.5 % reduction of the vertical force. It also should be noted that no certain pattern was found concerned with the effect of forward velocity on the induced vertical force. The increase of obstacle height resulted in 16.4 % increase of the vertical force while 13.2 % increase of the vertical force could be attributed to the increase of wheel load. On account of the aforesaid results, it could be concluded that the greatest effect among the tested parameters corresponded to that of obstacle height with the greatest share among others (Fig. 5.8). However, there is an interesting point that velocity had a significant trend of influence on the induced horizontal force. It was remarked that increment of velocity led to the increase of the induced horizontal force. The increased obstacle height, increased velocity and increased wheel load yielded 50, 23 and 10.1 % increase of the induced horizontal force, respectively, wherein decreased slippage could reduce the induced horizontal force up to 30 %. It is also noteworthy that when compared Figs. 5.7 and 5.8, it is deducible that wheel load has a greater effect on the vertical induced force rather than that of horizontal force. However, the other tested parameters such as velocity, obstacle height and slippage had a more noticeable influence on the latter. Another remarkable highlight is that during all experiments, the vertical force was greater than the horizontal force while traversing over the obstacles.

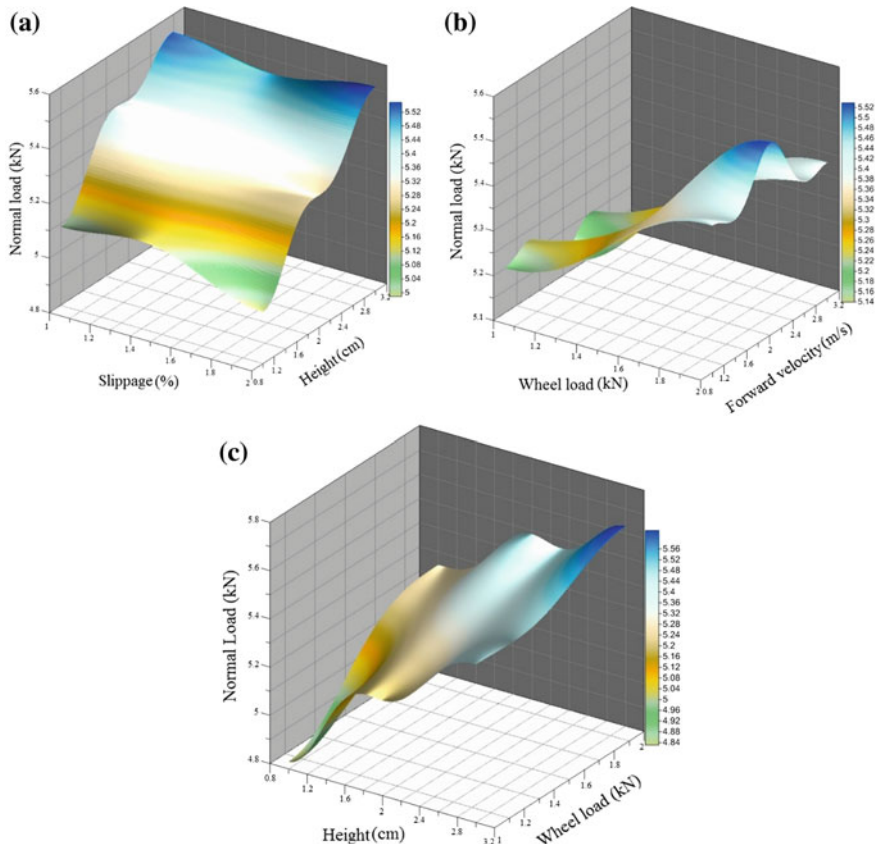


**Fig. 5.7** The 3D diagram of the induced normal load as affected by **a** slippage and height, **b** wheel load and forward velocity and **c** height and wheel load

For the effect of obstacle height, it can be said that due to the change of momentum in the vertical direction, a velocity change in the vertical direction of y (i.e.  $\Delta V_y$ ) is formed which results in the formation of linear impact in the same direction. Hence, an acceleration component in the same vertical direction of y is created owing to the aforesaid velocity change (i.e.  $\Delta V_y$ ) at the increased obstacle height leading to the increased vertically induced inertia forces. This process well describes the increase of vertical force with respect to the increase of obstacle height. Likewise, the increased obstacle height results in the reduction of the instant velocity of wheel at the horizontal direction which in turn, results in a significant change of the linear momentum and therefore greater linear impact in the horizontal direction is obtained.

Regarding the effect of slippage it should be pointed out that due to the relative displacement of wheel versus the obstacle owing to the slippage, the forces corresponding to the shear stresses of tire-obstacle interaction affect the vertical force.

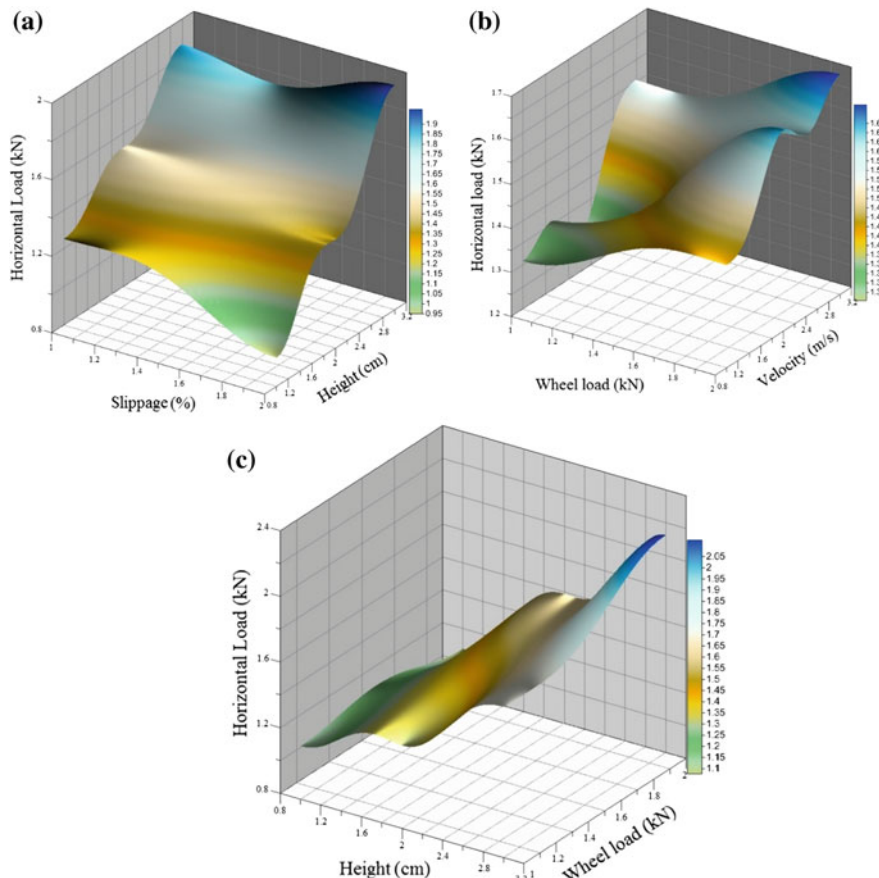


**Fig. 5.8** The 3D diagram of the induced normal load as affected by **a** slippage and height, **b** wheel load and forward velocity and **c** height and wheel load

Given the direction of the interaction forces, the reduction of vertical force during the increment of slippage could be justified. In another term, at the tire-obstacle interface, the relative velocity of the wheel has a component opposite to the obstacle climbing direction of the wheel that reduces a portion of the linear momentum and, therefore, the vertical force undergoes a reducing trend. This pattern of behavior is attributable to that of slippage effect with respect to the induced horizontal force.

Concerned with the effect of wheel load, it is worth to note that while the applied wheel loads (within the form of dead loads) are associated with the vertical inertia forces, the vertical induced force is increased due to the increase of the vertical inertia force as affected by the created acceleration in the vertical as previously discussed. Concerning the induced horizontal force, the greater wheel load increases the greater reaction force at the tire-obstacle contact which obviously increases the horizontally induced force as a result.

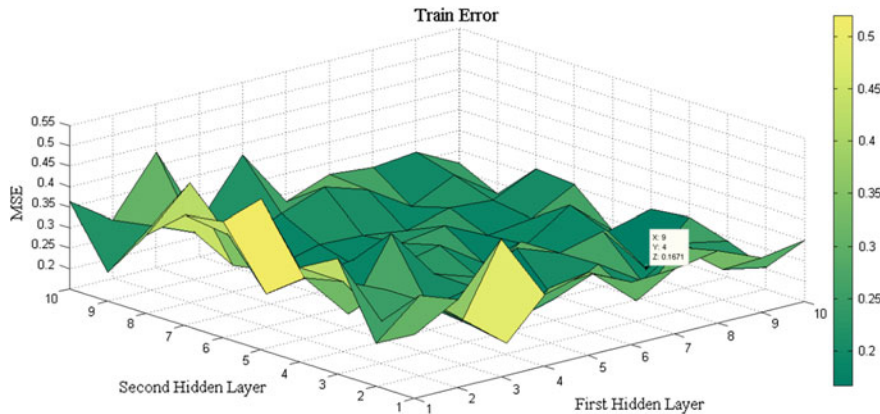


**Fig. 5.9** MSE variations with respect to the neurons in the two hidden layers with the best topology structure

Following the experimental investigation of the vertical and horizontal forces obtained in the controlled soil bin facility using a single-wheel tester, it was aimed at developing a competent model for inclusion of the tester parameters. To this end, the potential of two soft computing approaches was appraised. Given that the Levenberg-Marquardt training algorithm was adopted in the study, the effect of neurons in the two hidden layers was patterned. Figure 5.9 demonstrates that a feed-forward ANN with BP learning algorithm yielded MSE equal to 0.1671 at the structural topology of 5-9-4-2 which indicates that 9 neurons in the first hidden layer and 4 neurons in the second hidden layer outperformed the other tested ANN configurations. As of the second modeling tool, SVR approach was used with the benchmark of two radial basis function and polynomial function. The comparative results are tabulated in Table 5.1 regarding the statistical metrics of the obtained results from ANN and SVR techniques. As it can be appreciated from Table 5.1, polynomial based SVR denoted MSE equal to 0.0586 and  $R^2$  of 0.9991 in training phase and MSE equal to 0.0602 and  $R^2$  of 0.9986 in testing phase, respectively, which indicate that SVR-polynomial further succeeds to present a model with better capabilities. In this manner, Fig. 5.10 demonstrates the data mapping of ANN and SVR-polynomial for the vertical and horizontal forces. It is observed that SVR-polynomial presents closer mapping with those of experimental data when compared to ANN predicted results.

**Table 5.1** Performance indices of various approaches for the estimation of the horizontal and vertical induced forces

| Method         | Training |         | Testing |         |
|----------------|----------|---------|---------|---------|
|                | MSE      | $(R^2)$ | MSE     | $(R^2)$ |
| SVR-rbf        | 0.1424   | 0.9789  | 0.1587  | 0.9755  |
| SVR-polynomial | 0.0586   | 0.9991  | 0.0602  | 0.9986  |
| ANN            | 0.1671   | 0.9823  | 0.2015  | 0.9893  |

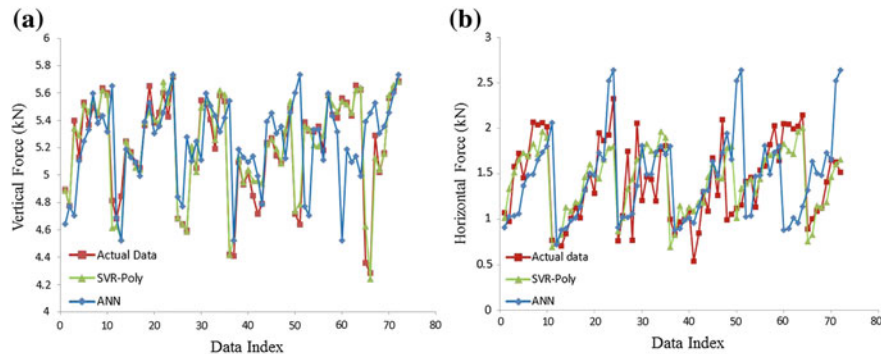


**Fig. 5.10** Data mapping of ANN and SVR-polynomial for the **a** vertical and **b** horizontal forces

#### 5.2.4 Takagi-Sugeno Type Neuro-Fuzzy Network with Modified Differential Evolution System

As a stochastic function minimizer, differential evolution DE is a method that optimizes a problem by iteratively trying to improve a candidate solution with regard to a given measure of quality [13]. DE is used for multidimensional real-value functions with no use of the gradient of the problem. DE optimizes a problem by keeping a population of candidate solutions and creating new candidate solutions by combining existing ones according to its simple formulae, and then keeping whichever candidate solution has the best score or fitness on the optimization problem at hand. In this way, the optimization problem is treated as a black box that merely provides a measure of quality given a candidate solution. The DE calculations are described as following [13].

For a given function to be optimized the following problem function is described  $f : X \subseteq R^D \rightarrow R$  at the region  $X \neq \phi$ , the minimization problem is defined as  $x^* \in X$  hence  $f(x^*) \leq f(x) \forall x \in X$  where  $f(x^*) \neq -\infty$ .

For an objective function of D real parameters, the size of the population N is ascertained. The parameter vectors are therefore yielded as:

$$x_{i,G} = [x_{1,i,G}, x_{2,i,G}, \dots, x_{D,i,G}] \quad \text{for } i = 1, 2, \dots, N \quad (5.21)$$

where G is the number of generation. The higher and lower limits for each parameter are described as:

$$x_j^L \leq x_{j,i,1} \leq x_j^U \quad (5.22)$$

where the randomly selected initial parameters were uniformly on the intervals  $[x_j^L, x_j^U]$ .

After the initialization step is finished, the parameter vectors go through mutation, recombination and selection stages. In the mutation the search space is expanded.

For a given parameter vector  $x_{i,G}$  randomly select three vectors  $x_{r1,G}$ ,  $x_{r2,G}$  and  $x_{r3,G}$  such that the indices  $i$ ,  $r_1$ ,  $r_2$  and  $r_3$  are distinct. The weighted difference of two of the vectors to the third are subsequently added:

$$v_{i,G+1} = x_{r1,G} + F(x_{r2,G} - x_{r3,G}) \quad (5.23)$$

where  $v_{i,G+1}$  is the donor vector. The mutation factor  $F$  is a constant from  $[0, 2]$ .

Recombination incorporates successful solutions from the previous generation.

$$u_{j,i,G+1} = \begin{cases} v_{j,i,G+1} & \text{if } rand_{j,i} \leq CR \text{ or } j = I_{random} \\ x_{j,i,G} & \text{if } rand_{j,i} \leq CR \text{ and } j \neq I_{random} \end{cases} \quad (5.24)$$

where  $random_{j,i} \sim U[0, 1]$ , and  $I_{random}$  is a random integer from  $[1, 2, \dots, D]$ .

In selection step, the target vector  $x_{i,G}$  is compared with the trial vector  $v_{i,G+1}$  and the one with the lowest function value is presented to the next generation

$$x_{i,G+1} = \begin{cases} u_{i,G+1} & \text{iff } (u_{i,G+1}) \leq f(x_{i,G}) \\ x_{i,G} & \text{otherwise} \end{cases} \quad i = 1, 2, \dots, N \quad (5.25)$$

Mutation, recombination, and selection iterate until at least one criterion is reached.

Takagi-Sugeno neuro-fuzzy computing method is the combination of neural network theorem and Mamdani-type fuzzy logic system technique as a robust tool for solving various problems with high level of uncertainty in science and engineering problems concerned with issues such as pattern recognition, identification, controlling.

The first-order Sugeno fuzzy model two fuzzy IF-THEN rules can be expressed as:

$$\begin{aligned} \text{If } x = A_1 \text{ and } y = B_1 \text{ then } f_1 = p_1 x + q_1 y + t_1 \\ \text{If } x = A_2 \text{ and } y = B_2 \text{ then } f_2 = p_2 x + q_2 y + t_2 \end{aligned}$$

Generally speaking, there are layers in the structure of Takagi-Sugeno-fuzzy computation method. The first layer consists of input variable membership functions (the fuzzification in which each node represents a membership function) where the nodes are equal to the number of input variables with node functions. A schematic Takagi-Sugeno fuzzy system architecture is depicted in Fig. 5.3.

$$O_i^1 = \mu_{A_i}(x), \quad i = 1, 2 \quad (5.26)$$

$$O_i^1 = \mu_{B-i}(y), \quad i = 3, 4$$

where  $\mu_A(x)$  and  $\mu_B(y)$  are membership functions with different forms such as Gaussian, bell-shaped, triangular, trapezoidal, etc.

The second layer (so-called membership layer) yields the strength of the rules by means of multiplication operator in each node. It takes the input values from the previous layer and operates as a membership function to characterize the fuzzy sets of the corresponding input variables.

$$O_i^2 = \mu_{Ai}(x)\mu_{Bi}(y), \quad i = 1, 2 \quad (5.27)$$

Third layer as the normalization layer (or the rule layer), normalizes the firing strength of the rules. Each node in these layers computes the weights, which are normalized. In this layer, the ratio of the firing strength of a rule to the sum of the total is calculated as following:

$$O_i^3 = \frac{w_i}{w_1 + w_2}, \quad i = 1, 2 \quad (5.28)$$

The fourth layer is defuzzification layer which represents the output values obtained from the inference of rules. Furthermore, this layer includes adaptive nodes that calculate a linear function with coefficients that are adapted by using the error function of the feed-forward neural network.

$$\overline{w_i}f_i = \overline{w_i}(p_i x + q_i y + t_i) \quad (5.29)$$

The last layer which has a single node refers to the summation of the inputs of the nodes from the previous layer. The output f is calculated as following:

$$f = \overline{w_1}f_1 + \overline{w_2}f_2 = \frac{w_1 f_1 + w_2 f_2}{w_1 + w_2} \quad (5.30)$$

A typical Takagi-Sugeno-Fuzzy computing approach adopts hybrid method of the gradient descent and the least-squares method methodology to define the optimal specifications for tuning the membership functions based on the back-propagation technique that computes error signals repetitively from the output layer backward to the input nodes. However, a hybrid method of Takagi-Sugeno type neuro-fuzzy network system with a modified DE optimization method can be a novel approach with great applicability in Terramechanics.

In another example, a feed-forward artificial neural network back-propagation was used. The experiment had three variables (speed, inflation pressure and wheel load) and one output [coefficient of motion resistance (CMR)], a neural network with one hidden layer can achieve acceptable performance. An increasing number of hidden layers may increase the efficiency of system, but causes more computational complexity. Hence, MLP neural network with 3-N<sub>1</sub>-1 architecture was considered at first. Determination of the number of neurons in hidden layer (N<sub>1</sub>) is

an important step in MLP neural network design. In order to determine the number of neurons in hidden layer,  $N_1$  was increased from 1 to 50. Initial weights and biases of neurons are chosen randomly. Therefore, for each number of hidden neurons (each network structure), network was trained for 100 times to overcome this problem. In each system training network is trained for 1000 epochs. Then, network with minimum value of MSE was considered for that structure. Of the several numerical indicators, the important one selected for the present study is MSE and is as given below:

$$\text{MSE} = \frac{1}{n} \sum_{i=1}^n (Y_i - \hat{Y}_j)^2 \quad (5.31)$$

where  $Y_i$  is the measured CMR and  $\hat{Y}_j$  is the predicted value. Since the range of input variables were different, in order to achieve fast convergence to minimal MSE, each of input variables was normalized in the range of -1 to 1 by following equation.

$$X_n = 2 \frac{X_r - X_{r,\min}}{X_{r,\max} - X_{r,\min}} - 1 \quad (5.32)$$

where  $X_n$  denotes normalized input variable,  $X_r$  is raw input variable, and  $X_{r,\min}$  and  $X_{r,\max}$  denote minimum and maximum of input variable, respectively. Since higher performance (higher  $R^2$  value and lower MSE) was decision parameter, also MLP neural network with 3- $N_1$ - $N_2$ -1 (i.e. two hidden layers) was developed.

Preliminary trials revealed that the learning and training ability of two hidden layer networks was better than one hidden layer ones. The general configuration of multilayer artificial neural network of current research is depicted in Fig. 5.11.

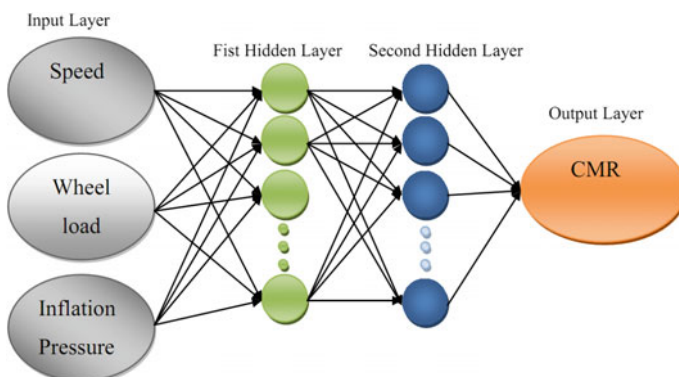


**Fig. 5.11** The general configuration of multilayer artificial neural network

For training function, *trainlm* was used that updates weight and bias values according to LM optimization and is often the fastest back propagation algorithm which is highly recommended as a first-choice supervised algorithm. LM is a very popular curve-fitting algorithm used in many software applications for solving generic curve-fitting problems. The LM algorithm provides a numerical solution to the problem of minimizing a (generally nonlinear) function and is a popular option to the Gauss-Newton technique of discovering the minimum of a function. The LM algorithm is an easy, however robust, method for a function approximating. Basically, it consists of solving the equation:

$$(J^T J + \lambda I) \delta = J^T E \quad (5.33)$$

where  $J$  is the Jacobian matrix for the system,  $\lambda$  is the Levenberg's damping factor,  $\delta$  is the weight update vector and  $E$  is the error vector containing the output errors for each input vector used for training the network. The  $\delta$  informs by how much network should change weights to achieve a (possibly) better solution. The  $J^T J$  matrix can also be known as the approximated Hessian.

*trainscg* is a network training function that updates weight and bias values according to the scaled conjugate gradient method. *trainscg* can train any network as long as its weight, net input, and transfer functions have derivative functions. BP is used to calculate derivatives of performance *perf* with respect to the weight and bias variables  $X$ .

*trainbfg* is a network training function that updates weight and bias values according to the BFGS quasi-Newton method. The training and testing performance (MSE) was selected to be the error criterion. Afterwards, a regression analysis between the predicted values and the measured values was performed to evaluate the network performance. Where various training functions were initially developed, *trainlm*, *trainbfg*, and *trainscg* were selected. Amongst transfer functions, *hardlim* and *tansig* functions were selected. MATLAB software (version 7.6, 2008, Mathworks Company) was used to develop ANN predictive representations.

Based on the MSE of the training and testing, it was found that compared to 3 layered ANN, 4-layer topologies provided better performance (Fig. 5.12). In BP networks, selection of hidden layer neurons concludes how well a dataset can be learned. Too many neurons provide the ability to memorize the problem but carries on little generalization between input and output relations. In the reverse condition, the generalization may be satisfied, however, the precision of learning a model fails significantly. Based on performance criteria a neural representation with 4-layer architecture was developed. Levenberg-Marquardt back-propagation algorithm with sigmoid transfer function for hidden neurons and linear transfer function for output layer neuron provided better performance. It was seen that minimum value of MSE was obtained for 3-47-40-1 structure with MSE equal to  $5.036 \times 10^{-6}$  (Fig. 5.12a). As it is inferred from Fig. 5.12a one hidden layer had the highest MSE value where the figure indicates that increasing the number of hidden layers increased the model capability and reduced the prediction problems. Other network structures such 3-41-46-1 (MSE of  $6.295 \times 10^{-6}$ ), 3-46-44-1 (MSE of  $5.932 \times 10^{-6}$ ) and

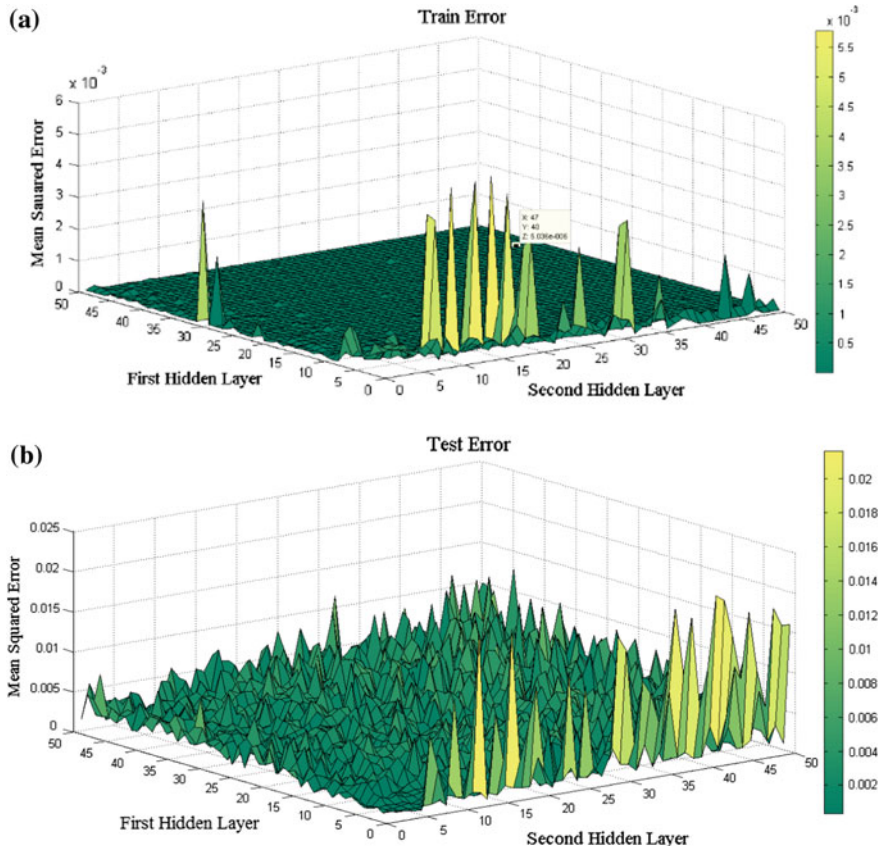


**Fig. 5.12** MSE of **a** training and **b** testing phases

**Table 5.2** Statistical specification of input and output variables for each of training, validation and testing steps

| Source             | Validation             | Train                  | Test                   |
|--------------------|------------------------|------------------------|------------------------|
| Min                | $2.89 \times 10^{-7}$  | $1.859 \times 10^{-6}$ | $2 \times 10^{-6}$     |
| Max                | $5.205 \times 10^{-4}$ | $5.242 \times 10^{-4}$ | $5.468 \times 10^{-4}$ |
| Mean               | $7.42 \times 10^{-5}$  | $6.92 \times 10^{-5}$  | $8.33 \times 10^{-5}$  |
| Median             | $1.31 \times 10^{-5}$  | $8.32 \times 10^{-6}$  | $1.45 \times 10^{-5}$  |
| Mode               | $2.89 \times 10^{-7}$  | $1.85 \times 10^{-6}$  | $2 \times 10^{-6}$     |
| Standard deviation | $1.61 \times 10^{-4}$  | $1.61 \times 10^{-4}$  | $1.713 \times 10^{-4}$ |
| Range              | $5.202 \times 10^{-4}$ | $5.224 \times 10^{-4}$ | $5.448 \times 10^{-4}$ |

3-50-48-1 ( $\text{MSE} = 5.458 \times 10^{-6}$ ) achieved low MSE values. Hence, the network with 3-47-41-1 structure was chosen. Statistical specification of input and output variables for each of training, validation and testing steps in Table 5.2. The same

**Table 5.3** Summary of various developed networks evaluated to yield the criteria of network performance

| Activation function                                   | Training rule | Net Topology | Testing error         | $R^2$  |
|---|---------------|--------------|-----------------------|--------|
| Hyperbolic tangent sigmoid transfer function (tansig) | trainlm       | 3-47-41-1    | $2.0 \times 10^{-6}$  | 0.9982 |
| Hard-limit transfer function (hardlim)                | trainlm       | 3-46-43-1    | $2.83 \times 10^{-6}$ | 0.9916 |
| Hyperbolic tangent sigmoid transfer function (tansig) | trainbfg      | 3-50-48-1    | $1.25 \times 10^{-5}$ | 0.9741 |
| Hard-limit transfer function (hardlim)                | trainbfg      | 3-47-71-1    | $1.81 \times 10^{-5}$ | 0.9627 |
| Hyperbolic tangent sigmoid transfer function (tansig) | trainscg      | 3-42-49-1    | $4.05 \times 10^{-6}$ | 0.9821 |
| Hard-limit transfer function (hardlim)                | trainscg      | 3-48-49-1    | $5.87 \times 10^{-6}$ | 0.9797 |

processes for computation of satisfactory performance were repeated in the case of other training and transfer functions which are shown in Table 5.3 with  $R^2$  and MSE values. However, it divulges that 3-47-40-1 structure with MSE equal to  $5.036 \times 10^{-6}$  was the best performance. Although it may seem that the simpler topologies could be utilized, however, in the case of soil-tool interactions due to unidentified behavior of soil and elastic-plastic reactions, nonlinear and complex relations are generally obtained. Complicated topology with higher performance is prior to a simple network structure with lower performance. Ideally, MSE close to zero indicates there are no significant differences between predicted and measured values. This proves that given proper hidden layers, MLP feed-forward network can estimate practically any desired function by any interest degree of accuracy.

The learning rate balances the level of descending the error after each epoch. The learning rate, LR, applies a larger or smaller portion of the respective adjustment to the old weight. If the factor is set to a large value, then the neural network may learn more quickly, however if there is a large changeability in the input set then the network may not learn very well or at all. In real terms, setting the learning rate to a large value is inappropriate and counter-productive to learning. Usually, it is better to set the factor to a small value and edge it upward if the learning rate seems slow. Momentum operates as a low pass filter to settle sudden changes in the progress. Momentum basically allows a change to the weights to persist for a number of adjustment cycles. The magnitude of the persistence is controlled by the momentum factor. If the momentum factor is set to nonzero value, then increasingly greater persistence of previous adjustments is permitted in modifying the current adjustment. This can improve the learning rate in some situations, by helping to smooth out unusual conditions in the training set.

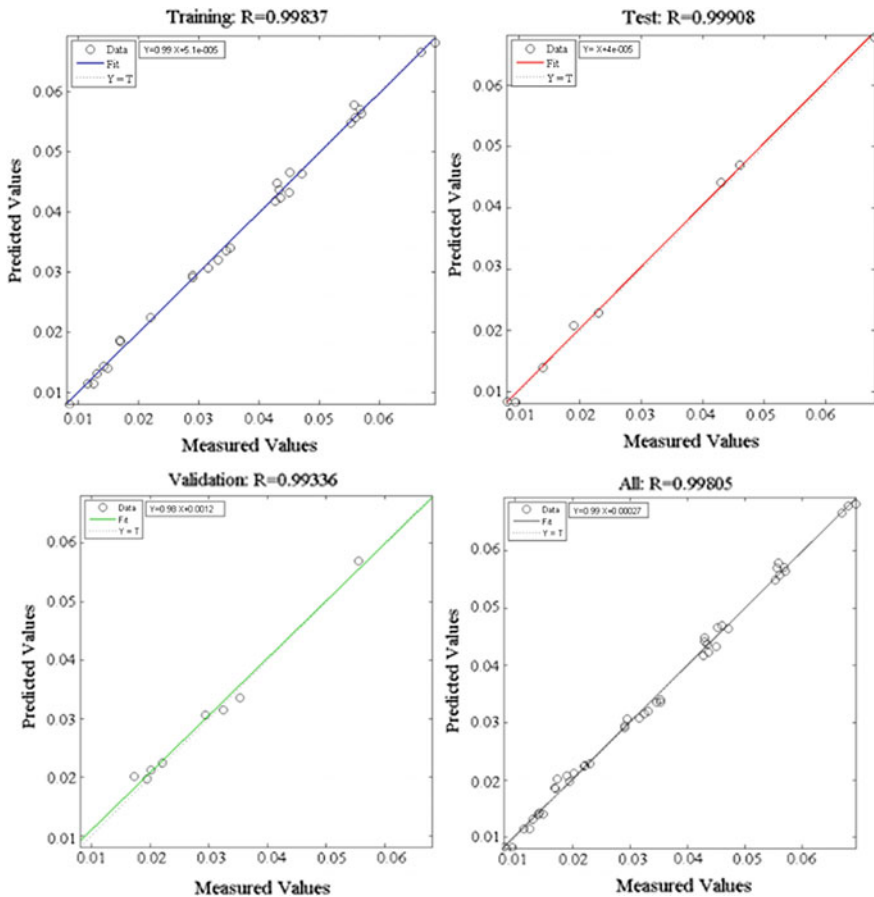


**Fig. 5.13** The regression analysis between the network response (outputs) and the corresponding targets

The optimum values of learning rate and momentum of ANN used to predict the process was 0.6 and 0.2, respectively. Training, test, and validation results of applied neural representation are presented in Fig. 5.13. Figure 5.13 shows the regression analysis between the network response (outputs) and the corresponding targets. According to this figure, the training process has been performed properly, where the correlation factor between measured and predicted values is 0.99837. testing, and validation results are 0.99908, and 0.99336, respectively. The optimum ANN structure (3-47-40-1) with the obtained bias and weight values, transfer and train functions was used to simulate the developed model and compare the results

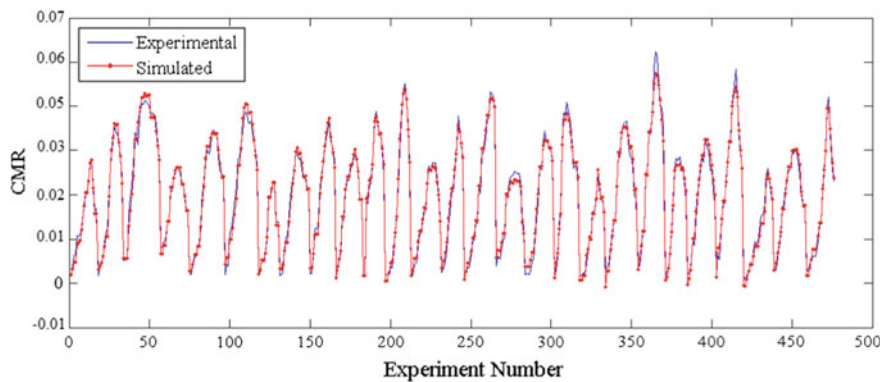


**Fig. 5.14** A comparison between simulated and experimental data

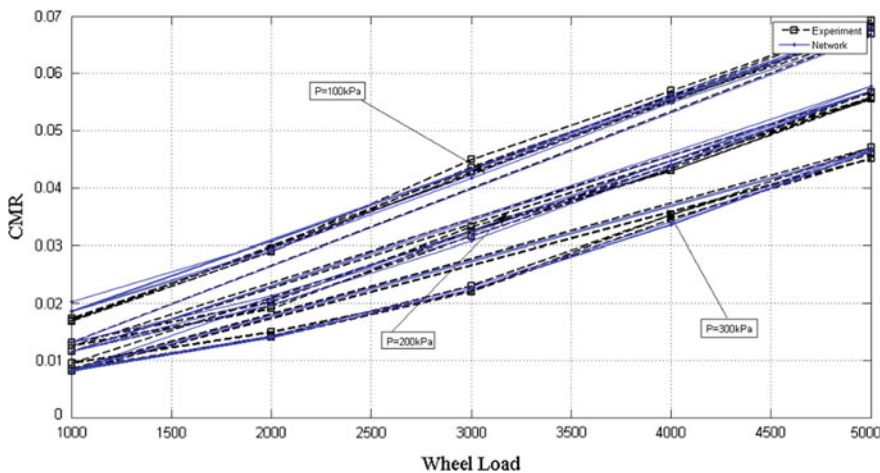


**Fig. 5.15** Variation of CMR due to the change in wheel load and tire inflation pressure predicted by ANN

with experimental data. A comparison between simulated and experimental data is depicted in Fig. 5.14. It demonstrates the conformity between the experimental output and the simulated output by optimal ANN model during experiment number (epochs). The results for comparison between experimental and simulated results divulged that wherein CMR decreased by increase of inflation pressure, it increased almost linearly with increase of wheel load (Fig. 5.15). Finally, the error variation in terms of mean squared error is demonstrated with respect to iteration number (Fig. 5.16).

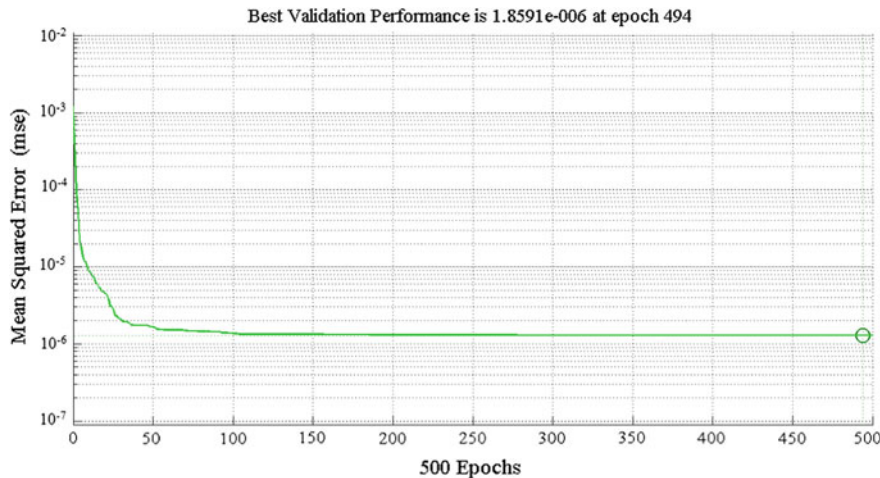


**Fig. 5.16** MSE variation with respect to iteration number

### 5.3 Optimization with Heuristics and Meta-Heuristics

In mathematics and the science of computing, optimization is the selection of a best response among the whole available solutions to achieve the global minima or maximum of a predefined function. Optimization problems are formed from three substantial processes of which the cost or objective function that is intended to be maximized or minimized is the first. It can be formulated based on the observations of real-world phenomena and also the obtained mathematical relationships of a system components. The components or the variables of the system that are verified to determine the best configuration of them to obtain the desired optima forms the second element of the optimization problem. The third element of an optimization problem is a set of constraints, which are limitations on the values that the variables can take.

Application of meta-heuristics has been a dynamic studying interest of the reliability optimization to determine idleness and reliability constituents. The application of a meta-heuristic evolutionary optimization method, imperialist competitive algorithm (ICA), for minimization of energy loss due to wheel rolling resistance in a soil bin facility equipped with single-wheel tester is discussed. The required data were collected thorough various designed experiments in the controlled soil bin environment. Local and global searching of the search space.

#### 5.3.1 *Imperialist Competitive Algorithm (ICA)*

The optimization problem is described to find the argument  $x$  with its optimum cost  $f(x)$  within the heuristic and meta-heuristic optimization algorithms. Imperialist

Competitive algorithm (ICA) was first introduced by Atashpaz-Gargari and Lucas [14] that has considerably been used in engineering applications. The objective in optimization is to reach the optimal value for the inputs. An array, which in genetic algorithm terminology is named “Chromosome” and in PSO “Particle”, is generated in ICA known as country. The pseudo-code of this algorithm is described as follows.

(i) *Formation of initial empires*

In a problem of  $N_{\text{var}}$  dimensional the country is introduced as following.

$$\text{country} = [P_1, P_2, P_3, \dots, P_{N_{\text{variable}}}] \quad (5.34)$$

The matrix of total countries is randomly formed as given.

$$\text{Country} = \begin{bmatrix} \text{country}_1 \\ \text{country}_2 \\ \text{country}_3 \\ \vdots \\ \text{country}_N \end{bmatrix} = \begin{bmatrix} KP_1 & KI_1 & KD_1 \\ KP_2 & KI_2 & KD_2 \\ KP_3 & KI_3 & KD_3 \\ \vdots & \vdots & \vdots \\ KP_N & KI_N & KD_N \end{bmatrix} \quad (5.35)$$

Each country's cost is defined by evaluation of the cost function  $f$  at variables  $(P_1, P_2, P_3, \dots, P_{N_{\text{var}}})$  to obtain the cost function as

$$\cos t_i = f(\text{country}) = f(P_1, P_2, P_3, \dots, P_{N_{\text{variable}}}) \quad (5.36)$$

The initial countries,  $N_{\text{country}}$ , are generated to start the algorithm.  $N_{\text{imp}}$  number of the best population, (i.e. countries with the lowest cost function values), are assigned as empires.  $N_{\text{col}}$  number of the remaining countries form the colonies each belong to an empire. The initial colonies are shared in proportion with each empire's power. To assign the colonies, the normalized cost of imperialists is described as

$$C_n = \max_i\{c_i\} - c_n \quad (5.37)$$

where  $c_n$ ,  $\max_i\{c_i\}$  and  $C_n$  are the cost of  $n$ th imperialist, the highest cost among imperialists and the normalized cost of imperialists, respectively. That is, the imperialist with the highest cost (weakest imperialist) denotes lower normalized cost. The relative normalized power of each imperialist, therefore, is defined by:

$$P_n = \left| \frac{C_n}{\sum_{i=1}^{N_{\text{imperialist}}} C_i} \right| \quad (5.38)$$

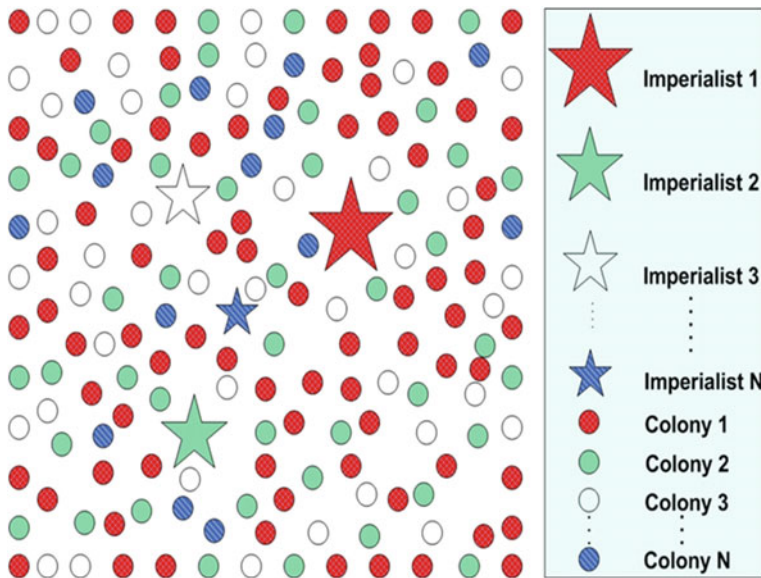


**Fig. 5.17** Process of forming initial imperialists in which the powerful imperialists possess more colonies

Based on which, the colonies are allocated among the imperialists. Thus, the initial number of each imperialist's colonies is described by

$$N.C_{.n} = \text{round}\{P_n.N_{\text{col}}\} \quad (5.39)$$

Where  $N.C_{.n}$  is the number of initial colonies of an imperialist and  $N_{\text{col}}$  is the total number of colonies and round is a function that yields the round number if it is approximate. Figure 5.17 shows the process of forming initial imperialists in which the powerful imperialists possess more colonies. Imperialist 1 is the most powerful among others that has possessed the highest number of colonies (see Fig. 5.17).

#### (ii) Assimilation

The assimilation policy follows to use social-political characteristics in their colonies on the basis of such as religion, culture and language. This part of ICA is shown in Fig. 5.18.

As the result of assimilation, the colony moves by  $x$  unit in the direction of the imperialist to the new position of colony. Thus  $x$  is defined as

$$x \sim U(0, \beta \times d) \quad (5.40)$$

where  $d$  is the distance between the colony and the imperialist,  $B$  is set between 1 and 2, however,  $\beta > 1$  moves toward the imperialist from both of the vectors.

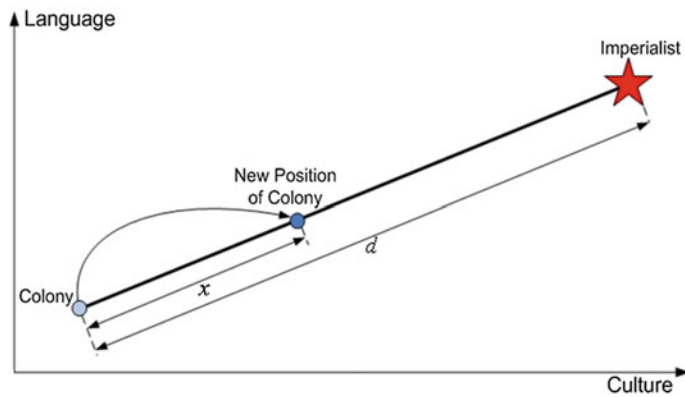


**Fig. 5.18** Assimilation policy to use social-political characteristics in the colonies

The absorption process, however, did not result in compliance with desires of imperialists. This implies that the real direction of movement toward the imperialist is not necessarily the shortest vector between the colony and the imperialist. These possible deviations in absorption are predicted in ICA by adding one random angle with uniform distribution,  $\theta$ , to the direction of colony's movement as described by

$$\theta \sim (-\gamma, \gamma) \quad (5.41)$$

where  $\gamma$  can possess any random value, however, increased value causes more extensive searching around the imperialist and lower value causes the colony to move toward the imperialist closer to the connecting vector. In most of implementations, a  $\theta$  value close to  $\pi/4$  results in better convergence of colonies to the imperialist. The actual assimilation movement toward the imperialist is shown in Fig. 5.19.

### (iii) Replacement of colony and imperialist

During the colony's movement toward the imperialist, it is possible that the colony can reach a lower cost function than imperialist. Then the imperialist and the colony would replace their positions. Thus, the algorithm continues with new colony and imperialist with the assimilation policy for newer colony and imperialist.

### (iv) The total power of an empire

The total power of an empire equals with the power of an imperialist added with a certain percent of possessed colonies' power. Therefore the total cost of an empire is defined as

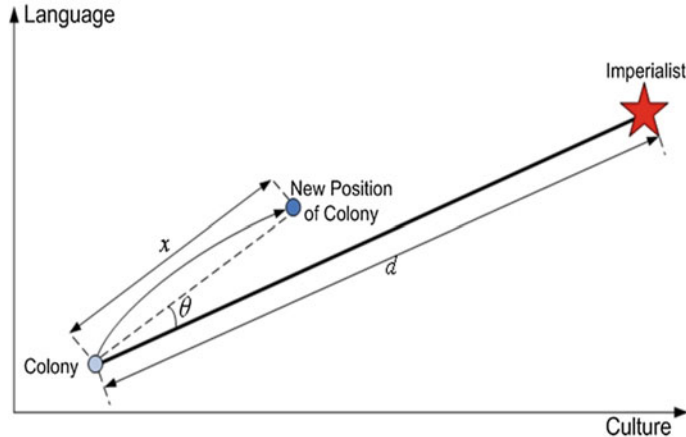


**Fig. 5.19** The actual assimilation movement toward the imperialist

$$T.C_n = \text{Cost}(\text{imperialist}_n) + \xi \text{mean}\{\text{Cost}(\text{colonies of empire}_n)\} \quad (5.42)$$

where  $T.C_n$  is the total cost of nth empire, and  $\xi$  is a positive value ranging between 0 and 1. Setting  $\xi$  to a small value results in equalization of costs for the empire and the imperialist, where a high  $\xi$  results the cost of empire to be highly affected by the colonies.  $\xi = 0.05$  has given good results in most of implementations.

#### (v) Imperialistic competitions

Each empire unable to increase the power defeats by the others during the imperialistic competition and ends is gradual collapse of the empire. That is, the weak empires lose their colonies and the powerful empires possess these colonies. Thus, one colony (can be more) of the weakest empire is competed to be possessed by a powerful empire (not necessarily the most powerful empire). Figure 5.20 shows this process clearly.

In Fig. 5.20, empire 1 is the weakest empire and one of its colonies is competed to be possessed by one of empires 2 to N. In order to model the competition among the empires, the probability of possessing each empire is defined which is in proportion with the total power of the empire. The normalized total cost of an empire is defined as

$$N.T.C_n = \max_i\{T.C_i\} - T.C_n \quad (5.43)$$

where  $T.C_n$  is the total cost of nth empire and  $N.T.C_n$  is the normalized total cost.  $T.C_n$  stands for the total cost of an empire where  $N.T.C_n$  is the total power of an empire. Therefore, increase of  $T.C_n$  has converse relation with  $N.T.C_n$ . Then the probability of possessing an empire ( $P_{pn}$ ) is obtained by

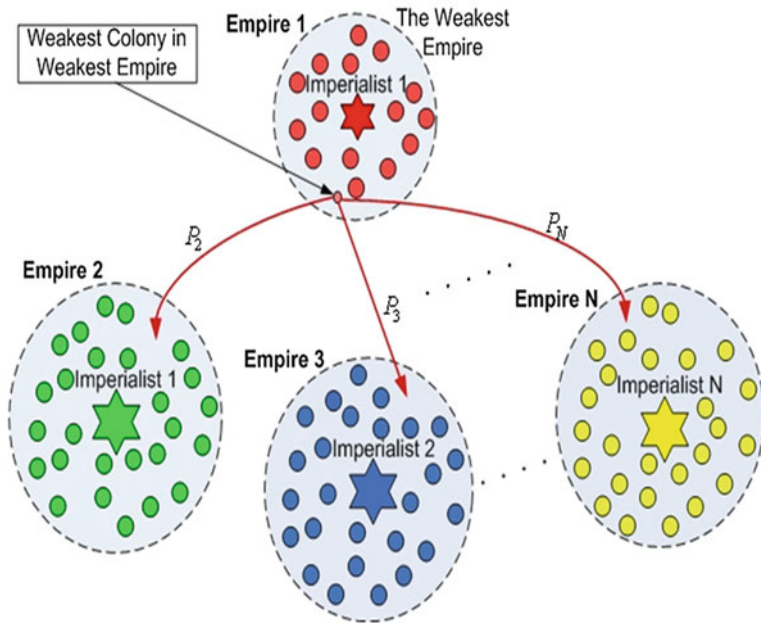


**Fig. 5.20** The imperialist competitions to find the most powerful one

$$P_n = \left| \frac{N \cdot T \cdot C_n}{\sum_{i=1}^{N_{imperialist}} N \cdot T \cdot C_i} \right| \quad (5.44)$$

The vector  $P$  is formed based on the  $(P_{pn})$  to share the colonies among the empires.

$$P = [P_{P1}, P_{P2}, P_{P3}, \dots, P_{PN_{imp}}] \quad (5.45)$$

$P$  vector is  $1 \times N_{imp}$  dimensional. Then  $R$  vector of  $1 \times N_{imp}$  dimensional is formed. The arrays of  $R$  vector are random values with uniform distribution in the range of  $[0, 1]$ .

$$R = [r_1, r_2, r_3, \dots, r_{N_{imp}}] \quad (5.46)$$

$$r_1, r_2, r_3, \dots, r_{N_{imp}} \sim U(0, 1) \quad (5.47)$$

Then vector  $D$  is formed as following.

$$P = [P_{P1} - r_1, P_{P2} - r_2, P_{P3} - r_3, \dots, P_{PN_{imp}} - r_{N_{imp}}] \quad (5.48)$$

The empire with the highest  $D$  vector index is the most powerful empire.

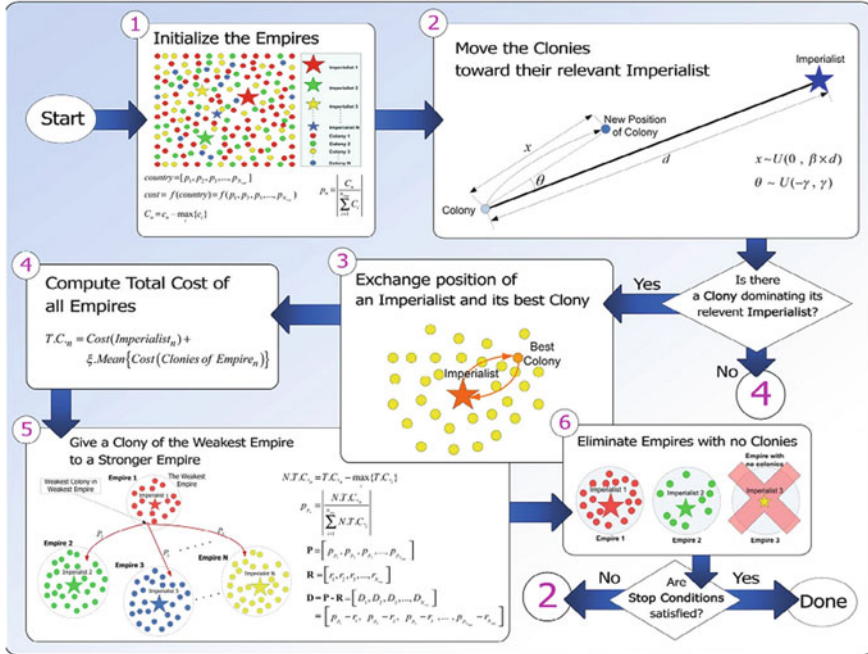


Fig. 5.21 The flowchart of ICA optimization algorithm [15]

#### (vi) Collapse of weak empires

During the mentioned competitions, the empires lose their colonies to the more powerful ones. In ICA, there are conditions for collapse of an empire if the most major one is to lose all the colonies.

#### (vii) Convergence

The algorithm continues to the point of reaching one of convergence conditions or reaching the described iterations. All empires gradually collapse and one empire stands as the most powerful empire and the countries are governed by a unique empire (Fig. 5.21).

### 5.3.2 Genetic Algorithm

Genetic Algorithms (GAs) are adaptive heuristic search algorithm premised on the evolutionary ideas of natural selection and genetic. The basic concept of GAs is designed to simulate processes in natural system necessary for evolution, particularly those that follow the principles first laid down by Charles Darwin of survival of the fittest. As such they represent an intelligent exploitation of a random search

within a defined search space to solve a problem. A population of individuals became fitter over the period of history and the process was developed as a technique for optimization. Population is involved of potential solutions in the arrangement of array of chromosomes. In this manner, a population of individuals was created to start genetic algorithm. Thereafter, a cost function (fitness function) was considered as the tractive power efficiency. The chromosomes of the population then were organized according to the maximum cost or the highest fitness. Certain percentages of the most elite members were straightly forwarded to the next generation based on their merit measured by the fitness function. At this stage forward, three GA operators (selection, crossover, mutation) will be activated to generate the rest of the next generation's population. Firstly, a weighted random selection scheme was adopted; therefore selection is biased toward parents of current population with a higher probability to be picked from qualified individuals with higher fitness. Consequently, pairs of parents will be handled by the crossover operator for the combination of their components (genes) at the crossover point to produce offspring. In order to avoid GA from converging to local optimum, searching space for candidate solution should be diversified by mutation operator. Mutation manipulates the genes of chromosomes arbitrarily as to capacitate GA to perform global exploration. At last, the new generation goes through the same procedure to produce a new population for the next generation. Successive generations were presented employing GA operators on population until acceptable results obtained at the first array of population in the last generation. The flowchart of the proposed GA algorithm is depicted in Fig. 5.22.

### 5.3.3 Particle Swarm Optimization

A basic variant of the PSO algorithm performs by taking a population (called a swarm) of candidate solutions (called particles). These particles are moved around the search-space based on some simple principles. The movements of the particles are guided by their own best known position in the search-space as well as the entire swarm's best known position. Once improved positions are being distinguished, these will then come to guide the movements of the swarm. The process is reiterated and a satisfactory solution will eventually be discovered. The function takes a candidate solution as an argument in the form of a vector of real numbers and produces a real number as output which indicates the objective function value of the given candidate solution. Each particle in PSO keeps track of its coordinates in the problem space which are associated with the best solution (fitness). This value is called *pbest*. Another "best" value that is tracked by the particle swarm optimizer is the best value, obtained so far by any particle in the neighbors of the particle. This location is called *lbest*. When a particle takes all the population as its topological neighbors, the best value is a global best and is called *gbest*. The flowchart of the proposed PSO algorithm is depicted in Fig. 5.23.

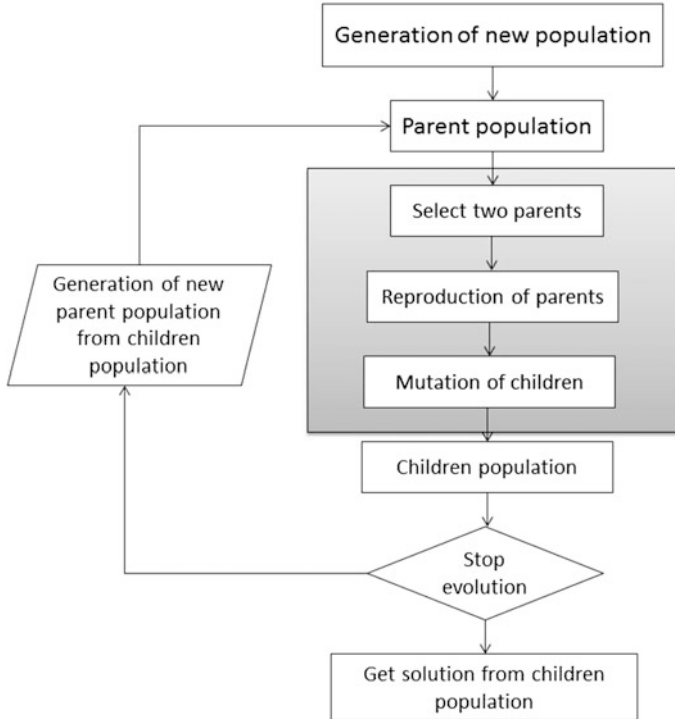


**Fig. 5.22** The flowchart of the proposed GA algorithm

- The drawbacks of pre-maturity and unpredictability in GA and bias of final results in PSO (due to requirement for initial guessing of particles) is overcome by ICA.
- Unlike GA, PSO and GA-PSO, ICA is independent of saving the previous location of agents. This increases its convergence speed.
- ICA determines the movement direction of agents by the best vector in empire (among pre-defined agents). This is performed in PSO in local and global vectors. The vector in ICA changes for different agents which results in exploration ability, while in PSO it is constant for all the agents in iteration. This, in turn, increases ICA's accuracy over PSO.

Finding the maximum energy efficiency is through the tractive performance of run-off-road vehicles is of great interest. Furthermore, tractive power efficiency which is a significant of energy efficiency index of off-road vehicles should be empirically analyzed prior to the implementation of optimization approaches. Then, disparate heuristic and meta-heuristic methods of genetic algorithm (GA), particle swarm optimization (PSO), GA-PSO and ICA can be adopted to achieve the most optimal result. The cost function, or so-called objective function in GA, should be optimized during the iteration process to find the global maximum. It is appreciated

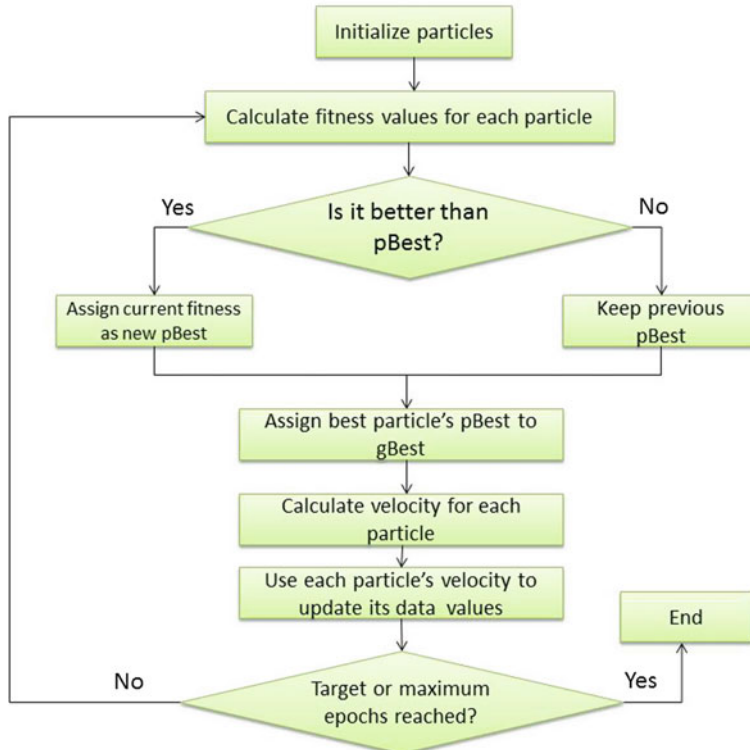


**Fig. 5.23** The flowchart of the proposed PSO algorithm

from Fig. 5.24 that increased iteration number of GA algorithm from 0 to 100 results in increase of tractive power efficiency to about 48.9 %. This shows that 2.44 times greater energy saving could be achieved when the GA algorithm with the designated iteration numbers was applied to the problem. However, it should be noted that the great iteration number of the GA approach requires a considerable deal of time for running the tool. Hence, when meta-heuristic approaches were employed, in contradictory to heuristic GA method, the permitted iteration number was designated to be 30. Figure 5.25 demonstrates the potential of PSO approach for the maximization of the energy efficiency. It is appreciated from Fig. 5.25 that the increase of iteration number from 0 to 30 resulted in the increased tractive power efficiency from 20 to 47.29 % which shows almost 2.36 times decrement of power loss. Although this amount is lower than that of GA approach, it should be considered that this value is attained at 30 iterations where GA was implemented for 100 iterations. These justifications imply the superior quality of PSO over GA when dealing with the problem. Due to the inherent advantages of GA and PSO methods reported in literature, it was decided to evaluate the ability of the hybridized GA-PSO method and make comparison between the other techniques.

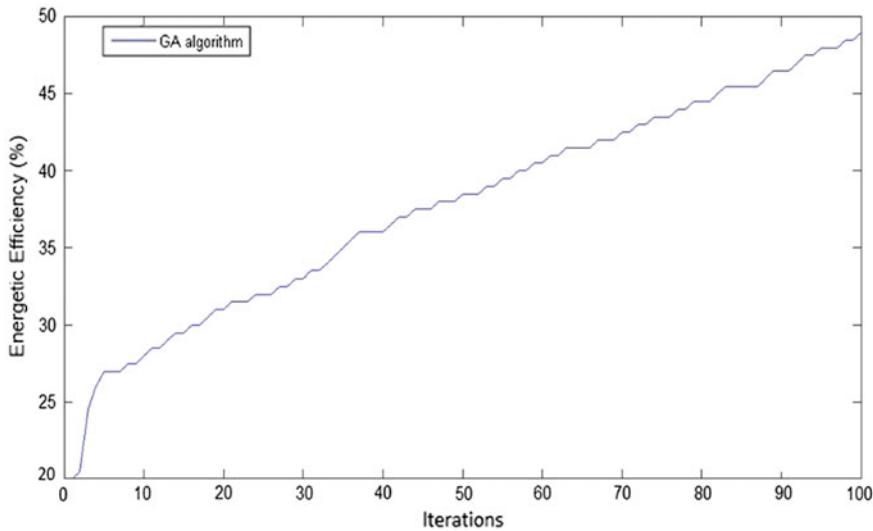


**Fig. 5.24** Tractive power efficiency variation with iterations in GA

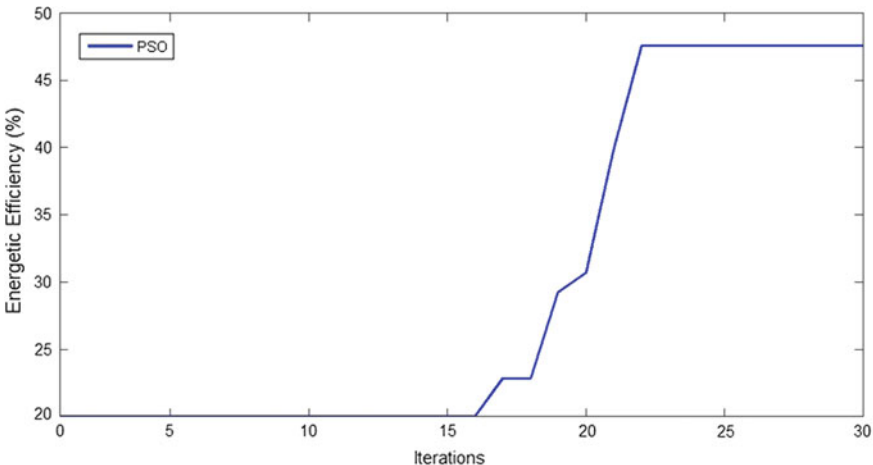


**Fig. 5.25** Tractive power efficiency variation with iterations in PSO

The implementation resulted in a significantly better performance of GA-PSO compared with ordinary GA and PSO methodologies (Fig. 5.26). Quick convergence of the objective parameter to the optimal value is observed from iteration 15 to 30. The optimal value of 57.61 % was achieved by the application of hybridized GA-PSO method which is a remarkable performance. ICA method was employed for the maximization of the objective parameter. In this regard, the algorithm adopts

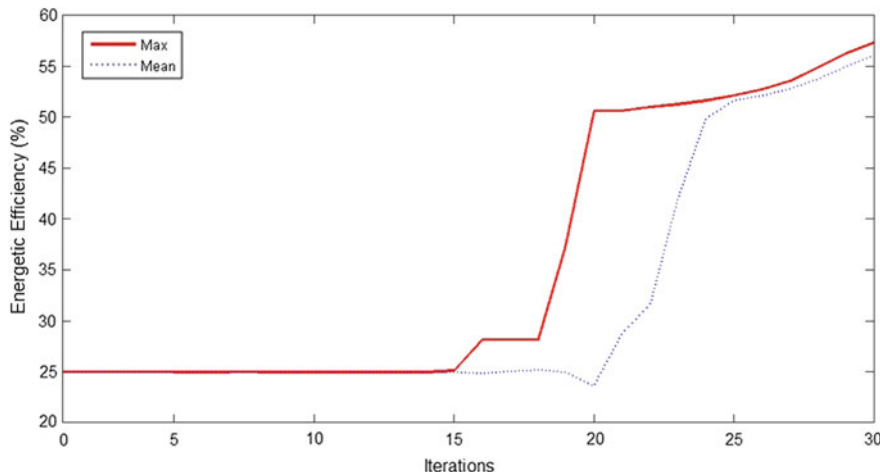


**Fig. 5.26** Tractive power efficiency variation with iterations in GA-PSO

**Table 5.4** Results of optimization

|   |     |
|---|-----|
| Number of total countries               | 80  |
| Number of initial imperialist countries | 4   |
| Number of iterations (epochs)           | 30  |
| Revolution rate                         | 0.3 |
| Assimilation coefficient                | 2   |
| Assimilation angle                      | 0.5 |

some random countries being the representatives of the corresponding input parameters. Countries then compete internally to maximize their costs to become the imperialist and denote the optimum level of the input variables, followed by the external competition among the imperialists resulting in the occupancy of the imperialists by an individual imperialist with the lowest cost function. The results of optimization are shown in Table 5.4. Figure 5.27 shows the minimum and mean cost of imperialists. Furthermore, Fig. 5.27 shows that the imperialist with the lowest cost function of 69.01 % could occupy the other imperialists after 23 iterations. It is concluded that ICA method outperformed the other employed methods for maximizing the energy efficiency of off-road vehicles. Moreover, it should be added that the improved performance of GA-PSO could be attributed to the selection of particle populations of PSO as chromosome weights of GA which allows better chromosomes to be included in the next generation and this evolution continues to reach the final answer.

Figure 5.28 depicts the spatial distribution of the final imperialist, empires with their colonized countries (with the same color) in the search space of the problem. Figure 5.28 illustrates that at wheel load of 2.23 kN, velocity of 0.8 m/s and slippage of 14.33 %, the imperialist with the greatest energy efficiency could

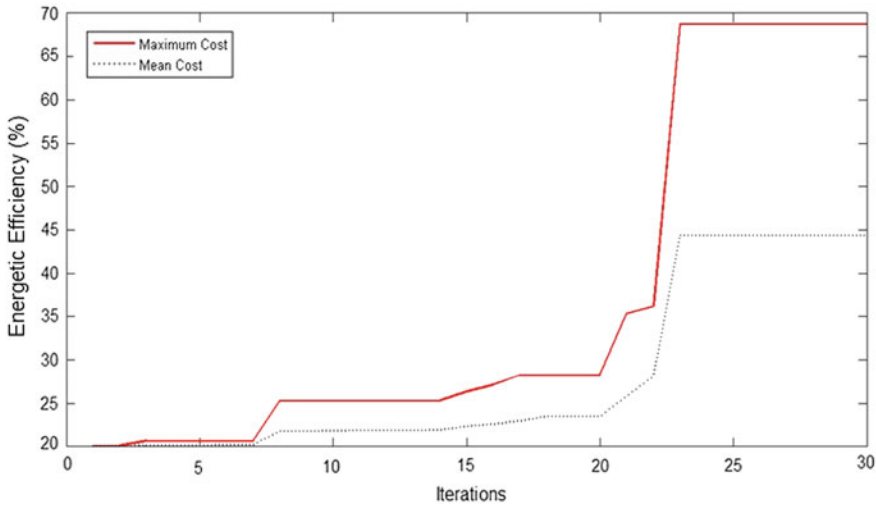


**Fig. 5.27** The variations of tractive power efficiency (%) with respect to iterations for ICA algorithm

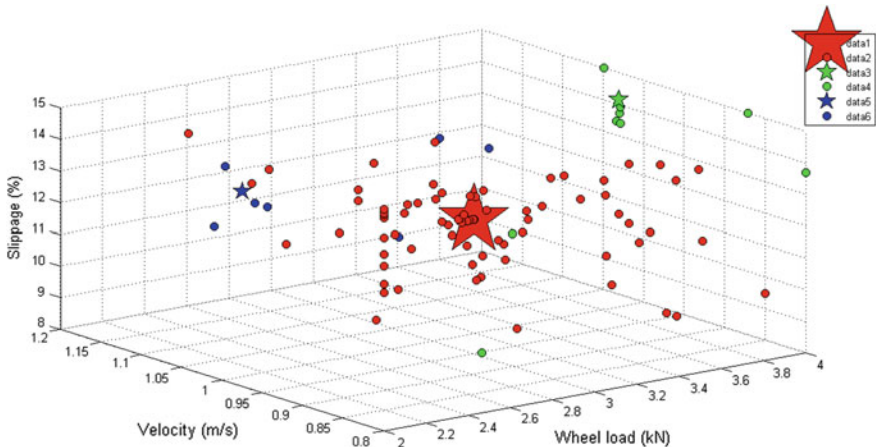


**Fig. 5.28** The spatial distribution of colonies, empires and imperialists of the outperformed ICA method in the search space of input parameters

possess other imperialists and form its empire and the including colonies (this is shown in ICA search space) with amount of 69.01 %. The specifications of parameter adjustments for ICA approach are detailed in Table 5.3. It is important to note that rolling resistance has direct relationship with wheel load where increased wheel load results in increased rolling resistance and thus decrease of tractive power

efficiency. Furthermore, an amount of slippage is required for tire when interacted by soil to compact the soil beneath for creating a supporting surface for applying the torque to the soil and initiation of the traversing. Hence, the values obtained by ICA approach are in good agreement with the literature. It is added that tractive power efficiency has nonlinear relationship with velocity and tire inflation pressure that necessitates the adoption of stochastic meta-heuristic approaches for problem optimization.

## 5.4 Application of Meta-Heuristics in Suspension Control

It is clear-cut that suspension system is formed from springs, shock absorbers and linkages that connect a vehicle to the wheels. The substantial duty of a vehicle suspension system is to decrease the vertical acceleration transmitted to the passenger and arrange for a satisfactory road comfort. A passive suspension is able to store and dissipate energy through a spring and a damper, respectively. The passive system parameters are fixed, being selected to achieve a definite level of compromise between handling, load support and ride comfort. An active suspension system has the ability to store, dissipate and to introduce energy to the system. In the case that the suspension system of the vehicle is externally controlled in reaction to the signals from an electronic controller then the system is a semi-active or active suspension.

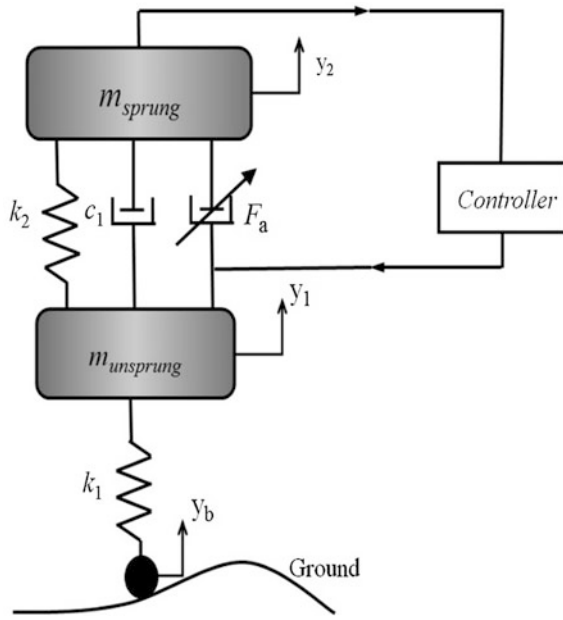
Conventional passive suspensions use a spring and damper between the car body and wheel assembly. The spring-damper characteristics are selected to emphasize one of several conflicting objectives such as passenger comfort, road handling, and suspension deflection. Active suspensions allow the designer to balance these objectives using a feedback-controller hydraulic actuator between the chassis and wheel assembly.

This example uses a quarter-car model of the active suspension system (see Fig. 5.29). The nature of the control problem with multiple objectives that have to be optimized as well as the uncertain parameters of the plant call for an  $H\infty$ -controller. By changing weighting filters different controllers can be designed, emphasizing either comfort or handling.

Active suspension can potentially offer a better performance of suspension through a functional control of force actuator that is a closed loop control system. The controller estimates to either add or dissipate energy from the system by application of sensors as an input. The sensors provide the data of road profile to the controller. Therefore, an active suspension system shown in Fig. 5.29 is needed where there is an active element inside the system to give both conditions so that it can improve the performance of the suspension system.

The mass,  $m_s$ , represents the car chassis (body) and the mass,  $m_u$ , represents the wheel assembly. The spring,  $k_2$ , and damper,  $c_1$ , represent the passive spring and

**Fig. 5.29** A quarter car model active suspension system



shock absorber placed between the car body and the wheel assembly. The spring,  $k_1$ , models the compressibility of the pneumatic tire. The variables  $y_2$ ,  $y_1$ , and  $y_b$  are the car body travel, the wheel travel, and the road disturbance, respectively. The force  $F_a$ , which is applied between the body and wheel assembly, is controlled by feedback. This force represents the active component of the suspension system.

Active suspension systems have any actuator type such as hydraulic actuators to the passive components of suspension system. The benefit of such a system is that although the active hydraulic actuator or the control system is disabled, the suspension system is converted to the passive system. The equations of motion can be stated as:

$$m_s \ddot{y}_2 + k_2(y_2 - y_1) + c_1(\dot{y}_2 - \dot{y}_1) - F_a = 0 \quad (5.49)$$

$$m_u \ddot{y}_1 + k_2(y_1 - y_2) + c_1(\dot{y}_1 - \dot{y}_2) + k_1(y_1 - y_b) + F_a = 0 \quad (5.50)$$

where  $F_a$  is the control force from the hydraulic actuator. It can be noted that if the control force  $F_a = 0$ , then above Equations become the equation of passive suspension system. Considering  $F_a$  as the control input, the state-space representation of equations become,

$$\begin{aligned}x_1 &= y_2 - y_1 \\x_2 &= y_2 - y_b \\x_3 &= \dot{y}_2 = \frac{d}{dt} y_2 \\x_4 &= \dot{y}_1 = \frac{d}{dt} y_1\end{aligned}\tag{5.51}$$

It can be resulted that:

$$\begin{aligned}\dot{x}_1 &= x_3 - x_4 \\ \dot{x}_2 &= x_4 - y_b \\ \dot{x}_3 &= \frac{(-c_1 \dot{x}_1 - k_2 x_1 + F_a)}{m_s} \\ \dot{x}_4 &= \frac{(c_1 \dot{x}_1 + k_2 x_1 - k_1 x_2 - F_a)}{m_u}\end{aligned}\tag{5.52}$$

Let's define the physical parameters of the system as following.

```
ms = 400; % sprung mass (kg)
mus = 50; % unsprung mass (kg)
cs = 1000; % damper (N/m/s)
ks = 15000 ; % spring stiffness (N/m)
kus = 200000; % spring stiffness (N/m)
```

Construct a state-space model quarter-car model representing these equations.

```
% Physical parameters
% Physical parameters
mb = 300; % kg
mw = 60; % kg
bs = 1000; % N/m/s
ks = 16000 ; % N/m
kt = 190000; % N/m

% State matrices
A = [ 0 1 0 0; [-ks -bs ks bs]/mb ; ...
      0 0 0 1; [ks bs -ks-kt -bs]/mw];
B = [ 0 0; 0 10000/mb ; 0 0 ; [kt -10000] /mw];
C = [1 0 0 0; 1 0 -1 0; A(2,:)];
D = [ 0 0; 0 0; B(2,:)];
```

```

qcar = ss(A,B,C,D);
qcar.StateName = {'body travel (m)' ; 'body vel (m/s)' ; ...
'wheel travel (m)' ; 'wheel vel (m/s)'};
qcar.InputName = {'r' ; 'fs'};
qcar.OutputName = {'xb' ; 'sd' ; 'ab'};

```

The transfer function from actuator to body travel and acceleration has an imaginary-axis zero with natural frequency 56.27 rad/s. This is called the tire-hop frequency.

```

tzero(qcar({'xb','ab'},'fs'))
ans =
-0.0000 +56.2731i
-0.0000 -56.2731i

```

Similarly, the transfer function from actuator to suspension deflection has an imaginary-axis zero with natural frequency 22.97 rad/s. This is called the rattlespace frequency.

```

zero(qcar('sd','fs'))
ans =
0.0000 +22.9734i
0.0000 -22.9734i

```

Road disturbances influence the motion of the car and suspension. Passenger comfort is associated with small body acceleration. The allowable suspension travel is constrained by limits on the actuator displacement. Plot the open-loop gain from road disturbance and actuator force to body acceleration and suspension displacement.

By use of these equations and parameter values to construct a state-space model, the quarter-car suspension system can be developed.

The frequency response of the quarter-car model from inputs of road irregularity and actuator force to outputs of suspension deflection and sprung mass acceleration are illustrated in the Bode plot (Fig. 5.30).

The transfer function from actuator to sprung mass travel and acceleration has an imaginary-axis zero. The natural frequency of this zero, 63.24 rad/s, is called the tire-hop frequency with the above-mentioned physical parameters of the system. Also the transfer function from the actuator to suspension deformation also has an imaginary-axis zero while the natural frequency of this zero (i.e. 21.08 rad/s) is called the rattlespace frequency.

### Nominal H-Infinity Design

Control of shock absorbers must account for unknown disturbances. For vehicle rides in particular these are changes of the road height or inertial forces and moments caused by unexpected driving maneuvers like braking, accelerating etc.

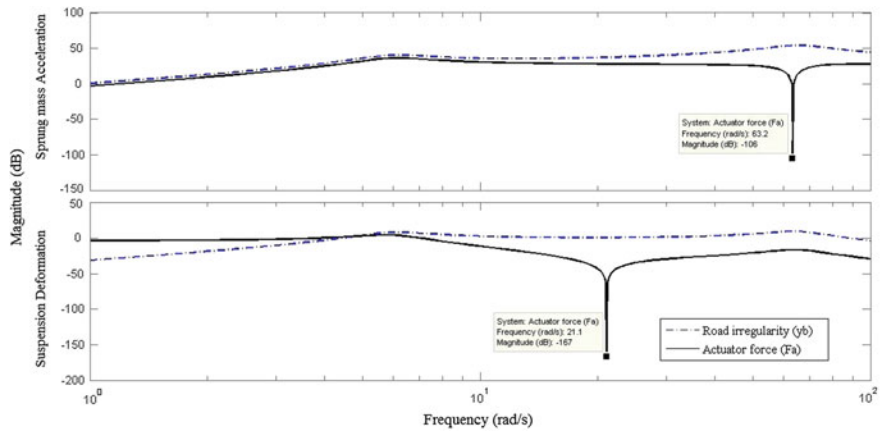


**Fig. 5.30** The frequency response of the quarter-car model from inputs of road irregularity and actuator force to outputs of suspension deflection and sprung mass acceleration

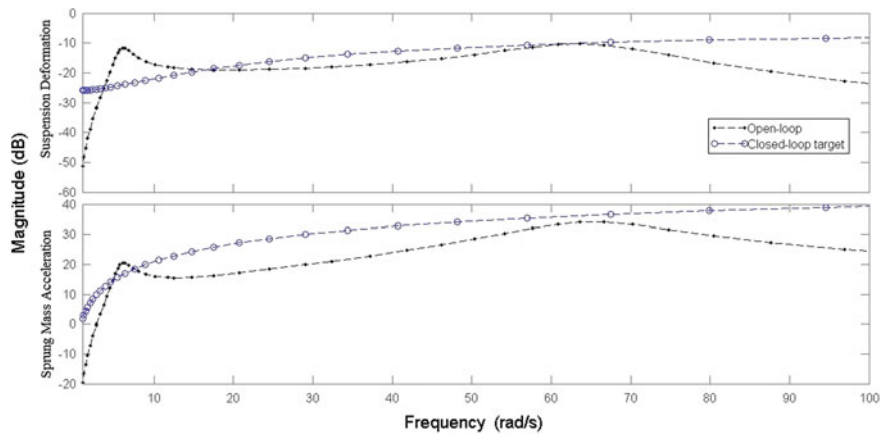


**Fig. 5.31** Suspension deformation and sprung mass acceleration in frequency domain

The  $H\infty$  control problem is one of disturbance rejection. In particular, it includes of minimizing the closed-loop root-mean-square (RMS) gain from the disturbance  $w$  to the output  $z$  in the control loop. The model's suspension deformation and sprung mass acceleration in frequency domain are presented in Fig. 5.31.

So far you have designed  $H\infty$  controllers that meet the performance objectives for the nominal actuator model. As discussed earlier, this model is only an approximation of the true actuator and you need to make sure that the controller performance is maintained in the face of model errors and uncertainty. This is called robust performance.

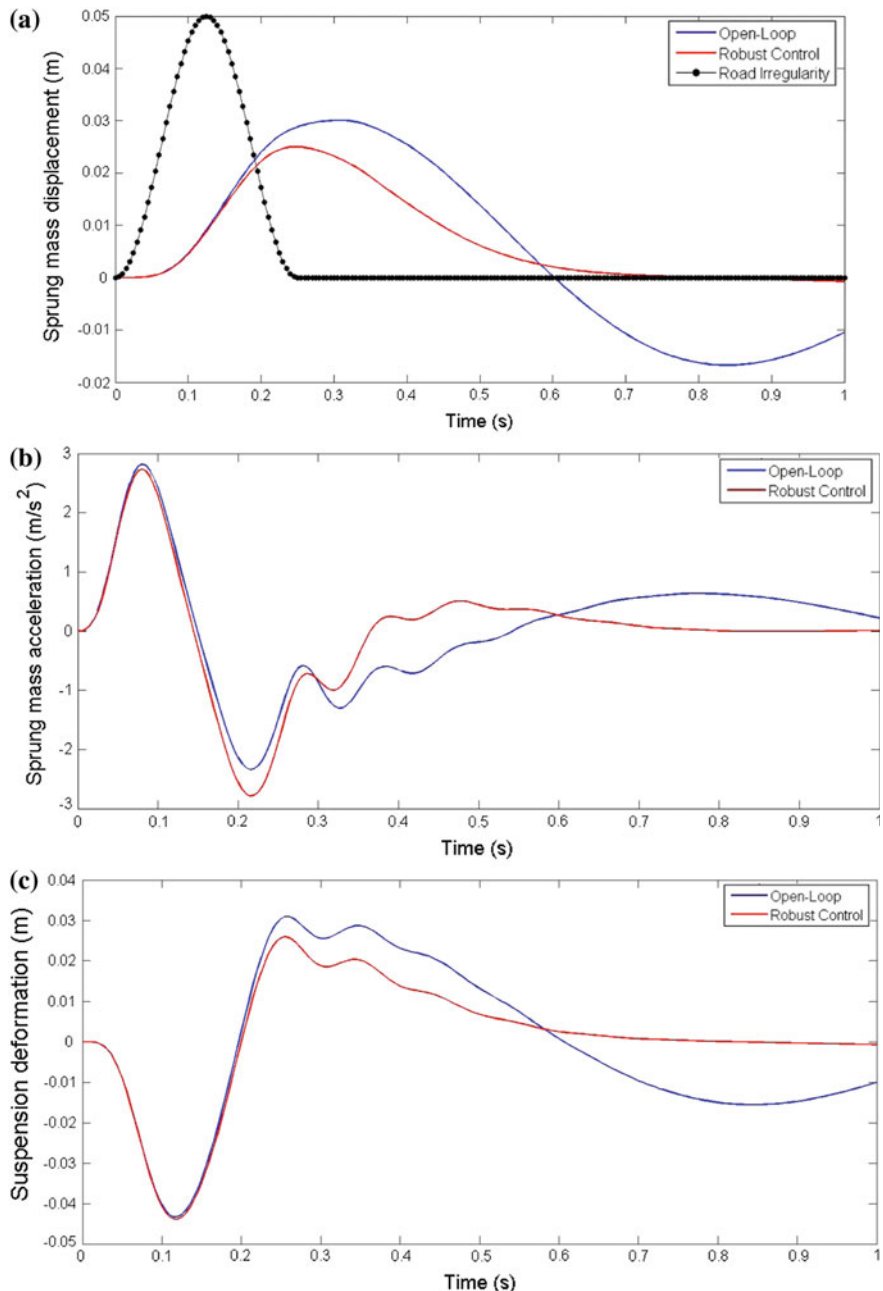


**Fig. 5.32** The sprung mass displacement, sprung mass acceleration, suspension deformation and force actuator

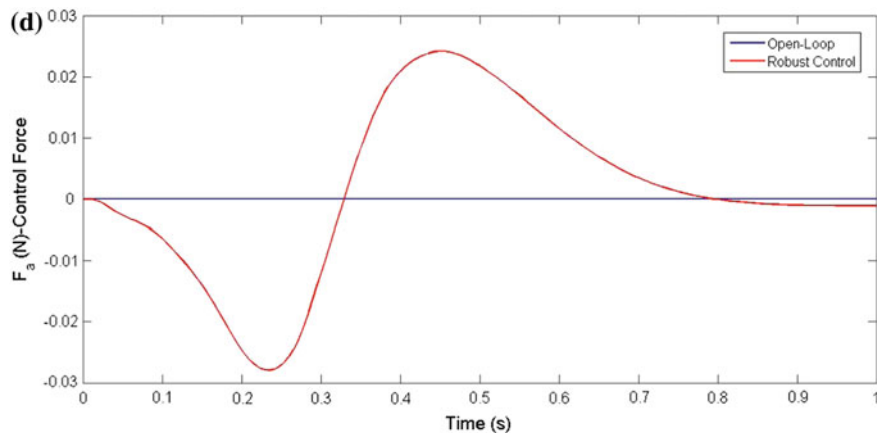


**Fig. 5.32** (continued)

Next use  $\mu$ -synthesis to design a controller that achieves robust performance for the entire family of actuator models. The robust controller is synthesized with the *dksyn* function using the uncertain model *lqcaric(:, :, 2)* corresponding to “balanced” performance ( $\beta = 0.5$ ). Simulate the nominal response to a road bump with the robust controller *Krob*. The responses are similar to those obtained with the “balanced”  $H\infty$  controller. The sprung mass displacement, sprung mass acceleration, suspension deformation and force actuator are presented in Fig. 5.32 for different conditions of open-loop and robust control condition and the differences can be appreciated.

In this manner, the strategy is to convert the robust control problem to an objective function/cost function of an optimization problem and to find a desired solution to the problem, accordingly. The core ideology is to design a system that can resist against the changes that can occur in the operating condition of the system, model or any uncertainty. Thus the aim is to provide a robustness against the performance of the desired optimized control problem. It can be mentioned that robust control is more likely better interpreted by the reliability. Although such a system might not have the equal performance such as optimal control, but the reliability of this system is more against any change and uncertainty happened in the system. As another example with different structure can be the adaptive control theory.

## References

1. Haykin, S. S. (1999). *Neural networks: A comprehensive foundation*. Upper Saddle River, NJ, USA: Prentice-Hall.
2. Jaiswal, S., Benson, E. R., Bernard, J. C., & Van Wicklen, G. L. (2005). Neural network modelling and sensitivity analysis of a mechanical poultry catching system. *Biosystems Engineering*, 92(1), 59–68.

3. Jang, J.-S. R. (1993). ANFIS: Adaptive-network-based fuzzy inference system. *IEEE Trans on Systems, Man and Cybernetics*, 23(3), 665–685.
4. Jang, J.-S. R., Sun, C.-T., & Mizutani, E. (1997). *Neurofuzzy and soft computing: A computational approach to learning and machine intelligence*. Upper Saddle River, NY: Prentice-Hall.
5. Takagi, T., & Sugeno, M. (1985). Fuzzy identification of systems and its applications to modeling and control. *Transactions on Systems, Man, and Cybernetics* 15, 116–132.
6. Petković, D., Gocic, M., Trajkovic, S., Shamshirband, S., Motamed, S., Hashim, R., & Bonakdari, H. (2015). Determination of the most influential weather parameters on reference evapotranspiration by adaptive neuro-fuzzy methodology. *Computers and Electronics in Agriculture*, 114, 277–284.
7. Karaağaç, B., Inal, M., & Deniz, V. (2012). Predicting optimum cure time of rubber compounds by means of ANFIS. *Materials and Design*, 35, 833–838.
8. Vapnik, V. (1995). *The nature of statistical learning theory* (2nd ed.). New York, NY: Springer. 309 pp.
9. Schölkopf, B., & Smola, A. J. (2002). *Learning with kernels: Support vector machines, regularization, optimization, and beyond*. Cambridge, MA: MIT Press. 626 pp.
10. Vapnik, V. N. (2000). *The nature of statistical learning theory*. New York: Springer.
11. Gunn, S. R. (1998). *Support vector machines for classification and regression*. Technical report. UK: Department of Electronics and Computer Science, University of Southampton.
12. Petković, D., Shamshirband, S., Saboohi, H., Ang, T. F., Anuar, N. B., & Pavlović, N. D. (2014). Support vector regression methodology for prediction of input displacement of adaptive compliant robotic gripper. *Applied Intelligence*, 41(3), 887–896.
13. Fleetwood, K. (2004, November). An introduction to differential evolution. In *Proceedings of Mathematics and Statistics of Complex Systems (MASCOS) One Day Symposium*, 26th November. Brisbane, Australia.
14. Atashpaz-Gargari, E., & Lucas, C. (2007). *Imperialist Competitive algorithm: An algorithm for optimization inspired by imperialistic competition*, IEEE congress on evolutionary computation (pp. 4661–4667).
15. Xing, B., & Gao, W. J. (2014). Imperialist competitive algorithm. In: Innovative computational intelligence: A rough guide to 134 clever algorithms (pp. 203–209). Berlin: Springer International Publishing.

# Chapter 6

## Applied Problems

1. Consider a running crawler tractor on (a) smooth rigid surface and (b) sloped surface as shown in Fig. 6.1. Given that the information of soil-tracked wheel contact length is 1.2 m ( $l = 1.2$  m), contact width is 0.6 m ( $b = 0.6$  m), tractor mass is 2.4 ton ( $m = 2400$  kg), soil cohesion is 15 kPa ( $c = 15$  kPa), soil internal friction angle is  $30^\circ$  ( $\varphi = 30^\circ$ ), and surface slope is  $10^\circ$  ( $\alpha = 10^\circ$ ) are available. Determine the gross traction and coefficient of traction:

### Answer

- (a) The gross traction is 24.4 kN and traction coefficient is 1.04.
- (b) By decomposing the forces along the slope surface:

$$\begin{aligned}H \cos \alpha + mg \sin \alpha &= H_{\max} = Ac + (mg \cos \alpha - H \sin \alpha) \tan \alpha \\H \cos \alpha + H \sin \alpha \tan \varphi &= Ac + mg \cos \alpha \tan \varphi - mg \sin \alpha \\H &= \frac{Ac + mg(\cos \alpha \tan \varphi - \sin \alpha)}{\cos \alpha + \sin \alpha \tan \varphi} \\&= \frac{1.2 \times 0.6 \times 15 \times 23.5(\cos 15 \tan 30 - \sin 15)}{\cos 15 + \sin 15 \tan 30} = 16 \text{ kN}\end{aligned}$$

$$\text{Traction Coefficient} = \frac{H}{mg \cos \alpha - H \sin \alpha} = \frac{16}{18.6} = 0.86$$

2. A common wheel supports the weight of  $W$  equal to 6 kN, creating contact area equal to  $0.1 \text{ m}^2$ . It is assumed that the pressure is uniformly distributed across the contact patch. Shear resistance with respect to normal stress for soil-soil and soil-tire interaction modes are presented in Fig. 6.2. Determine the maximum

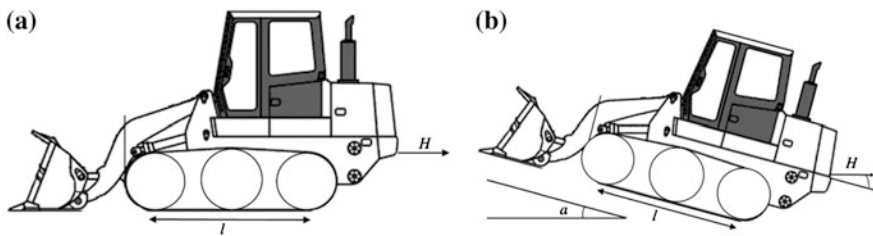
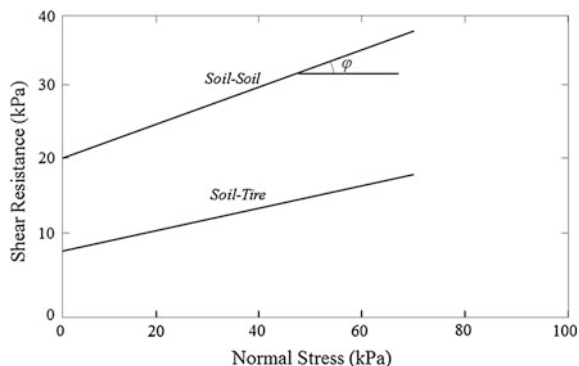


**Fig. 6.1** The crawler on **a** smooth rigid surface and **b** sloped surface

**Fig. 6.2** Shear resistance with respect to normal stress for soil-soil and soil-tire interaction modes



stress that the tire can produce when (a) wheel is equipped to a lugged tire and (b) wheel is not equipped to a lugged tire

### Answer

$$\sigma = \frac{6}{0.1} = 60 \text{ kPa}$$

$$H_{\max} = 36 \times 0.1 = 3.6 \text{ kN}$$

In another approach, it is possible to determine the soil shear stress using the Eq.  $Ac + W \tan \phi$ :

$$H_{\max} = 0.1 \times 20 + 6 \times 0.267 = 3.6 \text{ kN}$$

- (b) Using the same approach for the tire without lug, the tire soil contact is determined as following:

$$Ac + W \tan \varphi$$

$$H_{\max} = 0.1 \times 8 + 6 \times 0.142 = 1.65 \text{ kN}$$

3. Consider a trailer attached to an agricultural tractor through the hitch point given that the trailer mass is 60 kg and its center of gravity is positioned at 1.5 m from the rear axle and 1 m from the ground surface.
- In the case that the trailer contains a mass of 210 kg, determine the load on front wheels while traveling over a surface with no slope?
  - Determine the amount of water mass that can be filled inside the trailer and the tractor coefficient in the condition of traveling over a surface with the slope of 10° with the minimum load of 4 kN on front wheels.
  - Determine the maximum load on front wheels and the traction coefficient when the trailer is empty and the tractor is going down a hill with the slope of 10°.

### Answer

- (a) 5.92 kN  
 (b) Based on the vehicle performance Chap. 3 of this book, through Eqs. 3.7–3.19:

$$\begin{aligned} F_d &= \frac{W \cos \alpha x_G - W \sin \alpha (r + y_a) - W'_f l}{\cos \theta y' + \sin \theta x'} \\ &= \frac{27.9(0.532 - 0.133) - 7.52}{0.147 + 1.48} = 2.18 \text{ kN} = 224 \text{ kg} \end{aligned}$$

$$\text{Water mass} = 224 - 60 = 164 \text{ kg}$$

$$\psi' = \frac{W \sin \alpha + P \cos \theta}{W'_f} = \frac{27.9 \times 0.174 + 2.18 \times 0.174}{25.6} = 0.2$$

c)  $F_d = 9.48 \text{ kN}$ ,  $\psi' = -0.27$

4. Determine the height of the three-point-hitch of a tractor at the maximum tractive force that generates the tractor instability given that the contact area is 0.076 m<sup>2</sup>, soil cohesion is 2 kPa, and the internal friction angle is 32°.

Based on the vehicle performance Chap. 3 of this book, through Eqs. 3.7–3.19,  $W'_f$  will be zero in instability condition.

$$H = Ac + W \tan \varphi$$

With taking the moment about point O:

$$\begin{aligned} Hy' &= Wx' \\ Ac + W \tan \varphi y' &= Wx' \\ y' &= \frac{Wx'}{Ac + W \tan \varphi} \end{aligned}$$

This indicates that the height is a function of soil characteristics and its stiffness.

$$y' = \frac{285 \times 9.81 \times 0.54}{0.076 \times 2 \times 2000 + 2850 \times 9.81 + 0.625} = 0.85$$

5. Consider a vehicle with the net traction force of F, mass of M and acceleration of a:

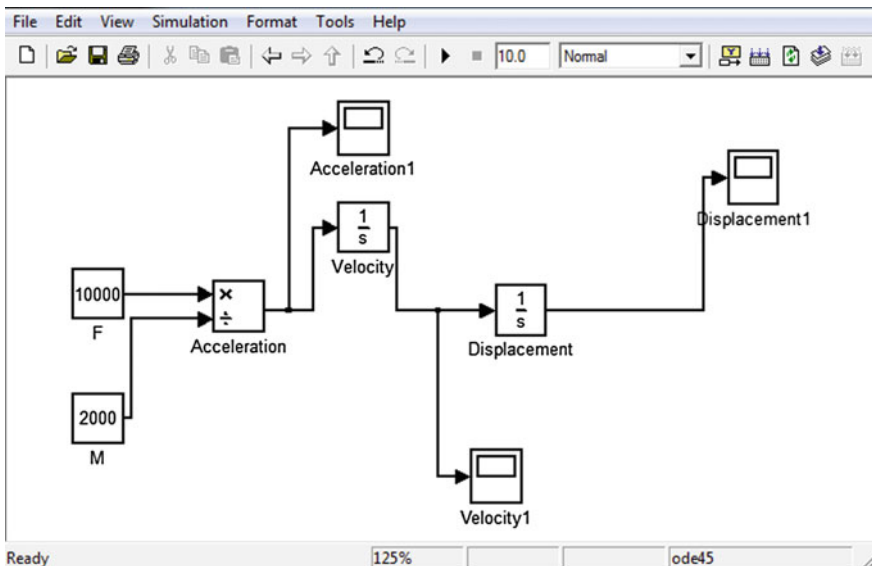
The acceleration of the car is presented by:

$$a = \frac{F}{M}$$

The velocity and displacement of car are also presented by:

$$a = \frac{dv}{dt}, \quad v = \frac{ds}{dt}$$

In order to construct a Simulink model of velocity and car displacement during a period of 10 s for a car with a constant net traction of 10 kN and vehicle mass of 2000 kg, the following is presented:



If the system is constructed in Simulink as abovementioned through its library, the following results on vehicle displacement, velocity and acceleration are presented in time history of 10 s.

